Università degli Studi di Trieste

DEPARTMENT OF PHYSICS
Master Degree Programme in Physics
Curriculum in Astrophysics and Cosmology, Earth and Environmental Physics
Sub-programme in Astrophysics and Cosmology

Master Thesis

Characterizing Galaxy Clusters through the Population of their Star-Forming Galaxies

Candidate:
Stefania Barsanti

Supervisor:
Prof. Marisa Girardi

Co-supervisors:
Dr. Andrea Biviano
Prof. Stefano Borgani

Academic Year 2014–2015

Sommario

Gli ammassi di galassie sono i sistemi legati gravitazionalmente più massicci nell'Universo. Per l'Universo locale è noto che le galassie con formazione stellare attiva tracciano la materia accresciuta dagli ammassi recentemente e che rappresentano una componente minore dell'intera popolazione galattica degli ammassi vicini. Tuttavia, tali galassie sono molto più comuni negli ammassi ad alto redshift ed alcune evidenze osservative suggeriscono che ci sia un'inversione della relazione densità-tasso di formazione stellare negli ammassi massicci a $z \sim 1.5-2$ rispetto a quella che caratterizza l'Universo locale.
Questa tesi ha come argomento lo studio delle galassie star-forming negli ammassi a redshift intermedio ed alto, ed aspira ad un duplice scopo:

- Il *primo obiettivo* riguarda l'analisi della cinematica delle galassie con formazione stellare attiva rispetto a quella delle galassie passive. Infatti, è ben noto che la dispersione di velocità delle galassie blu/ultimi tipi morfologici/con formazione stellare sia maggiore di quella delle galassie rosse/primi tipi morfologici/passive negli ammassi vicini e che, probabilmente, ciò sia dovuto alle anisotropie di velocità (e.g., Biviano et al. 1997 e referenze contenute). Tuttavia, la questione è ancora in discussione, in particolare per quanto riguarda gli ammassi a medio ed alto redshift (e.g., Biviano e Poggianti 2009; Girardi et al. 2015).

- Il *secondo obiettivo* si colloca nel contesto di preparazione della scienza per la missione spaziale ESA Euclid (lancio programmato per il 2020) ed è focalizzato sull'indagine dell' affidabilità della dispersione di velocità dei membri degli ammassi come mass proxy, cioè come stimatore della totale massa collassata dell'ammasso, negli ammassi distanti. Infatti, nel caso di Euclid lo strumento NISP potrà misurare solo i redshift delle galassie con forte formazione stellare attraverso la rilevazione delle linea spettrale Hα a $z \gtrsim 0.9$ (Laureijs et al. 2011, Sartoris et al. 2015).

Questo studio consiste nell'analisi di un campione di 52 ammassi di galassie ad intermedio ed alto redshift, $0.40 \leq z \leq 1.46$, per i quali ho raccolto i dati da letteratura per 7400 galassie: principalmente si tratta di dati nella banda ottica contenenti posizioni, velocità, magnitudini, colori, e caratteristiche spettrali delle galassie. I dati provenivano da autori diversi e quindi la costruzione del catalogo ha richiesto un attento lavoro di omogeneizzazione.
Per quanto riguarda il *primo obiettivo* i problemi affrontati e risolti sono stati i seguenti:

1. selezione delle galassie membri degli ammassi (P+G, Girardi et al. 2015; altre procedure classiche ampiamente usate in letteratura);

2. determinazione delle principali proprietà cinematiche e dinamiche degli ammassi: dispersione di velocità σ_v e massa viriale M_{200} (dalla relazione $\sigma_v - M_{200}$ di Munari et al. 2013);

3. separazione delle galassie rosse/passive dalle blu/con formazione stellare usando i diagrammi colore-magnitudine e le misure della larghezza equivalente della linea spettrale di emissione [OII];

4. uso di vari test statistici, anche non parametrici, per confrontare le dispersioni di velocità delle popolazioni rosse e blu, σ_{red} e σ_{blue}, rispettivamente; (test di Kolmogorov-Smirnov, Wilcoxon, del segno, F-test e t-test);

5. analisi dello spazio delle fasi proiettate.

Per quanto riguarda il *secondo obiettivo* i problemi esaminati e risolti sono stati:

1. selezione delle galassie con formazione stellare per un campione di 17 ammassi distanti nel range $0.80 \leq z \leq 1.46$;

2. calcolo del flusso in Hα per ogni galassia e selezione delle galassie con un flusso maggiore dei seguenti flussi limite in Hα: $F(\mathrm{H}\alpha)_{\mathrm{lim,obs}} = 2 \times 10^{-16}$ erg cm^{-2} s^{-1} per simulare il satellite Euclid e $F(\mathrm{H}\alpha)_{\mathrm{lim,obs}} = 1 \times 10^{-16}$ erg cm^{-2} s^{-1} per tenere conto di una possibile inversione della relazione densità-tasso di formazione stellare ad alti z;

3. procedura di selezione delle galassie appartenenti agli ammassi ed analisi cinematica.

I risultati ottenuti riguardanti il confronto cinematico tra le diverse popolazioni galattiche estendono agli ammassi a redshift intermedio le conclusioni stabilite in letteratura per gli ammassi locali. Considerando un campione di 32 ammassi a redshift intermedio ($0.40 \leq z < 0.80$), i miei risultati possono essere riassunti come segue:

- le galassie blu e quelle rosse sono segregate nello spazio delle velocità, essendo $\sigma_{blue} > \sigma_{red}$. In particolare, il test del segno e quello di Wilcoxon mostrano che la probabilità per la distribuzione delle dispersioni di velocità delle galassie blu di essere maggiore di quella delle galassie rosse è 99.65% e 99.62%, rispettivamente;

- le galassie più luminose sono segregate in velocità in accordo con uno scenario dovuto al processo di attrito dinamico.

La spiegazione generalmente adottata per questo quadro fenomenologico consiste nel fatto che le galassie blu negli ammassi locali ed a redshift intermedio rappresentano una popolazione accresciuta molto recentemente, mentre le galassie rosse, le quali appartengono all'ammasso da un tempo più lungo, sono una popolazione più rilassata dinamicamente.
D'altra parte, in base all' analisi di un campione di 14 ammassi ad alto redshift ($0.80 \leq z \leq 1.46$), ho ottenuto che:

- non si ha evidenza di segregazioni in velocità o in luminosità negli ammassi distanti: questo è il risultato più importante della mia tesi.

L'interpretazione di questo ultimo effetto osservativo è che gli ammassi ad alto redshift sono osservati più vicini alla loro epoca di formazione rispetto agli ammassi locali, per cui sia le galassie rosse sia quelle blu vengono accresciute recentemente e quindi hanno proprietà cinematiche simili. In particolare, l'attrito dinamico non ha ancora avuto il tempo di influenzare la cinematica delle galassie. Questo scenario può essere plausibile nel caso in cui le galassie rosse partecipino alla formazione dell'ammasso insieme a quelle blu (ad esempio se entrambe appartengono a piccoli gruppi), e/o nel caso in cui una possibile trasformazione morfologica dal tipo blu a quello rosso avvenga molto velocemente, con un tempo caratteristico molto più piccolo del tempo coinvolto nella segregazione cinematica.
Nel caso degli ammassi locali è noto che le popolazioni di galassie rosse e blu, sebbene caratterizzate da una differente relazione dispersione di velocità-massa dell'ammasso, possono essere entrambe usate come traccianti del potenziale gravitazionale. Al contrario, per gli ammassi distanti, la mia tesi fornisce la prima evidenza osservativa secondo cui la cinematica delle galassie blu/con formazione stellare è indistinguibile da quella delle galassie rosse/passive. I punti da chiarire con studi futuri consistono nel comprendere quanto entrambe le popolazioni siano buoni traccianti del potenziale gravitazionale dell'ammasso e, soprattutto, nel calibrare la relazione dispersione di velocità-massa dell'ammasso.

La mia analisi riguardante gli ammassi ad alto redshift ($0.80 \leq z \leq 1.46$) continua in quello che è il primo studio di previsione dei risultati provenienti dalle future osservazioni spettroscopiche del satellite Euclid ed è focalizzato sul determinare l'affidabilità delle stime di σ_v. Indicando con $\sigma_{\mathrm{H}\alpha}$ la dispersione di velocità delle galassie luminose in Hα, i risultati ottenuti possono essere riassunti nei seguenti punti:

- la soglia del flusso limite in Hα limita fortemente il numero di ammassi osservabili spettroscopicamente da NISP e il numero delle galassie membro; questo problema è già stato suggerito da precedenti studi (e.g., Sartoris et al., 2015);
- applicando il test F per ognuno dei 4 ammassi rimanenti che ho analizzato, non ho trovato una differenza significativa tra $\sigma_{\mathrm{H}\alpha}$ e σ_{blue} entro le rispettive incertezze;
- qualitativamente, i miei risultati suggeriscono che tipicamente $\sigma_{\mathrm{H}\alpha} > \sigma_{blue}$, i.e. c'è un effetto di segregazione in velocità tra le galassie luminose in Hα e quelle blu. Tuttavia, disponendo di un campione di solo 4 ammassi non mi è possibile fornire un preciso risultato statistico.

L'efficienza delle procedure di selezione dei membri nel caso dei campioni di galassie luminose in Hα (in particolare, il metodo P+G) suggerisce che le stime delle dispersioni di velocità di queste galassie, e quindi quelle basate sui futuri dati spettroscopici di NISP, possono essere utili mass proxy dopo un'appropriata calibrazione.
Inoltre, l'evidenza presentata nel terzo punto, sebbene qualitativa, è in accordo con uno scenario più generale in cui il fenomeno della segregazione cinematica avviene tra differenti tipi di galassie, considerando che le galassie luminose in Hα sono quelle più blu entro la popolazione galattica blu. Tenendo in considerazione anche i risultati della prima parte della mia tesi, la soglia in colore tra le galassie segregate e quelle non segregate è più blu a redshift più alti, o - usando l'asse temporale in senso crescente - essa è più rossa a redshift più bassi. Dunque, i miei risultati possono avere interessanti implicazioni per i processi dinamici che regolano l'evoluzione delle galassie legata all'evoluzione degli ammassi. Tuttavia, un campione di ammassi più numeroso è ovviamente necessario per confermare i miei risultati riguardanti le galassie luminose in Hα negli ammassi distanti.
Il naturale passo successivo in questo progetto di ricerca sarà studiare la relazione tra la dispersione di velocità e la massa degli ammassi a redshift intermedio ed alto, calcolando le dispersioni di velocità usando differenti popolazioni - in particolare le galassie blu e quelle luminose in Hα - e con stime di massa ottenute da altri indicatori o lavorando con appropriate simulazioni di ammassi con massa nota. Questo studio sarà utile sia per determinare la calibrazione della relazione dispersione di velocità-massa sia per interpretare in un modo più ampio i risultati di questa tesi riguardo alla segregazione cinematica.

Contents

Contents

List of Figures

List of Tables

Introduction

Galaxy clusters are the largest gravitationally bound systems in Universe and are characterized by different physical features, like number of member galaxies, mass, radius, velocity dispersion, luminosity and X-ray temperature. The distribution functions of such observational cluster quantities and their dependence on redshift can provide strong constraints on cosmological scenarios. Moreover, mass proxies, like velocity dispersion, are able to define cosmological parameters.
Clusters are important laboratories in which to study the evolution of galaxy populations and distant clusters contain an amount of star-forming galaxies larger than nearby ones.
The aim of this thesis is to study the evolution of galaxy populations and the properties of star-forming galaxies in distant clusters. This topic is particularly important in the context of the preparatory science for the ESA Euclid mission (launch date planned for 2020), which will study only star-forming galaxies.
This thesis analyzes 52 clusters at intermediate and high redshift, $0.4 \leq z \leq 1.4$, with a twofold purpose. The first purpose is to probe the kinematics of late-type/blue/star-forming galaxies within clusters in comparison with early-type/red/passive galaxies, which is a question still under discussion, in particular at high redshifts. The second purpose is to investigate the performance of velocity dispersion of member galaxies as a proxy for the total collapsed cluster mass. In the Euclid case, only redshifts for star-forming galaxies will be measured through the detection of the Hα line at $z \gtrsim 0.9$.
For each cluster, I select cluster members and carry out the analysis of photometric data drawing the color-magnitude diagram in order to separate galaxies belonging to the red sequence from bluer galaxies. When available, I also use the equivalent width of the spectral line [OII]. In order to study the kinematics of different galaxy populations, I calculate the velocity dispersions of red and blue galaxies separately, checking for any difference and analyzing a possible trend with cluster redshift. For star-forming galaxies I use magnitudes and colors to estimate stellar masses and star formation rates, and finally Hα fluxes to compare with Hα limit flux expected for Euclid.
This thesis is organized as follows:

- from Chapter 1 to Chapter 4, I present the properties of clusters, their galaxy populations and the ESA space mission Euclid;
- from Chapter 5 to Chapter 12, I describe the data catalogue, cluster member selection methods, velocity dispersion estimates, separation between star-forming galaxy members and passive ones, and comparison of their velocity dispersion distributions and values;
- from Chapter 13 to Chapter 16, I mimic Euclid spectroscopic observations for blue galaxies, repeating the procedures of member selection and velocity dispersion estimation;
- finally, in Chapter 17, I write my conclusions and future perspectives.

In this thesis I assume the following cosmological parameters: $H_0 = 70\ \mathrm{kms^{-1}Mpc^{-1}}$, $\Omega_m = 0.30$ and $\Omega_\Lambda = 0.70$.

Chapter 1

Clusters of galaxies

1.1 Clusters as multicomponent systems

Galaxies are not smoothly distributed in space and form systems of all sizes: galaxy pairs, small groups, large clusters and superclusters formed from several groups and clusters.
Galaxy clusters are structures containing from 10 to 1000 bright galaxies and are the largest known gravitationally bound, quasi virialized, systems in the universe. The mass budget of massive clusters consists of 85−90% dark matter and 10−15% baryons, primarily hot X-ray-emitting plasma, and only ∼1% in stars. Thus, the dominant component of galaxy clusters is dark matter, without which it is impossible to explain their total mass: the first evidence of dark matter was found in the 1930s by Fritz Zwicky in the Coma cluster, when he noted a large discrepancy between its virial and luminous mass (Zwicky, 1937).
The typical cluster radius is about 1-2 Mpc, the typical mass is $10^{14} - 10^{15}$ $M_{\odot}$ and the typical value of velocity dispersion of cluster galaxies is 600−1000 kms^{-1}.
Clusters are suitable laboratories in which to study galaxy populations, providing clues to better understand the effects of the local environment on galaxy proprieties and galaxy evolution (e.g., Demarco et al., 2007). The combination of optical photometry and spectroscopy, X-ray observations and studies of the Sunyaev-Zel'dovich effect allows us to get important insights into physical properties of the cluster members, the intracluster medium (ICM) and the determination of the gravitational mass and its distribution with independent methods.
The figures 1.1, 1.2 and 1.3 represent examples of galaxy clusters in the optical band at different distances from Earth.

Figure 1.1: Virgo cluster, 60 millions of light years from Earth (credit to Eagle Ridge Observatory, Foresthill, CA).

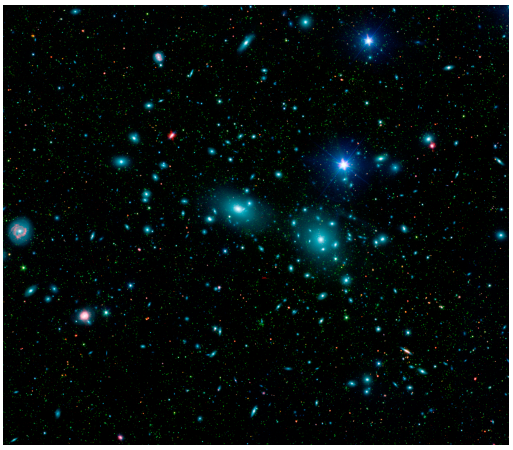

Figure 1.2: Coma cluster, 350 millions of light years from Earth (mosaic credit to Sloan Digital Sky Survey/Spitzer Space Telescope).

Figure 1.3: Abell 1689, 2.5 billions of light years from Earth (credit to Hubble Space Telescope).

1.2 Clusters as cosmological probes

Clusters of galaxies are visible tracers of the network of matter in the universe, making the high-density regions where filaments of dark matter join together. In the hierarchical scenario of large-scale structure, clusters form via merging of smaller clumps and accretion of material from large scale filaments (e.g., Borgani and Guzzo, 2001; Evrard and Gioia, 2002): they form at the nodes of filaments, growing through the continuous accretion of individual galaxies and groups from the surrounding field. The precursors of the filaments should be present around distant clusters, containing many of the galaxies which will eventually infall into the virialized core and form the cluster population observed today. From the observational side, signatures of past merging processes are found in cluster substructure and evidence of ongoing cluster mergers comes from optical and X-ray studies (Böhringer and Schuecker, 2001; Buote, 2002; Girardi and Biviano, 2002; Evrard, 2004).

1 Clusters of galaxies

Figure 1.4 shows a simulated universe: a cosmic web which connects individual galaxies, groups and clusters by filaments of dark matter, surrounding large underdense voids.

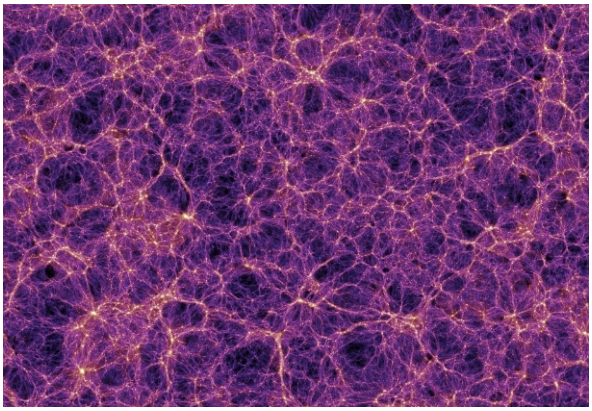

Figure 1.4: Simulations of galaxy clustering: galaxy clusters as nodes of dark matter filaments (from Millennium Simulation project).

Galaxy clusters have long served as a bridge between astrophysics and cosmology. Their distribution at varying masses, across space and time, is an important tool with which to constrain cosmological models, since their abundance as a function of redshift is very sensitive to both the underlying geometry of the universe and the growth of structure on large scale. The knowledge of the proprieties of galaxy clusters and their evolution plays an important role in the study of large-scale structure formation constraining cosmological parameters. In fact, clusters are tracers of the matter density peaks in the universe and studying them over a wide range in redshift provides an insight into the process of mass assembly of structures through cosmic history.
There are a lot of different methods based on galaxy clusters as cosmological probe:

- The mass function of nearby clusters constrains the amplitude of power spectrum at the scale of clusters. The evolution of this mass function is bound to the linear growth rate of density perturbations and provides estimates for the density parameters of baryonic+dark matter Ω_m and of dark energy Ω_Λ.
- The large-scale distribution of clusters contains information about shape and amplitude of the dark matter power spectrum.
- The mass-to-light ratio in optical band is used to estimate the matter density parameter, assuming to know the mean luminosity density of the universe under the assumption that light traces mass with the same efficiency both inside and outside cluster.
- The baryonic fraction in nearby clusters helps us to evaluate Ω_m, by knowing the cosmic density parameter of baryons. Moreover, the baryonic fraction of distant clusters is an important cosmological test to constrain features of dark energy, assuming baryons inside clusters do not evolve.

Results from galaxy clusters can be successfully combined to results based on other cosmological probes, such as type-Ia supernovae and cosmic microwave background (CMB). Figure 1.5 shows best fit confidence regions in the Ω_Λ versus Ω_m plane. The diagonal line represents a flat universe. The plot illustrates that almost 70% of the total energy density in the universe is in the form of dark energy, which causes the expansion of the universe to accelerate.

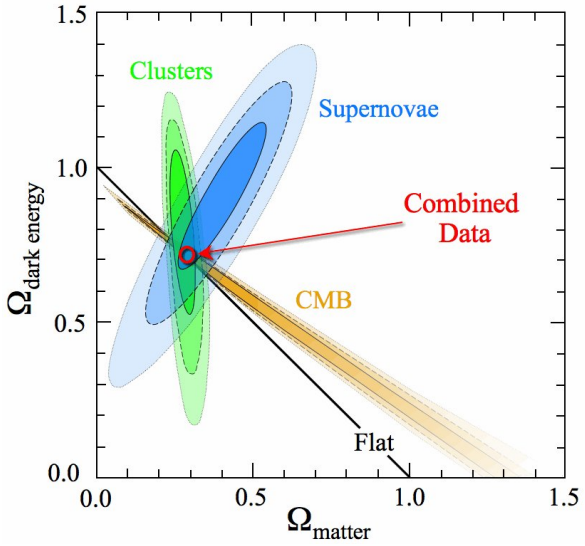

Figure 1.5: Lambda-CDM model (credit to Dark Matter Group of University Collage London).

In particular, distant galaxy clusters are among the most promising cosmological probes to shed new light on the properties and evolution of dark energy. In fact, massive galaxy clusters at high redshift are unique laboratories to explore the structure and growth of the underlying virialized dark matter halos.

1.3 Cluster mass determination and mass proxies

Since clusters provide a powerful tool tracing the growth of cosmic structures and constraining cosmological parameters, a crucial aspect in the cosmological application of galaxy clusters concerns the reliability of mass estimates to investigate the evolution of the mass function.
Mass of clusters is not a directly observable quantity but can be determined in several ways, e.g. by assuming the condition of equilibrium of the intracluster plasma (e.g., Ettori et al., 2002) or galaxies (e.g., Katgert et al., 2004) within the cluster potential well, or by measuring the gravitational lensing distortion of the images of background galaxies by cluster gravitational field (e.g., Hoekstra, 2003). The X-ray and the lensing techniques are two methods that are widely used to infer the mass profile of galaxy clusters. The former makes use of the observations of the X-ray emission of the hot ICM. The lensing technique is based on the relativistic effect of distortion of the trajectories of light emitted by distant background galaxies caused by the mass of the observed cluster. Both methods have some limitations. In the case of X-ray technique, the limitation comes from the usual assumption that the plasma of the cluster is in hydrostatic equilibrium, and the cluster approximately spherically symmetric (Ettori et al., 2002) with no important recent merger activity (Böhringer and Werner, 2010). As for the lensing technique, its limitation is that it only allows computing the projected mass, and this includes all the line-of-sight (LOS) mass contributions. Moreover, these two methods of mass measurements can only be applied to clusters for which high-quality data are available. When these are not available, it is still possible to infer cluster mass from other observed quantities, the so-called mass proxies, which are at the same time relatively easy to measure and characterized by tight scaling relations with cluster mass (Kravtsov and Borgani, 2012), that need to be calibrated with precise mass measurements. Examples of such mass proxies are the total thermal content

of the intracluster plasma, measured from either X-ray or Sunyaev-Zel'dovich (SZ) observations, the optical luminosity or richness traced by the cluster galaxy population, and velocity dispersion of member galaxies (Biviano et al., 2006; Saro et al., 2013).
The velocity dispersion (σ) is the statistical dispersion of velocities with respect to the mean velocity for a group of celestial objects. The use of velocity dispersion as a mass proxy for cluster mass is particularly interesting in view of ongoing (BOSS, White et al. 2011) and forthcoming (Euclid, Laureijs et al. 2011) large spectroscopic galaxy surveys. It is crucial to understand whether a cluster velocity dispersion measured on its member galaxies is a reliable proxy for its mass. The evidence of a fair equipartition between galaxy and gas energy suggests that σ, like the X-ray temperature of the ICM, can be a good estimate of cluster potential well (Girardi et al., 1996). The potential well of the cluster, due to the mass, is the main driver of the orbital motion of the galaxies, which in the absence of mutual interactions, can be treated as test collisionless particles in the gravitational potential of the cluster. The kinematics of galaxies therefore carries the information about the mass content of the cluster. A full description of the dynamics should be given in a six-dimensional phase space, but the observations are able to capture only three of these dimensions, namely two for the position on the sky and one for the LOS velocity. This is one of the most important limitations of a mass estimate via observation of the kinematics of galaxies and, to overcome this problem, most methods assume spherical symmetry (Munari et al., 2014).
Many efforts have been devoted to the calibration of the observable-mass scaling relations at different wave bands (Arnaud et al., 2010; Planck Collaboration, 2011; Reichert et al., 2011; Rozo et al., 2011; Rykoff et al., 2012; Ettori, 2013; Rozo et al., 2014; Mantz et al., 2015) and in the definition of mass proxies which are at the same time precise, (i.e. characterized by a small scatter in the scaling against cluster mass), and robust, (i.e. relatively insensitive to the details of cluster astrophysics) (Kravtsov et al., 2006). Calibration of scaling relations σ-M can be based on detailed multiwavelength observations of control samples of galaxy clusters. On the other hand, detailed cosmological simulations are quite useful to calibrate such scaling relations independently of possible observational systematic effects (Borgani and Kravtsov, 2011). The implementation of baryonic physics can play a fundamental role in such analyses. Since galaxies are nearly collisionless tracers of the gravitational potential, we expect velocity dispersion to be more robust than X-ray and SZ mass proxies against the effects induced by the presence of baryons and by their thermal history (Munari et al., 2013).
Finally, an important aspect relative to mass proxies concerns the determination of the mass density profile for a representative cluster sample over a wide radial range, from kpc to Mpc scales. In fact, a very accurate cluster mass density profile can be achieved only if all methodologies available to measure the mass distribution of clusters are employed, namely gravitational lensing, galaxy dynamics and X-ray hydrostatic equilibrium. The reason is that each method is most sensitive to a different radial range and is prone to different inherent systematic effects: e.g., structure along the line of sight for lensing, substructure and velocity anisotropy of orbits for dynamical masses, deviations from hydrostatic equilibrium for X-ray masses. Only by combining and cross-checking mass determinations from all these methods can cluster density profiles be recovered with the required accuracy, provided that a high quality and homogeneous dataset is available for a representative sample of clusters, with a known selection function (Rosati et al., 2014).

Chapter 2

Star-forming and passive galaxies

2.1 Morphological classification

The universe is characterized by different morphological kinds of galaxies: some galaxies have smooth light profiles with elliptical isophotes, others have spiral arms together with an elliptical-like central bulge, and still others have irregular or peculiar morphologies. Based on such features, Hubble ordered galaxies in a morphological sequence, which is now referred to as the Hubble sequence. The following figure 2.1 shows the schematic representation of the Hubble sequence.

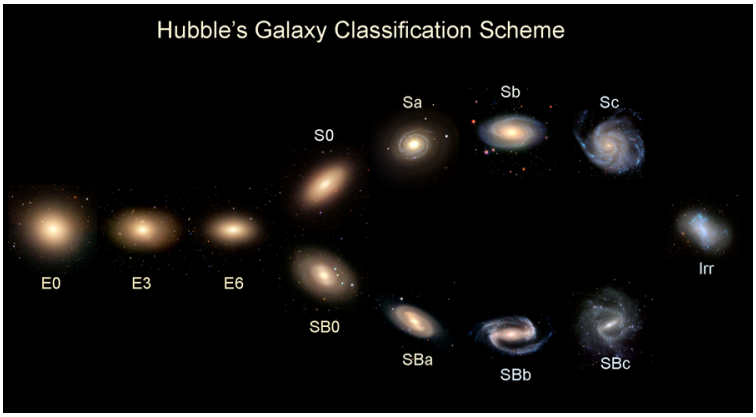

Figure 2.1: Hubble sequence of galaxy morphologies (credit to Lectures of Prof. James Imamura, University of Oregon).

Hubble's scheme classifies galaxies into four broad classes:

1. **Elliptical galaxies**: these have smooth, almost elliptical isophotes and are divided into subtypes E0,E1,...,E7, where the integer is the one closest to $10(1 - b/a)$, with a and b the lengths of the semimajor and semiminor axes.

2. **Spiral galaxies**: these have thin disks with spiral arm structures. They are divided into two branches, barred spirals and normal spirals, according to whether or not a recognizable bar-like structure is present in the central part of the galaxy. On each branch, galaxies are further divided into three classes, a, b, c, according to the following three criteria:

   - the fraction of the light in the central bulge;
   - the tightness with which the spiral arms are wound;

- the degree to which the spiral arms are resolved into stars, HII regions and ordered dust lanes.

3. **Lenticular or S0 galaxies**: this class is intermediate between ellipticals and spirals. Like ellipticals, lenticulars have a smooth light distribution with no spiral arms or HII regions. Like spirals they have a thin disk and a bulge, but the bulge is more dominant than that in a spiral galaxy. They may also have a central bar, in which case they are classified as SB0.

4. **Irregular galaxies**: these objects have neither a dominating bulge nor a rotationally symmetric disk and lack any obvious symmetry. Rather, their appearance is generally patchy, dominated by a few HII regions. Hubble did not include this class in his original sequence because he was uncertain whether it should be considered an extension of any of the other classes. Nowadays irregulars are usually included as an extension to the spiral galaxies.

Ellipticals and lenticulars together are often referred to as early-type galaxies, while the spirals and irregulars make up the class of late-type galaxies. Indeed, traversing the Hubble sequence from the left to the right the morphologies are said to change from early- to late-type. This historical nomenclature has no direct physical basis: the reference to early- or late-type should not be interpreted as reflecting a property of the galaxy's evolutionary state.
The figures 2.2, 2.3 and 2.4 show examples of spiral and elliptical galaxies.

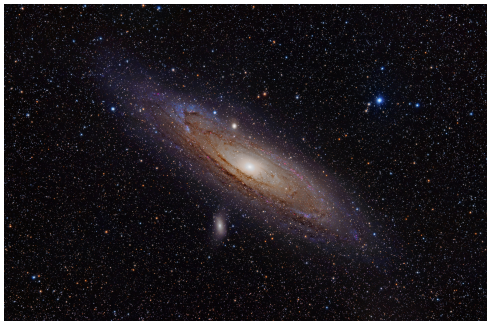

Figure 2.2: Spiral galaxy Andromeda (credit to Hubble Space Telescope).

Figure 2.3: Barred spiral galaxy NGC 1300 (credit to Hubble Space Telescope).

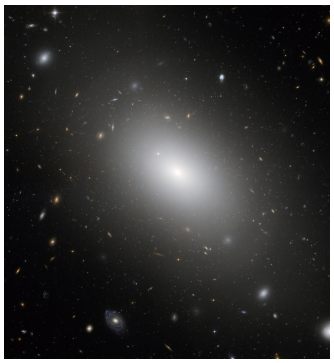

Figure 2.4: Elliptical galaxy NGC 1132 (credit to Hubble Space Telescope).

2.2 Photometric-Spectroscopic classification

The precise determination of the galaxy morphology requires extremely high resolution observations, especially for distant galaxies. On the other hand, analyzing spectroscopic and photometric data, it is possible to understand if a galaxy is forming stars or not. Thus, there is a more general galaxy classification which divides galaxies between star-forming/blue/late-type and passive/red/early-type.

- **Star-forming/Blue/Late-type galaxies**: these galaxies have an active star formation activity and contain a large amount of dust and gas, which are indispensable for the star formation process. They are characterized by a young and metal poor stellar population which provides the blue color and, from the morphological point of view, they are in general spiral and irregular galaxies, commonly called late-type galaxies. These galaxies contain a disk and spiral arms where the star formation process occurs. Their spectrum shows strong emission lines, especially Hα(λ6563) and [OII](λ3727), due to the light produced by hot young stars, which heat and ionize the interstellar medium.

- **Passive/Red/Early-type galaxies**: these systems are characterized by smooth, elliptical surface brightness distributions, contain little cold gas and dust, and have red photometric colors, characteristic of an old and metal rich stellar population. They are not forming stars, contain a small amount of gas and dust and are mainly ellipticals and lenticulars, thus early-type galaxies. All stars form during the first life phases of these galaxies, consuming almost the whole available gas. The remaining gas is heated by violent processes like supernovae explosions and then is expelled out the galaxy. Their spectrum illustrates absorption lines and has no emission lines because of the absence of star formation activity.

The comparison between spectra of star-forming galaxies and that of passive galaxies is shown in figure 2.5: the typical spectrum of a star-forming galaxy is characterized by strong Hα and [OII] emission lines, due to hot young stars which heat the surrounding gas, and by absorption features due to the older, underlying stellar population; the typical spectrum of a passive galaxy contains strong absorption lines, due to metals in the stellar atmospheres of the low luminosity stellar population, and few to no emission lines, as there are essentially no young stars and no hot interstellar gas.
From ellipticals to late-types, the blue continuum and emission lines become systematically stronger. For early-type galaxies, which lack hot, young stars, most of the light emerges at the longest wavelengths, where one sees absorption lines characteristic of cool K stars. In the blue, the spectrum of early-type galaxies has strong H and K absorption lines of calcium and the G band, typical of solar type stars. Such galaxies emit little light at wavelengths shorter than 4000 Å break and have no emission lines. The 4000 Å break occurs because many heavy elements in the atmospheres of old stars absorb some of the starlight around this particular wavelength. In contrast, late-type galaxies and starbursts emit most of their light in the blue and near-ultraviolet, giving rise to strong emission lines.

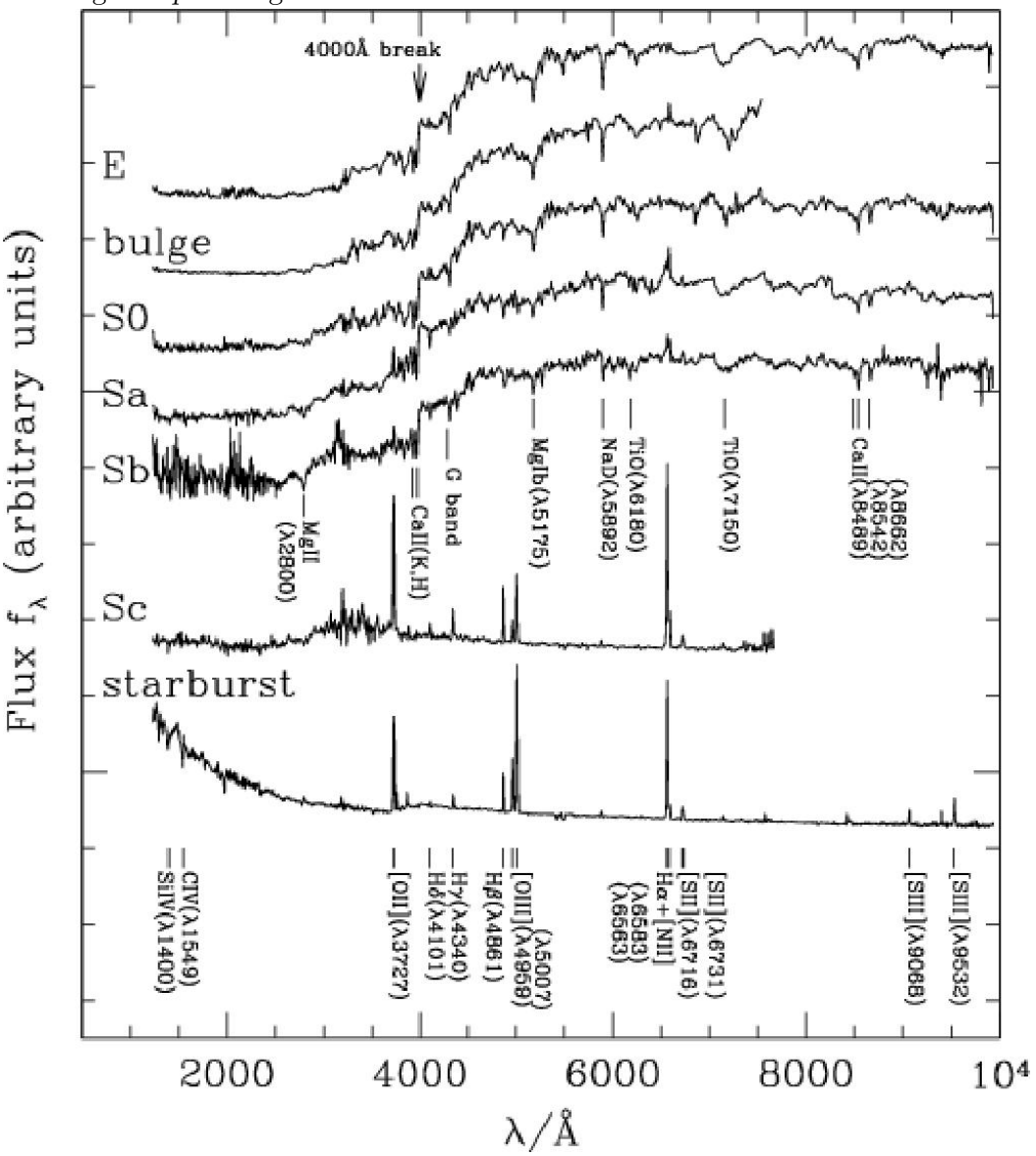

Figure 2.5: Comparison between passive and star-forming spectra (credit to Lectures of Prof. James Schombert, University of Oregon).

2.3 Hα and [OII] spectral lines as star formation tracers

Star formation rates (SFRs) in galaxies provide vital clues to the physical nature of the Hubble sequence and are key probes of the evolutionary histories of galaxies (Kennicutt, 1998). The Hα and [OII] spectral lines are important star formation tracers and indicate that star-forming galaxies are characterized by high values of SFRs whereas early-types, which don't form stars, have a SFR that goes to zero at the present day.
The most dramatic change in the integrated spectrum with galaxy type is a rapid increase in the strengths of the nebular emission lines from early- to late-type . The nebular lines effectively re-emit the integrated stellar luminosity of galaxies shortward of the Lyman limit, so they provide a direct, sensitive probe of the young massive stellar population. Most applications of this

method have been based on measurements of the Hα line, which is a specific deep-red visible spectral line in the Balmer series created by hydrogen with a wavelength of 6562.8 Å. Hα line occurs when a hydrogen electron falls from its third to second lowest energy level and it is a typical strong emission line of star-forming galaxies. The conversion factor between ionizing flux and the SFR is usually computed using evolutionary synthesis model. Only stars with masses $\geq$ 10 $M_\odot$ and lifetimes $\leq$ 20 Myr contribute significantly to the integrated ionizing flux, so the emission lines provide a nearly instantaneous measure of the SFR, independent of the previous star formation history. The calibration of Kennicutt et al. (1994) yields, for the Salpeter initial mass function (IMF) over the mass range 0.1-100 $M_\odot$, $\psi(m)\ \alpha\ m^{-2.35}$, and for solar abundances, the following relation:

$$\mathrm{SFR}(M_\odot \mathrm{yr}^{-1}) = 7.9 \times 10^{-42} \mathrm{L}(\mathrm{H}\alpha)(\mathrm{erg\ s}^{-1}), \tag{2.1}$$

where L(Hα) is the Hα luminosity.

The largest limitations of this method are its sensitivity to uncertainties in the extinction internal to the galaxy, the assumption of an IMF and the hypothesis that all of the massive star formation is traced by the ionized gas. Extinction is probably the most important source of systematic error in Hα-derived SFRs and can be measured by comparing Hα fluxes with those of IR recombination lines or thermal radio continuum. The ionizing flux is produced almost exclusively by stars with $M \geq 10$ $M_\odot$, so Hα-derived SFRs are especially sensitive to the form of the IMF. Fortunately, the Hα equivalent widths and broadband colors of galaxies are very sensitive to the slope of the IMF over the mass range $1 - 30$ $M_\odot$, and these can be used to constrain the IMF slope (Kennicutt, 1993; Kennicutt et al., 1994). The properties of normal disks are well fitted by a Salpeter IMF, consistent with observations of resolved stellar population in nearby galaxies.

Since the Hα emission line is redshifted out of the visible window beyond $z \sim 0.5$, there is considerable interest in calibrating bluer emission lines as quantitative SFR tracers. Unfortunately, the integrated strengths of Hβ and the higher order Balmer emission lines are poor SFR diagnostic because these lines are weak and stellar absorption influences more strongly the emission-line fluxes. These lines, in fact, are rarely seen in emission at all in the integrated spectra of galaxies earlier than Sc.

The strongest emission feature in the blue is the [OII] forbidden-line doublet. The [OII] spectral line has the wavelength 3727 Å and is due to the only once ionized oxygen. It is a forbidden line because it isn't allowed by the selection rules of quantum mechanics. Although the transitions are nominally "forbidden", there is a small probability of their spontaneous occurrence, should an atomic nucleus, atom or molecule be raised to an excited state. More precisely, there is a certain probability that such an excited entity will make a forbidden transition to a lower energy state per unit time; by definition, this probability is much lower than that for any transition permitted or allowed by the selection rules. Therefore, if a state can de-excite via a permitted transition (or otherwise, e.g. via collisions) it will almost certainly do so rather than choosing the forbidden route. Nevertheless, most "forbidden" transitions are only relatively unlikely: states that can only decay in this way (so-called meta-stable states) usually have lifetimes of order milliseconds to seconds, compared to less than a microsecond for decay via permitted transitions. Forbidden emission lines have only been observed in extremely low-density gases and plasmas, either in outer space or in the extreme upper atmosphere of Earth. Even the hardest laboratory vacuum on Earth is still too dense for forbidden line emission to occur before atoms are collisionally de-excited. However, in space environments, densities may be only a few atoms per cubic centimeter, making atomic collisions unlikely. Under such conditions, once an atom or molecule has been excited for any reason into a meta-stable state, then it is almost certain to decay by emitting a forbidden-line photon. Since meta-stable states are rather

common, forbidden transitions account for a significant percentage of the photons emitted by the ultra-low density gas in space.
The luminosities of forbidden lines are not directly coupled to the ionizing luminosity, and their excitation is sensitive to abundance and the ionization state of the gas. However, the excitation of [OII] is sufficiently well behaved that it can be calibrated empirically (through Hα) as a quantitative SFR tracer. This indirect calibration is extremely useful for studies of distant galaxies because [OII] can be observed in the visible out to redshifts $z \sim 1.6$, and it has been measured in several large samples of faint galaxies. The relation between SFR and [OII] luminosity is:

$$\mathrm{SFR}(\mathrm{M}_{\odot}\mathrm{yr}^{-1}) = (1.4 \pm 0.4) \times 10^{-41}\mathrm{L[OII]}(\mathrm{erg\ s}^{-1}), \tag{2.2}$$

where the uncertainty indicates the range between blue emission-line galaxies (lower limit) and samples of more luminous spiral and irregular galaxies (upper limit). As with Equation (2.1), the observed luminosities must be corrected for extinction. The SFRs derived from [OII] are less precise than those from Hα because the mean [OII]/Hα ratios in individual galaxies vary considerably, over $0.5 - 1.0$ dex. The [OII]-derived SFRs may also prone to systematic errors from extinction and variations in the diffuse gas fraction. Moreover, the dust reddening influences more the [OII]-derived SFRs than the Hα-derived SFRs because the amount of extinction becomes larger for shorter wavelengths. In fact, going from red to ultraviolet, the extinction is roughly inversely proportional to wavelength. On the other hand, metal abundance has a relatively small effect on the [OII] calibration, over most of the abundance range of interest ($0.05\mathrm{Z}_{\odot} \leq \mathrm{Z} \leq 1\mathrm{Z}_{\odot}$).
The excitation of [OII] is especially high in the diffuse ionized gas in starburst galaxies and overall the [OII] lines provide an important estimate of the systematics of SFRs in samples of galaxies. In addition, they are very useful as a consistency check on SFRs derived in other ways.
Another useful physical quantity bound to the SFR and that help us to constrain galaxy type is the stellar birthrate parameter b, which is the ratio of the present SFR to that averaged over the past:

$$b = \frac{\mathrm{SFR}}{< \mathrm{SFR} >_{\mathrm{past}}}. \tag{2.3}$$

Figure 2.6 shows the distribution of b (right axis scale) for an Hα-selected sample of galaxies (Kennicutt, 1998). The typical late-type spiral has formed stars at a roughly constant rate ($b \approx 1$). By contrast, early-type spiral galaxies are characterized by rapidly declining SFRs, with $b \approx 0.01-0.1$, whereas elliptical and S0 galaxies have essentially ceased forming stars (b=0). Although the values of b given above are based only on synthesis modeling of the Hα equivalent widths (EWs), analysis of the integrated colors and spectra of disks yields similar results (Kennicutt, 1983; Gallagher et al., 1984; Bruzual A. and Charlot, 1993; Kennicutt et al., 1994). A more detailed analysis by Kennicutt et al. (1994) includes corrections for bulge contamination on the Hα EWs. The mean value of b (for the disk alone) increases from ≤ 0.07 for Sa disks to 0.3 for Sb disks and 1.0 for Sc disks. This change is much larger than the change in bulge mass fraction over the same range of galaxy types, implying that most of the variation in the integrated photometric properties of spiral galaxies is produced by changes in the star formation histories of the disks, not in the bulge-to-disk ratio. Variations in the bulge-disk structure may play an important role, however, in physically driving the evolution of the disks.

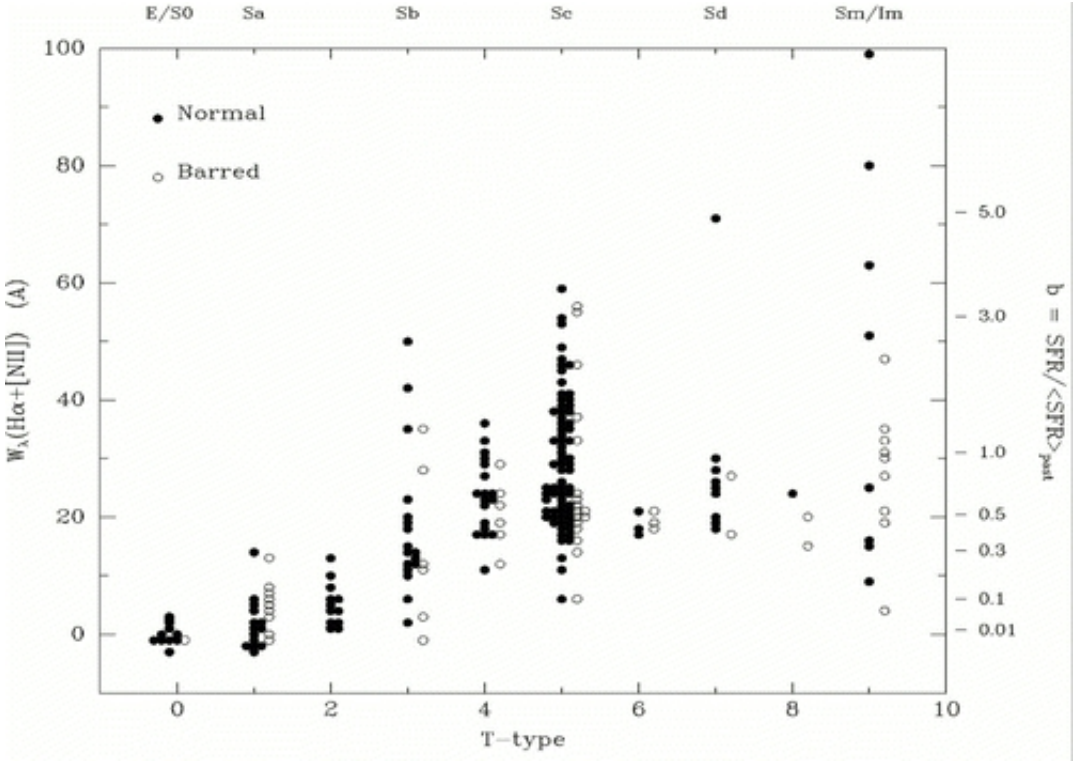

Figure 2.6: Distribution of integrated Hα+[NII] emission-line EWs for a large sample of nearby spiral galaxies, subdivided by Hubble type and bar morphology (from Kennicutt, 1998).

A schematic illustration of the trends in star formation histories is shown in figure 2.7. The *left plot* compares the stellar birthrate histories of typical elliptical galaxies (and spiral bulges) and the disks of Sa, Sb and Sc galaxies, following Sandage (1986). The curves for the spiral disks are exponential functions that correspond to the average values of b from Kennicutt et al. (1994). For illustrative purposes, an exponentially declining SFR with an e-folding time scale of 0.5 Gyr is also shown, as might be appropriate for an old spheroidal population. The Hubble sequence is primarily dictated by the characteristic time scale for star formation. In the more contemporary hierarchical pictures of galaxies formation, these smooth histories would be punctuated by merger-induced starbursts, but the basic long-term histories would be similar, especially for the disks. The *right plot* shows the same star formation histories but transformed into SFRs as a function of redshift (assuming $\Omega_m = 0.3$ and a formation redshift z_f=5). This diagram illustrates how the dominant star forming (massive) host galaxy populations might evolve with redshift. Most star formation at the present epoch resides in late-type gas-rich galaxies, but by $z \sim 1$, all spiral types are predicted to have comparable SFRs, and (present-day) early-type systems become increasingly dominant at higher redshifts. The tendency of early-type galaxies to have higher masses will make the change in population with redshift even stronger in a flux-limited sample.

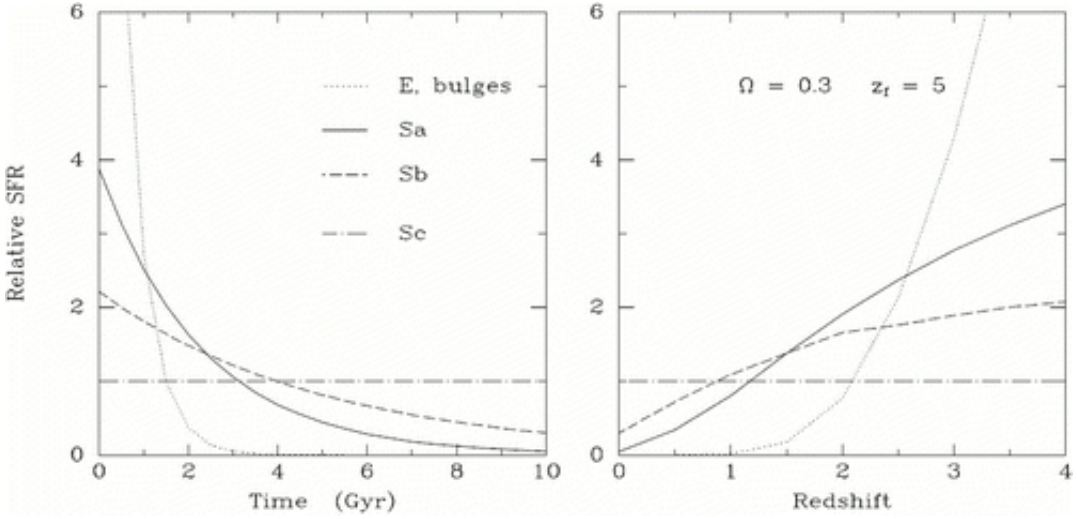

Figure 2.7: A schematic illustration of the evolution of the stellar birthrate for different Hubble types. The *left plot* shows the SFR trends as function of time; the *right plot* illustrates the corresponding evolution in SFR with redshift, for an assumed cosmological density parameter $\Omega_m = 0.3$ and an assumed formation redshift z_f=5 (from Kennicutt, 1998).

Analyzing these panels we can see that the SFR trend for Sc spirals remains constant in function of time and redshift, the SFR for Sa and Sb galaxies decreases with time and increases with redshift and the SFR behavior for ellipticals decreases with time and increases with redshift but with a much faster rate than spirals. These trends are due to the fact that ellipticals form all stars during their first life phase at high redshift and then, after few Gyrs, their star formation process stops; instead spirals form stars from a slightly decreasing to a continuum way.
However, the morphological galaxy classes are not closed boxes: the galaxies can suffer several physical processes which can change their morphological type. There are many experimental evidences about the differential evolution of galaxy types as the luminosity function for spectral type: Cucciati et al. (2012), computing the luminosity function for early- and late-type galaxies separately, showed that their samples at $0.2 < z < 0.8$ have an excess of faint early-type galaxies and of bright late-type galaxies.

Chapter 3

Cluster galaxy populations

3.1 Morphology-Density relation

Clusters are characterized by different types of galaxies and their galaxy population is a function of their redshift, richness and environment. In particular, nearby clusters are mainly composed by elliptical galaxies in the core region and by spiral galaxies towards the outskirts.
There is evidence of a high concentration of early-type galaxies with redder color and lower star formation rate, which form the densest central region of the cluster, and a decreasing space density of late-type galaxies with blue color and active star formation towards the cluster center: this morphological segregation in clusters, that depends on the cluster content, is the evidence for the existence of a morphology-density relation.
The morphology-density relation was quantified by Dressler in 1980, analyzing the galaxy morphology in 55 rich clusters with very low redshifts. The relative proportion of spirals+irregulars decreases monotonically with increasing density, and conversely, the proportions of lenticulars and ellipticals increase. Figure 3.1 of Dressler (1980) shows the strikingly well-behaved relationship when the data for all galaxies in the 55 clusters are combined. The plot also contains estimates of the true space density at these projected densities, which demonstrates that the populations change smoothly with density over five orders of magnitude, from 10^{-2} to 10^{3} galaxies Mpc^{-3}.
According to Dressler (1980), the advantage afforded by the use of density instead of radius as the independent parameter in the study of population gradients is illustrated in figure 3.2: the gradients are much more striking when the density is employed as the independent parameter, which indicates that the local density enhancements represent real physical associations and that populations are largely a function of local rather than global conditions.
A lot of consecutive studies have investigated the connection between cluster environment and the morphological gradients (Postman and Geller, 1984; Whitmore et al., 1993; Dressler et al., 1997; Domínguez et al., 2001) in order to understand which independent parameter between the clustercentric distance of a galaxy and the local projected galaxy density is more appropriate to characterize the cluster environment. Both of them, however, are projected parameters.

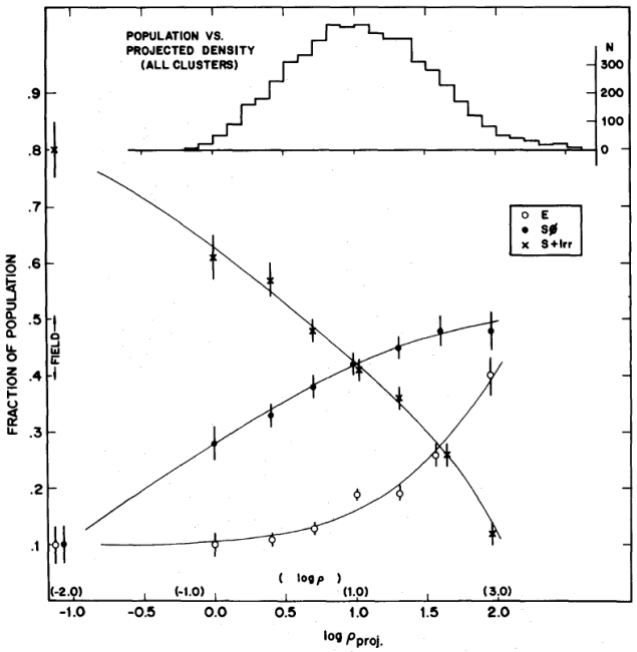

Figure 3.1: The fraction of E, S0, and S+I galaxies as a function of the logarithm of the projected density, in galaxies Mpc^{-2}. The upper histogram shows the number distribution of the galaxies over the bins of projected density (from Dressler, 1980).

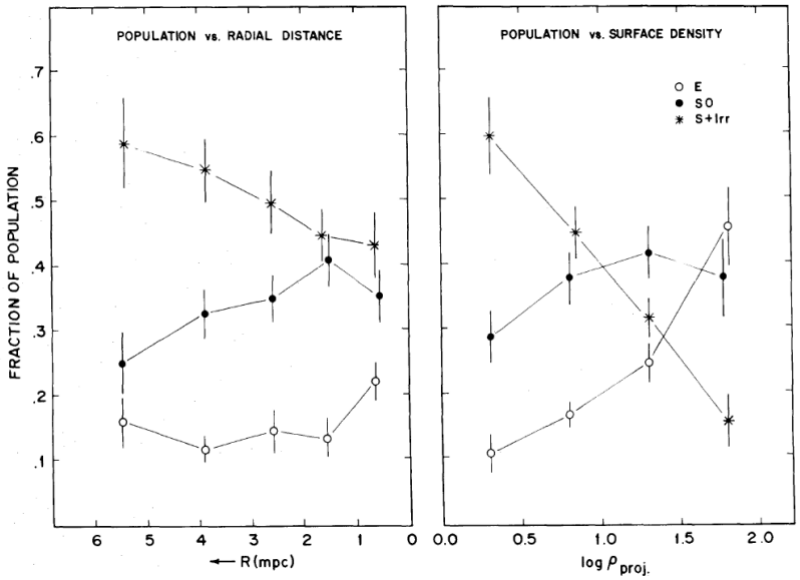

Figure 3.2: Population gradient in 6 clusters as a function of radial distance from the cluster centroid and as a function of local surface density (from Dressler, 1980).

In order to illustrate the radial gradient of the different galaxy populations in a cluster, I report in figure 3.3 the spatial distribution, projected on the sky, of galaxy members for the very rich cluster MACS J1206.2-0847 at intermediate redshift $z = 0.44$ from Girardi et al. (2015).
The red color represents early-types galaxies, instead the blue color is for late-type galaxies. Different symbols represent a detailed galaxy photometric-spectroscopic classification: PAS for passive (small red circles), HDSRs for strong Hδ absorption (due to A-type stars which indicate a relative young star formation process of about 1 Gyr) & red color (magenta crosses), HDSRb for strong Hδ absorption & blue color (large blue crosses), wELG for weak emission lines (green triangles), mELG for medium emission lines (blue triangles), sELG for strong emission lines (blue squares) and vsELG for very strong emission lines (blue circles). We see that PAS and HDSr galaxies are more spatially clustered than ELGs, but that also some star-forming galaxies are located in the cluster core.

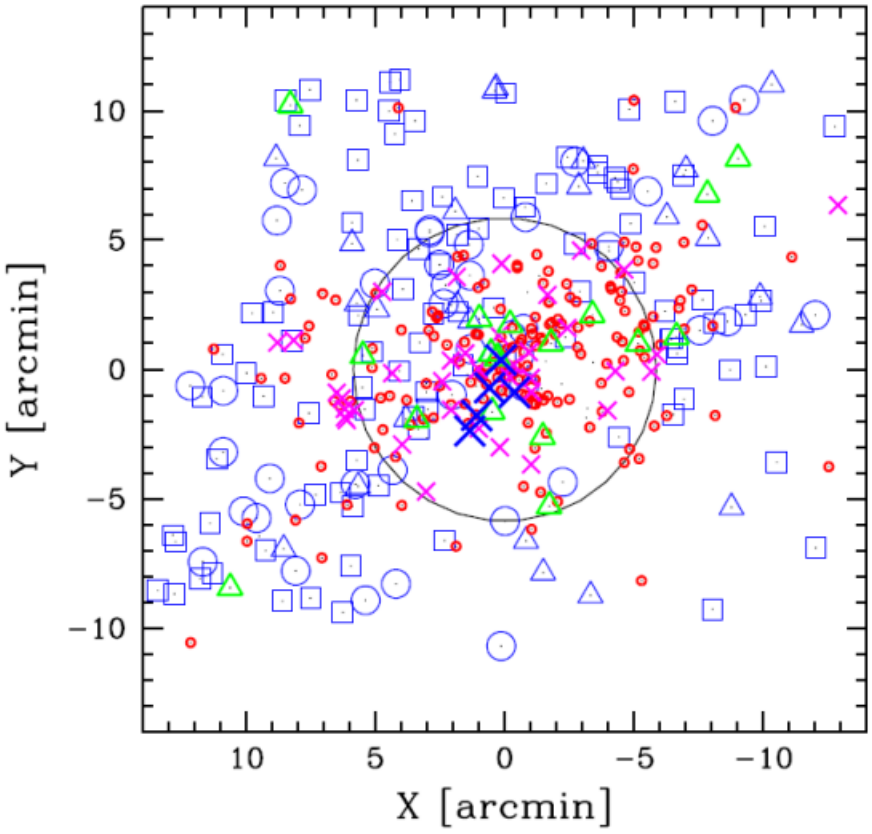

Figure 3.3: The spatial distribution of cluster members highlights the spatial segregation between early- and late-type galaxies. PAS and HDSr galaxies are more spatially clustered than ELGs. The circle encloses the R_{200} region: R_{200} is the radius of a sphere enclosing a mean density which is 200 times the critical cosmic density at redshift z. (from Girardi et al., 2015).

I also show in figure 3.4 the cumulative distributions of clustercentric distance R of galaxies per spectral class, showing the spatial segregation from early- through late-type galaxies.

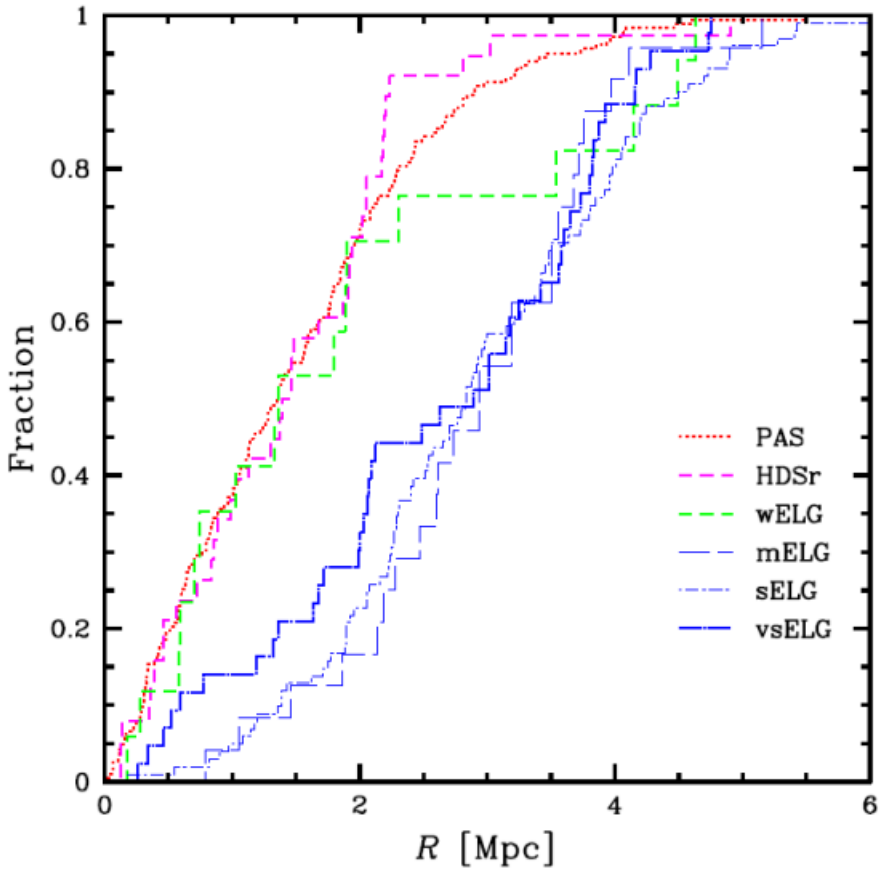

Figure 3.4: Cumulative distributions of clustercentric distance R of galaxies per spectral class (from Girardi et al., 2015).

A lot of studies have also found color gradient and SFR gradient in clusters according to the dichotomy between red/passive/early-type galaxies and blue/star-forming/late-type galaxies. The color gradient is consistent with the fact that galaxies with lower SFRs are in high density regions like cluster cores and that the star formation activity of galaxies depends on the environment. Drawing the color-magnitude (CM) diagram, where color is the difference between the magnitudes in two photometric bands, it is possible to see that the early-type galaxies are concentrated in the upper zone because of their redder color and form the so-called red sequence, instead, the late-type galaxies are below this sequence because of their bluer color and form the so-called blue cloud. The age of stellar populations divides star-forming from passive galaxies, while the effect of metallicity defines a clear CM relation for early-type cluster members: the redder is the galaxy, the more metals it contains.
The following figure 3.5 from Girardi et al. (2015) shows a typical CM diagram $B - R_c$ vs R_c for galaxy members with high quality spectroscopic data of the cluster MACS J1206.2-0847. The black solid line fits the red sequence and it is the CM relation $(B - R_c)_{diff} = 0$. The two red dashed lines indicate the locus of the red sequence galaxies, $\mid (B - R_c)_{diff} \mid \leq 0.3$.

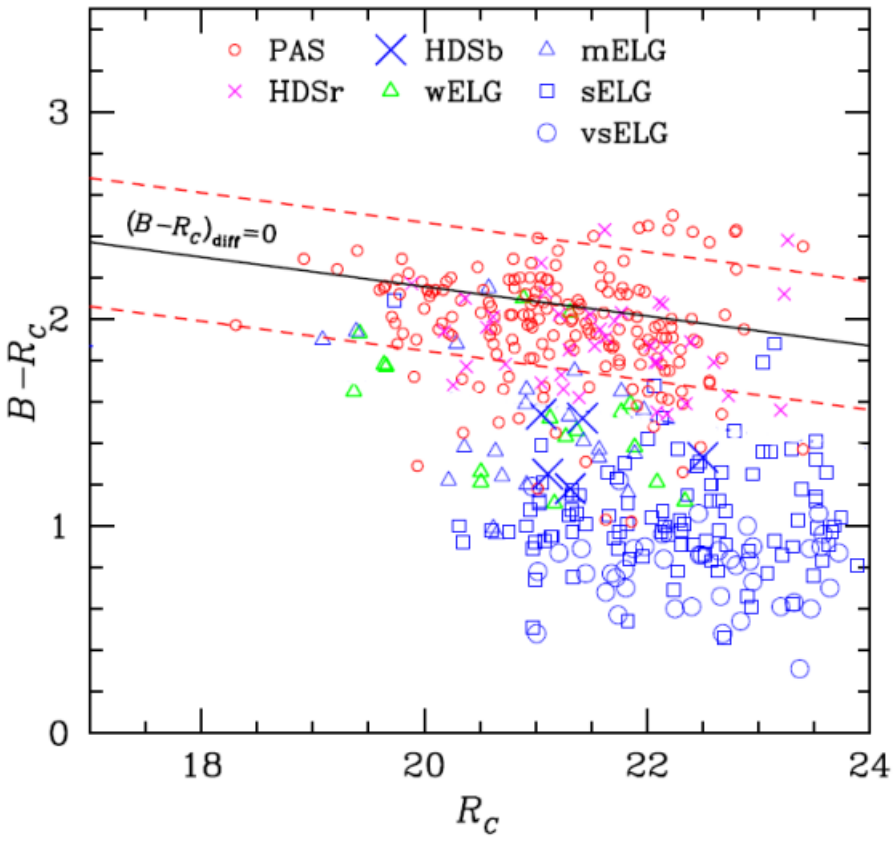

Figure 3.5: $B-R_c$ vs R_c color-magnitude diagram for the intermediate redshift cluster MACS J1206.2-0847. The red region is formed by passive/early-type galaxies and the blue one by star-forming/late-type galaxies (from Girardi et al., 2015).

In order to analyze the star formation properties of galaxies in clusters, I consider two low redshift clusters VMF73 and VMF74 with $z = 0.25$ and $z = 0.18$, respectively.
The figure 3.6 below (from Gerken et al. 2004) displays the behavior of Hα and [OII] equivalent widths, which are important SFR tracers (see section 2.3: *Hα and [OII] spectral lines as star formation tracers*), as a function of clustercentric radius for both clusters: squares and triangles represent galaxies of VMF73 and VMF74, respectively. The strength of [Hα] and [OII] emission lines increases towards the outer regions of clusters that are mainly populated by star-forming galaxies. The mean of the line strength distribution grows from the inner parts towards the cluster outskirts. Likewise, the fraction of star-forming galaxies increases from $\sim$ 15% in the center to $\sim$ 64% in the outer parts. The same trend has been found for [OII]: the fraction of star-forming galaxies increases from $\sim$15% to $\sim$50%.

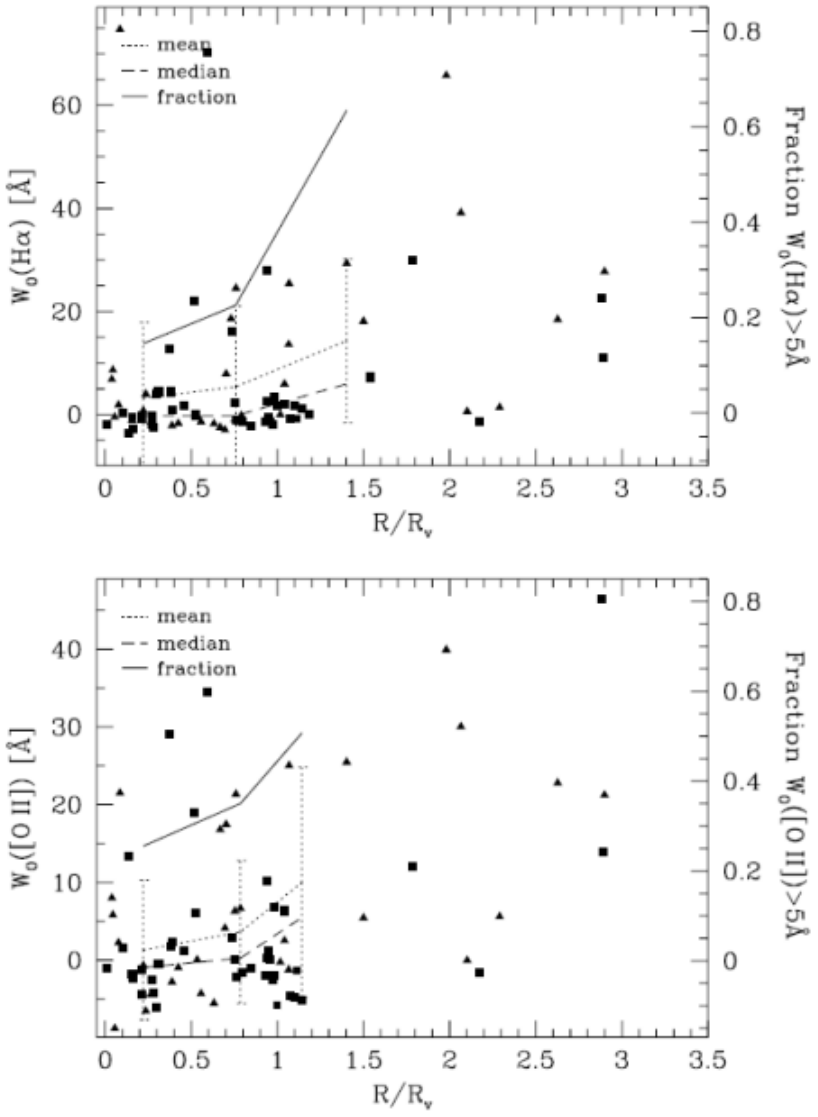

Figure 3.6: Hα and [OII] line strength distribution and fraction of star-forming galaxies with EW_0(Hα)≥5Å and EW_0[OII]≥5Å out to the infall regions as a function of clustercentric radius, which is normalized for the virial radius R_v. In both the Hα and [OII] distribution, the mean, median and the star-forming galaxy fraction go up with increasing clustercentric distance (from Gerken et al., 2004).

The Hα and [OII] line strength distributions of galaxies in the clusters VMF73 and VMF74 are shown in figure 3.7. The sample is devided into inner fields (represented by a solid line) and outer fields (dotted line): this division corresponds to galaxies within and beyond $1R_v$, respectively. In the Hα as well as in the [OII] distribution, the galaxies in the inner fields show a strong peak at line strengths of ∼0Å with a tail towards larger line strengths. Galaxies in the outer fields show a flat distribution in the [OII] line strengths and a slight peak around ∼15Å in the Hα distribution. In the inner regions, a galaxy fraction of 19% has Hα emission stronger than 5Å, while in the outer regions this fraction is 79%. A similar trend has been found in the [OII] distribution with 20% of galaxies with EW_0[OII]≥5Å in the inner fields and a fraction of 77% of these galaxies in the outer fields.

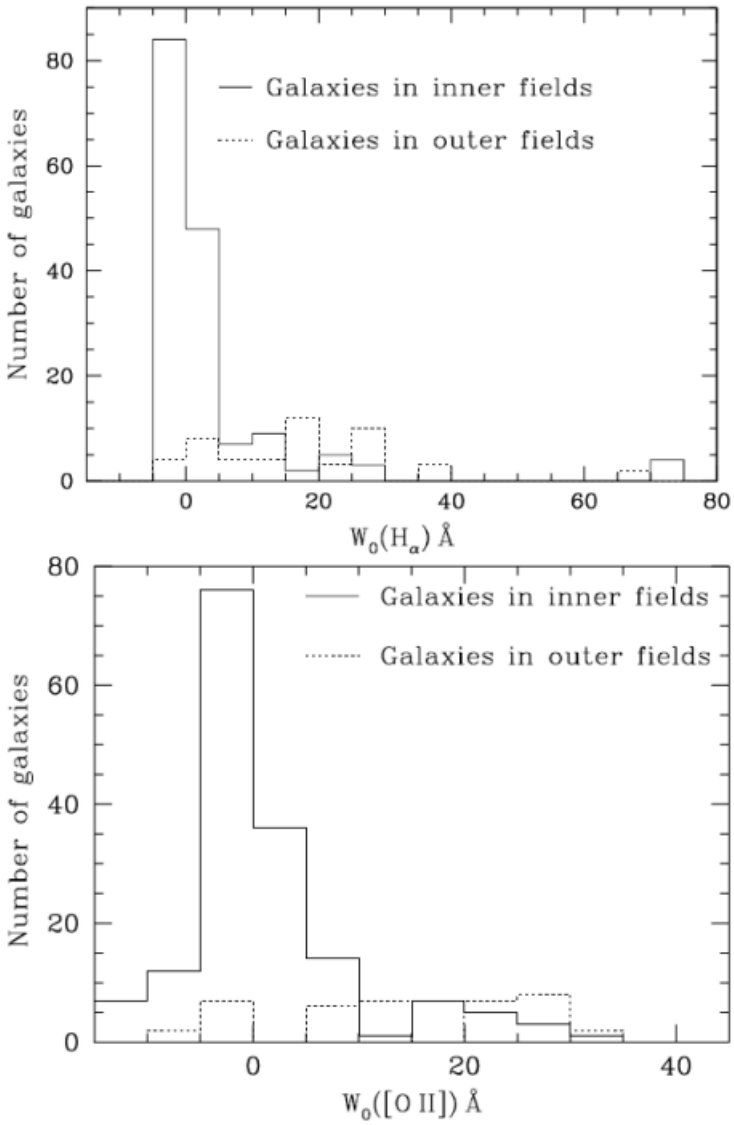

Figure 3.7: Hα and [OII] distribution for galaxies in the inner (solid line) and outer fields (dotted line) (from Gerken et al., 2004).

The dominant effect consists in the change of fractions of $EW_0(H\alpha)$ and EW_0[OII], while the variations of the EWs with the distance from the cluster center are smallest. This can be due to the fact that a galaxy can stay unaffected in the cluster for a long period of time and then suddenly undergo a rapid transformation.
According to the evolutionary interpretation, the blue component of local clusters is composed by field galaxies that infall into the cluster, which expands and increases mass, in agreement with a hierarchical bottom-up scenario in which galaxies form first and then merge into clusters. Thus, star-forming galaxies trace the recent matter infall in nearby clusters and represent a minor component of the whole galaxy population at low redshift. In this scenario the most massive galaxies collapse first because of their mutual gravitational attraction stronger, forming the cluster core, and then other galaxies follow.

3.2 Environmental processes

Cluster galaxies are not isolated bodies but interact with different astrophysical systems such as other cluster galaxies, the ICM and the whole cluster. Environmental processes affect both the star formation and morphological characteristics of galaxies and, even if the precise details of the connection between galaxy evolution and cluster environment are still unknown, several physical mechanisms can be involved in modifying galaxies in the cluster environment and in explaining the evolution of galaxy populations of clusters. We distinguish the following physical processes based on the counterpart that interacts with cluster galaxies:

1. **Galaxy-Galaxy Interaction**

   - **Two-Body Relaxation**: Velocity and spatial distributions of galaxies in regular, compact clusters are in a relaxed, quasistationary state and the most important elastic two-body collisions are gravitational. However, gravitational relaxation between galaxies takes a longer time than the age of the universe and it is therefore unlikely that the apparently relaxed state of regular clusters results from two-body collisions. Nevertheless, this process can affect the more massive galaxies near the cluster center.
   - **High-velocity encounters**: These encounters are mathematically described by the impulsive approximation: they can be considered as generators of small perturbations for systems otherwise in stationary state. In fact, effects of the encounters between stellar systems on internal structures of galaxies are weaker for a high-velocity collision than for a low-velocity one. The collision time is very short for a high-velocity encounter and so, this collision influences only star velocities and not their positions. The total collision energy is transformed into internal kinetic energy of the stellar systems, instead, the density distribution in each system remains constant during the encounter. Thus, we can approximate stellar systems during a high-velocity encounter as extended rigid bodies.
   - **Harassment**: It was discovered by Moore et al. (1996) using simulations and concerns dwarf and weakly luminous galaxies, which change morphology and lose mass because of the multiple high-speed encounters between galaxies. Harassment is able to transform dwarf spirals into dwarf ellipticals.
   - **Tidal Interaction**: Tidal perturbation origins velocity increments which are inclined to deform the sphere of stars into an ellipsoid. Major axis of the ellipsoid is directed along the nearest point from the system with which the sphere of stars interacts.
   - **Collisional Stripping**: Cluster galaxies are stripped from dust, gas and stars because of galaxy collisions.
   - **Merging**: Galaxy mergers can occur when two or more galaxies collide. They are the most violent type of galaxy interaction. Although galaxy mergers do not involve stars or star systems actually colliding, due to the vast distances between stars in most circumstances, the gravitational interactions between galaxies and the friction between the gas and dust have major effects on the galaxies involved. Major mergers between typical large galaxies are relatively rare, but minor mergers between galaxies of very different masses are much more common. The exact effects of such mergers depend on a wide variety of parameters such as collision angles, speeds, and relative size/composition, and are currently an extremely active area of research. In fact, galaxy mergers are important because the merger rate is a fundamental measurement of galaxy evolution.

2. **Galaxy-Cluster Interaction**

   - **Violent Relaxation**: After a collision between two bodies the total kinetic energy of the perturbed system increases and this body is not more in virial equilibrium. At this point the violent relaxation occurs and induces the perturbed system to a new equilibrium configuration because of the interaction with the whole cluster. This relaxation decreases the total kinetic energy of the perturbed system by a factor that is two times the energy increment. As a consequence of the internal kinetic energy reduction, stars with velocity grater than the escape velocity are able to escape the galaxy and so, the system loses mass. This process is able to produce a velocity distribution independent of the galaxy mass.
   - **Dynamical Friction**: Galaxies move across the cluster and so, the distribution of galaxies and dark matter particles around the moving galaxy becomes asymmetric. Gravitational force produces a frictional force which slows the orbital motions. This deceleration is a galaxy mass function: more massive is the galaxy, faster is the slowing rate. For galaxies with M$\leq 10^{12} M_{\odot}$ this process is negligible because their dynamical friction time is larger than the Hubble time.
   - **Tidal Truncation**: A system, which is continuously subjected to tidal perturbations is preserved from possible accretions and has a density profile that goes to zero at the typical tidal radius. This density profile isn't characterized by a slow decrement to zero but has a clear truncation at the tidal radius, which is the radius where stars and gas of the perturbed system are contained.

3. **Galaxy-ICM Interaction**

   - **Ram Pressure**: Gunn and Gott (1972) suggested that the rapid motion of galaxies across the ICM produces a loss of the interstellar medium (ISM) of these galaxies. The ISM can be removed from a galaxy if the ram pressure force of the hot gas is grater than the gravitational force that bounds the ISM to the galaxy. This process is stronger for more massive and hotter clusters and in the more central regions of the cluster: a galaxy can lose its entire gas during only one transit across the core region of the cluster. Finally, as a consequence of the ISM loss, the galaxy halts star formation activity.
   - **Evaporation Stripping**: In this case the gas loss isn't a consequence of the galaxy motion in the cluster, but is due to the fact that a galaxy orbits in a hot ICM, which increases density and temperature in regions near the galaxy. If the radiative flux is higher than the cooling flux, then it is possible for the ISM to evaporate from the galaxy.
   - **Viscosity and Turbulence of the ICM Motions**: The viscosity and turbulence processes can also cause the gas loss from a galaxy.
   - **Strangulation**: According to this process a galaxy loses its gas reservoir located in the external regions. So, the star formation is reduced due to strangulation, but in a time scale much longer than that due to ram pressure stripping.

3 Cluster galaxy populations

The following figure 3.8 from Treu et al. (2003) shows some of the most important galaxy interaction processes as a function of the distance from cluster center: merging doesn't take place in central regions because galaxies in the cluster core are characterized by a too high relative velocity; harassment process depends on gravitational potential of cluster and it is able to occur at large radii too; ram pressure stripping is more efficient in the core that towards the outskirts because galaxy density and velocity are higher in central cluster region.

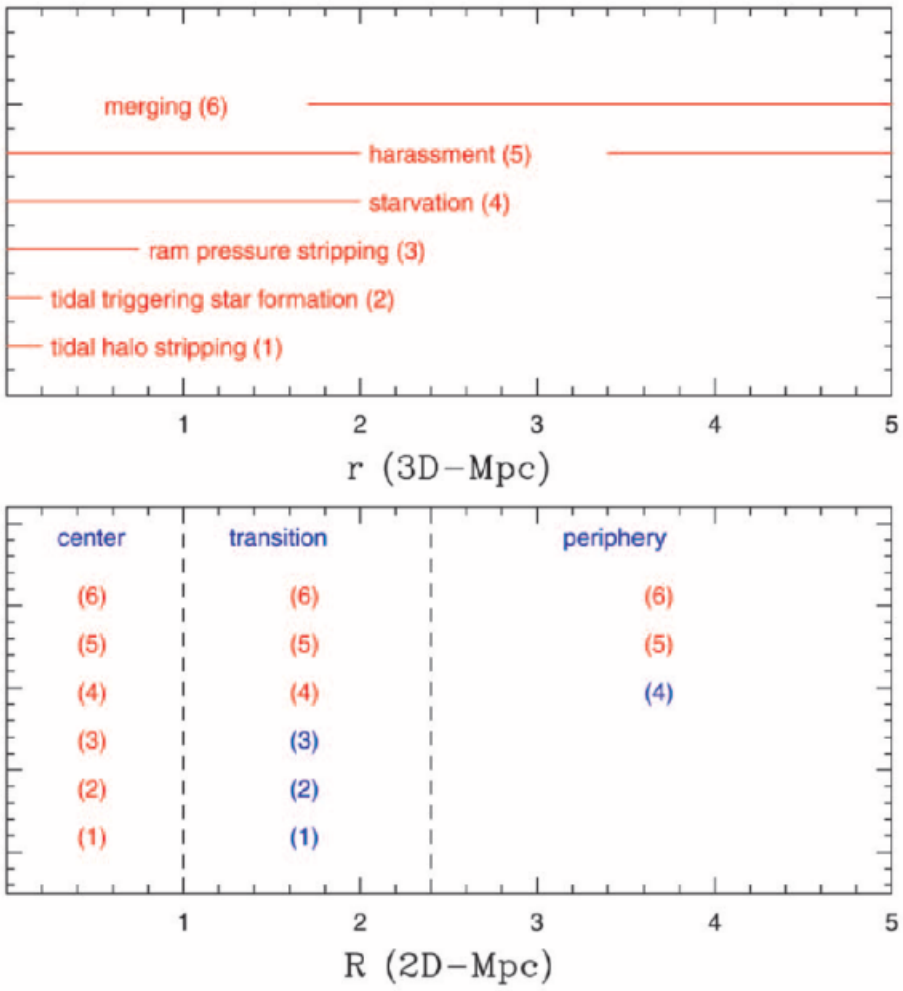

Figure 3.8: Summary of the regions where key physical mechanisms are likely to operate. The label *starvation* indicates a slow decrease in the star formation rate independent of the precise physical process. *Top*: horizontal lines indicate the radial region where the mechanisms are most effective (in three-dimensional space; note that *harassment* is effective in the entire range). *Bottom*: the mechanisms that could have affected the galaxy in a determined projected annulus is in red, whereas the blue numbers indicate processes that are marginally at work (from Treu et al., 2003).

3.3 Velocity dispersion as a mass proxy and velocity segregation

The velocity dispersion of cluster galaxy population plays a fundamental role in the estimate of cluster mass. In fact, the velocity dispersion of a galaxy population, which is in dynamical equilibrium within the cluster and traces the whole system, is directly linked to the total gravitational potential via the virial theorem. The precise relation between mass and velocity dispersion depends on assumptions about the relative distribution of mass and galaxies. Considering a stationary system and applying the virial theorem, the relation between the cluster mass M and the velocity dispersion σ of the galaxy populations is:

$$M = \frac{r_v \sigma^2}{G}, \tag{3.1}$$

where r_v is the virial radius $r_v = 2r_h$ with r_h harmonic radius, σ is the 3D-velocity dispersion and G is the universal gravitational constant. The projected harmonic radius R_h is defined as $R_h = \frac{\mathrm{N(N-1)}}{2} \sum_{i<j}^{\mathrm{N-1}} \sum_{j=i+1}^{\mathrm{N}} R_{ij}^{-1}$, where R_{ij} is the projected distance between the ith and the jth galaxies for a total number of N objects in the system.
The observational quantities bound to the cluster mass are the projected radius R_v and the line-of-sight velocity dispersion σ_{1D}. In this case the equation becomes:

$$M = \frac{3\pi R_v \sigma_{1D}^2}{2G}, \tag{3.2}$$

where $\frac{\pi}{2}$ and 3 are the projection factors for the radius and velocity dispersion, respectively. Equation (3.1) is strictly valid in the case that the galaxy population is a good tracer of the cluster mass distribution, i.e. the galaxy density distribution is proportional to the cluster mass density distribution. Otherwise, one has to consider a corrective factor k, $M = k\frac{R_v \sigma^2}{G}$, or better, the Jeans equation (Binney and Tremaine, 1987).
Velocity dispersion is a useful cluster mass proxy, but a fair estimate of this physical quantity faces some problems: limited amount of data available, presence of foreground and background interlopers, existence of substructures, cluster asphericity, velocity anisotropy in galaxy orbits and use of galaxy populations as tracers of mass distribution.
In this context, the question of velocity segregation among different cluster galaxy populations is fundamental.
In the framework of cluster formation, the process of violent relaxation is thought to produce a velocity distribution independent of the galaxy mass and type. In practice, there is a wide observational evidence for a phenomenon of velocity segregation: early and late-type cluster galaxies not only differ in their spatial distribution (see subsection 3.1: *Morphology-Density relation*), but also in their kinematics. In particular, many studies have shown that the velocity dispersion of star-forming galaxies is higher than that of passive galaxies in local clusters.
Moss and Dickens (1977) claimed that the velocity dispersion, σ_v, of the population of late-type galaxies is significantly larger than that of early-type galaxies, in 4 of the 5 clusters for which they could determine velocity dispersions for early- and late-type galaxies separately. Their study was a follow-up of earlier suggestions that the kinematics of early- and late-type galaxies in the Virgo cluster are different (Tammann, 1972). The σ_v-difference was subsequently confirmed (Binggeli et al., 1987). The early claim of Moss and Dickens (1977) was verified by Sodre et al. (1989) and Biviano et al. (1992), from data on galaxies in 15 and 37 galaxy clusters respectively. On the other hand, Zabludoff and Franx (1993) have found that the early- and late-type galaxies have different average velocities in 3 of 6 clusters studied, while the velocity dispersions are not different. Biviano et al. (1996) instead, studying the distribution and kinematics of emission-line galaxies, for the ESO nearby Abell cluster survey, confirmed a systematically larger σ_v for star-forming galaxies than for passive ones. Other evidences of this fact came

from Colless and Dunn (1996), Biviano et al. (1997), Adami et al. (1998), and Dressler et al. (1999). In particular, Girardi et al. (1996) considered 17 rich clusters at low redshift and found that the probability for the early- and late-type galaxy populations to have different velocity distributions was larger than 0.95 for 8 clusters.
Moss and Dickens (1977) explained velocity segregation as an evidence for an infalling population of field galaxies into the clusters. Also Biviano et al. (1997) interpreted the larger σ_v of blue galaxies as a generic aspect of the dynamics of galaxy clusters. This result probably indicates that the spirals that we see today avoid the central regions because they either have not yet got there, or have passed by the core on orbits that did not traverse the very dense central region. In other words: the kinematical state of the emission-line galaxies reflects the phase of fairly ordered infall rather than the virialized condition in the relaxed core. In this picture, the orbits of the blue galaxies are expected to be fairly radial, and their velocity distribution is expected to be quite anisotropic.
Despite their differences in position and velocity, if both star-forming and passive galaxies are in equilibrium with the cluster gravitational potential, they trace a statistically identical mass profile.
Analyzing the Canadian Network for Observational Cosmology cluster sample ($< z > \sim 0.3$), Carlberg et al. (1997) found that the virial radius of the red galaxy population is, on the average, a factor of 2.05 ± 0.34 smaller than that of the blue population. The red galaxies also have a smaller rms velocity dispersion, a factor of 1.31 ± 0.13 within their sample. Consequently, the virial mass calculated from the blue galaxies is 3.5 ± 1.3 times larger than from the red galaxies. However, applying the Jeans equation of stellar hydrodynamic equilibrium to the red and blue subsamples separately, Carlberg obtained statistically identical cluster mass profiles and masses. This strong evidence proves that clusters are effectively equilibrium systems and demonstrates empirically that the masses in virialized regions are reliably estimated using dynamical techniques. But, this also implies that the velocity dispersion of different galaxy populations is a mass proxy to be used with much caution, given that its application to tracers with a different mix of early/late-types produces different results.

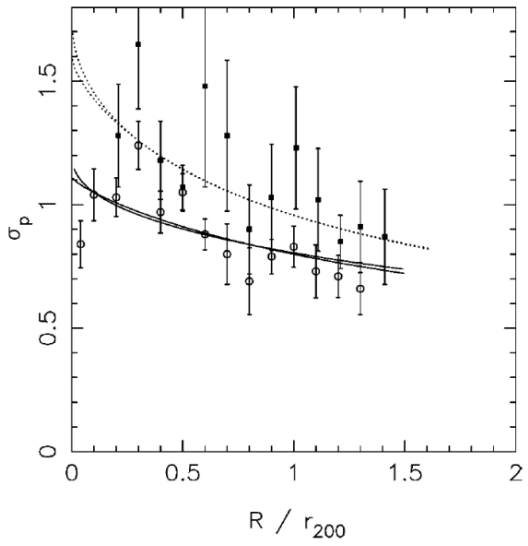

Figure 3.9: The rms line-of-sight velocity dispersion, σ_p, as a function of projected radius. The blue galaxies (*filled squares and dotted fit line*) have a larger σ_p than the red ones (*open circles and solid fit line*). Again the errors are from the symmetrized bootstrap confidence range (from Carlberg et al., 1997).

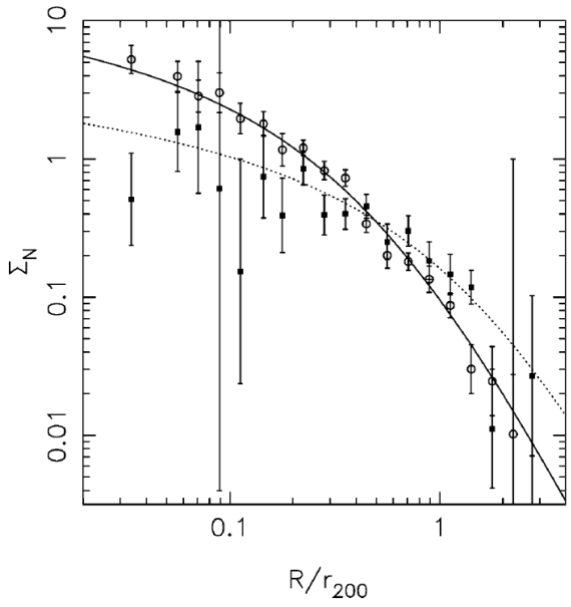

Figure 3.10: The projected number density profiles of blue (*filled squares and dotted fit line*) and red (*open circles and solid fit line*) cluster galaxies. The 1 σ confidence range from a bootstrap error estimate is shown (from Carlberg et al., 1997.)

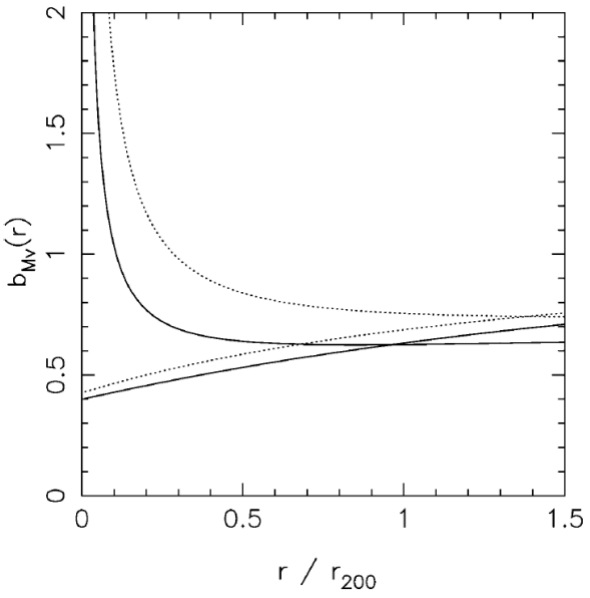

Figure 3.11: The bias function referred to the total light profile, $b_{M_v}(r)$, calculated from the mass profiles derived from blue (*dotted lines*) and red (*solid lines*) subsamples. The large uncertainties in the profile are connected with the difficulty in the determination of galaxy orbits (see Biviano et al., 1997). In fact, the upper line for both subsamples is for $\beta = 0$ (isotropic orbits), whereas the lower line is for $\beta = 0.5$ (radial orbits in the outer regions): β is a parameter that traces velocity anisotropies (from Carlberg et al., 1997).

To date the question of velocity segregation is still under discussion. There are several recent studies claiming for a velocity distribution which does not depend dramatically on galaxy color or spectral type (Rines et al., 2005, 2013; Girardi et al., 2015). In particular, for nearby clusters with $cz \leq 15.000$ kms^{-1}, Rines et al. (2005) showed that the kinematics of star-forming galaxies in the infall region closely match those of absorption-dominated galaxies. For clusters with $0.1 \leq z \leq 0.3$, Rines et al. (2013) demonstrated that the determination of velocity dispersion and dynamical mass is insensitive to the inclusion of bluer members (a small fraction of the cluster population) and that the velocity dispersion of the ensemble cluster (all galaxies) is only 0.8% larger than that of the red-sequence galaxies. Girardi et al. (2015), using galaxies of CLASH-VLT clusters at intermediate redshift, found that passive and star-forming galaxy populations do not differ for their velocity dispersions. However, a more careful analysis of their σ_v-profiles showed a small difference at fixed radius.
The cause for this controversy may lie in:

- the selection criteria of member galaxies;
- the dynamical status of the analyzed clusters;
- an evolutionary trend when considering clusters at different redshifts;
- the radius at which the velocity dispersions of the two populations are estimated.

Finally, there is also an evidence of velocity segregation with respect to the galaxy luminosity, i. e. the more luminous galaxies move more slowly than fainter ones (Biviano et al., 1992). This fact can be explained by the dynamical friction process that transfers kinetic energy from more massive galaxies to less massive ones (Sarazin, 1986). The more massive galaxies are slowed down and spiral in toward the cluster center. In this framework, a lower velocity dispersion should be seen in the central galaxies and in the more luminous ones as well. Thus, the dynamical friction process can induce this type of segregation because its relaxation time depends on the mass of the galaxy considered, as well as on the cluster velocity dispersion and core radius.
Galaxy clusters may be in different evolutionary states and, consequently, in different dynamical states. Thus, their dynamical and evolutionary status can be described by the galaxy velocity field. In the regions of massive central dominant (cD) galaxies a mix of galaxy orbits may exist: a bound, low-dispersion population soon to be consumed by the central galaxy as well as galaxies on predominantly radial orbits. On large scales, a fraction of infalling spirals may have yet to complete their first cluster crossing, thus it cannot be in equilibrium with the underlying mass distribution and is characterized by predominantly radial orbits (Biviano et al., 1996; Biviano and Katgert, 2004).
Summarizing, in the case of nearby clusters, the topics of velocity segregation and velocity dispersion are widely studied and it is generally understood that the red, passive galaxies are a better tracer of the cluster dynamics since this population is likely to have resided for a long time in clusters, and thus have achieved dynamical equilibrium. However, for clusters at intermediate- and high-z the question is still open. In fact, the population of blue galaxies is more abundant in higher redshift clusters (see the following section 3.4: *High-z clusters*) and it is easier to measure their redshifts (see the following chapter 4: *Cooming soon: galaxy clusters with the satellite Euclid*).

3.4 High-z clusters

3.4.1 Evolution of cluster galaxy populations

Galaxy properties such as color, morphology and spectral characteristics are functions of redshift as well as of galaxy environment.
An evolution of galaxy properties with redshift is provided by studies which show that the universal average star formation rate has been rapidly declining since $z \sim 1$ (Lilly et al., 1996; Madau et al., 1996; Blain et al., 1999; Somerville et al., 2001). However, at a given epoch, cluster galaxies always show suppressed star formation compared with the field population at the same redshift (Balogh et al., 1997). Models of hierarchical structure formation predict a continuous accumulation of material and substructure to more and more massive galaxies, groups and clusters as time progresses (Kauffmann, 1996; Kauffmann et al., 1999; Cole et al., 2000). Therefore, it may be possible to link the decline in the global star formation rate to the growth of large scale structure in the universe.
The properties of clusters and cluster galaxies are relatively well known at low redshift. In particular, it has been assessed that the central regions of massive clusters are dominated by red sequence galaxies with old stellar populations formed at $z \geq 2$, but it is more uncertain the main epoch at which these stellar populations assembled into the single galactic units that we see in the local universe.
At $z \leq 0.4$ both the mean color and the color-magnitude relation are consistent with those of present-day elliptical galaxies (Aragon-Salamanca et al., 1991; Dressler and Gunn, 1992; Stanford et al., 1995, 1997). The CM relation is also valid for distant clusters, but the red envelope of the early-type cluster population moves blueward with redshift. At $z \sim 0.9$ there are few galaxies with colors as red as present-day elliptical galaxies (Aragon-Salamanca et al., 1993; Rakos and Schombert, 1995; Oke et al., 1996; Lubin, 1996; Ellis et al., 1997). This color evolution is consistent with passive evolution of an old stellar population formed at an early cosmic age. The amount of color evolution is similar from cluster to cluster at a given redshift and is independent of the cluster richness or X-ray luminosity. These results indicate that the history of early-type galaxies may be insensitive to environment; that is, these galaxies appear to be coeval with a common star formation history.
The majority of red sequence galaxies have spectra that show no obvious signs of current or recent star formation. In conjunction with the red population there is a fraction of blue cluster members that is increasing with redshift, the so-called Butcher-Oemler effect (Butcher and Oemler, 1978). The Butcher-Oemler effect has been discovered analyzing galaxy clusters at intermediate redshift ($z \sim 0.3$): distant clusters contain a larger fraction of blue galaxies than the cores of low redshift clusters. According to this phenomenon, the blue fraction of cluster members increases with redshift.
Most of blue galaxies appear as normal spiral galaxies or have peculiar morphologies. A large fraction of this blue spiral population exhibits exceptionally strong Balmer lines and/or [OII] emission, which indicates that a significant fraction of the cluster members have recently undergone or are currently undergoing a high level of star formation activity (Poggianti and Barbaro, 1996).
An issue connected to the Butcher-Oemler effect is the fraction of S0 galaxies. Local clusters like the Coma cluster are dominated by S0 galaxies, which form only a small fraction in higher redshift clusters at $z \sim 0.5$, whereas spiral galaxies are more abundant in distant than in local clusters. This observation has raised the question whether the spiral galaxies in distant clusters are the progenitors of S0 galaxies in local clusters, and which kind of processes may be responsible for a transformation of one morphological type into another (Dressler et al., 1997; Poggianti et al., 1999). Studies of distant clusters indicate that the morphological composition of clusters

evolves with redshift and confirm that the Butcher-Oemler effect continues to strengthen up $z = 0.9$.
To date, it is recognized that the fraction of cluster galaxies with strong emission lines increases from local regions to $z \geq 0.5$ while the fraction of luminous quiescent galaxies (no significant [OII] emission) decreases from $z = 0.3$ to $z \geq 0.5$ (Postman et al., 1998).
The redshift range $0.7 \leq z \leq 1.5$ is likely to be a period in which massive clusters are undergoing (or have recently completed) virialization and in which many galaxies are only 1 or 2 Gyr past the peak in the cosmic star formation history (Madau et al., 1998).
Recent observations at higher redshifts suggest that, while galaxy populations in the centers of massive clusters show little change out to $z \sim 1.5$ (Mei et al., 2009; Strazzullo et al., 2010), in higher redshifts clusters, intense star formation becomes common, even in the cores and in the most massive galaxies (Hilton et al., 2010; Tran et al., 2010; Hayashi et al., 2011; Santos et al., 2011; Brodwin et al., 2013; Santos et al., 2014, 2015; Dannerbauer et al., 2014; Fassbender et al., 2014).
In particular, Brodwin et al. (2013) have analyzed the star formation properties of 16 infrared-selected, spectroscopically confirmed galaxy clusters at $1 < z < 1.5$ and found that $z \sim 1.4$ represents a transition redshift for this sample, with clear evidence of an unquenched era of cluster star formation at earlier times. Beyond this redshift, the fraction of star-forming cluster members increases monotonically toward the cluster centers. Indeed, the specific star formation rate in the cores of these distant clusters is consistent with field values at similar redshifts, indicating that at $z > 1.4$ environment-dependent quenching had not yet been established in these clusters.
More recently, Santos et al. (2015) have investigated the dust-obscured star formation in the galaxy cluster XDCP J0044.0-2033 at $z = 1.58$, the most massive cluster at $z > 1.5$, and performed an analysis of the spectral energy distributions of 12 cluster members (5 spectroscopically confirmed), all ultraluminous infrared galaxies. The individual SFRs lie in the range $155 - 824\,\mathrm{M_\odot yr^{-1}}$. They measured a strikingly high amount of star formation in the cluster core, $\mathrm{SFR}(\leq 250\mathrm{kpc}) \geq 1875 \pm 158\,\mathrm{M_\odot yr^{-1}}$, four times higher than the amount of SF in the cluster outskirts. This scenario is unprecedented in a galaxy cluster, showing for the first time a reversal of the SF-density relation at $z \sim 1.6$ in a massive cluster.
The discovery of the Butcher-Oemler effect, the proof that the blue populations of the Butcher-Oemler clusters are the result of a high star formation activity and the increasing opportunity of available distant galaxy spectra with high quality, make possible to characterize high-redshift clusters through their blue members (Dressler et al., 2004), which are more common at large distances, with a possible reversal of the star-formation density relation at $z \sim 1.5 - 2$ in massive clusters. This type of parameterization is not efficient for local clusters dominated by red galaxies. In fact, in the nearby universe star-forming galaxies are known to trace the recent matter infall in clusters and represent a minor component of the whole galaxy population.

3.4.2 Detection and study of distant clusters

Only in the last twenty years or so the study of high-redshift clusters has become, because observations of galaxy clusters with $z \geq 0.6$ face the following difficulties:

1. the galaxies are approaching the sensitivity limits of optical spectrographs on 4 m-class telescopes;

2. the interloper contamination by foreground and background galaxies, physically unrelated to the cluster, becomes substantial;

3. the well-understood rest-wavelength region redward of 4000 Å, which contains characteristic spectral features, moves into the near-infrared.

The identification of clusters at $z > 1-2$ (or protoclusters, somewhat loosely defined as systems that exhibit a significant overdensity of galaxies, not yet gravitationally bound, but that may collapse to form a cluster at later time) becomes difficult, due both to increasing detection challenges and intrinsic rareness. Also, a detailed determination of the properties of their galaxies is progressively uncertain.
Nevertheless, the study of high-z clusters is now an active field of research, as testified by the fact that even the redshift barrier of $z = 1.5$ has been broken in the last few years by the mid-infrared, X-ray and SZ selection. Observations of high-z clusters help us to understand questions concerning the evolution of galaxy populations in clusters which requires a special treatment of the various processes driving it, such as star formation, active galactic nuclei (AGN) activity, feedback and dynamical interactions (Granato et al., 2015). Galaxy clusters over cosmic time are prime laboratories for these processes acting together, which results in a clear environmental dependence of the basic properties of galaxies, and of their evolutionary history.
To shed light directly on the history of assembly of galaxy clusters, it is clear that larger samples are highly demanded at high redshift, greater than $1 - 1.5$. Moreover, various samples should be selected by means of different techniques, in order to capture different evolutionary stages of clusters or protoclusters. A widely used method to discover high-redshift clusters has been to look for the effects of their hot gas component, namely its X-ray emission or the Sunyaev-Zel'dovich effect it produces on the cosmic microwave background. The former type of selection becomes rapidly inefficient at $z \geq 1.5$, due to sensitivity limitations, and both require massive and well-relaxed structures, whose number density is expected to be rapidly declining at such early cosmic epochs. A complementary possibility, which has been exploited in the past few years, is to pre-select overdensities of galaxies whose near-infrared photometric properties are characteristic of high redshift systems. These overdensities require later spectroscopic confirmation. At $z \geq 2$ most efforts have been devoted in the search of protoclusters using high-z giant radiogalaxies as tracers.
The next future will see appear on the astrophysical and cosmological scene the Euclid satellite (see next chapter 4: *Cooming soon: galaxy clusters with the satellite Euclid*), which will be able to observe 60.000 clusters between $z = 0.2$ and $z = 2.0$, with 10.000 having $z \geq 1$.
Also other future observational campaigns of galaxy clusters will help us to understand better the physics of such systems in different wavelength bands: SPT3G for the millimetric part; LSST and WFIRST in the near-infrared and optical bands; eROSITA for X-ray surveys.

Chapter 4

Coming soon: galaxy clusters with the Euclid mission

4.1 ESA space mission Euclid

Euclid is a medium class space mission of the European Space Agency (ESA) Cosmic Vision 2015-2025 programme (*Euclid Red Book*, Laureijs et al., 2011) and its aim is mapping the geometry of dark universe. Its launch date is planned for 2020 and it is characterized by a 1.2 m Korsch telescope designed to provide a large field of view. The following figure shows a simulated appearance of the Euclid satellite:

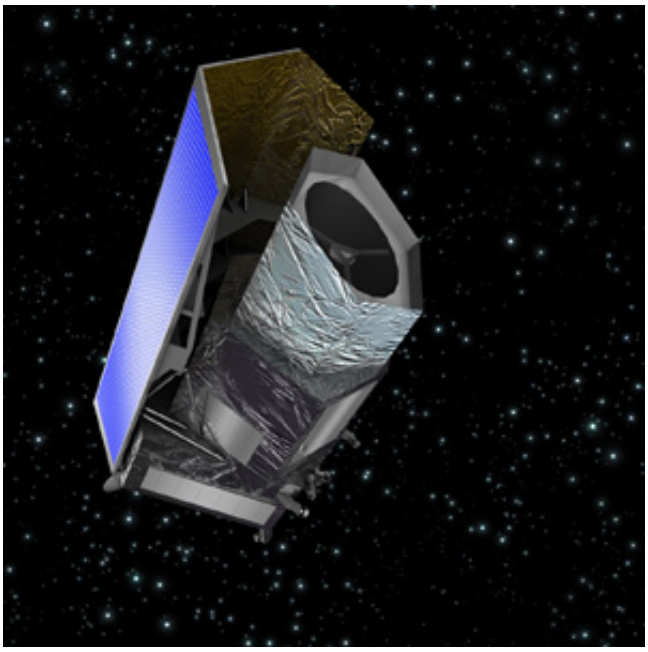

Figure 4.1: Simulated appearance of the satellite Euclid (credit to ESA/C. Carreau).

Euclid will study the evolution of the cosmic web up to $z \sim 2$, collecting optical and infrared imaging data for $2{\times}10^9$ galaxies and providing spectra for $5{\times}10^7$ galaxies with $0.9 \leq z \leq 1.8$. It is characterized by two different instruments: VIS for Visible Imaging and NISP for NearInfraRed Imaging Photometry and NearInfraRed Spectroscopy. The wide survey covers 15.000 deg^2 of the

extragalactic sky, instead the sky coverage of the deep survey is 40 deg^2 and is two magnitudes deeper than the wide one. The objectives of this satellite are:

- Mapping dark and luminous matter for 1/3 of the sky and up to $z \sim 2$;
- Discovering the nature of dark matter;
- Tracing the origin of cosmic acceleration.

Understanding the acceleration of the expansion of the universe is one of the most compelling challenges of cosmology and fundamental physics. The Euclid surveys will show how cosmic acceleration modifies the expansion history and the 3-dimensional distribution of matter in the universe. To achieve this, Euclid will measure the shapes of over a billion galaxies and accurate redshifts of tens of millions of galaxies for weak gravitational lensing and galaxy clustering studies. This mission is designed to understand the origin of the universe accelerating expansion. It will use cosmological probes to investigate the nature of dark energy, dark matter and gravity by tracking their observational signatures on the geometry of the universe and on the cosmic history of structure formation. Euclid will map large-scale structure over a cosmic time covering the last 10 billion years, more than 75% the age of the universe. The mission is optimized for two independent primary cosmological probes: Weak gravitational Lensing (WL) and Baryonic Acoustic Oscillations (BAO). Both probes require a very high degree of system stability to minimize systematic effects, and the ability to survey a major fraction of the extra-galactic sky. Such a combination of requirements cannot be met with observations from the ground, and demands a wide-field-of-view space mission: Euclid is designed for this purpose.
To understand the nature of dark energy, its equation of state needs to be determined. Euclid uses WL and BAO to measure the constant and time varying terms of the dark energy equation of state to a 1-sigma precision of 0.02 and 0.1, sufficient to make a decisive statement on the nature of dark energy. Euclid tests the validity of General Relativity by measuring the rate of cosmic structure growth to a 1-sigma precision of $\leq$0.02, sufficient to distinguish General Relativity from a wide range of modified-gravity theories. As Euclid maps the dark matter distribution with unprecedented accuracy, subtle features produced by neutrinos are measured, providing constraints on the sum of the neutrino masses with a 1-sigma precision better than 0.03 eV. Likewise, the initial conditions of the seeds of cosmic structure growth are unveiled by determining the power spectrum of density perturbations to one percent accuracy. Euclid and Planck together measure deviations from a Gaussian distribution of initial perturbations with a precision one order of magnitude better than current constraints, allowing Euclid to test a broad range of inflation models. Euclid is therefore poised to uncover new physics by challenging all sectors of the cosmological model and, although the mission is optimized for the measurement of cosmological WL and galaxy clustering, it will also provide data usable for other important complementary cosmological probes, such as galaxy clusters.

4.2 Studying galaxy clusters with Euclid

Over the past decade, surveys of galaxy clusters for cosmological use have been collected and analyzed, based on observations at different wavelengths: X-ray (Borgani et al., 2001; Vikhlinin et al., 2009; Rapetti et al., 2010; Clerc et al., 2012); sub-mm, through the Sunyaev-Zel'dovich (1972) distortion (Staniszewski et al., 2009; Benson et al., 2013; Planck Collaboration et al., 2014a; Burenin and Vikhlinin, 2012), and optical (Rozo et al., 2010) bands. Further improvements can be obtained from the spatial clustering of galaxy clusters (Schuecker et al., 2003; Hütsi, 2010; Mana et al., 2013). The resulting cosmological constraints turn out to be complementary to those of other cosmological probes such as type Ia supernovae (Betoule et al.,

2014), Cosmic Microwave Background radiation (Hinshaw et al., 2013; Planck Collaboration et al., 2014b), the BAO (Anderson et al., 2014), and cosmic shear (Kitching et al., 2014). These cluster catalogues are however characterized either by a large number of objects that cover a relatively small redshift range, or rather small samples that span a wide redshift range. Ideally, in order to exploit the redshift leverage with good statistics, one should have access to a survey that can provide a high number of well characterized clusters over a wide redshift range: the Euclid mission is thought to achieve this goal.
Clusters detection with Euclid will be possible in three different ways:

1. using photometric data;
2. using spectroscopic data;
3. through gravitational (most weak) lensing, which may be combined for more efficiency.

The most efficient method to detect clusters with Euclid relies on analyzing the photometric data, an approach that has been clearly demonstrated by the SDSS at low redshifts (Koester et al., 2007) and that now is used by DES to investigate the origin of the accelerating universe. Euclid will be able to push towards much higher redshifts over a large area, thanks to its unique capabilities in the infrared, which cannot be matched from the ground. Conservative estimates, based on simulated catalogues, indicate that Euclid will find of order 60.000 clusters with an S/N of better than 3, between $z = 0.2$ and $z = 2.0$, with 10.000 having $z \geq 1$. With such good statistics, our cluster-based constraints on cosmological parameters will be limited by our understanding of the catalogue selection function, systematic errors and, most important, the cluster mass determinations and their uncertainty. This is where the strength of Euclid lies: it is able to calibrate the important mass-observable relations and their scatter through lensing measurements. The exquisite image quality and high number density of sources will enable Euclid to measure masses of clusters much more accurately and out to higher redshifts than is possible from the ground (*Euclid Red Book*, Laureijs et al., 2011).
Figure 4.2 by Sartoris et al. (2015) displays for Euclid cluster survey the mass selection function $\log(\mathrm{M_{200,c}}/\mathrm{M_\odot})$ (where $\mathrm{M_{200,c}}$ is the mass within a mean overdensity of 200 times the critical density of the universe at the cluster redshift) as a function of redshift and for two different values of the detection threshold. This latter is indicated as $N_{500,c}/\sigma_{field}$, where $N_{500,c}$ is the number of cluster galaxies within $r_{500,c}$ and σ_{field} is the root mean square of the field counts within the same radius.
The shape of the selection functions is somewhat counter-intuitive because it is higher at $z \sim 0.2$ than at $z \sim 0.7$. Naively one would expect that clusters of lower mass would be easier to detect at lower redshifts. This feature seems to depend on the details of the assumptions used to derive the selection function from phenomenological analytical calculations, and it should not be taken too literally. A better estimate of the selection function of the Euclid cluster survey will be provided by the analysis of mock catalogs, which is an ongoing effort in the clusters of galaxies work package within the Euclid consortium.
In the following figure 4.3 by Sartoris et al. (2015) I show the histograms corresponding to the redshift distributions, $n(z)$, of Euclid photometric galaxy clusters, obtained by adopting the two selection functions, which correspond to the two different detection thresholds $N_{500,c}/\sigma_{field} > 3$ and 5. In figure 4.3 the two curves indicate the corresponding cumulative redshift distributions, $n(> z)$, i.e., the total number of clusters detected above a given redshift. Euclid will detect $\sim 2 \times 10^5$ objects with $N_{500,c}/\sigma_{field} > 5$ at all redshifts, with about $\sim 4 \times 10^4$ of them at $z > 1$. By lowering the detection threshold down to $N_{500,c}/\sigma_{field} = 3$, these numbers rise up to $\sim 2 \times 10^6$ clusters at all redshifts, with $\sim 4 \times 10^5$ of them at $z > 1$.

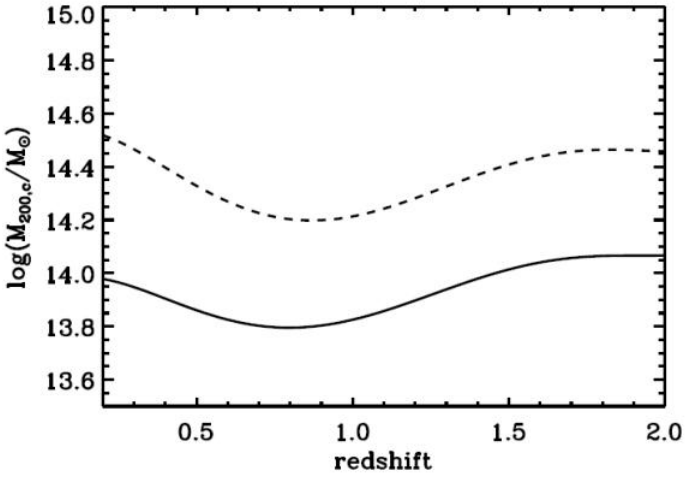

Figure 4.2: Galaxy cluster mass selection function for the Euclid photometric survey. Solid and dashed lines are for detection thresholds $N_{500,c}/\sigma_{field} = 3$ and 5, respectively (from Sartoris et al., 2015).

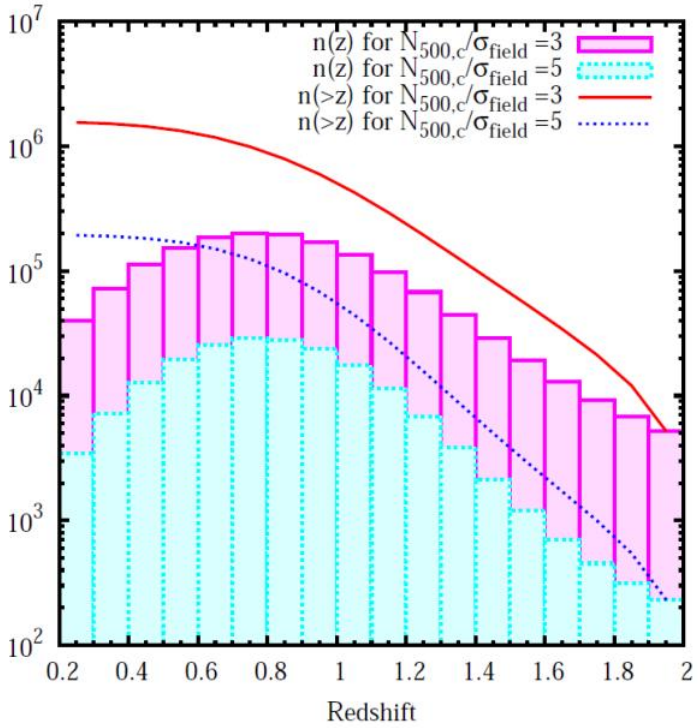

Figure 4.3: Number of clusters above a given redshift to be detected with overdensities $N_{500,c}/\sigma_{field} > 5$ and > 3 in the Euclid photometric survey (dotted blue and solid red lines, respectively). I also show the number density of clusters expected to be detected within redshift bins of width $\Delta z = 0.1$ for the same detection thresholds (dotted cyan and solid magenta histograms, respectively) (from Sartoris et al., 2015).

Moreover, Euclid internal data will provide a precise calibration of the relation between cluster richness, which characterizes photometrically-identified clusters, and their actual mass (Sartoris et al., 2015). In this context it will be possible to cross-correlate Euclid data with those from other cluster surveys - such as eRosita (Merloni et al., 2012), XCS (Mehrtens et al., 2012), the South Pole Telescope (Carlstrom et al., 2011), and the Atacama Cosmology Telescope (Marriage et al., 2011).

4.3 Euclid clusters and spectroscopic data

In the case of Euclid, only redshifts for star-forming galaxies will be measured through the detection of the Hα line at $0.9 \leq z \leq 1.8$, which is the detectability range of the Hα line in the Euclid survey. The Hα limit flux of the Euclid spectroscopic survey is 2×10^{-16}erg s^{-1}cm^{-2}, predicted to be sufficiently low to yield over 50 million galaxy redshifts with a completeness higher than 45%. This limiting line flux is set by the features of the NIR spectrograph, which covers the wavelength range $1100 - 2000$ nm. Simulations of NISP in spectroscopic mode show that Euclid can measure 3.000 redshifts/deg^2 with the required S/N, completeness (fraction of spectra measured down to the expected Hα flux limit) and purity (fraction of spectra for which the measured redshift is correct).
The spectroscopic part of the Euclid survey will provide velocities for a few cluster members in each cluster detected with photometric data. Stacking these velocities for many clusters in bins of richness and redshift will allow a precise calibration of the velocity dispersion vs. richness relation, and from this of the mass-richness relation.
In figure 4.4 (credit to Sartoris et al., 2015), I show the number of spectroscopic cluster members that will be available for stacks of clusters of given mass as a function of redshift. The curves show the number of cluster galaxies in bins of $\Delta z = 0.1$ and $\Delta \log M_{200,c} = 0.2$, for central values of the cluster mass bins of $\log(M_{200,c}/M_\odot) = 14.2, 14.4, 14.6$ (red, blue, green curves, respectively). The estimate is done only for clusters with a mass limit above that required for a minimum of 5 members with concordant spectroscopic redshift, in order to be sure of the existence of the cluster. This requirement restricts the curve for $\log(M_{200,c}/M_\odot) = 14.2$ to $z \leq 1.25$. The dotted line shows the value of 500 galaxies as a reference.

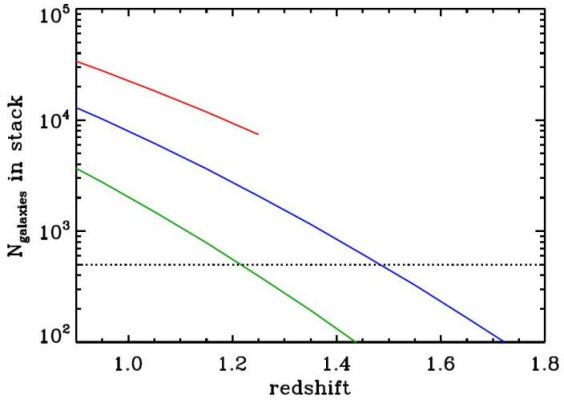

Figure 4.4: Euclid spectroscopic survey: expected numbers of cluster galaxies as function of redshift. The red, blue and green curves show the number of cluster galaxies in bins of $\Delta z = 0.1$ and $\Delta \log M_{200,c} = 0.2$, for central values of the cluster mass bins of $\log(M_{200,c}/M_\odot) = 14.2, 14.4$ and 14.6, respectively. (from Sartoris et al., 2015).

In the context of preparatory science for the ESA space mission Euclid, the purpose of this thesis is bound to the kinematics of galaxy clusters and consists in investigating the performance of the estimate of velocity dispersion of member galaxies as a proxy for the total virial cluster mass. In particular, I will mimic the Euclid spectroscopic observations for star-forming galaxies in order to do a first approximate prevision of which galaxies Euclid will be able to detect for the selected high-redshift clusters.

Chapter 5

The cluster sample

The bulk of this thesis consists in the analysis of a survey of 52 galaxy clusters at intermediate and high redshifts, $0.40 \leq z \leq 1.46$. Cluster data are collected from the literature and are mainly optical data like positions, redshifts with respective errors, magnitudes, colors, and spectral features, in particular the equivalent width of [OII] line, of galaxies for the whole surveys.
In order to consider all the clusters analyzed in the literature with this type of available data and with these constraints in redshift, I map the entire sky in right ascension, from 00 to 24 hours, and declination, from 90 to -90 degrees, using the catalogues of NED (NASA/IPAC Extragalactic Database). I select galaxy data for the entire field and not only for cluster members, since one of the objectives of this thesis is to identify cluster members from the respective survey.
Figure 5.1 shows the number of clusters in the sample as a function of redshift and figure 5.2 exhibits the redshift survey for clusters that the Euclid satellite will be able to detect, in the redshift range $0.8 \leq z \leq 1.4$.
I analyze 7404 galaxies and the median number of member galaxies per cluster is 32.5. Figure 5.3 represents all combined data of galaxies as a function of redshift.

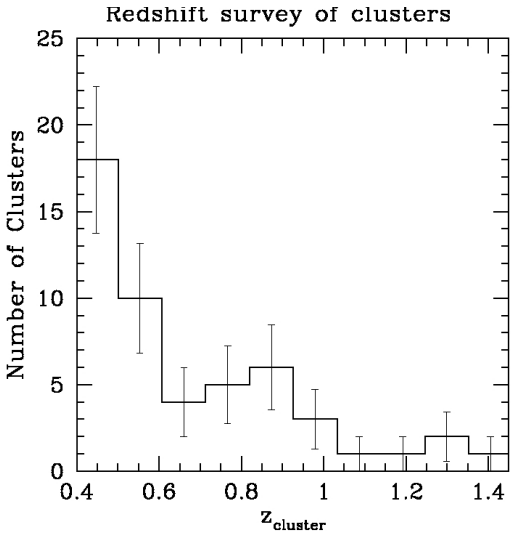

Figure 5.1: All combined data of clusters as a function of redshift: the number of clusters decreases as the redshift increases.

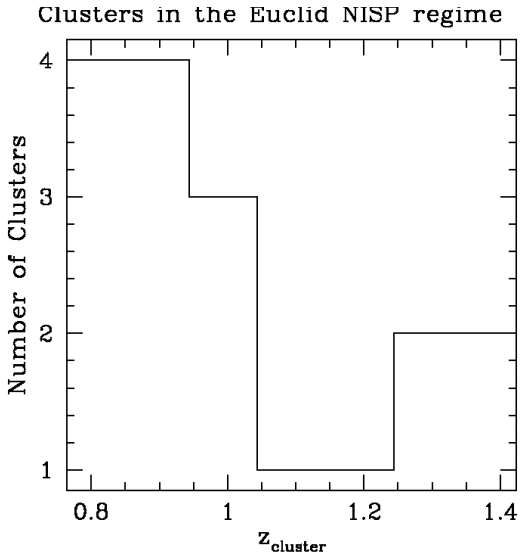

Figure 5.2: All combined data of clusters having $z_{cluster} \geq 0.8$ as a function of redshift: for these clusters NISP Euclid spectroscopic observations will be possible.

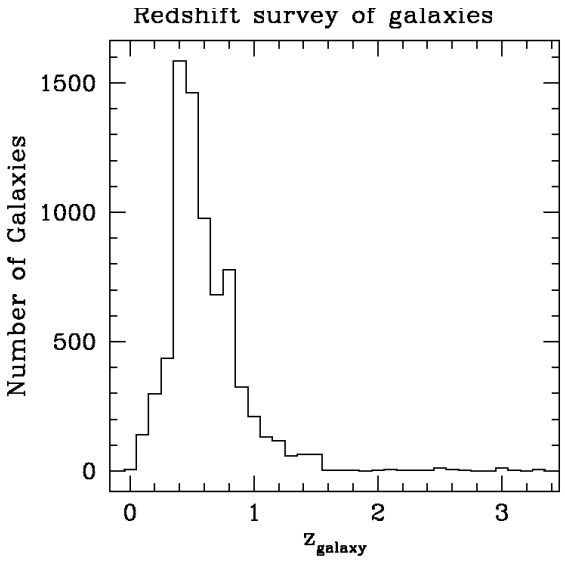

Figure 5.3: All combined data for cluster and field galaxies as a function of redshift: most galaxies are located in the redshift range $0.1 \leq z \leq 1.4$.

5 The cluster sample

Table 5.1 lists all 52 clusters considered in ascending order of redshift: in column (1) I write the cluster name; in column (2) the number of galaxies for the entire survey, N_{tot}; in column (3) the available magnitude bands; in column (4) the data references. I will report the mean redshift and the coordinates of the center for each cluster in Table 7.1 in Chapter 7.

Table 5.1: Cluster sample

Cluster name	N_{tot}	Magnitude	References
CL 0024+16	130	g, r	1,2
CL 1301.7−1139a	87	B, V, I	3,4
CL 0939+47	132	g, r	1,2
CL 0303+17	84	g, r	1,2
CL 1202.7−1224	73	B, V, I	3,4
MS 0302.5+1717	43	R, I	2,5
MS 0302.7+1658	96	g, r	2,6
CL 1037.9−1243a	131	V, R, I	3,4
MS 1621.5+2640	262	g, r	2,6
MACS J1206.2−0847	2535	B, R_c, I_c	7
CL 1138.2−1133a	112	V, R, I	3,4
CL 1059.2−1253	85	B, V, I	3,4
3C 295	35	g, r	1,2
CL 1018.8−1211	71	B, V, I	3,4
CL 1138.2−1133	112	V, R, I	3,4
CL 1301.7−1139	87	B, V, I	3,4
RX J1117.4+0743	75	g, r	8
CL 1420.3−1236	73	B, V, I	3,4
CL 1411.1−1148	78	B, V, I	3,4
CL 1601+42	98	g, r	1,2
MS 0451.6−0305	70	g', r', i', z'	9
CL 1232.5−1250	94	B, V, I	4,10
MS 0015.9+1609	111	g, r	2,11
CL 1119.3−1129	67	B, V, I	3,4
CL 0054−27	25	V, I	1,2
CL 1037.9−1243	131	V, R, I	3,4
CL 1353.0−1137	68	B, V, I	3,4
CL 1354.2−1230a	126	V, R, I	3,4
CL 1103.7−1245a	106	V, R, I	3,4
CL 1054.4−1146	108	V, R, I	4,10
CL 1103.7−1245b	106	V, R, I	3,4
CL 1040.7−1155	119	V, R, I	4,10
CL 1054.7−1245	100	V, R, I	4,10
CL 1324+3011	181	B, V, R, I	12,13
CL 1354.2−1230	126	V, R, I	3,4
CL 1216.8−1201	118	V, R, I	4,10
RX J1716+67	37	r, i, z	2,14
MS 1054−03	145	V, i	15
RX J0152.7−1357	219	r, K_s	16,17,18
CL 0023+0423	107	B, V, R, I	2,19
RX J1226.9+3332	119	r', i', z'	9
CL 1604+4304	96	B, V, R, I	12,13,19

CL 1604+4321	135	B, V, R, I	12,13,19
CL 1103.7−1245	178	V, R, I	4,20
XMMU J1230.3+1339	15	r, i, z	21,22
AX J2016+1127	30	R, I	23
RDCS J0910+54	156	V, R, K	24
RDCS J1252.9−2927	227	R, K_s	25
RX J0848.9+4452	8	R, I, J, K	26
RX J0848.6+4453	17	R, K	27
XMMU J2235.3−2557	179	J, K_s	28,29
XMMXCS J2215.9−1738	44	I, K_s	30

REFERENCES.−(1) Dressler et al. 1999. (2) Girardi and Mezzetti 2001. (3) Milvang-Jensen et al. 2008. (4) White et al. 2005. (5) Fabricant et al. 1994. (6) Ellingson et al. 1997. (7) Biviano et al. 2013. (8) Carrasco et al. 2007. (9) Jørgensen and Chiboucas 2013. (10) Halliday et al. 2004. (11) Ellingson et al. 1998. (12) Postman et al. 2001. (13) Lubin et al. 2002. (14) Gioia et al. 1999. (15) Tran et al. 2007. (16) Demarco et al. 2005. (17) Girardi et al. 2005. (18) Demarco et al. 2010. (19) Postman et al. 1998. (20) Vulcani et al. 2012. (21) Lerchster et al. 2011. (22) Fassbender et al. 2011. (23) Soucail et al. 2001. (24) Tanaka et al. 2008. (25) Demarco et al. 2007. (26) Rosati et al. 1999. (27) Stanford et al. 1997. (28) Rosati et al. 2009. (29) Santos et al. 2013. (30) Hilton et al. 2010.

All magnitudes are in the AB system, except for the clusters of Fabricant et al. (1994), Ellingson et al. (1997), (1998), and Dressler et al. (1999), which are in the Vega system.
There are different available magnitude bands: Johnson filters $BVRIJK$, SDSS bands $griz$ and near-SDSS $g'r'i'z'$, magnitudes of Kron R_c and I_c and 2MASS K_s band.
Clusters whose names are characterized by the letter "a" or "b" belong to a data sample from which I extract at least two systems with similar center coordinates and different redshifts.
As regards the best sampled cluster MACS J1206.2−0847, it is a massive and very rich system of the CLASH-VLT VIMOS Large Programme, which is thought to map the dark matter mass distribution in galaxy clusters and to probe distant lensed galaxies (Rosati et al., 2014).
In the following kinematical analysis, I will use $v = cz$ as the line-of-sight velocity of a galaxy at redshift z, and

$$v_{rf} = \frac{v - cz_{cluster}}{(1 + z_{cluster})} \tag{5.1}$$

as the line-of-sight velocity in the cluster rest frame, for which $z_{cluster}$ is the cluster redshift and $(1 + z_{cluster})$ is the cosmological correction.

Chapter 6

Software update

To perform cluster analysis I use many Fortran 77/90 programs and the Supermongo graphic software. I write several programs, but I also use many of them that has been written for the analysis of data samples of nearby clusters by the research group on galaxy clusters of the Observatory of Trieste (M. Girardi, A. Biviano et al.). I update these programs to adapt them to the data samples of distant clusters. The most important difference is the format of the position coordinates. In both cases, units of right ascension are hours, minutes and seconds, and units of declination are degrees, arcminutes and arcseconds. However, the values of position for distant clusters are characterized by a higher precision on seconds for right ascension and arcseconds for declination.
I report in figure 6.2 an example of input/output data file used in many programs for the kinematical analysis of distant clusters.
The first line of data file contains the name of the cluster and the available magnitude bands, the following rows show the data of galaxies: galaxy identification number, position coordinates in right ascension (J2000) and declination (J2000), apparent magnitude in R band when available, line-of-sight velocities with respective errors and other apparent magnitudes.
I use 99.00 when I haven't a measurement of apparent magnitude.
The used format file is:

```
format(a8,2(i2),f6.3,a1,2(i2),f5.2,10x,f5.2,i6,1x,i3,3x,f5.2,3x,f5.2)
```

Figure 6.1: Format of a typical data file.

where a8 is the galaxy identification number; 2(i2) and f6.3 indicate hours, minutes and seconds of right ascension; a1, 2(i2) and f5.2 are sign, degrees, arcminutes and arcseconds of declination; f5.2 is R magnitude; i6 and i3 represent galaxy velocities and their errors; other f5.2 are various apparent magnitudes.
To show an example I consider the galaxy members of cluster CL 1040.7−1155 at redshift $z = 0.70$, for which I have V, R and I magnitude bands.
In this case, all measurements of magnitudes are available and the error on galaxy velocities is always 90 kms^{-1}.

```
CL 1040.7-1155 R.V.I
  7     104038.960-115340.80          23.59211594  90   24.55   22.62
  8     104035.860-115358.30          20.99211114  90   21.69   20.30
 18     104034.620-115551.10          22.89212493  90   23.81   22.02
 19     104040.270-1156 4.20          21.33210454  90   22.50   20.00
 21     104040.970-115634.50          22.14210125  90   23.14   21.03
 23     104041.500-115655.90          22.04210065  90   22.84   21.18
 24     104036.860-115714.10          21.52211414  90   22.61   20.32
 27     104037.330-115747.90          23.57210664  90   24.35   22.68
 29     104035.040-115759.40          22.83211144  90   23.54   22.08
 31     104032.860-115821.80          21.50210334  90   22.42   20.60
 38     104038.510-1154 8.40          23.21211174  90   24.07   22.36
 39     104038.510-1154 6.20          24.73211024  90   25.55   23.89
 45     104039.560-115518.30          22.27211234  90   23.37   20.95
 49     104040.650-1156 1.50          22.04210754  90   23.16   20.68
 51     104040.940-115628.20          21.90209765  90   22.68   21.08
 53     104035.510-115653.70          22.56211683  90   23.64   21.49
 56     104033.720-115723.10          21.28211384  90   22.30   20.30
 66     104038.300-115317.60          22.98210994  90   24.19   21.74
 69     104039.860-115354.30          23.22211624  90   24.05   22.32
 72     104041.370-115437.60          23.51211474  90   24.56   22.46
 80     104047.430-115547.00          23.00212193  90   23.81   22.17
 81     104040.220-115558.70          22.62210784  90   23.79   21.39
 83     104038.340-115631.10          22.60211953  90   23.39   21.81
 87     104032.860-115728.40          23.92211773  90   24.99   22.74
 89     104034.650-115756.60          21.86210574  90   22.95   20.62
103     104046.030-115426.00          23.25210724  90   24.05   22.47
110     104041.120-115543.10          23.43210934  90   24.19   22.68
112     104041.010-115559.00          21.39212223  90   22.20   20.48
131     104039.760-1154 5.60          23.32211174  90   24.26   22.42
141     104035.610-1156 2.60          21.74212283  90   22.86   20.47
```

Figure 6.2: Typical data file.

6 Software update
I list the most important used programs for the:

1. Kinematical analysis
   - crea_fileorig.f tagliov_pesatoz.f centro.f coord.f opera.f;
   - amm_calc_dis_new.f sel_amm_dis_v_new.f fadlum.f ass1sep.f estrai1.f;
   - anelli_zmed_new.f marirosta1distOUT.f estraegal.f srobus.f wgapn.f;
   - show2vdist_new.f k1_mul_labels.f k1_new.f veldist_mul.f;
   - cfrpos.f massar200z.f mediac.f tab_col.f col_tab.f;
   - ks_2.f matkwo.f tutestnew.f sign99.f signWilcoxon.f .
   - alltogether_dis.f. binna.f chiquadro2.f.
2. Photometric analysis
   - selrosse.f selblu.f cormag_ellittiche.f cormag_spirali.f kmm.f ;
   - mag.f selectnomi.f select99.f sigma_clipping.f feigreg.f;
   - calcoloSFR.f SFRtoFHa.f.

As for kinematical analysis, I use the 1st row of programs to create the input data files, the 2nd and 3rd to estimate redshift, velocity dispersion and other physical quantities with the corresponding errors, the 4th to display plots, the 5th and 6th to apply statistical tests. As photometric analysis, I use the 1st and 2nd line to draw the color-magnitude diagrams, and the 3rd to derive SFRs and Hα fluxes.
Finally, I display a part of a my new program calcoloSFR.f used to estimate SFRs from colors.

```
      do  n=1,30000
      read(20,120,end=1100) s2,MasV,s3,MasR,s4,MasI,nome
120   format(a1,f5.2,1x,a1,f5.2,1x,a1,f5.2,2x,i3)
      V_I=-MasV+MasI
      logMstar_L=a+b*V_I
      Mstar_L=10**(logMstar_L)
      esp=-0.4*(-MasV-Msol)
      L=10**esp
      Mstar=Mstar_L*L
      logMstar_Msol=log10(Mstar)
      log_SFR=-27.40+5.02*logMstar_Msol-0.22*(logMstar_Msol**2)
      SFR=10**(log_SFR)
      write(30,130) SFR,nome
130   format(f6.3,2x,i3)
      enddo
1100  close(20)
1200  close(30)
      write(*,*) 'fine lavoro'
      stop
      end
```

Figure 6.3: Example of a Fortran 77/90 program: calcoloSFR.f.

Chapter 7

Selection of cluster members

In order to select cluster member galaxies from each sample, I apply the two-step method called "peak+gap" (P+G) already used by Girardi et al. (2015), Biviano et al. (2013) and several previous studies (Girardi et al., 2011, 1998; Fadda et al., 1996). The procedure is a combination of the 1D adaptive-kernel method DEDICA (Pisani, 1993, 1996) and the "shifting gapper", which uses both position and velocity information (Fadda et al., 1996; Girardi et al., 1996).
I use the adaptive kernel method to find the significant peaks in velocity distributions. The adaptive kernel technique is a nonparametric method for the evaluation of the density probability function underlying an observational discrete data set. For each detected peak, the method gives the corresponding significance and object density, as well as the associated objects. The main cluster body is naturally identified as the highest significant peak. All galaxies not belonging to this peak are rejected as noncluster members. I require that peaks be significant at the 99% confidence level, and for 3 clusters characterized by possible merger evidences I group secondary peaks with a velocity separation of about $\Delta v \simeq 2500\,\mathrm{kms}^{-1}$ (in the appropriate cluster rest frame) into unique structures. In dealing with distant clusters, I apply the peak analysis to some poor samples, thus obtaining small peak probability: in a few fields I identify clusters with the highest peak having a significance of less than 99% (but always $> 95\%$).
The combination of position and velocity information, represented by plots of velocity versus clustercentric distance, reveals the presence of surviving interlopers. To identify these interlopers in the above-detected systems, I apply the procedure of the "shifting gapper". I use the fixed gap method to a bin shifting along the distance from the cluster center: I apply a gap $\geq 1000\,\mathrm{kms}^{-1}$ (in the cluster rest frame) and a bin of 0.6 Mpc, large enough to include 15 galaxies. As for very poor distant clusters (with less than 15 members), galaxies are rejected only according to the first procedure, since the second one is useless.
In summary, the main steps of the "peak+gap" method are:

- peak detection of galaxies in the velocity distribution;
- "shifting gapper" in the velocity-clustercentric distance space.

Table 7.1 lists the results of this member selection procedure. In column (1) I list the cluster name; in column (2) the number of galaxies of the entire survey, N_{tot}; in column (3) the number of galaxies found by the adaptive kernel method in each peak, N_p; in column (4) the number of galaxies left after the "shifting gapper", N_g, and used to compute the mean redshift determined via the biweight estimator (Beers et al., 1990) and reported in column (5) with jackknife error; in column (6) and (7) the cluster center as determined via the biweight mean of right ascension and declination.

Table 7.1: Cluster membership

Cluster name	N_{tot}	N_p	N_g	$< z > \pm\delta < z >$	R.A. (J2000)	Decl. (J2000)
CL 0024+16	130	107	100	0.3937±0.0003	00 26 33.821	+17 10 06.76
CL 1301.7−1139a	87	17	17	0.3969±0.0003	13 01 36.740	−11 39 24.93
CL 0939+47	132	72	70	0.4060±0.0005	09 42 58.678	+46 58 59.89
CL 0303+17	84	47	46	0.4190±0.0004	03 06 14.410	+17 18 01.31
CL 1202.7−1224	73	21	21	0.4240±0.0004	12 02 43.180	−12 24 11.89
MS 0302.5+1717	43	30	28	0.4242±0.0004	03 05 17.990	+17 28 29.99
MS 0302.7+1658	96	38	34	0.4248±0.0005	03 05 31.692	+17 10 05.23
CL 1037.9−1243a	131	47	47	0.4255±0.0003	10 37 49.769	− 12 44 45.30
MS 1621.5+2640	262	119	104	0.4267±0.0002	16 23 35.137	+26 35 05.01
MACS J1206.2−0847	2535	605	599	0.4399±0.0002	12 06 13.938	−08 47 41.35
CL 1138.2−1133a	112	14	14	0.4546±0.0005	11 38 06.088	−11 36 15.13
CL 1059.2−1253	85	42	42	0.4564±0.0003	10 59 08.834	−12 53 45.36
3C 295	35	25	25	0.4593±0.0011	14 11 20.057	+52 12 16.54
CL 1018.8−1211	71	34	34	0.4736±0.0003	10 18 47.129	−12 11 51.37
CL 1138.2−1133	112	49	49	0.4797±0.0003	11 38 09.868	−11 33 37.22
CL 1301.7−1139	87	39	37	0.4832±0.0004	13 01 38.941	−11 39 56.26
RX J1117.4+0743	75	37	37	0.4857±0.0008	11 17 26.238	−07 43 50.37
CL 1420.3−1236	73	28	27	0.4961±0.0002	14 20 15.805	−12 35 53.98
CL 1411.1−1148	78	26	25	0.5196±0.0005	14 11 04.304	−11 48 18.75
CL 1601+42	98	59	55	0.5400±0.0003	16 03 10.030	+42 45 16.80
MS 0451.6−0305	70	53	44	0.5401±0.0006	04 54 10.962	+03 01 07.81
CL 1232.5−1250	94	56	54	0.5418±0.0005	12 32 30.760	−12 50 41.13
MS 0015.9+1609	111	63	50	0.5492±0.0005	00 18 31.504	+16 25 27.94
CL 1119.3−1129	67	23	20	0.5499±0.0001	11 19 16.615	−11 30 00.02
CL 0054−27	25	12	12	0.5608±0.0010	00 56 56.360	−27 40 27.71
CL 1037.9−1243	131	19	19	0.5784±0.0004	10 37 53.480	−12 43 45.60
CL 1353.0−1137	68	21	21	0.5878±0.0005	13 53 02.350	−11 37 28.73
CL 1354.2−1230a	126	21	17	0.5958±0.0005	13 54 08.764	−12 31 50.25
CL 1103.7−1245a	106	15	15	0.6261±0.0003	11 03 37.299	−12 46 48.51
CL 1054.4−1146	108	49	49	0.6976±0.0003	10 54 26.612	−11 47 21.26
CL 1103.7−1245b	106	15	15	0.7032±0.0003	11 03 42.498	−12 45 36.53
CL 1040.7−1155	119	30	30	0.7044±0.0003	10 40 38.444	−11 55 54.09
CL 1054.7−1245	100	37	36	0.7500±0.0003	10 54 42.805	−12 46 10.32
CL 1324+3011	181	51	44	0.7547±0.0004	13 24 48.554	+30 11 23.97
CL 1354.2−1230	126	23	23	0.7612±0.0005	13 54 10.260	−12 31 03.90
CL 1216.8−1201	118	67	66	0.7939±0.0004	12 16 44.582	−12 01 18.67
RX J1716+67	37	37	31	0.8065±0.0008	17 16 51.116	−67 08 25.78
MS 1054−03	145	145	143	0.8306±0.0003	10 57 00.424	−03 37 31.84
RX J0152.7−1357	219	135	125	0.8359±0.0004	01 52 42.255	−13 57 53.21
CL 0023+0423	107	24	16	0.8453±0.0002	00 23 51.631	+04 22 02.39
RX J1226.9+3332	119	59	50	0.8910±0.0005	12 26 58.504	+33 32 51.66
CL 1604+4304	96	23	16	0.8978±0.0006	16 04 24.690	+43 04 56.24
CL 1604+4321	135	42	37	0.9219±0.0004	16 04 34.070	+43 20 56.80
CL 1103.7−1245	178	24	22	0.9578±0.0004	11 03 46.334	−12 45 30.71
XMMU J1230.3+1339	15	13	13	0.9737±0.0007	12 30 15.819	+13 39 26.69
AX J2016+1127	30	6	6	1.0044±0.0013	20 19 18.279	+11 27 15.70

RDCS J0910+54	156	28	23	1.0998±0.0005	09 10 43.478	+54 22 02.16
RDCS J1252.9−2927	227	38	38	1.2370±0.0004	12 52 55.040	−29 27 08.91
RX J0848.9+4452	8	6	6	1.2602±0.0011	08 48 58.615	+44 51 49.70
RX J0848.6+4453	17	9	9	1.2727±0.0008	08 48 34.813	+44 53 47.00
XMMU J2235.3−2557	179	31	30	1.3905±0.0005	22 35 20.729	−25 57 32.26
XMMXCS J2215.9−1738	44	44	41	1.4589±0.0004	22 15 58.373	−17 37 58.58

NOTE.−Units of right ascension (R.A.) are hours, minutes and seconds, and units of declination (Decl.) are degrees, arcminutes and arcseconds.

In figure 7.1 I show the XY plots of galaxy positions for each survey. The selected cluster members are highlighted in red.

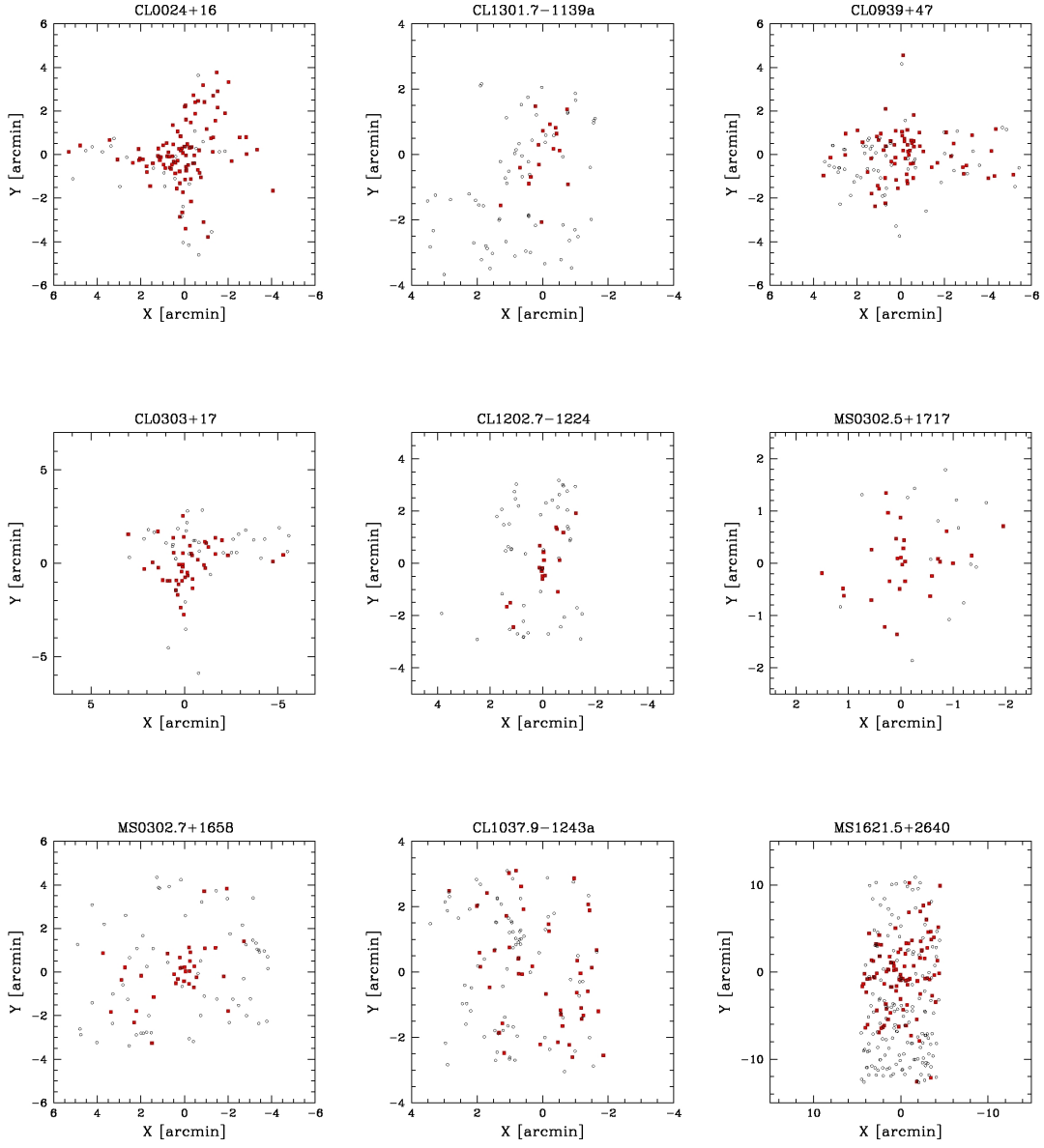

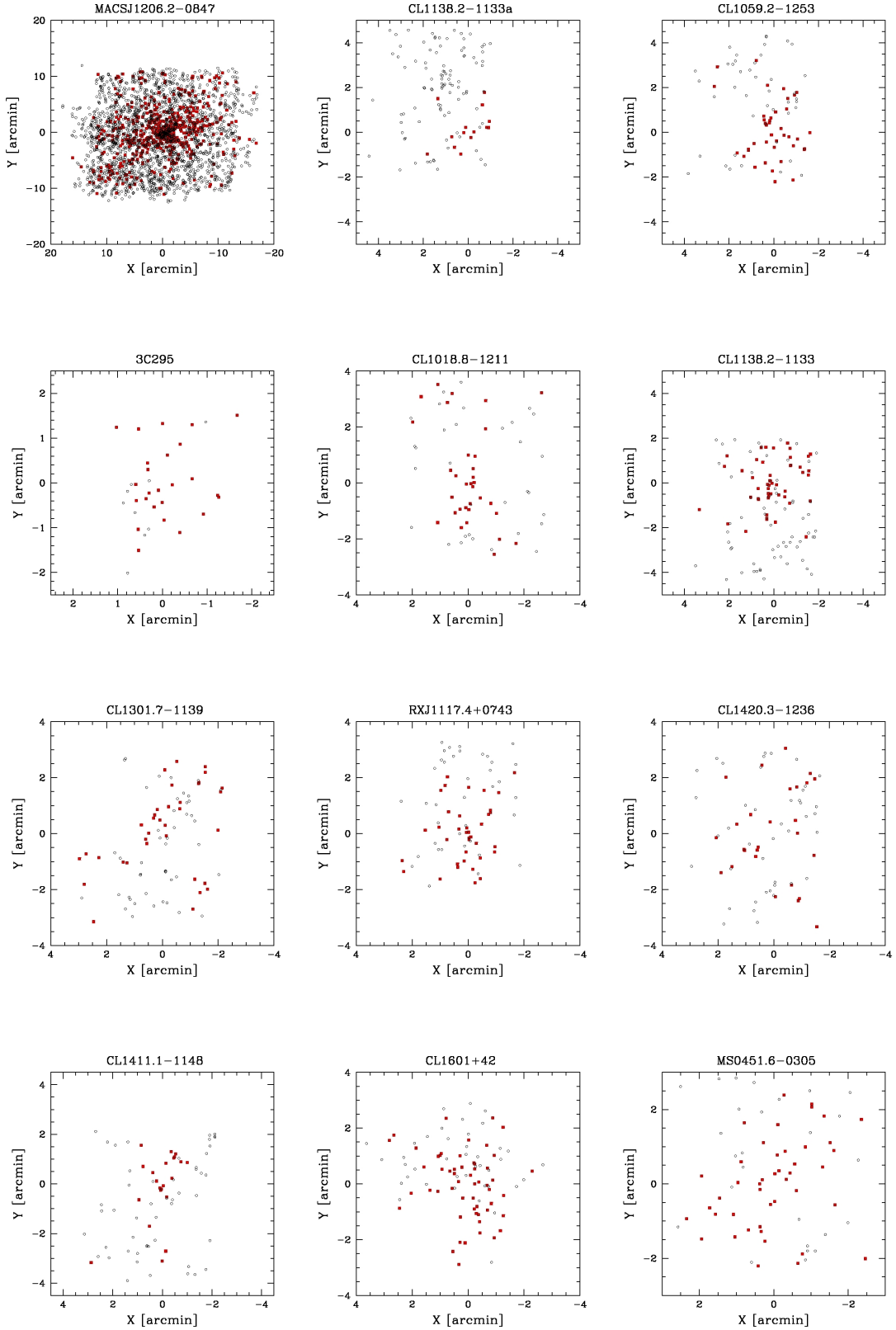
MACSJ1206.2−0847
CL1138.2−1133a
CL1059.2−1253
3C295
CL1018.8−1211
CL1138.2−1133
CL1301.7−1139
RXJ1117.4+0743
CL1420.3−1236
CL1411.1−1148
CL1601+42
MS0451.6−0305
X [arcmin]
Y [arcmin]

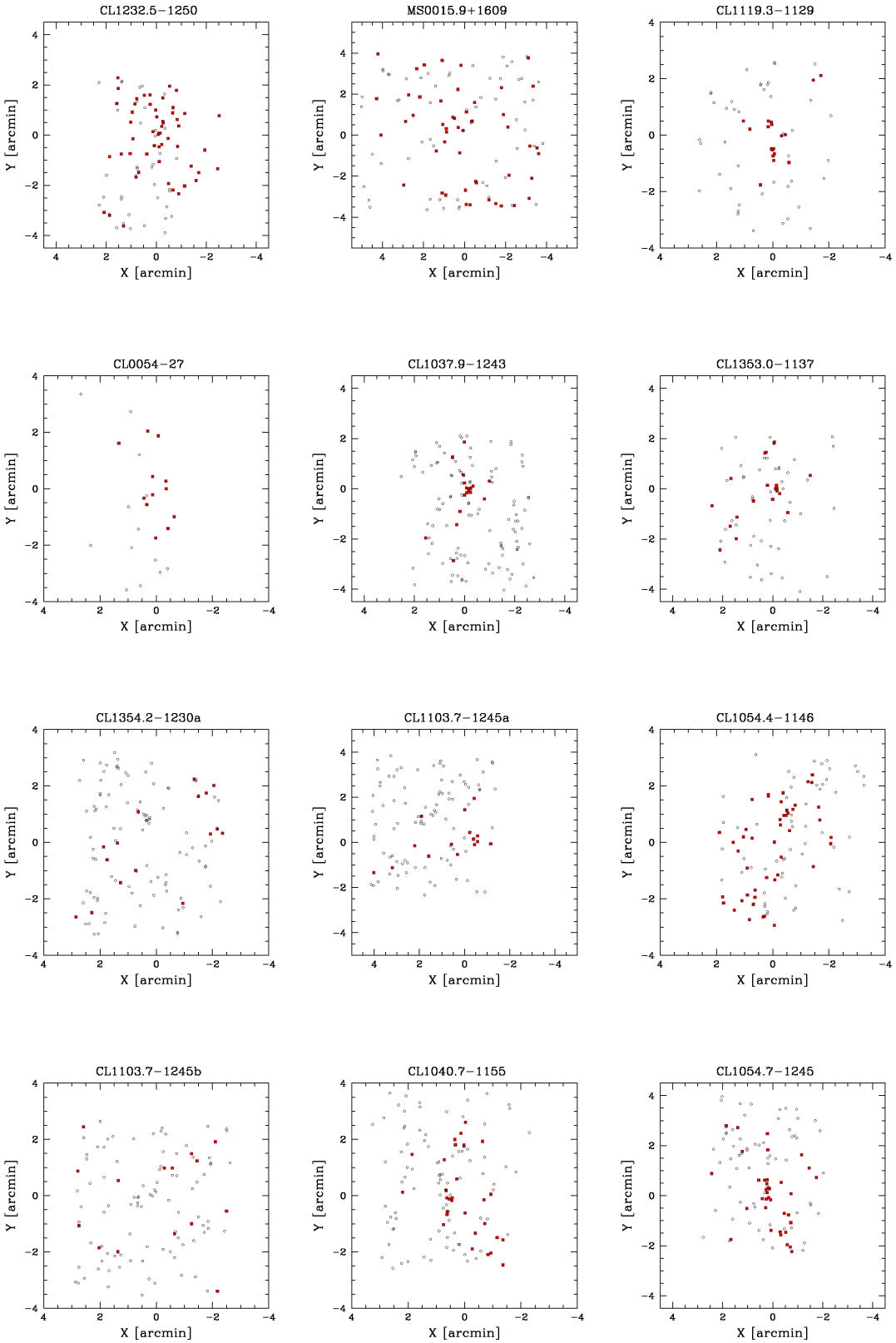
CL1232.5−1250
MS0015.9+1609
CL1119.3−1129
CL0054−27
CL1037.9−1243
CL1353.0−1137
CL1354.2−1230a
CL1103.7−1245a
CL1054.4−1146
CL1103.7−1245b
CL1040.7−1155
CL1054.7−1245
X [arcmin]
Y [arcmin]

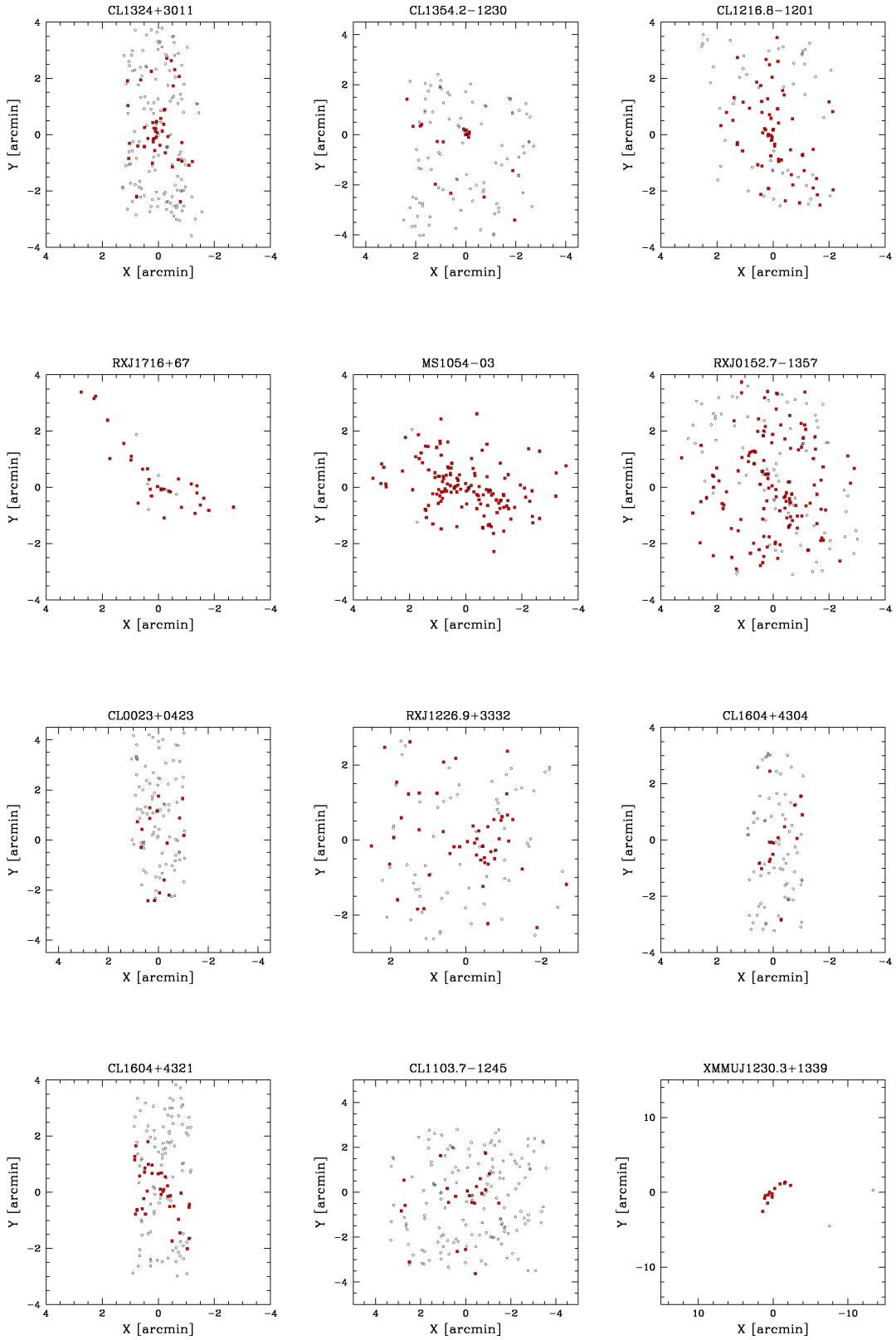
CL1324+3011
CL1354.2−1230
CL1216.8−1201
RXJ1716+67
MS1054−03
RXJ0152.7−1357
CL0023+0423
RXJ1226.9+3332
CL1604+4304
CL1604+4321
CL1103.7−1245
XMMUJ1230.3+1339
X [arcmin]
Y [arcmin]

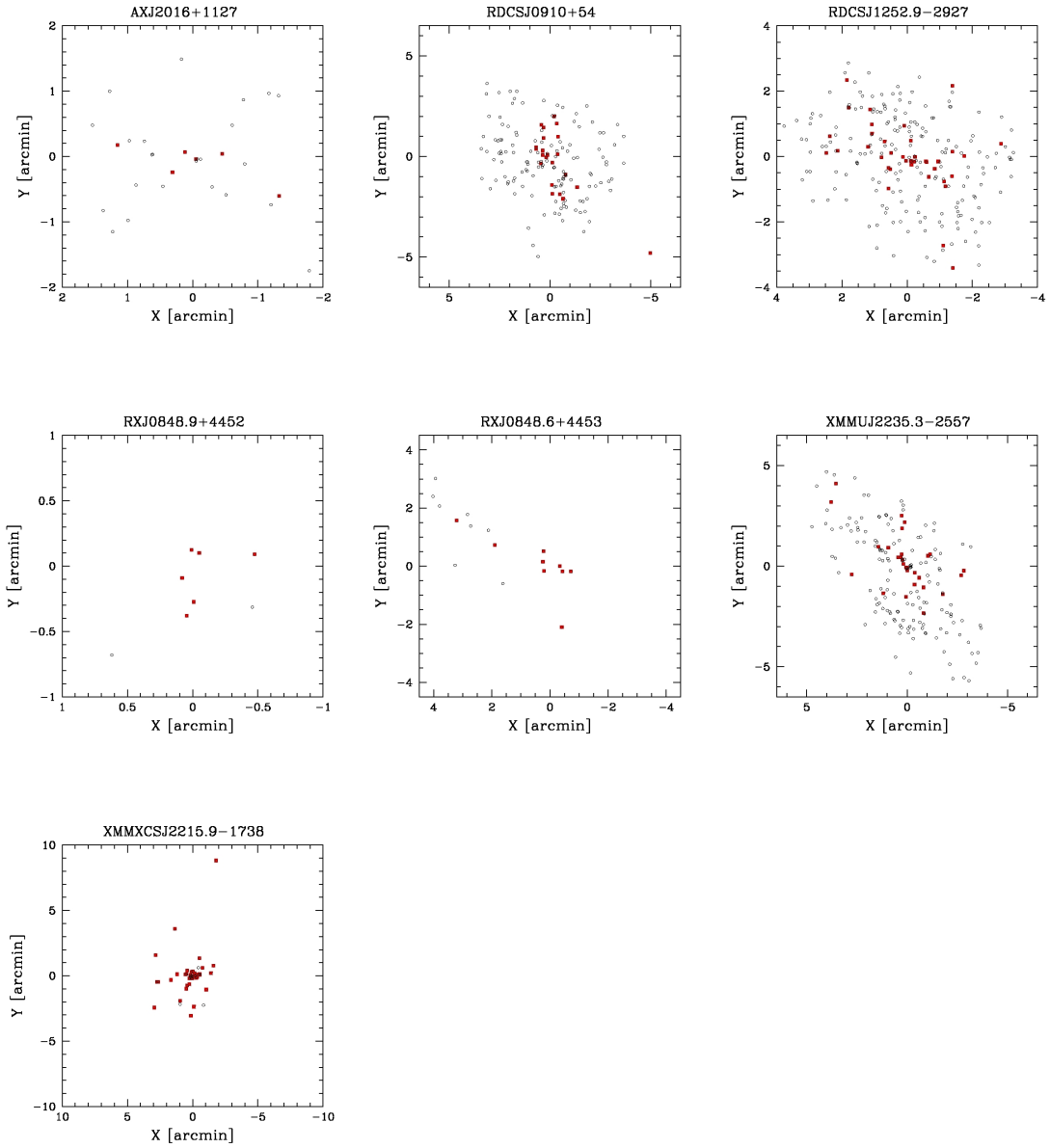

Figure 7.1: Plots of galaxy positions centered on cluster center. Axis scales are in units of arcminutes. The cluster name is indicated at the top of each plot. Red squares show the positions of cluster members, open circles indicate all the other galaxies of the survey.

I also show in figure7.2 the distribution of galaxies as a function of redshift for each cluster survey. From this kind of histogram it is possible to recognize the density peak, which corresponds to the main cluster body. Again the cluster name is indicated at the top of each plot.

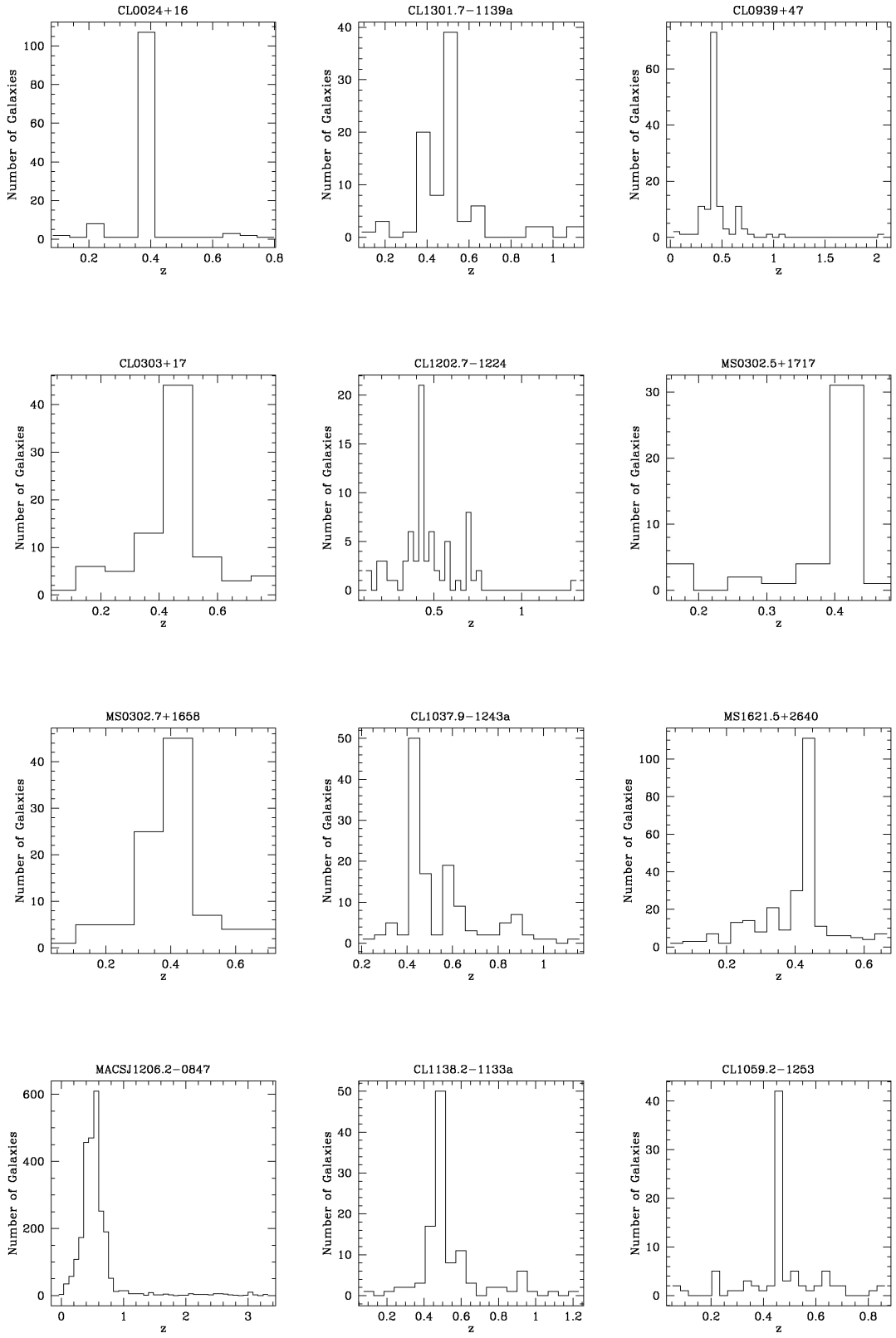
CL0024+16
CL1301.7−1139a
CL0939+47
CL0303+17
CL1202.7−1224
MS0302.5+1717
MS0302.7+1658
CL1037.9−1243a
MS1621.5+2640
MACSJ1206.2−0847
CL1138.2−1133a
CL1059.2−1253
Number of Galaxies
z

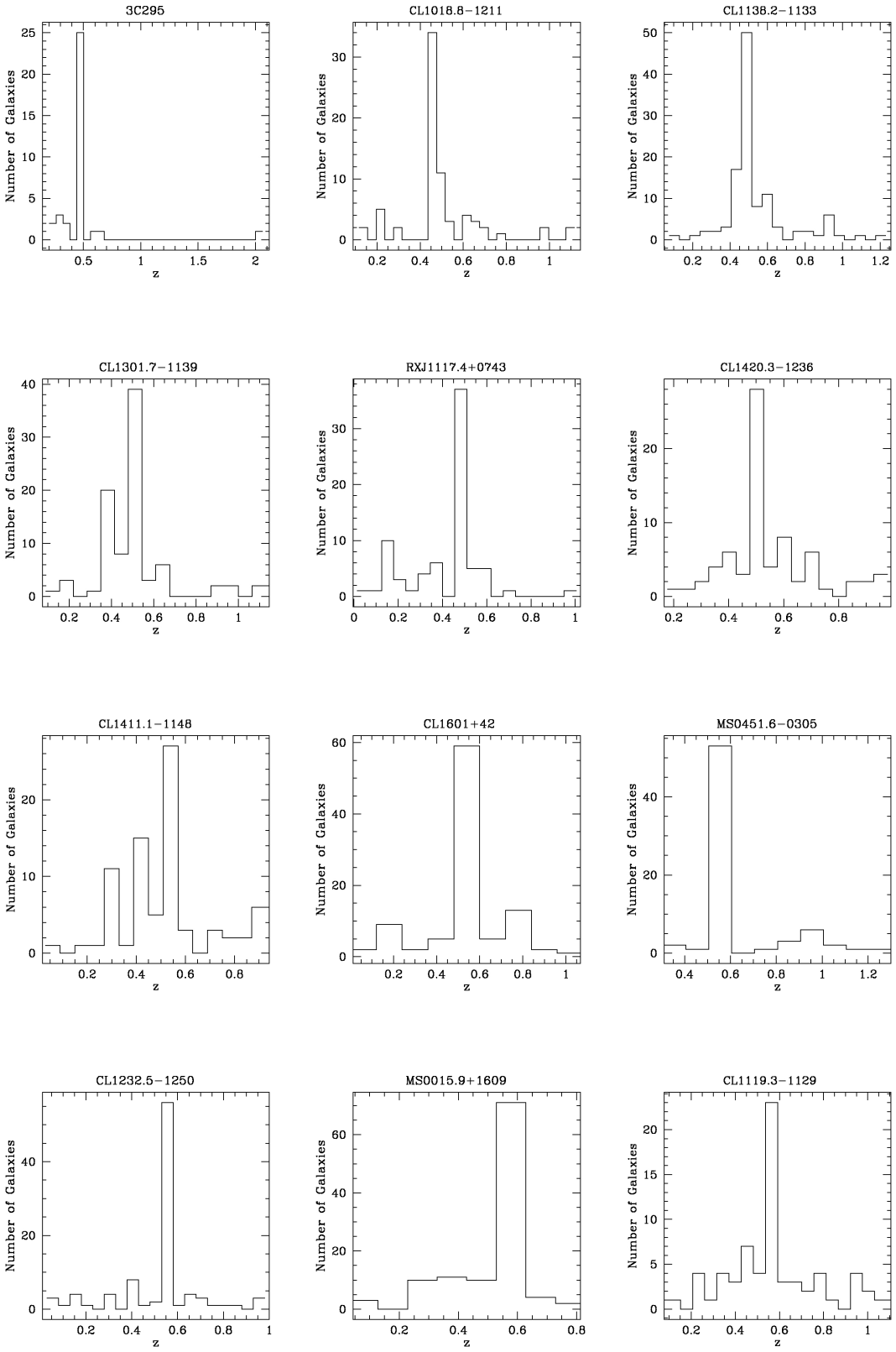
3C295
CL1018.8−1211
CL1138.2−1133
CL1301.7−1139
RXJ1117.4+0743
CL1420.3−1236
CL1411.1−1148
CL1601+42
MS0451.6−0305
CL1232.5−1250
MS0015.9+1609
CL1119.3−1129
Number of Galaxies
z

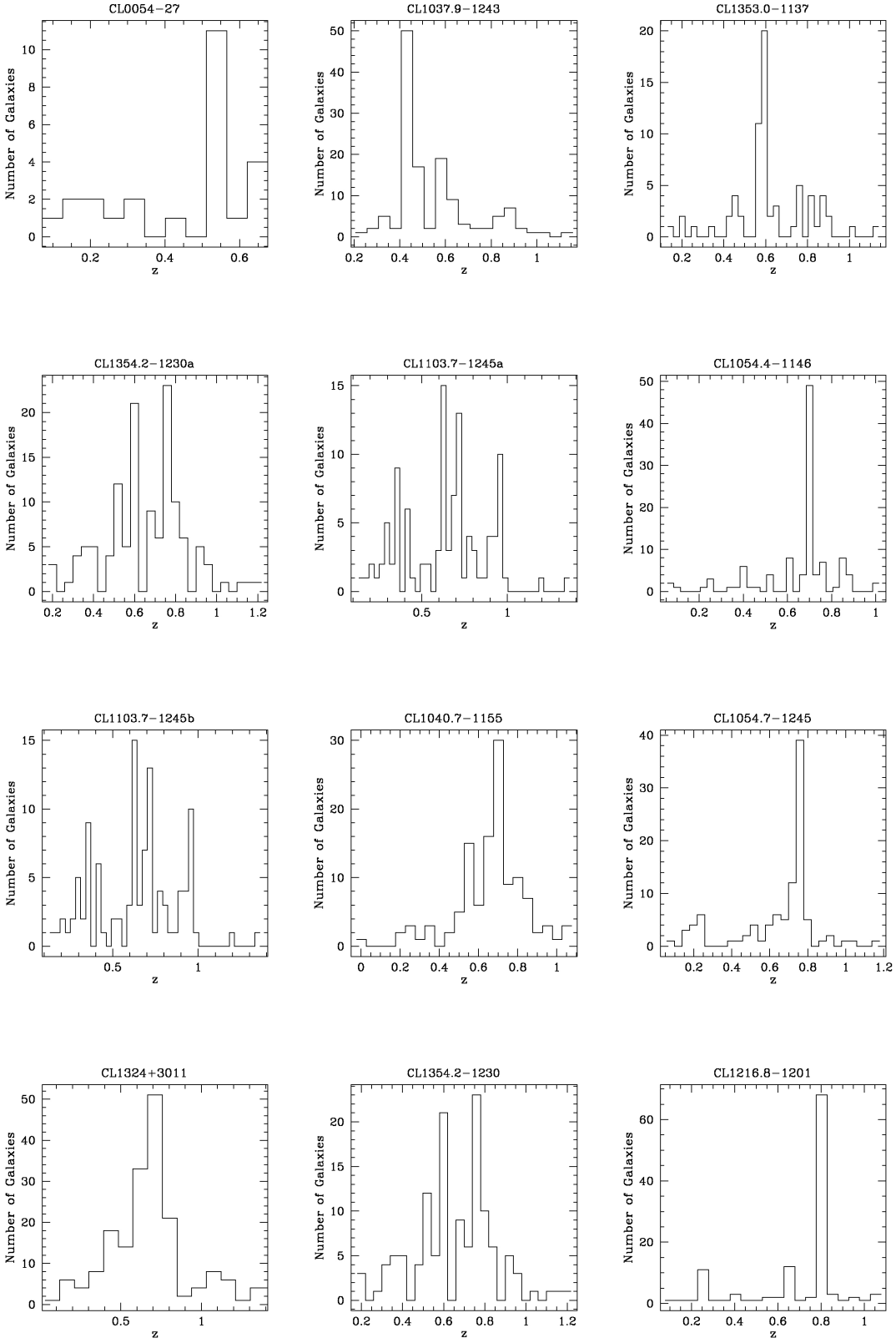
CL0054−27
CL1037.9−1243
CL1353.0−1137
CL1354.2−1230a
CL1103.7−1245a
CL1054.4−1146
CL1103.7−1245b
CL1040.7−1155
CL1054.7−1245
CL1324+3011
CL1354.2−1230
CL1216.8−1201
Number of Galaxies
z

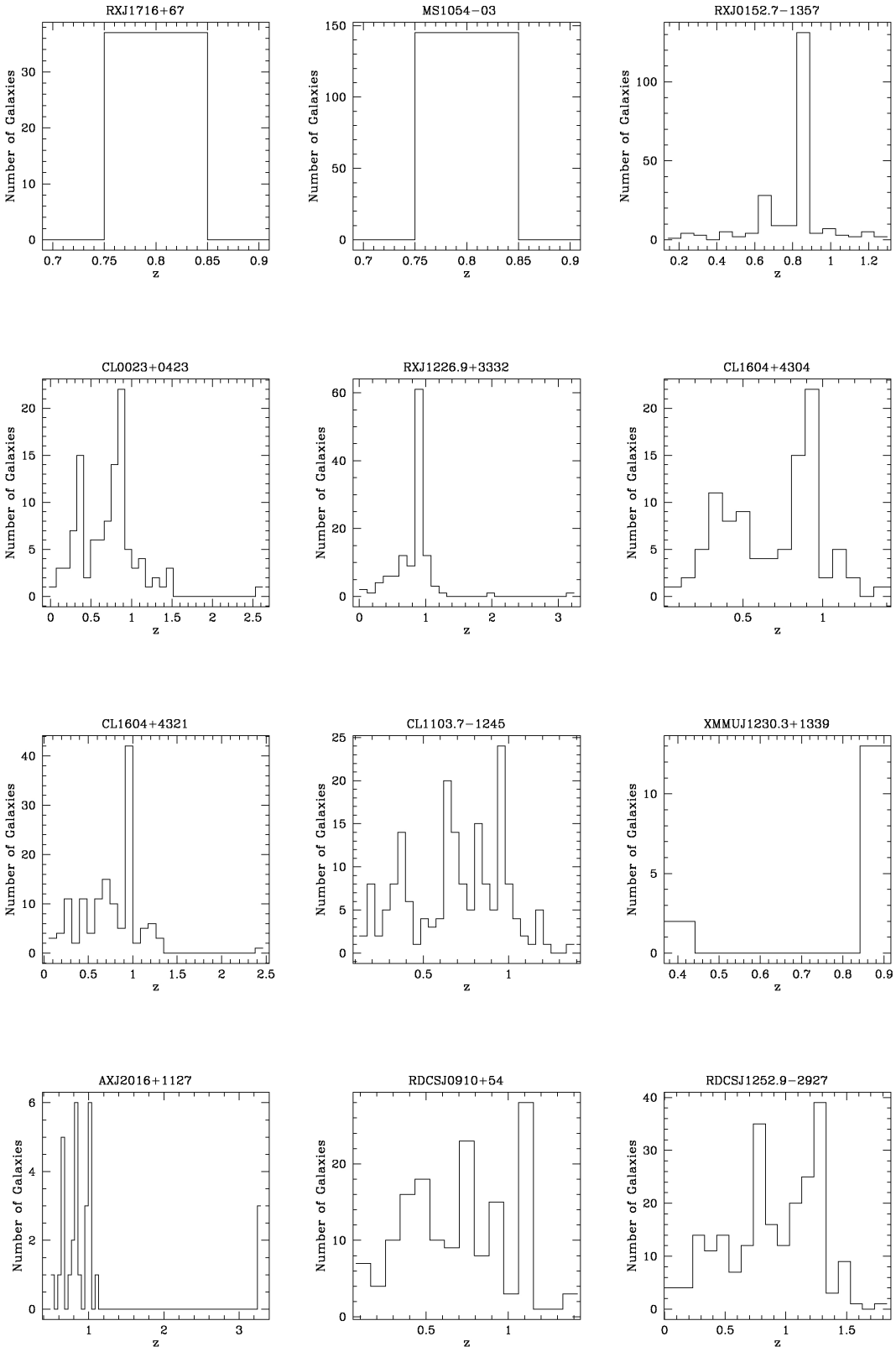
RXJ1716+67
MS1054−03
RXJ0152.7−1357
CL0023+0423
RXJ1226.9+3332
CL1604+4304
CL1604+4321
CL1103.7−1245
XMMUJ1230.3+1339
AXJ2016+1127
RDCSJ0910+54
RDCSJ1252.9−2927
Number of Galaxies
z

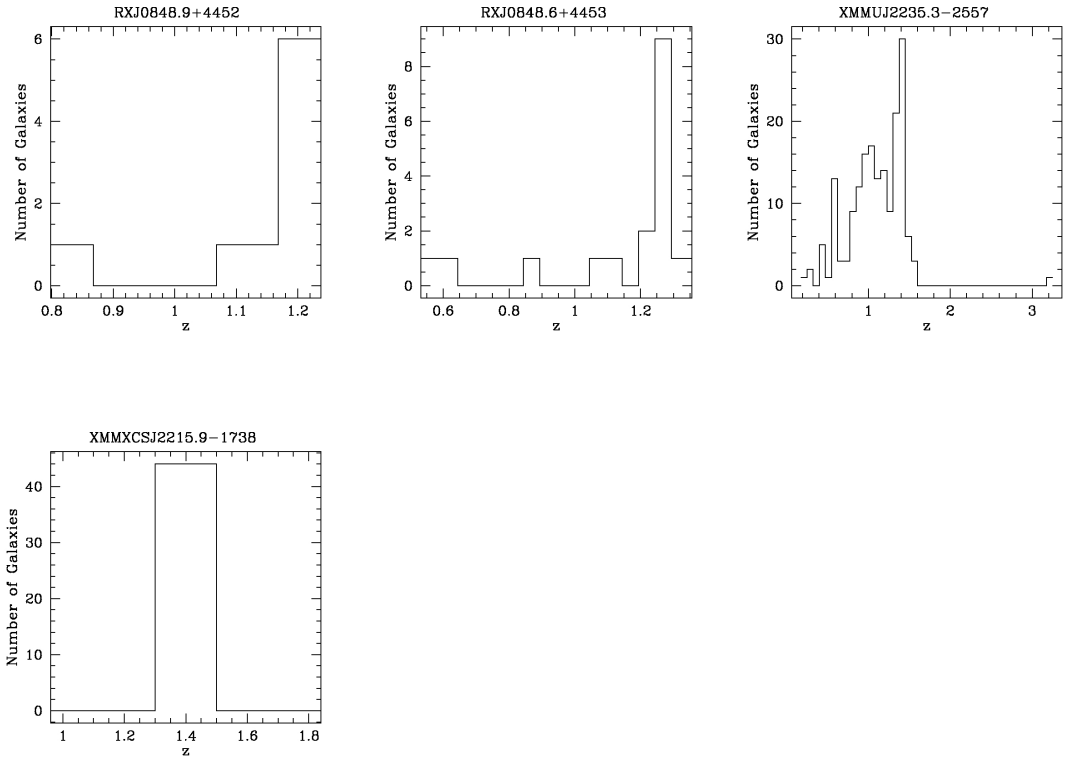

Figure 7.2: Distribution of galaxies in redshift for each cluster survey.

I fit the probability density function in the radial velocity space with the one-dimensional adaptive-kernel method in order to select the galaxies belonging to the peak. Figure 7.3 shows an example of output results for cluster CL 0024+16 after the peak analysis with program ass1sep.f: in column (1) there is the peak number; in (2) the number of galaxies belonging to each peak and used to estimate the mean velocity in column (3); in (4) the significance of the peak; in (5), (6) and (7) the number of galaxies belonging to the previous [−1], current [0] and next [+1] peak, respectively; finally, in column (8) the relative galaxy density in arbitrary units.

p	ngal	cz	significance	-1	0	+1	rel. dens.
1	3	33531.6	0.65949921E+00	1	2	0	0.008415881263
2	6	64300.6	0.92437408E+00	0	6	0	0.024905649877
3	3	73102.2	0.35107313E+00	1	2	0	0.010067928207
4	1	103021.9	0.00000000E+00	1	0	0	0.002838927719
5	107	118277.4	0.10000000E+01	0	107	0	1.000000000000
6	2	139426.6	0.00000000E+00	2	0	0	0.004295838902
7	1	166624.0	0.00000000E+00	1	0	0	0.002821664763
8	1	186929.7	0.00000000E+00	1	0	0	0.002836025303
9	3	196639.5	0.87842795E+00	0	3	0	0.014233361025
10	2	210988.2	0.11305071E-03	2	0	0	0.004624254000
11	1	242502.0	0.00000000E+00	1	0	0	0.002821611698

Figure 7.3: Example of output results of the peak analysis for CL 0024+16: the peak with significance of 100% is the number 5, which contains 107 galaxies at $< z >= 0.3945$.

I plot in figure 7.4 the significant peaks in the velocity space $v = cz$ for each cluster.

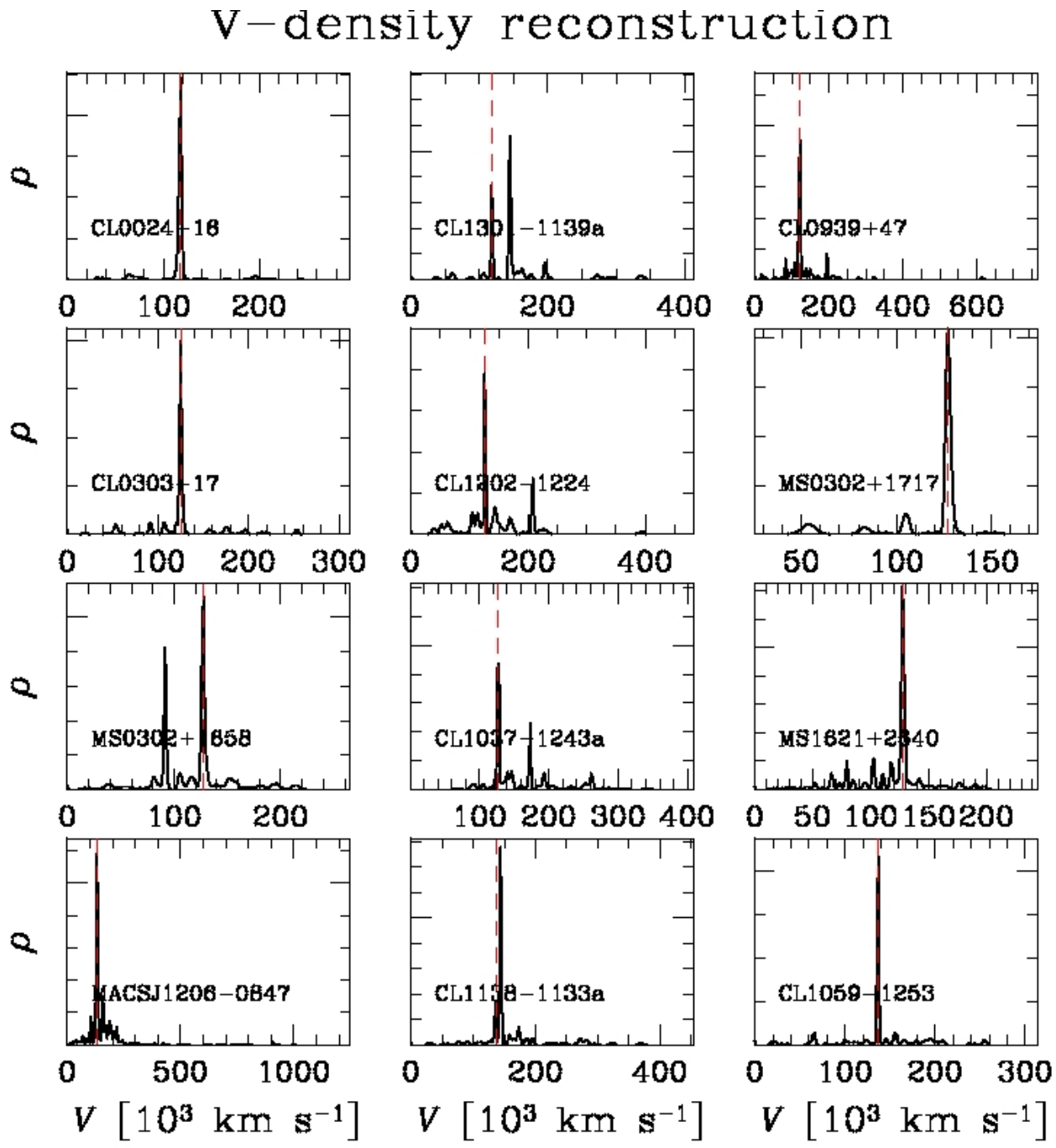

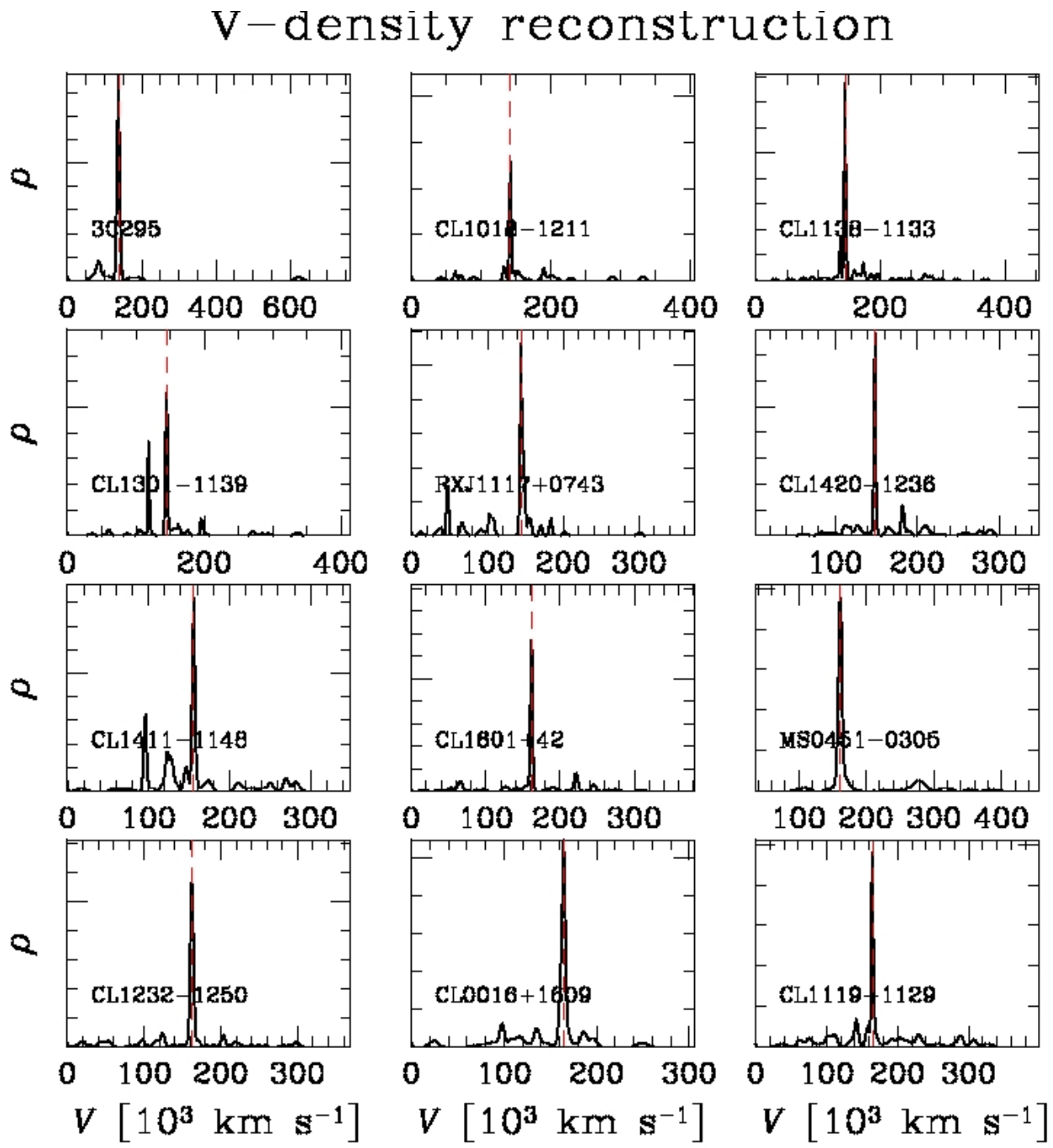
V−density reconstruction
ρ
30295
CL1018−1211
CL1138−1133
CL130 −1139
RXJ1117+0743
CL1420−1236
CL1411−1148
CL1601+42
MS0451−0305
CL1232−1250
CL0016+1609
CL1119+1129
0 200 400 600
0 200 400
0 200 400
0 200 400
0 100 200 300
100 200 300
0 100 200 300
0 100 200 300
100 200 300 400
0 100 200 300
0 100 200 300
0 100 200 300
V [10³ km s⁻¹]
V [10³ km s⁻¹]
V [10³ km s⁻¹]

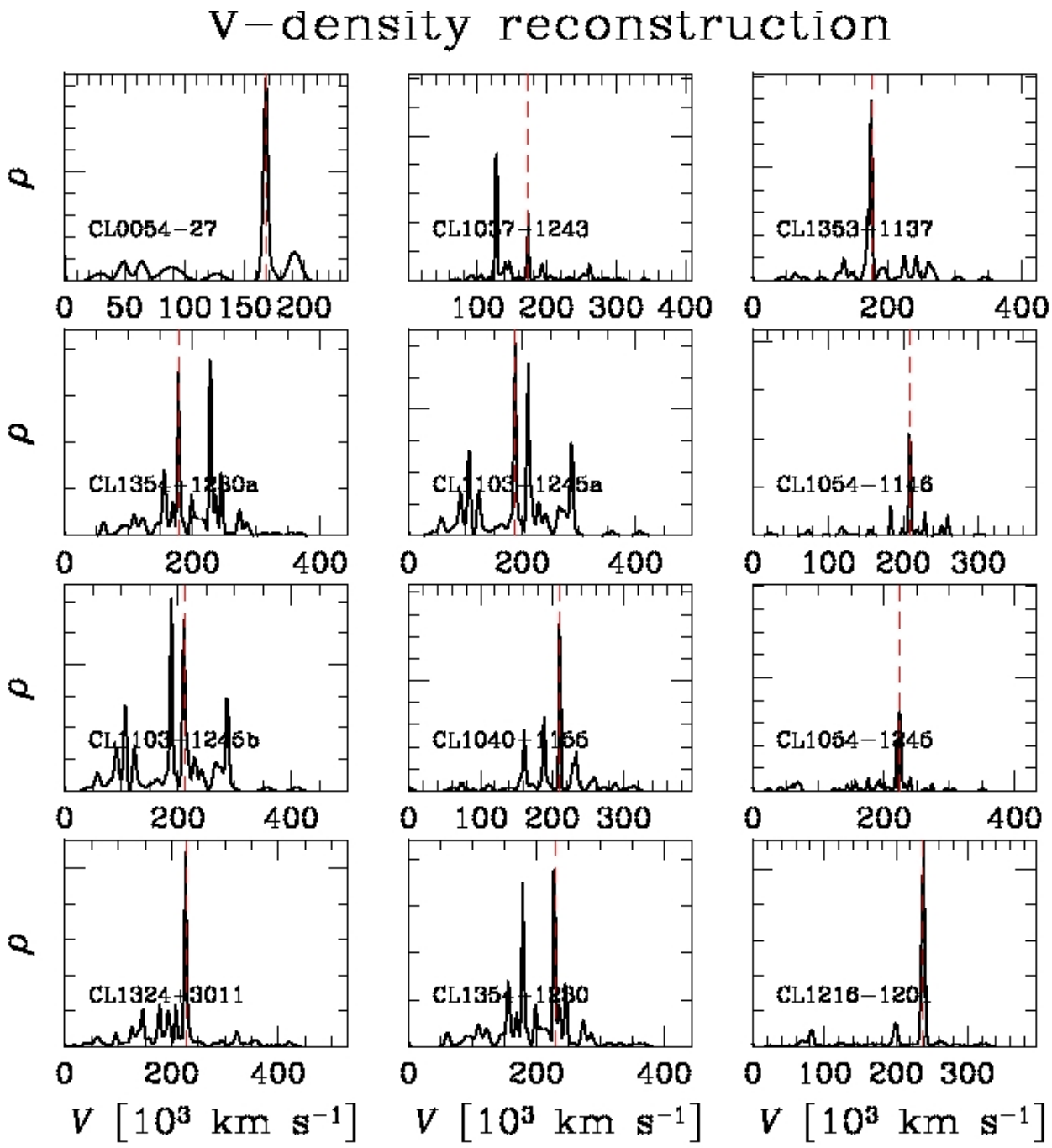
V−density reconstruction
ρ
CL0054−27
CL1037−1243
CL1353+1137
CL1354+1230a
CL1103−1245a
CL1054−1146
CL1103−1245b
CL1040+1155
CL1054−1245
CL1324+3011
CL1354+1230
CL1216−1201
0 50 100 150 200
100 200 300 400
0 200 400
0 100 200 300
V [10³ km s⁻¹]

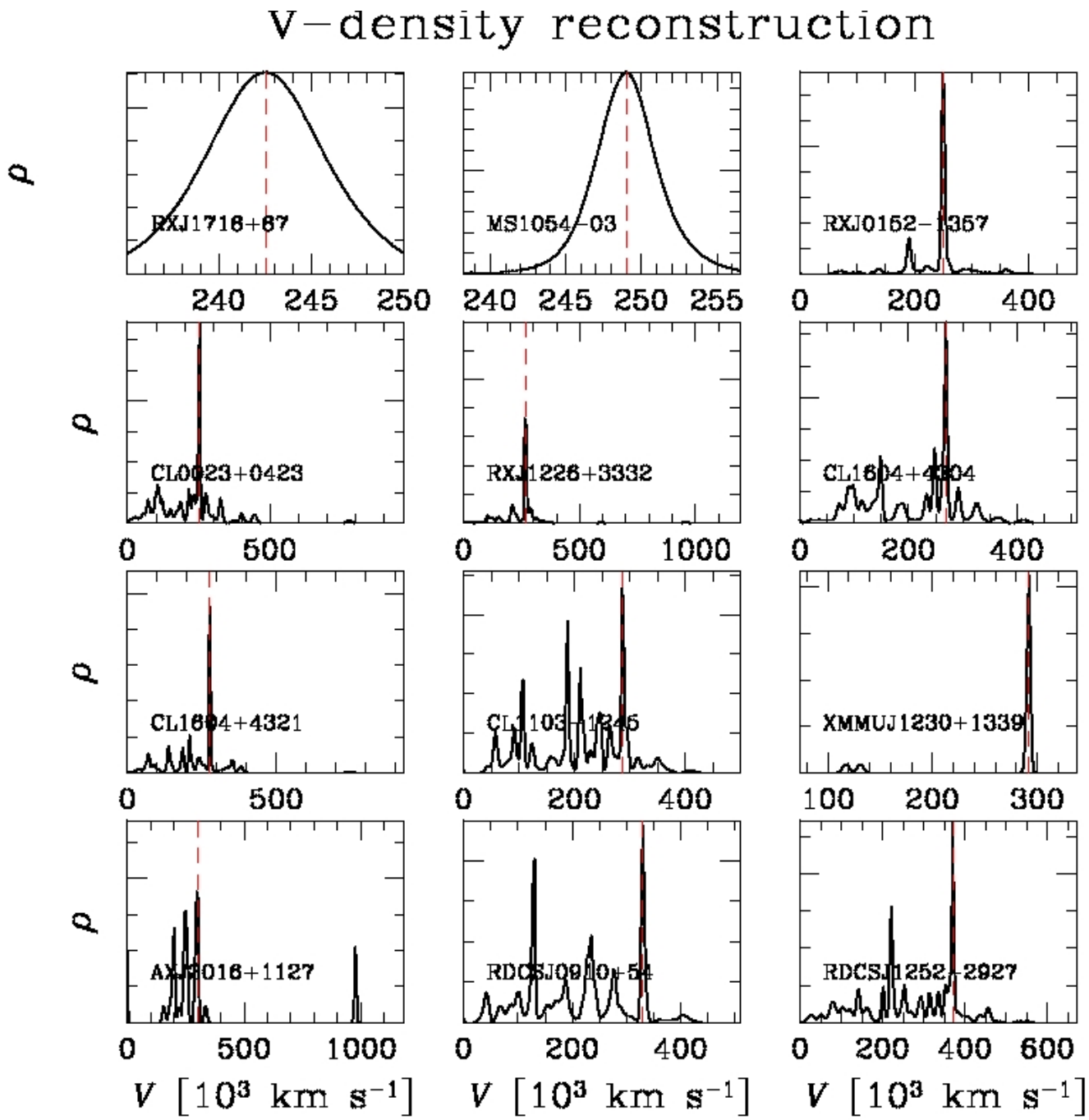
V−density reconstruction
ρ
RXJ1716+67
MS1054−03
RXJ0152−1357
CL0023+0423
RXJ1226+3332
CL1604+4304
CL1604+4321
XMMUJ1230+1339
AXJ2016+1127
RDCSJ1252−2927
V [10³ km s⁻¹]

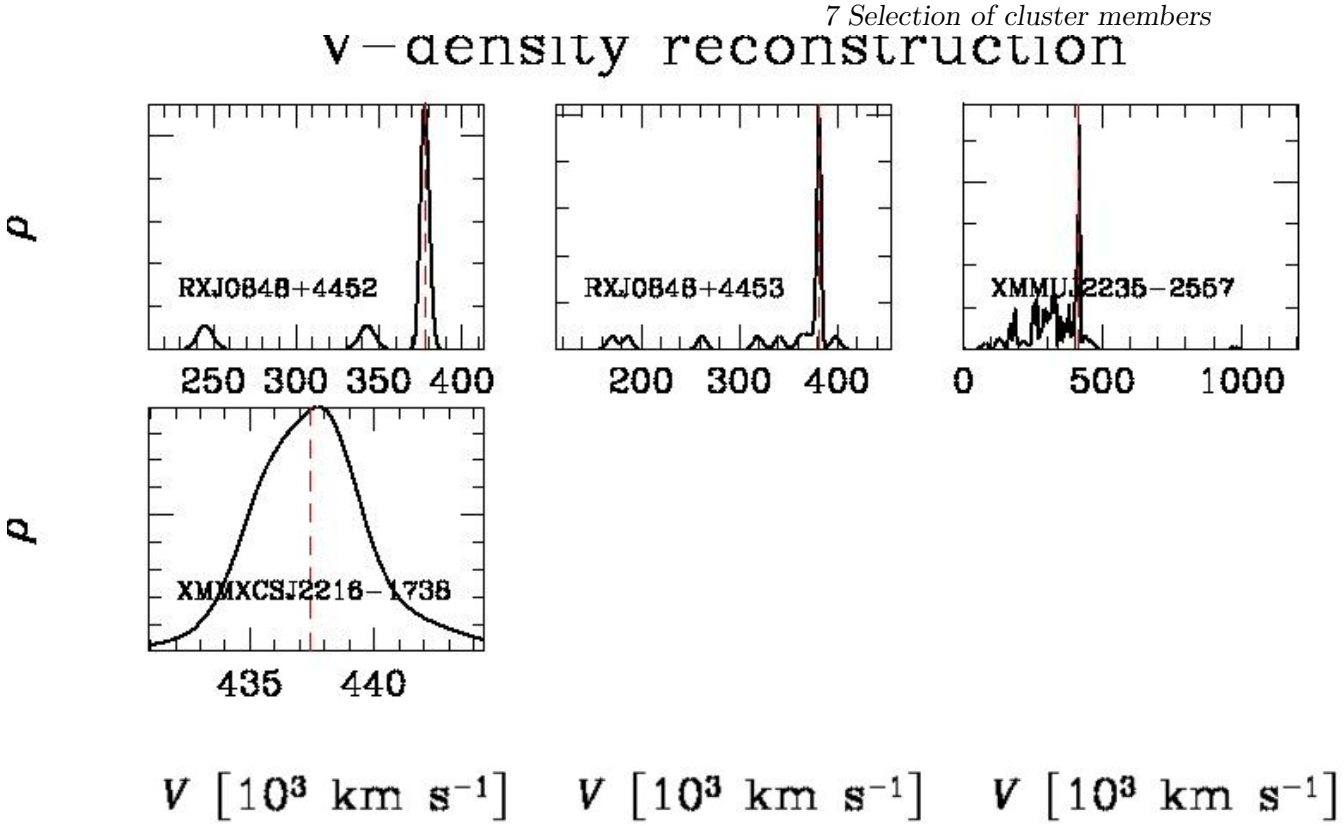

Figure 7.4: 1D adaptive-kernel method: identification of the significant peaks in velocity distribution. The horizontal axis is the radial velocity $v = cz$ in units of 10^3 kms^{-1} and the vertical axis represents the galaxy density in arbitrary units. The red dotted vertical line highlights the mean velocity.

I complete the "peak+gap" member selection method, applying the "shifting gapper" to the galaxies belonging to the most significant peaks. For 29 clusters with at least 30 final members I plot the velocity− density reconstruction in figure 7.5. When the peak has the shape of a perfect Gaussian with at half the dotted line representing the mean velocity, the procedure isolates only cluster members from the survey. However, for many clusters the Gaussian is characterized by a long right and/or left tail, evidence of the fact that there are some interlopers. Several curves show small peaks or deformations, which represent possible structures composed by different clumps or are due to the substructures of the clusters.
Systems with less than 30 members have been excluded since their apparent deviation form a Gaussian distribution can be due to low statistics.

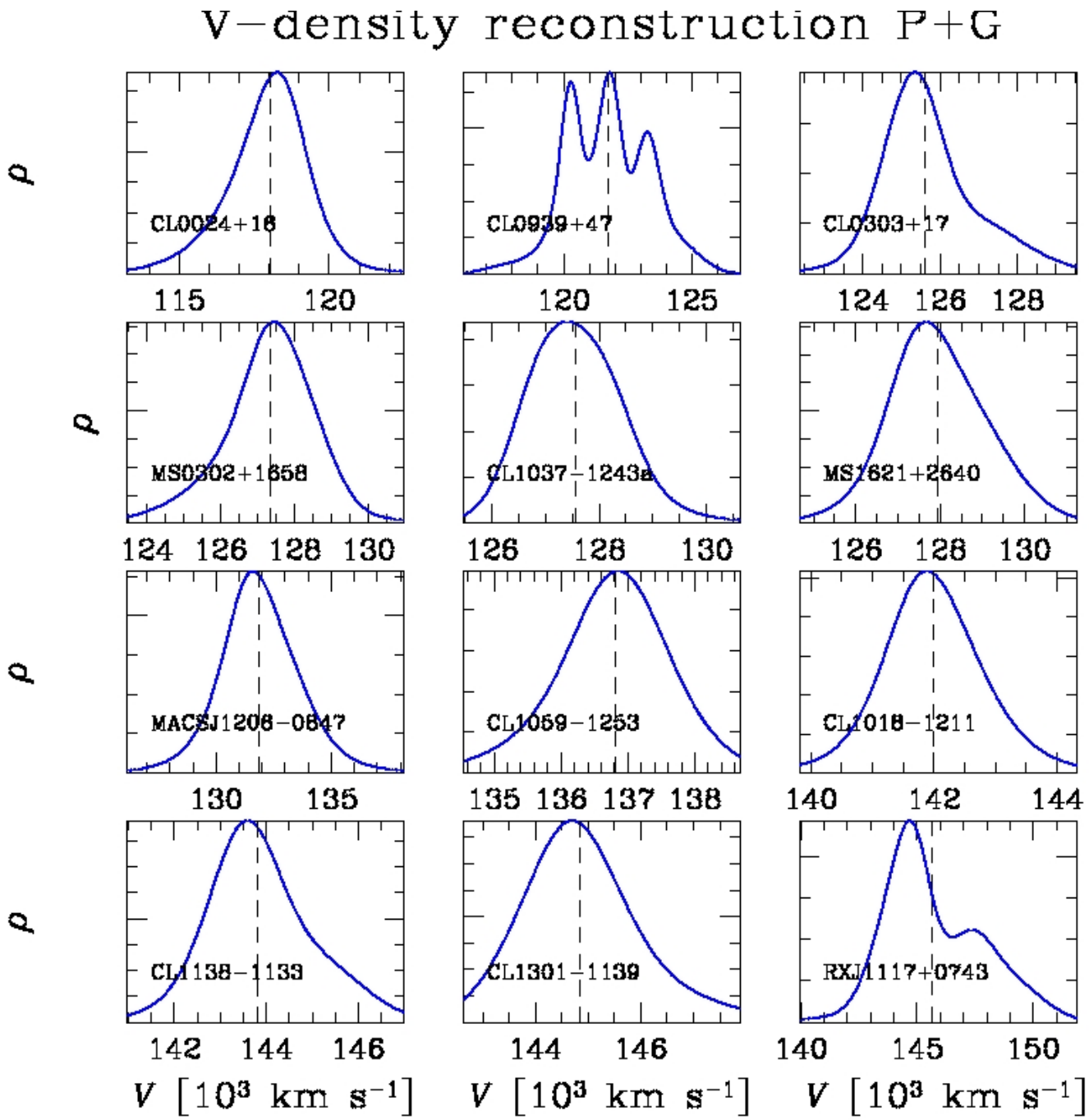
V−density reconstruction P+G
ρ
CL0024+16
CL0939+47
CL0303+17
MS0302+1658
CL1037−1243a
MS1621+2640
MACSJ1206−0847
CL1059−1253
CL1018−1211
CL1138−1133
CL1301−1139
RXJ1117+0743
V [10³ km s⁻¹]

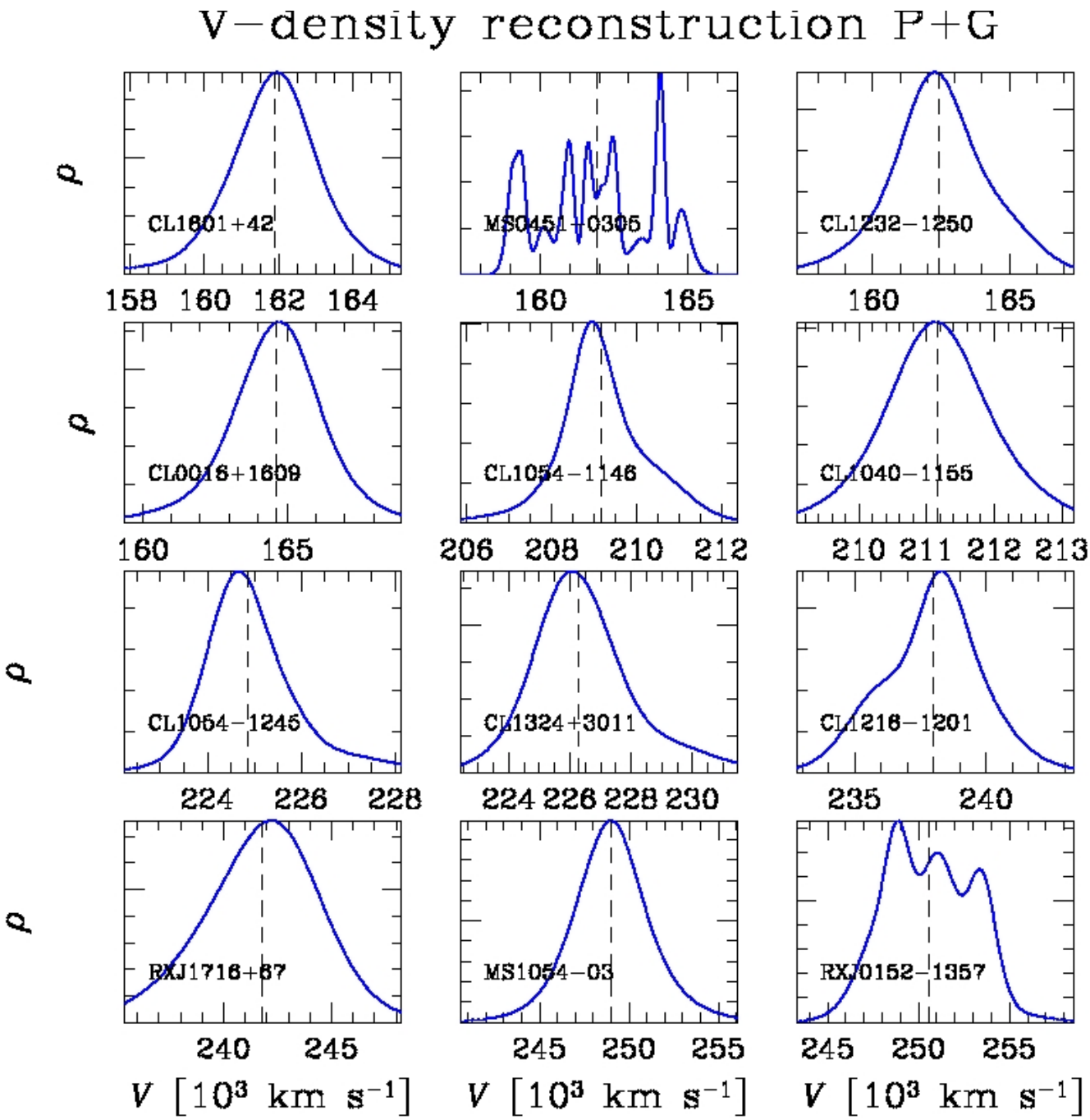
V−density reconstruction P+G
ρ
CL1601+42
158 160 162 164
MS0451+0305
160 165
CL1232−1250
160 165
CL0016+1609
160 165
CL1054−1146
206 208 210 212
CL1040−1155
210 211 212 213
CL1054−1245
224 226 228
CL1324+3011
224 226 228 230
CL1216−1201
235 240
RXJ1716+67
240 245
MS1054−03
245 250 255
RXJ0152−1357
245 250 255
V [10³ km s⁻¹]
V [10³ km s⁻¹]
V [10³ km s⁻¹]

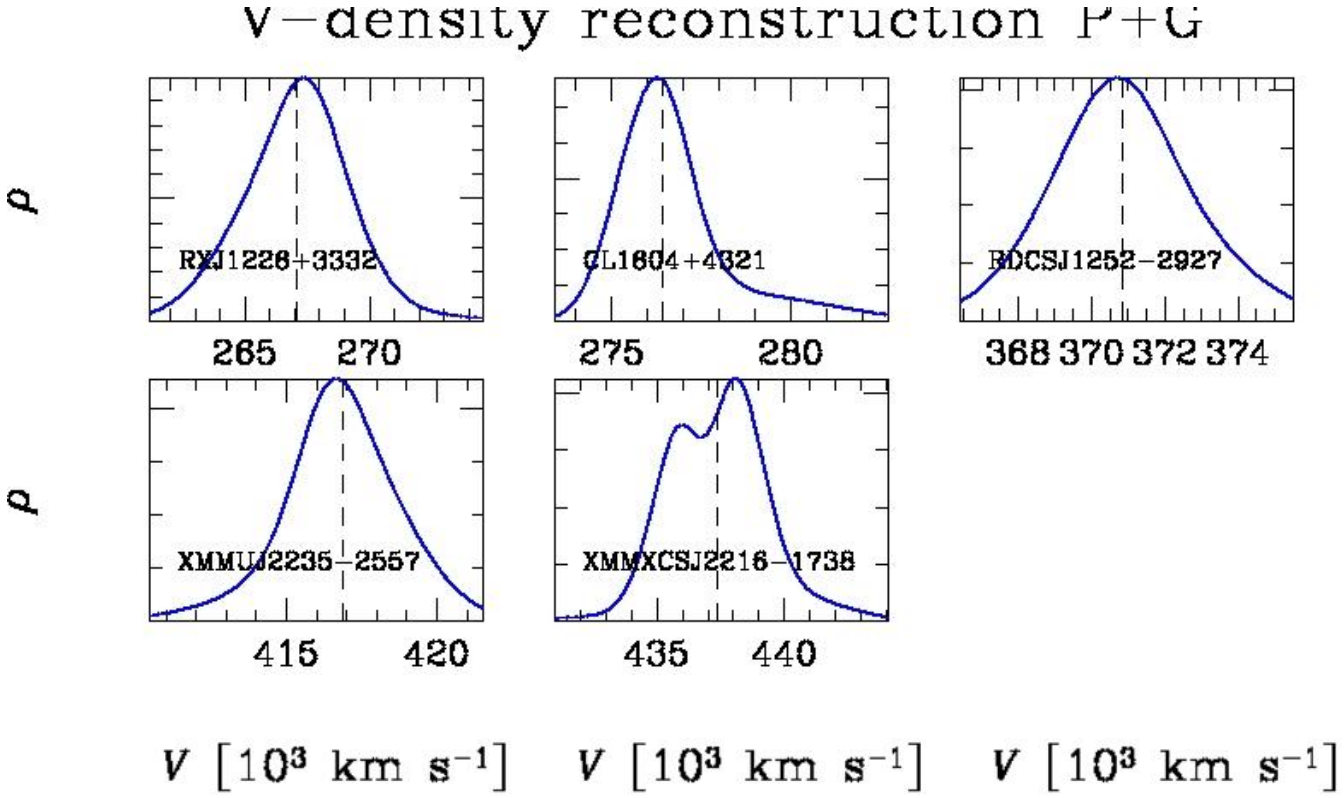

Figure 7.5: Velocity− density reconstruction for final members. I consider only clusters with at least 30 member galaxies, i.e. those with sufficient statistics. The horizontal axis is the radial velocity and the vertical axis represents the galaxy density. The dotted vertical line highlights the mean velocity.

In order to show the velocity distribution of cluster member galaxies as a function of cluster-centric distance (projected phase space), I plot in the following figures the difference between galaxy velocity and mean velocity as a function of distance from cluster center. Dividing the mean velocity by the speed of light I obtain the mean redshift of the cluster.
I draw all galaxies of the survey in the velocity range $\pm 10\,000$ kms^{-1} from the mean velocity and until a distance of 4 Mpc from the cluster center. The small black crosses indicate the final member galaxies belonging to the clusters according to the "peak+gap" method for the cluster member selection. The bigger circles represent galaxies of the survey belonging to the field.
The clusters CL 1138.2−1133a, CL 0054−27, XMMU J1230.3+1339, AX J2016+1127, RX J0848.9+4452, RX J0848.6+4453 have a number of member galaxies less than 15. So, the second step "shifting gapper", with a gap of 1000 kms^{-1} (in the cluster rest frame) and a bin of 0.6 Mpc, doesn't remove galaxies.

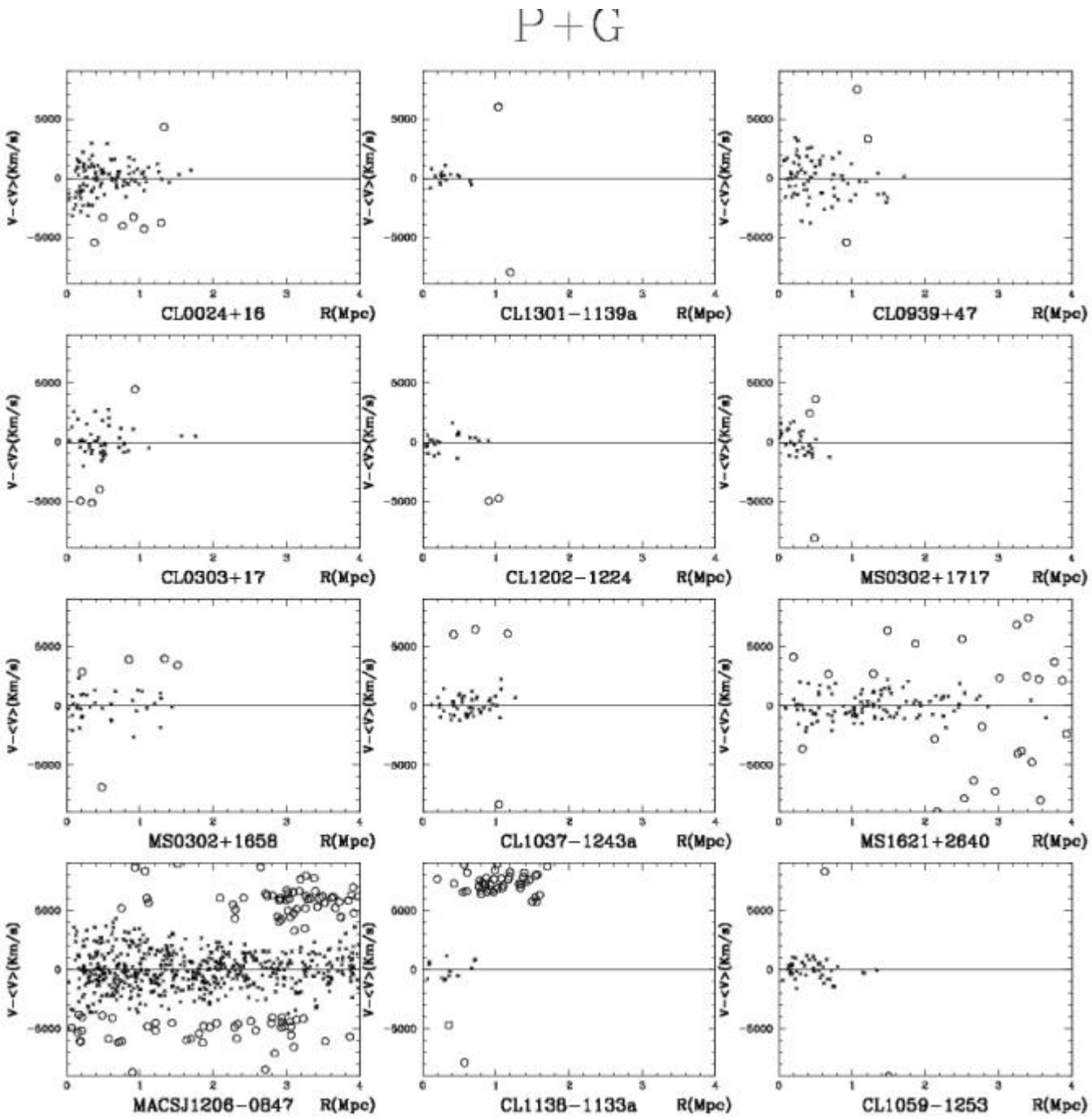
P+G
V−<V>(Km/s)
R(Mpc)
CL0024+16
CL1301−1139a
CL0939+47
CL0303+17
CL1202−1224
MS0302+1717
MS0302+1658
CL1037−1243a
MS1621+2640
MACSJ1206−0847
CL1138−1133a
CL1059−1253

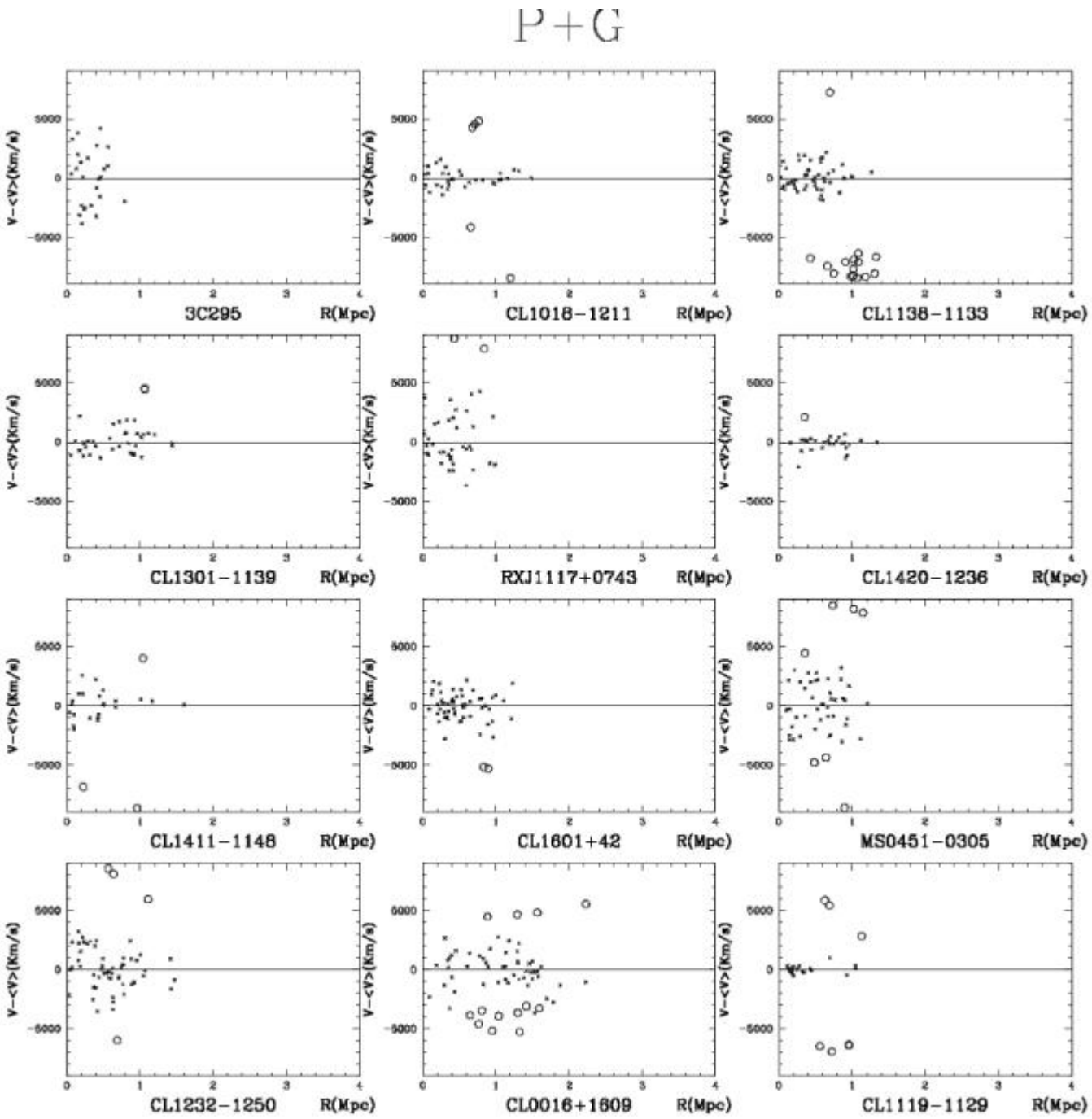
P+G
V−<V>(Km/s)
R(Mpc)
3C295
CL1018−1211
CL1138−1133
CL1301−1139
RXJ1117+0743
CL1420−1236
CL1411−1148
CL1601+42
MS0451−0305
CL1232−1250
CL0016+1609
CL1119−1129

P+G

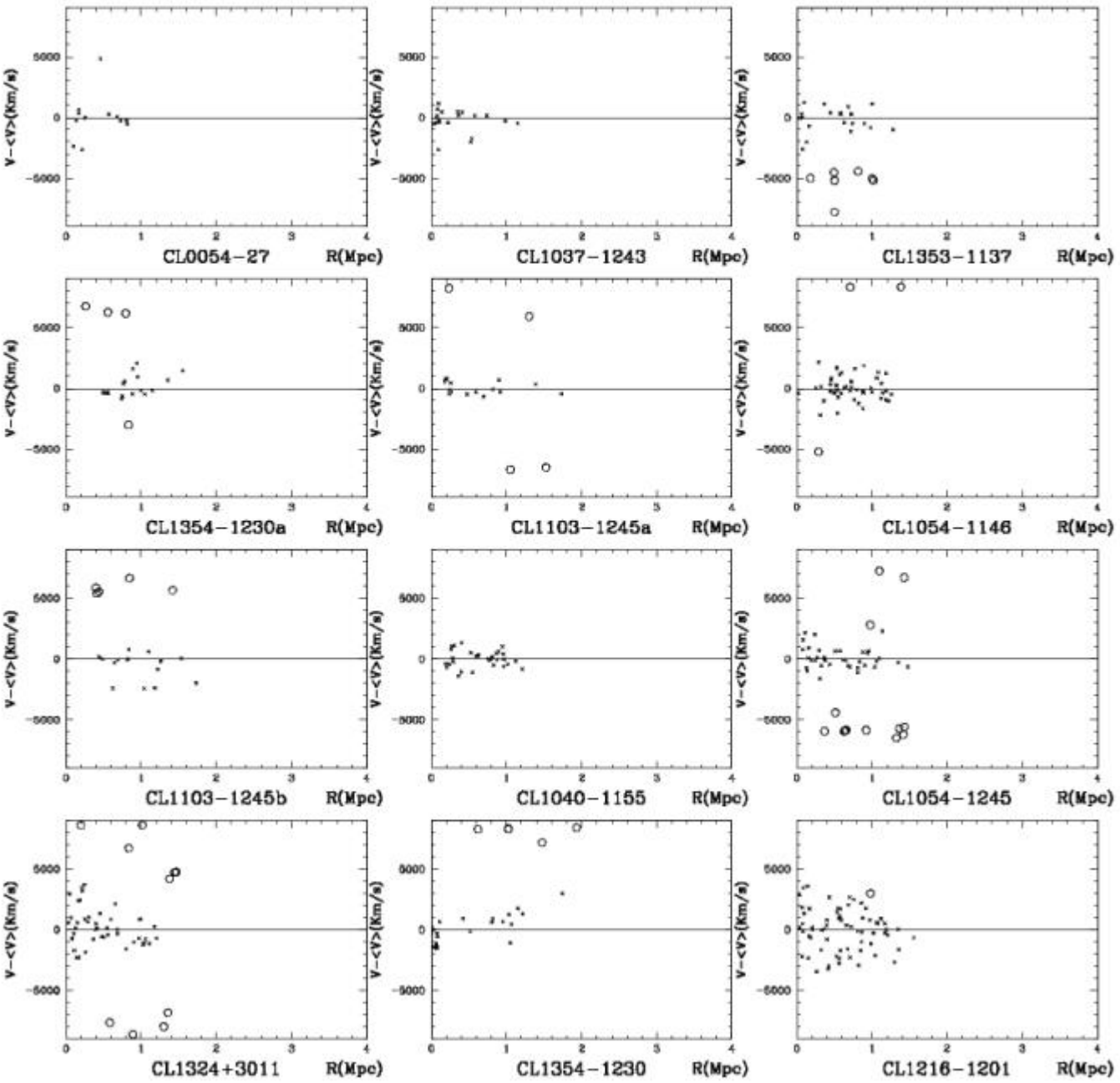
V−<V>(Km/s)
R(Mpc)
CL0054−27
CL1037−1243
CL1353−1137
CL1354−1230a
CL1103−1245a
CL1054−1146
CL1103−1245b
CL1040−1155
CL1054−1245
CL1324+3011
CL1354−1230
CL1216−1201

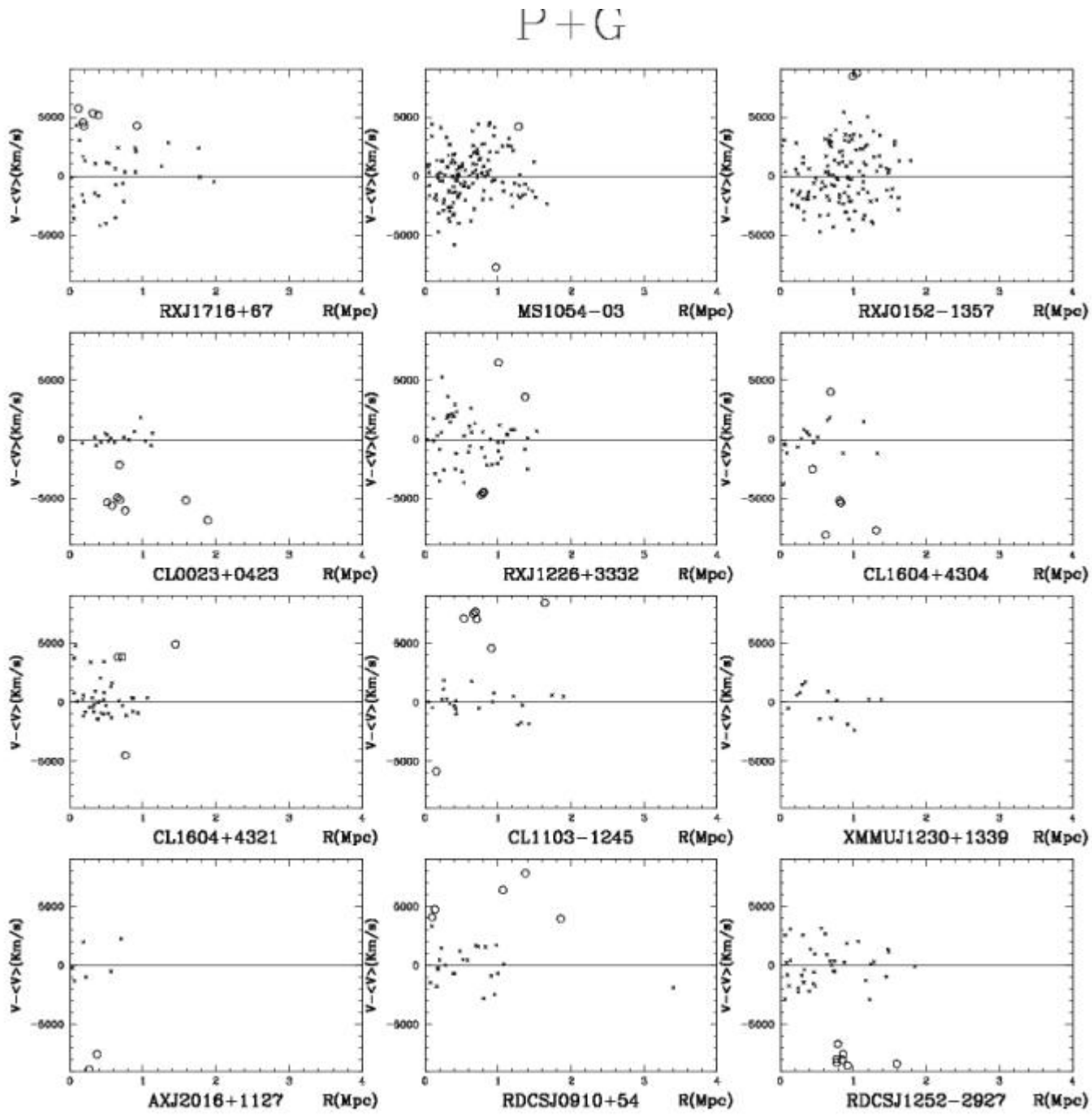
P+G
V−<V>(Km/s)
R(Mpc)
RXJ1716+67
MS1054−03
RXJ0152−1357
CL0023+0423
RXJ1226+3332
CL1604+4304
CL1604+4321
CL1103−1245
XMMUJ1230+1339
AXJ2016+1127
RDCSJ0910+54
RDCSJ1252−2927

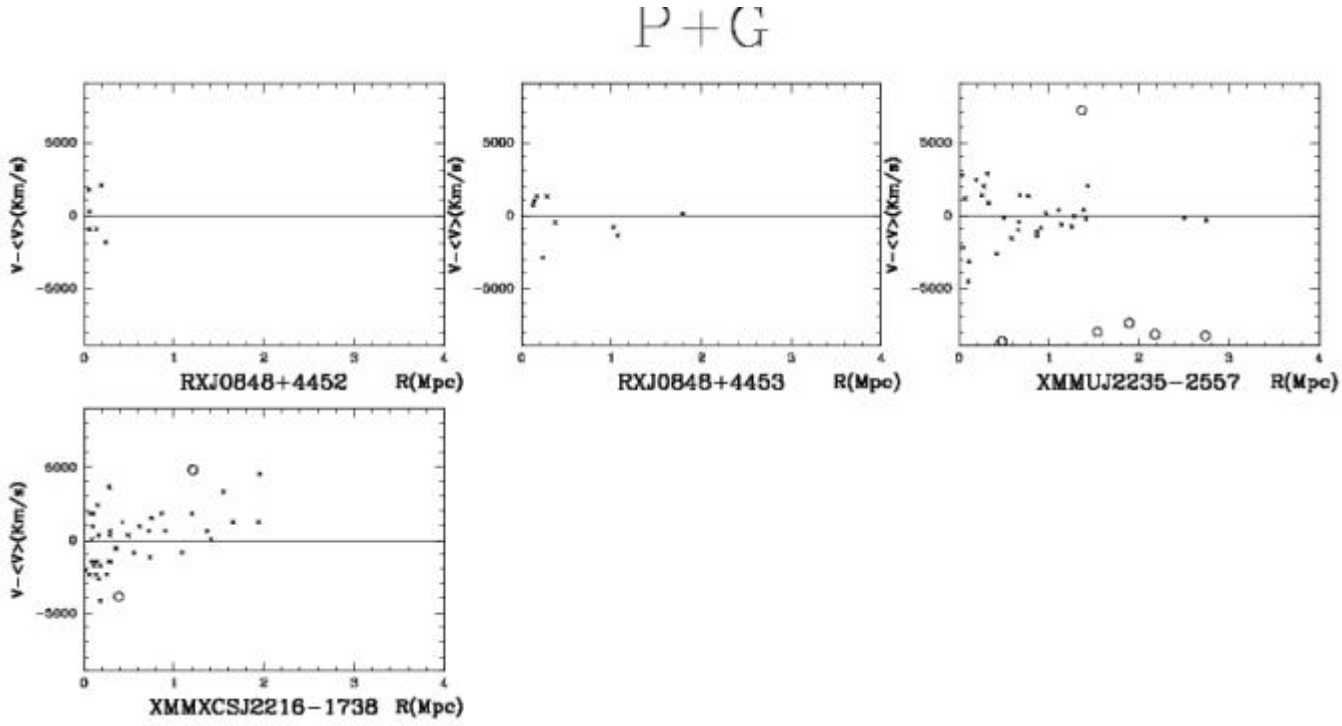

Figure 7.6: Projected phase space: velocity of galaxies vs projected clustercentric distance. The units of x and y axis are Mpc and kms^{-1}, respectively. The cluster name is written on the bottom of each plot. The small black crosses indicate the final cluster member galaxies. The bigger circles represent galaxies of the survey belonging to the field. The horizontal line marks the zero difference between galaxy velocity and mean velocity.

Chapter 8

Velocity dispersion estimates

8.1 Robust estimates

In astronomy, the velocity dispersion (σ_v) is the statistical dispersion of velocities with respect to the mean velocity for a group of celestial objects.
I estimate the "robust" velocity dispersion along the line of sight, σ_v, of the cluster members by using the biweight and the gapper estimators when the galaxy number is larger and smaller than 15, respectively (ROSTAT routines; see Beers et al., 1990), and applying the cosmological correction and the usual correction for velocity errors, $\sigma_v^2 = \sigma_{v,oss}^2 - \delta v^2$ where $\sigma_{v,oss}$ is the observed velocity dispersion and δv is the error on velocity, (Danese et al., 1980). In particular, for a few cases in which the velocity error is not available, I assume a velocity error of 300 kms^{-1}.
In order to do a complete dynamical analysis of each cluster, I use the computed velocity dispersions and mean redshifts to obtain R_{200}, which is the radius of a sphere enclosing a mean density that is 200 times the critical cosmic density at redshift z, and M_{200}, which is the mass of the sphere with radius R_{200}, according to the relation $\sigma_v - M_{200}$ of Munari et al. (2013).
Since $M_{200}\ \alpha\ \sigma_v^3$ and $R_{200}\ \alpha\ M_{200}^{1/3}$, I can calculate errors on R_{200} and M_{200} from the uncertainties on σ_v: $\delta R_{200} = \frac{\delta\sigma_v}{\sigma_v} \times R_{200}$ and $\delta M_{200} = 3\frac{\delta\sigma_v}{\sigma_v} \times M_{200}$. These are the errors listed in Table 8.1. The median values of percentage errors are about 13%, 13% and 40% on σ_v, R_{200} and M_{200}, respectively.
In Table 8.1 I report the value of σ_v computed considering all member galaxies. I list in column (1) the cluster name; in column (2) the number of cluster members after the "peak+gap" method selection, N_g; in column (3) the clustercentric distance of the most distant galaxy from the cluster center, R_{max}; in column (4) the robust line-of-sight velocity dispersion with bootstrap errors at the 68% confidence level (c.l.), σ_v; in column (5) R_{200} and in column (6) M_{200}.
Comparing R_{max} with R_{200} there are 18/52 clusters with $R_{max} \geq R_{200}$: this may be due to the fact that for distant clusters the instruments sampled larger regions with respect to that of nearby systems using the same telescopes. The median value of R_{max}/R_{200} is 0.78.

Table 8.1: Dynamical properties of galaxy clusters

Cluster name	N_g	R_{max}	σ_v	R_{200}	M_{200}
		(Mpc)	(km s^{-1})	(Mpc)	(10^{14} M$_\odot$)
CL 0024+16	100	1.02	888^{+57}_{-88}	$1.54^{+0.10}_{-0.15}$	$6.28^{+1.21}_{-1.87}$
CL 1301.7−1139a	17	0.40	388^{+74}_{-64}	$0.67^{+0.13}_{-0.11}$	$0.52^{+0.30}_{-0.26}$
CL 0939+47	70	1.02	1156^{+96}_{-86}	$1.99^{+0.16}_{-0.14}$	$13.77^{+3.43}_{-3.07}$
CL 0303+17	46	1.05	785^{+101}_{-120}	$1.34^{+0.17}_{-0.20}$	$4.28^{+1.65}_{-1.96}$
CL 1202.7−1224	21	0.53	499^{+112}_{-80}	$0.85^{+0.19}_{-0.14}$	$1.10^{+0.74}_{-0.53}$
MS 0302.5+1717	28	0.41	666^{+62}_{-72}	$1.13^{+0.10}_{-0.12}$	$2.60^{+0.73}_{-0.84}$
MS 0302.7+1658	34	0.85	779^{+119}_{-90}	$1.32^{+0.20}_{-0.16}$	$4.16^{+1.91}_{-1.44}$
CL 1037.9−1243a	47	0.75	554^{+67}_{-45}	$0.94^{+0.11}_{-0.07}$	$1.49^{+0.54}_{-0.36}$
MS 1621.5+2640	104	2.53	749^{+48}_{-41}	$1.27^{+0.08}_{-0.06}$	$3.70^{+0.71}_{-0.61}$
MACS J1206.2−0847	599	3.60	1105^{+29}_{-38}	$1.86^{+0.05}_{-0.05}$	$11.77^{+0.93}_{-1.21}$
CL 1138.2−1133a	14	0.42	510^{+74}_{-63}	$0.85^{+0.13}_{-0.10}$	$1.15^{+0.50}_{-0.43}$
CL 1059.2−1253	42	0.79	503^{+62}_{-46}	$0.84^{+0.10}_{-0.07}$	$1.10^{+0.41}_{-0.30}$
3C 295[b]	25	0.46	1677^{+192}_{-147}	$2.80^{+0.31}_{-0.25}$	$40.72^{+13.99}_{-10.71}$
CL 1018.8−1211	34	0.87	484^{+62}_{-58}	$0.80^{+0.10}_{-0.10}$	$0.97^{+0.37}_{-0.35}$
CL 1138.2−1133	49	0.74	710^{+76}_{-64}	$1.17^{+0.13}_{-0.10}$	$3.05^{+0.98}_{-0.82}$
CL 1301.7−1139	37	0.84	648^{+100}_{-66}	$1.07^{+0.16}_{-0.11}$	$2.32^{+1.07}_{-0.71}$
RX J1117.4+0743[b,d]	37	0.58	1426^{+219}_{-97}	$2.34^{+0.35}_{-0.16}$	$24.64^{+11.35}_{-5.03}$
CL 1420.3−1236	27	0.78	255^{+92}_{-78}	$0.41^{+0.15}_{-0.13}$	$0.14^{+0.15}_{-0.13}$
CL 1411.1−1148	25	0.93	764^{+134}_{-106}	$1.23^{+0.22}_{-0.17}$	$3.71^{+1.95}_{-1.54}$
CL 1601+42	55	0.71	715^{+68}_{-92}	$1.14^{+0.11}_{-0.15}$	$3.01^{+0.86}_{-1.16}$
MS 0451.6−0305	44	0.70	1242^{+72}_{-106}	$1.97^{+0.12}_{-0.18}$	$15.78^{+2.74}_{-4.04}$
CL 1232.5−1250	54	0.85	1089^{+108}_{-100}	$1.73^{+0.17}_{-0.15}$	$10.62^{+3.16}_{-2.92}$
MS 0015.9+1609	50	1.28	954^{+127}_{-97}	$1.51^{+0.20}_{-0.15}$	$7.11^{+2.84}_{-2.17}$
CL 1119.3−1129[d]	20	0.60	185^{+54}_{-34}	$0.29^{+0.08}_{-0.05}$	$0.05^{+0.04}_{-0.03}$
CL 0054−27[a,b]	12	0.47	1013^{+752}_{-169}	$1.59^{+1.18}_{-0.27}$	$8.44^{+18.80}_{-4.22}$
CL 1037.9−1243[b]	19	0.66	504^{+210}_{-149}	$0.78^{+0.33}_{-0.23}$	$1.03^{+1.29}_{-0.91}$
CL 1353.0−1137[b]	21	0.73	614^{+179}_{-77}	$0.95^{+0.27}_{-0.12}$	$1.85^{+1.62}_{-0.70}$
CL 1354.2−1230a[b]	17	0.88	557^{+178}_{-91}	$0.86^{+0.27}_{-0.14}$	$1.38^{+1.32}_{-0.68}$
CL 1103.7−1245a	15	0.98	330^{+51}_{-39}	$0.50^{+0.07}_{-0.06}$	$0.28^{+0.13}_{-0.10}$
CL 1054.4−1146	49	0.70	579^{+75}_{-70}	$0.84^{+0.11}_{-0.10}$	$1.45^{+0.56}_{-0.52}$
CL 1103.7−1245b[b]	15	0.97	330^{+446}_{-194}	$0.47^{+0.63}_{-0.28}$	$0.27^{+1.09}_{-0.48}$
CL 1040.7−1155	30	0.67	415^{+60}_{-42}	$0.60^{+0.08}_{-0.06}$	$0.53^{+0.23}_{-0.16}$
CL 1054.7−1245	36	0.82	499^{+121}_{-59}	$0.70^{+0.17}_{-0.08}$	$0.90^{+0.65}_{-0.32}$
CL 1324+3011	44	0.67	844^{+136}_{-105}	$1.18^{+0.19}_{-0.14}$	$4.36^{+2.11}_{-1.63}$
CL 1354.2−1230	23	0.96	689^{+130}_{-75}	$0.96^{+0.18}_{-0.10}$	$2.35^{+1.33}_{-0.77}$
CL 1216.8−1201	66	0.85	1002^{+87}_{-58}	$1.37^{+0.12}_{-0.08}$	$7.11^{+1.85}_{-1.23}$
RX J1716+67[b,c]	31	1.08	1250^{+122}_{-164}	$1.70^{+0.17}_{-0.22}$	$13.72^{+4.02}_{-5.40}$
MS 1054−03	143	0.91	1112^{+80}_{-58}	$1.49^{+0.10}_{-0.07}$	$9.53^{+2.06}_{-1.49}$
RX J0152.7−1357	125	0.97	1330^{+68}_{-64}	$1.77^{+0.09}_{-0.09}$	$16.22^{+2.49}_{-2.34}$
CL 0023+0423[c,d]	16	0.61	248^{+125}_{-42}	$0.33^{+0.16}_{-0.06}$	$0.10^{+0.15}_{-0.05}$
RX J1226.9+3332	50	0.83	1019^{+111}_{-98}	$1.31^{+0.14}_{-0.13}$	$7.07^{+2.31}_{-2.04}$
CL 1604+4304[b]	16	0.72	655^{+240}_{-102}	$0.84^{+0.31}_{-0.13}$	$1.86^{+2.04}_{-0.87}$
CL 1604+4321[b]	37	0.57	649^{+247}_{-102}	$0.82^{+0.31}_{-0.13}$	$1.79^{+2.04}_{-0.84}$
CL 1103.7−1245	22	1.01	500^{+90}_{-126}	$0.62^{+0.11}_{-0.15}$	$0.80^{+0.43}_{-0.60}$
XMMU J1230.3+1339[a,b]	13	0.74	683^{+163}_{-51}	$0.84^{+0.20}_{-0.06}$	$2.03^{+1.45}_{-0.45}$

AX J2016+1127[b,c]	6	0.37	790^{+160}_{-54}	$0.95^{+0.19}_{-0.07}$	$3.08^{+1.87}_{-0.63}$
RDCS J0910+54	23	1.78	729^{+91}_{-106}	$0.83^{+0.10}_{-0.12}$	$2.30^{+0.86}_{-1.00}$
RDCS J1252.9−2927	38	0.95	761^{+91}_{-58}	$0.80^{+0.10}_{-0.06}$	$2.42^{+0.87}_{-0.55}$
RX J0848.9+4452[a,b,c]	6	0.12	689^{+174}_{-110}	$0.72^{+0.18}_{-0.11}$	$1.77^{+1.34}_{-0.85}$
RX J0848.6+4453[a,b]	9	0.92	640^{+278}_{-101}	$0.66^{+0.28}_{-0.10}$	$1.40^{+1.82}_{-0.66}$
XMMU J2235.3−2557	30	1.40	732^{+136}_{-77}	$0.71^{+0.13}_{-0.08}$	$1.98^{+1.10}_{-0.62}$
XMMXCS J2215.9−1738	41	2.31	753^{+81}_{-92}	$0.71^{+0.09}_{-0.08}$	$2.07^{+0.67}_{-0.76}$

NOTE.

[a] Clusters having in their field less than 30 galaxies with available redshift (see Table 6.1).

[b] Clusters with an error on $\sigma_v \geq 150$ kms^{-1}.

[c] Clusters with a peak in the velocity distribution less significant than 99%.

[d] Clusters with secondary peaks grouped into an unique structure.

8.2 Comparison with previous studies

I compare the results for the number of cluster members and the velocity dispersions obtained in this thesis with previous studies conducted by different authors.
As regards the cluster RX J1117.4+0743, I consider it formed by two different structures S1 and S2, in order to compare my estimates with the results of Carrasco et al. (2007).
In Table 8.2 I list in columns (2) and (3) the number of cluster members estimated in this thesis, N_g, and that defined by previous work, N_{paper}, respectively; in columns (4) and (5) the value of velocity dispersion estimated in this thesis, σ_v, and that calculated by previous studies, $\sigma_{v,paper}$, respectively. I write bootstrap errors at 68% confidence level, except for the clusters RX J1117.4+0743 S1 and S2, MS 1054−03, XMMU J1230.3+1339, RDCS J0910+54, RX J0848.9+4452, RX J0848.6+4453 and XMMXCS J2215.9−1738, for which I consider jackknife errors in order to be in agreement with the methods used to estimate errors by the authors. Finally, in column (6) I give the reference number to the paper with which I compare my values (the references are listed in the notes of Table 5.1).

Table 8.2: Comparison of the results with previous studies

Cluster name	N_g	N_{paper}	σ_v (km s^{-1})	$\sigma_{v,paper}$ (km s^{-1})	Reference
CL 0024+16	100	95	888^{+57}_{-88}	911^{+81}_{-107}	2
CL 1301.7−1139a	17	17	388^{+74}_{-64}	391^{+63}_{-69}	3
CL 0939+47	70	65	1156^{+96}_{-86}	1067^{+89}_{-96}	2
CL 0303+17	46	43	785^{+101}_{-120}	876^{+144}_{-140}	2
CL 1202.7−1224	21	19	499^{+112}_{-80}	518^{+92}_{-104}	3
MS 0302.5+1717	28	26	666^{+62}_{-72}	664^{+67}_{-77}	2
MS 0302.7+1658	34	33	779^{+119}_{-90}	735^{+109}_{-80}	2
CL 1037.9−1243a	47	45	554^{+67}_{-45}	537^{+46}_{-48}	3
MS 1621.5+2640	104	106	749^{+48}_{-41}	735^{+53}_{-53}	2
MACS J1206.2−0847	599	592	1105^{+29}_{-38}	1087^{+53}_{-55}	7
CL 1138.2−1133a	14	14	510^{+74}_{-63}	542^{+63}_{-71}	3
CL 1059.2−1253	42	41	503^{+62}_{-46}	510^{+52}_{-56}	3
3C 295	25	21	1677^{+192}_{-147}	1642^{+224}_{-187}	2
CL 1018.8−1211	34	33	484^{+62}_{-58}	486^{+59}_{-63}	3

CL 1138.2−1133	49	49	710^{+76}_{-64}	732^{+72}_{-76}	3
CL 1301.7−1139	37	35	648^{+100}_{-66}	687^{+81}_{-86}	3
RX J1117.4+0743 S1	24	23	$661_{\pm 109}$	$592_{\pm 82}$	8
RX J1117.4+0743 S2*	13	9	$744_{\pm 114}$	$391_{\pm 85}$	8
CL 1420.3−1236	27	24	255^{+92}_{-78}	218^{+43}_{-50}	3
CL 1411.1−1148	25	22	764^{+134}_{-106}	710^{+125}_{-133}	3
CL 1601+42	55	53	715^{+68}_{-92}	646^{+84}_{-87}	2
MS 0451.6−0305	44	44	1242^{+72}_{-106}	1262^{+81}_{-103}	9
CL 1232.5−1250	54	54	1089^{+108}_{-100}	1080^{+119}_{-89}	10
MS 0015.9+1609	50	50	954^{+127}_{-97}	984^{+130}_{-95}	2
CL 1119.3−1129	20	17	185^{+54}_{-34}	166^{+27}_{-29}	3
CL 0054−27	12	9	1013^{+752}_{-169}	742^{+599}_{-147}	2
CL 1037.9−1243	19	16	504^{+210}_{-149}	319^{+53}_{-52}	3
CL 1353.0−1137	21	20	614^{+179}_{-77}	666^{+136}_{-139}	3
CL 1354.2−1230a	17	15	557^{+178}_{-91}	433^{+95}_{-104}	3
CL 1103.7−1245a	15	15	330^{+51}_{-39}	336^{+36}_{-40}	3
CL 1054.4−1146	49	49	579^{+75}_{-70}	589^{+78}_{-70}	10
CL 1103.7−1245b	15	11	330^{+446}_{-194}	252^{+65}_{-85}	3
CL 1040.7−1155	30	30	415^{+60}_{-42}	418^{+55}_{-46}	10
CL 1054.7−1245	36	36	499^{+121}_{-59}	504^{+113}_{-65}	10
CL 1324+3011	44	47	844^{+136}_{-105}	1016^{+126}_{-93}	13
CL 1354.2−1230	23	21	689^{+130}_{-75}	648^{+105}_{-110}	3
CL 1216.8−1201	66	67	1002^{+87}_{-58}	1018^{+73}_{-77}	10
RX J1716+67	31	32	1250^{+122}_{-164}	1445^{+288}_{-218}	2
MS 1054−03	143	153	$1112_{\pm 73}$	$1156_{\pm 82}$	15
RX J0152.7−1357	125	95	1330^{+68}_{-64}	1322^{+74}_{-68}	17
CL 0023+0423	16	14	248^{+125}_{-42}	283^{+53}_{-17}	2
RX J1226.9+3332	50	55	1019^{+111}_{-98}	1298^{+122}_{-137}	9
CL 1604+4304*	16	22	655^{+240}_{-102}	1226^{+245}_{-154}	12
CL 1604+4321	37	41	649^{+247}_{-102}	935^{+126}_{-91}	12
CL 1103.7−1245	22	22	500^{+90}_{-126}	522^{+111}_{-111}	20
XMMU J1230.3+1339	13	13	$683_{\pm 122}$	$658_{\pm 277}$	22
AX J2016+1127	6	9	790^{+160}_{-54}	771^{+430}_{-160}	23
RDCS J0910+54	23	20	$729_{\pm 108}$	$716_{\pm 141}$	24
RDCS J1252.9−2927	38	38	761^{+91}_{-58}	747^{+74}_{-84}	25
RX J0848.9+4452	6	10	$689_{\pm 547}$	$640_{\pm 90}$	26
RX J0848.6+4453	9	8	$640_{\pm 191}$	$700_{\pm 180}$	27
XMMU J2235.3−2557	30	34	732^{+136}_{-77}	802^{+77}_{-48}	28
XMMXCS J2215.9−1738	41	44	$753_{\pm 102}$	$890_{\pm 110}$	30

NOTE.− * Clusters with a difference $\geq 2\sigma$ between the obtained value in this thesis and the previous estimate of σ_v.

In order to show graphically the comparison between my velocity dispersions and the values estimated by different authors, I plot all the results in figure 8.1 and I draw the bisector line as reference. Most points are located along the bisector, and there isn't a systematic difference between the two sets of values.
I apply the statistical sign test in order to investigate a possible systematic effect: I find that my estimates are larger for 28/53 couples of values, indicating a non-significant difference between

the two sets of values (60.82% c.l.).

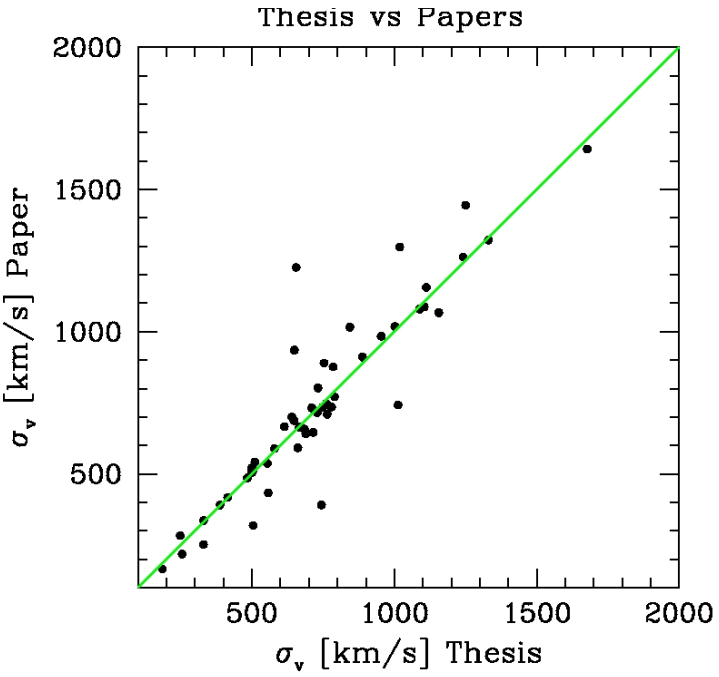

Figure 8.1: Comparison between velocity dispersions estimated in this thesis and those evaluated by previous studies.

Different authors use different cluster selection methods and not always the "peak+gap" procedure. I summarize the various techniques:

- (2) Girardi and Mezzetti (2001) used the "peak+gap" procedure but with a bin of 0.4 h^{-1}Mpc with $H_0 = 100\,h$ kms^{-1}Mpc.

- (3) Milvang-Jensen et al. (2008), (10) Halliday et al. (2004) and (20) Vulcani et al. (2012) employed the following method to estimate the number of members and velocity dispersions: a first estimate of cluster redshift, z_{cl}, is obtained from a visual inspection of the redshift histogram and galaxies with redshifts outside the region $z_{cl} \pm 0.015$, corresponding to the velocity range $v \pm 4500$ kms^{-1}, are removed. The median redshift of the remaining galaxies becomes a new estimate of z_{cl}, and is used to calculate the peculiar velocity of the galaxies in the cluster rest frame v_{rf}. The standard deviation of the v_{rf} values is used as the initial estimate of the cluster rest frame velocity dispersion. The iteration then starts, using the median to estimate z_{cl}, and the biweight scale estimator to estimate σ_v. In the event that the final number of cluster members is below 10, the process is repeated using the gapper scale estimator instead of the biweight scale estimator (Beers et al., 1990). The 68% asymmetric error bars on σ_v are determined by generating bootstrap samples from the final set of v_{rf} values for the cluster members. For each bootstrap sample, a value of σ_v is measured excluding the cluster members with doubtful redshifts and with redshift errors higher than the average uncertainty.

- (7) Biviano et al. (2013) adopted the "peak+gap" method, but with a small gap of 800 kms^{-1} since the sample of MACS J1206.2−0847 is very numerous.

- (8) Carrasco et al. (2007) used an iterative procedure by calculating the location and scale robust biweight estimators using the ROSTAT program and applying a 3σ clipping algorithm to the results. The 3σ clipping method implies to calculate the mean velocity of the selected galaxies, excluding galaxies with velocities beyond $\pm 3\sigma$ and repeat the procedure until the velocity dispersion converges to a constant value.

- (9) Jørgensen et al. (2013) considered the 3σ clipping procedure and estimated velocity dispersions using the biweight method described by Beers et al. (1990).

- (12) Postman et al. (2001) and (13) Lubin et al. (2002) followed the 3σ clipping method (Yahil and Vidal, 1977): they selected a broad redshift range of $\Delta z = \pm 0.06$ centered on the approximate redshift of the cluster. Then, they computed the biweight mean and standard deviation of the velocity distribution and identified the galaxy with the largest deviation from the mean. If this galaxy differs from the biweight median either by more than 3σ or by more than $3500\,\mathrm{kms}^{-1}$, it is excluded, and the computations are redone. The procedure continues until no further galaxies satisfy the above criteria. The clipping procedure is conservative and does not impose a Gaussian distribution on the final redshift distribution. The $3500\,\mathrm{kms}^{-1}$ limit is based on extensive data available for low z clusters.

- (15) Tran et al. (2007) using the biweight and jackknife methods (Beers et al., 1990) measured the line-of-sight velocity dispersion of 129 members with high quality measures of redshift, rejecting galaxies with doubtful redshifts.

- (17) Girardi et al. (2005) used the "peak+gap" procedure with my same parameters. However, they start from a different sample having redshift data for only 187 galaxies, instead I have available data for 219 galaxies.

- (22) Fassbender et al. (2010) performed a color cut of ± 0.2 mag around the median bright-end color of $R-z \sim 2.05$. They identified 13 cluster members, confirmed spectroscopically, and calculated the velocity dispersion using the robust estimator.

- (23) Soucail et al. (2001) employed an optical color selection to identify most of the brighter cluster galaxies. As for the fainter cluster members, they used the deep IR imaging because the foreground contamination is less important in the near-IR. Then, all the members was confirmed spectroscopically.

- (24) Tanaka et al. (2008) used galaxies in the redshift range $1.07 < z < 1.13$ to estimate the biweight estimator and jackknife errors.

- (25) Demarco et al. (2007) performed the "peak+gap" method to search for the significant peaks in the velocity distribution, and used the biweight estimator where errors are estimated through a bootstrap technique.

- (26) Rosati et al. (1999) and (27) Stanford et al. (1997) selected a redshift range and confirmed spectroscopically cluster members.

- (29) Rosati et al. (2009) identified galaxies lying within $\pm 2000\,\mathrm{kms}^{-1}$ of the median redshift $z = 1.390$ as cluster members.

- (30) Hilton et al. (2010) considered galaxies found within $\pm 3000\,\mathrm{kms}^{-1}$ of the recession velocity corresponding to the cluster redshift $z = 1.46$ as members, and used a biweight scale estimator to calculate velocity dispersions.

8 Velocity dispersion estimates

Only for 2 systems my estimates of velocity dispersion have a difference $\geq 2\sigma$ with respect to the reference values: RX J1117.4+0743 S2 for which the velocity dispersion of Carrasco et al. (2007) is lower than mine, and CL 1604+4304 for which the velocity dispersion estimated by Postman et al. (2001) is higher than my value.

8.3 The effect of the sampling radius

I apply to all galaxy data radial cuts of 3 Mpc and 1 Mpc from the cluster center estimated earlier. I repeat the "peak+gap" method to estimate the number of member galaxies within these distances and I calculate their velocity dispersions. I call these selections as P+G(3Mpc) and P+G(1Mpc).

In Table 8.3 I list the number of galaxies belonging to the peak and the number of cluster members for the cluster selection methods without a radial cut (N_p; N_g), with a cut of 3 Mpc ($N_{p,3\mathrm{Mpc}}$; $N_{g,3\mathrm{Mpc}}$) and with a cut of 1 Mpc ($N_{p,1\mathrm{Mpc}}$; $N_{g,1\mathrm{Mpc}}$). Only the 4 clusters MS 1621.5+2640, MACS J1206.2−0847, RDCS J0910+54 and XMMXCS J2215.9−1738 have member galaxies outside 4 Mpc.

Figures A.1 and A.2 in Appendix A show the projected phase space for galaxy members resulting after the application of the P+G(3Mpc) and P+G(1Mpc) methods. The corresponding plots for the P+G selection are given in figure 7.6 of Chapter 7.

Table 8.3: Cluster members according to the methods P+G, P+G(3Mpc) and P+G(1Mpc)

Cluster name	P+G		P+G(3Mpc)		P+G(1Mpc)	
	N_p	N_g	$N_{p,3\mathrm{Mpc}}$	$N_{g,3\mathrm{Mpc}}$	$N_{p,1\mathrm{Mpc}}$	$N_{g,1\mathrm{Mpc}}$
CL 0024+16	107	100	107	100	92	88
CL 1301.7−1139a	17	17	17	17	17	17
CL 0939+47	72	70	72	70	61	60
CL 0303+17	47	46	47	46	44	43
CL 1202.7−1224	21	21	21	21	21	21
MS 0302.5+1717	30	28	30	28	30	28
MS 0302.7+1658	38	34	38	34	29	28
CL 1037.9−1243a	47	47	47	47	42	42
MS 1621.5+2640[a]	119	104	110	102	27	27
MACS J1206.2−0847[a]	605	599	511	469	149	145
CL 1138.2−1133a	14	14	14	14	23	23
CL 1059.2−1253	42	42	42	42	39	39
3C 295	25	25	25	25	25	25
CL 1018.8−1211	34	34	34	34	28	27
CL 1138.2−1133	49	49	49	49	47	47
CL 1301.7−1139	39	37	39	37	29	29
RX J1117.4+0743	37	37	37	37	37	37
CL 1420.3−1236	28	27	28	27	26	25
CL 1411.1−1148	26	25	26	25	22	22
CL 1601+42	59	55	59	55	56	52
MS 0451.6−0305	53	44	53	44	49	42
CL 1232.5−1250	56	54	56	54	49	48
MS 0015.9+1609	63	50	63	50	25	20

CL 1119.3−1129	23	20	23	20	24	18
CL 0054−27	12	12	12	12	9	9
CL 1037.9−1243	19	19	19	19	18	18
CL 1353.0−1137	21	21	21	21	19	19
CL 1354.2−1230a	21	17	21	17	14	14
CL 1103.7−1245a	15	15	15	15	13	13
CL 1054.4−1146	49	49	49	49	38	38
CL 1103.7−1245b	15	15	15	15	11	11
CL 1040.7−1155	30	30	30	30	27	27
CL 1054.7−1245	37	36	37	36	31	30
CL 1324+3011	51	44	51	44	40	37
CL 1354.2−1230	23	23	23	23	17	17
CL 1216.8−1201	67	66	67	66	54	54
RX J1716+67	37	31	37	31	32	26
MS 1054−03	145	143	145	143	122	121
RX J0152.7−1357	135	125	135	125	89	84
CL 0023+0423	24	16	24	16	19	14
RX J1226.9+3332	59	50	59	50	41	37
CL 1604+4304	23	16	23	16	20	15
CL 1604+4321	42	37	42	37	39	36
CL 1103.7−1245	24	22	24	22	18	15
XMMU J1230.3+1339	13	13	13	13	10	10
AX J2016+1127	6	6	6	6	6	6
RDCS J0910+54[a]	28	23	27	22	23	22
RDCS J1252.9−2927	38	38	38	38	41	29
RX J0848.9+4452	6	6	6	6	6	6
RX J0848.6+4453	9	9	9	9	5	5
XMMU J2235.3−2557	31	30	31	30	23	21
XMMXCS J2215.9−1738[a]	44	41	43	40	33	33

NOTE.− [a] Clusters with member galaxies outside 3 Mpc.

I compare the velocity dispersions σ_v, $\sigma_{v,3\mathrm{Mpc}}$ and $\sigma_{v,1\mathrm{Mpc}}$ for the cluster members obtained with the methods P+G, P+G(3Mpc) and P+G(1Mpc), respectively, and I write their values with jackknife errors in Table 8.4.

Table 8.4: Robust velocity dispersions according to P+G, P+G(3Mpc) and P+G(1Mpc)

Cluster name	P+G	P+G(3Mpc)	P+G(1Mpc)
	$\sigma_v \pm \delta\sigma_v$ (km s^{-1})	$\sigma_{v,3\mathrm{Mpc}} \pm \delta\sigma_{v,3\mathrm{Mpc}}$ (km s^{-1})	$\sigma_{v,1\mathrm{Mpc}} \pm \delta\sigma_{v,1\mathrm{Mpc}}$ (km s^{-1})
CL 0024+16	888 ± 75	888 ± 75	943 ± 71
CL 1301.7−1139a	388 ± 75	388 ± 75	388 ± 75
CL 0939+47	1156 ± 97	1156 ± 97	1193 ± 108
CL 0303+17	785 ± 114	785 ± 114	816 ± 122
CL 1202.7−1224	499 ± 102	499 ± 102	499 ± 102
MS 0302.5+1717	666 ± 74	666 ± 74	666 ± 74

MS 0302.7+1658	779 ± 109	779 ± 109	876 ± 144
CL 1037.9−1243a	554 ± 57	554 ± 57	502 ± 43
MS 1621.5+2640[a]	749 ± 44	764 ± 49	538 ± 91
MACS J1206.2−0847	1105 ± 33	1177 ± 45	1010 ± 93
CL 1138.2−1133a	510 ± 57	510 ± 57	647 ± 128
CL 1059.2−1253	503 ± 61	503 ± 61	523 ± 59
3C 295	1677 ± 165	1677 ± 165	1677 ± 165
CL 1018.8−1211	484 ± 64	484 ± 64	532 ± 75
CL 1138.2−1133	710 ± 73	710 ± 73	727 ± 73
CL 1301.7−1139	648 ± 81	648 ± 81	702 ± 99
RX J1117.4+0743	1426 ± 162	1426 ± 162	1426 ± 162
CL 1420.3−1236	255 ± 110	255 ± 110	314 ± 112
CL 1411.1−1148	764 ± 121	764 ± 121	820 ± 130
CL 1601+42	715 ± 84	715 ± 84	705 ± 89
MS 0451.6−0305	1242 ± 92	1242 ± 92	1237 ± 94
CL 1232.5−1250	1089 ± 120	1089 ± 120	1137 ± 86
MS 0015.9+1609	954 ± 108	954 ± 108	975 ± 245
CL 1119.3−1129	185 ± 52	185 ± 52	176 ± 57
CL 0054−27[a]	1013 ± 496	1013 ± 496	180 ± 0
CL 1037.9−1243	504 ± 178	504 ± 178	496 ± 174
CL 1353.0−1137	614 ± 127	614 ± 127	586 ± 142
CL 1354.2−1230a	557 ± 219	557 ± 219	727 ± 231
CL 1103.7−1245a	330 ± 41	330 ± 41	326 ± 46
CL 1054.4−1146	579 ± 73	579 ± 73	598 ± 111
CL 1103.7−1245b[a]	330 ± 132	330 ± 132	1862 ± 345
CL 1040.7−1155	415 ± 58	415 ± 58	421 ± 61
CL 1054.7−1245	499 ± 81	499 ± 81	495 ± 81
CL 1324+3011	844 ± 124	844 ± 124	904 ± 144
CL 1354.2−1230	689 ± 100	689 ± 100	530 ± 56
CL 1216.8−1201	1002 ± 59	1002 ± 59	1078 ± 90
RX J1716+67	1250 ± 162	1250 ± 162	1313 ± 161
MS 1054−03	1112 ± 73	1112 ± 73	1124 ± 86
RX J0152.7−1357	1330 ± 68	1330 ± 68	1329 ± 80
CL 0023+0423	248 ± 102	248 ± 102	420 ± 166
RX J1226.9+3332	1019 ± 110	1019 ± 110	1159 ± 130
CL 1604+4304	655 ± 175	655 ± 175	722 ± 215
CL 1604+4321	649 ± 176	649 ± 176	665 ± 158
CL 1103.7−1245	500 ± 138	500 ± 138	402 ± 139
XMMU J1230.3+1339	683 ± 122	683 ± 122	681 ± 116
AX J2016+1127	790 ± 251	790 ± 251	790 ± 251
RDCS J0910+54	729 ± 108	715 ± 126	817 ± 148
RDCS J1252.9−2927	761 ± 67	761 ± 67	789 ± 85
RX J0848.9+4452	689 ± 547	689 ± 547	689 ± 547
RX J0848.6+4453	640 ± 191	640 ± 191	323 ± 277
XMMU J2235.3−2557	732 ± 108	732 ± 108	881 ± 136
XMMXCS J2215.9−1738	753 ± 102	765 ± 106	769 ± 105

NOTE.− [a] Clusters with velocity dispersions obtained with the selection P+G(1Mpc) that are $\geq 2\sigma$ different from the values obtained with the P+G selection method.

All clusters have σ_v and $\sigma_{v,3\mathrm{Mpc}}$ in agreement within 2σ from the error ranges. Only the clusters MS 1621.5+2640, CL 0054−27 and CL 1103.7−1245b have $\sigma_{v,1\mathrm{Mpc}}$ which differs significantly from σ_v or $\sigma_{v,3\mathrm{Mpc}}$ more than 2σ, because the number of members contained in 1 Mpc from cluster center is much lower than the total one.
In order to compare the velocity dispersions obtained with the P+G method with those related to P+G(3Mpc) and P+G(1Mpc) procedures, I combine all values in three different velocity dispersion distributions and apply two statistical tests:

1. **Kolmogorov−Smirnov test:** performing the two−sample KS test and considering that a probability of about 95% means that the two samples are different and don't belong to the same population, I obtain the following probabilities from the comparison of the velocity dispersion distributions $\sigma_{\mathrm{P+G}}$, $\sigma_{\mathrm{P+G(3Mpc)}}$ and $\sigma_{\mathrm{P+G(1Mpc)}}$:

   - $\sigma_{\mathrm{P+G}}$ vs $\sigma_{\mathrm{P+G(3Mpc)}}$, 0.00%: the two samples belong to the same distribution;
   - $\sigma_{\mathrm{P+G}}$ vs $\sigma_{\mathrm{P+G(1Mpc)}}$, 14.20%: there isn't a significant difference and the probability that the two groups are extracted from the same population is about 86%;
   - $\sigma_{\mathrm{P+G(3Mpc)}}$ vs $\sigma_{\mathrm{P+G(1Mpc)}}$, 13.41%: this is not a significant difference and the probability that the two samples belong to the same population is about 87%.

   The KS test therefore indicates that there isn't a significant difference between the velocity dispersion distributions obtained without a radial cut, with a radial cut of 3 Mpc and a cut of 1 Mpc.
   Figure 8.2 shows the comparison between the three cumulative distribution functions of velocity dispersions: they are very close to each others. The x axis represents the velocity dispersion σ measured in kms^{-1}, the y axis is the cumulative probability normalized to 1. The blue, red and green lines indicate the obtained velocity dispersion distributions using P+G, P+G(3Mpc) and P+G(1Mpc) methods, respectively.

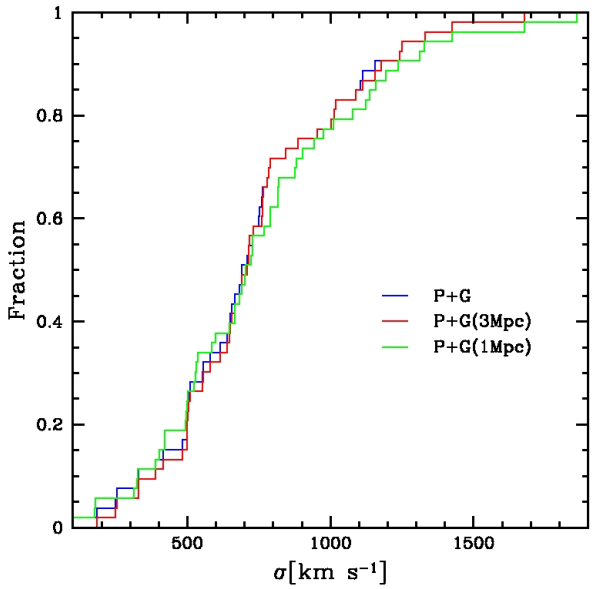

Figure 8.2: Cumulative distributions of velocity dispersion: $\sigma_{\mathrm{P+G}}$ vs $\sigma_{\mathrm{P+G(3Mpc)}}$ vs $\sigma_{\mathrm{P+G(1Mpc)}}$.

2. **Sign test:** applying the sign test I obtain that 36/52 estimates of velocity dispersion with P+G(1Mpc) are larger than those determined inside 3 Mpc. In this case, the two distributions are different at the 99.58% c.l. due to the radial profile of velocity dispersion, which generally decreases as the clustercentric distance increases (e.g., Girardi and Mezzetti, 2001).

3. **F−test:** I estimate for all the 52 clusters the probabilities P that the velocity dispersions derived by the methods P+G, P+G(3Mpc) and P+G(1Mpc) are diverse, according to the F-test. When the value of probability is larger than 0.95, velocity dispersions are different. Table 8.5 lists only the clusters with one probability value larger than 0.95, whereas the results for all the 52 clusters are given in Appendix E in Table E.1.

Table 8.5: Significant results of the F-test for the velocity dispersions obtained with P+G, P+G(3Mpc) and P+G(1Mpc)

Cluster name	$P(\sigma_v$ vs $\sigma_{v,3\mathrm{Mpc}})$	$P(\sigma_v$ vs $\sigma_{v,1\mathrm{Mpc}})$	$P(\sigma_{v,3\mathrm{Mpc}}$ vs $\sigma_{v,1\mathrm{Mpc}})$
MS 1621.5+2640	0.1588	0.9451	0.9573
MACS J1206.2−0847	0.8537	0.8120	0.9709
CL 0054−27	0.0000	1.0000	1.0000
CL 1103.7−1245b	0.0000	1.0000	1.0000

As regards σ_v vs $\sigma_{v,3\mathrm{Mpc}}$ no cluster has a probability value larger than 0.95. As σ_v vs $\sigma_{v,1\mathrm{Mpc}}$, clusters CL 0054−27 and CL 1103.7−1245b have different velocity dispersions. As $\sigma_{v,3\mathrm{Mpc}}$ vs $\sigma_{v,1\mathrm{Mpc}}$, MS 1621.5+2640, MACS J1206.2−0847, CL 0054−27 and CL 1103.7−1245b have $P > 0.95$.
Figures 8.3, 8.4, 8.5 display graphically the comparisons σ_v vs $\sigma_{v,3\mathrm{Mpc}}$, σ_v vs $\sigma_{v,1\mathrm{Mpc}}$ and $\sigma_{v,3\mathrm{Mpc}}$ vs $\sigma_{v,1\mathrm{Mpc}}$, respectively. I plot the velocity dispersion values with their jackknife errors and I draw the bisector line as reference.

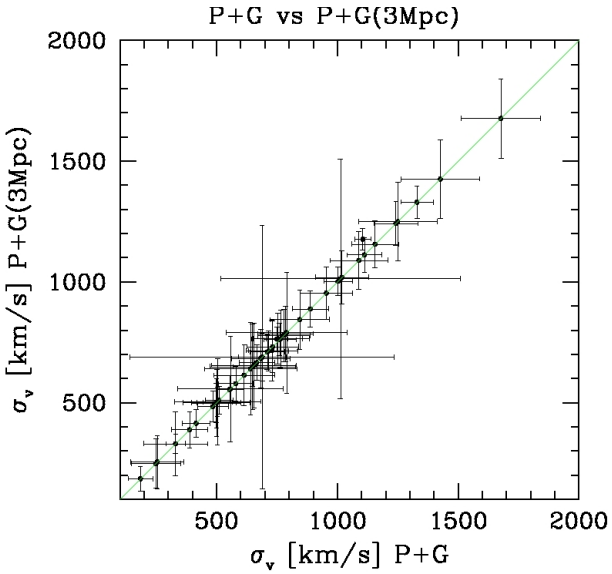

Figure 8.3: σ_v vs $\sigma_{v,3\mathrm{Mpc}}$: all points are located along the bisector line.

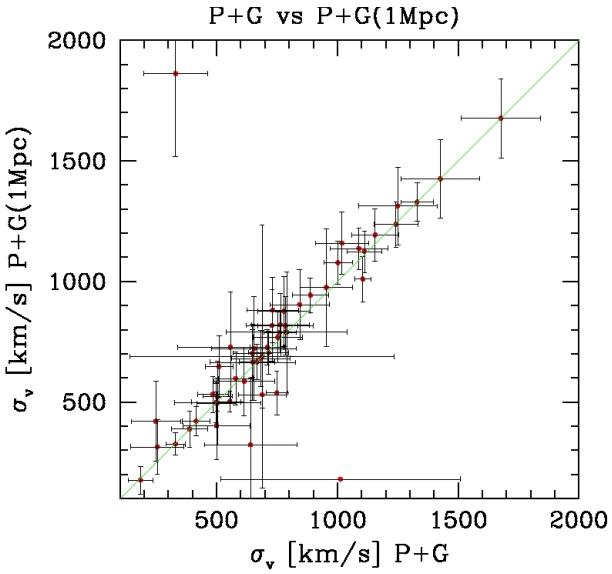

Figure 8.4: σ_v vs $\sigma_{v,1\mathrm{Mpc}}$: two points are located very distant from the bisector and correspond to the velocity dispersions of clusters CL 0054−27 and CL 1103.7−1245b. However, the members contained in 1 Mpc from the cluster center are much fewer than the total one and likely they do not trace the cluster population.

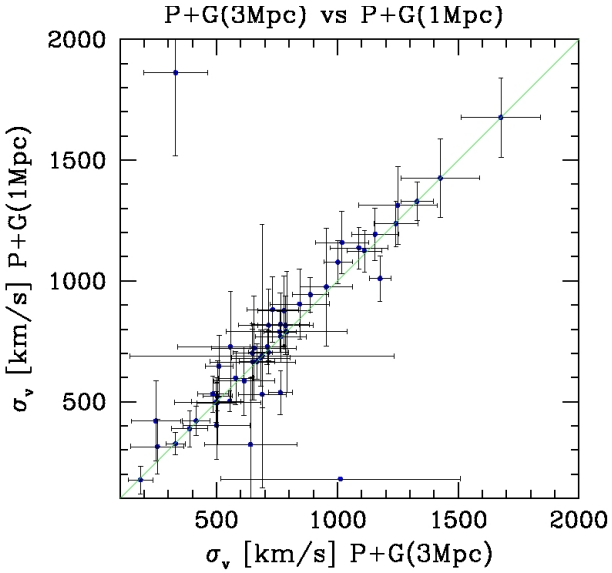

Figure 8.5: $\sigma_{v,3\mathrm{Mpc}}$ vs $\sigma_{v,1\mathrm{Mpc}}$: there are about the same results of the previous plot since the velocity dispersions obtained with P+G aren't different from the P+G(3Mpc) ones.

Chapter 9

Alternative member selection methods

I employ two different cluster member selection techniques and compare their results with the estimates obtained by the P+G method.
In both techniques, I apply to all galaxies a radial cut of 3 Mpc from the cluster center and a velocity cut of $\pm 10\,000$ kms^{-1} (in the appropriate cluster rest frame) from the cluster velocity center, computed via the biweight location estimator.

9.1 Procedure of Zabludoff et al. (1990)

This cluster selection method is based on the work of Zabludoff et al. (1990) and is called ZHG. Firstly, I exclude interloping galaxies which are more than 2000 kms^{-1} (in the cluster rest frame) from the nearest galaxy in the main velocity histogram. I calculate the mean velocity and velocity dispersion of the remaining galaxies. After sorting objects with velocities greater than the mean velocity in order of increasing peculiar velocity, I classify as nonmember any galaxy separated by more than the estimated velocity dispersion from the previous one. Galaxies with peculiar motions larger than a nonmember are also nonmembers. I employ the same procedure for galaxies with velocities below the mean velocity. Finally, I use the robust estimator to calculate the line-of-sight velocity dispersion.
In summary, the main steps of the ZHG method are:

- exclusion of galaxies separated in velocity by more than 2000 kms^{-1} from the nearest galaxy;
- exclusion of any galaxy separated by more than the estimated velocity dispersion from the previous one.

9.2 Procedure based on the "weighted gap"

This procedure (WG in short) has been introduced by Girardi et al. (1993). Firstly, I perform a rejection of interloping galaxies based on weighted gaps in the velocity distributions. A weighted gap in the space of the ordered velocities, $v_1 \leq v_2 \leq ... \leq v_n$, is defined as the difference between two contiguous velocities, weighted according to their positions in the ordered distribution: the closer to the center of the distribution is the gap, the higher is its weight (ROSTAT routines; see Beers et al., 1990). Specifically, I have rejected galaxies separated in velocity space from the main cluster body by a weighted gap > 2.5 and a weighted gap > 4. I named these

two procedures WG 2.5 and WG 4, respectively. I also define a third type of "weighted gap" method, called WG4+YV: after the WG 4 procedure, I apply a 3σ clipping technique (Yahil and Vidal, 1977). In the 3σ clipping method one must compute the mean velocity of the selected galaxies, exclude galaxies with velocities beyond $\pm 3\sigma$ and repeat the procedure until the velocity dispersion converges to a robust constant value.
In summary, the main steps of the WG method are:

- definition of a value for the weighted gap;
- rejection of galaxies separated in velocity space from the main cluster body by the weighted gap;
- (only for WG4+YV: application of the 3σ clipping technique.)

9.3 Comparison with alternative methods

I compare five different methods used to select cluster members and to estimate velocity dispersions: (1) "peak+gap" method, P+G (since the statistical difference with P+G(3Mpc) is 0.00%); (2) procedure of Zabludoff et al. (1990), ZHG; (3) method with a weigthed gap > 2.5, WG 2.5; (4) method with a weigthed gap > 4, WG 4; and (5) method with a weigthed gap > 4 followed by a 3σ clipping technique, WG4+YV.
In Tables 9.1, 9.2, 9.3 and 9.4 I list cluster redshifts, mean velocities with jackknife errors, number of members and velocity dispersions with jackknife errors, obtained by the considered procedures, respectively. In addition to the cluster samples used so far, I also take into account 5 subsamples: 4 subgroups of the most numerous cluster MACS J1206.2−0847 obtained with cuts in apparent magnitudes and 1 subgroup of cluster RX J0152.7−1357 studied by Jørgensen et al. (2005). I decide to consider 4 subgroups of MACS J1206.2−0847 since it is the most sampled cluster. In this way, it is possible to obtain 4 subsamples with a number of galaxies comparable with those in the other cluster samples. Instead, I consider the subgroup of RX J0152.7−1357 because only for it magnitudes for both member and nonmember galaxies are available in the literature.
I name the subgroups as:

- MACS J1206.2−0847(1B) obtained with an apparent magnitude cut of 21.90 in B band in order to have a survey of about 100 galaxies.
- MACS J1206.2−0847(2B) obtained with an apparent magnitude cut of 22.45 in B band in order to have a survey of about 300 galaxies.
- MACS J1206.2−0847(1R) obtained with an apparent magnitude cut of 20.00 in R band in order to have a survey of about 100 galaxies.
- MACS J1206.2−0847(2R) obtained with an apparent magnitude cut of 20.70 in R band in order to have a survey of about 300 galaxies.
- RX J0152.7−1357(1) characterized by a reduced survey of 41 galaxies and studied by Jørgensen et al. (2005).

Clusters and subgroups are written in ascending order of the mean redshift derived by the P+G method.

Table 9.1: Mean redshifts according to the methods P+G, ZHG, WG 2.5, WG 4 and WG4+YV

	P+G	ZHG	WG 2.5	WG 4	WG4+YV
Cluster name	$< z_g >$	$< z_{zhg} >$	$< z_{wg2.5} >$	$< z_{wg4} >$	$< z_{wg4+yv} >$
CL 0024+16	0.3937	0.3935	0.3950	0.3934	0.3934
CL 1301.7−1139a	0.3969	0.3969	0.3969	0.3969	0.3969
CL 0939+47	0.4060	0.4060	0.4061	0.4061	0.4061
CL 0303+17	0.4190	0.4190	0.4178	0.4190	0.4190
CL 1202.7−1224	0.4240	0.4239	0.4240	0.4240	0.4240
MS 0302.5+1717	0.4242	0.4244	0.4245	0.4245	0.4244
MS 0302.7+1658	0.4248	0.4254	0.4254	0.4255	0.4254
CL 1037.9−1243a	0.4255	0.4255	0.4254	0.4255	0.4254
MS 1621.5+2640	0.4267	0.4267	0.4268	0.4268	0.4268
MACS J1206.2−0847(1B)	0.4350	0.4348	0.4348	0.4349	0.4349
MACS J1206.2−0847(2R)	0.4384	0.4383	0.4401	0.4383	0.4383
MACS J1206.2−0847(2B)	0.4388	0.4380	0.4352	0.4382	0.4382
MACS J1206.2−0847(1R)	0.4393	0.4406	0.4406	0.4406	0.4406
MACS J1206.2−0847*	0.4399	0.4393	0.4759	0.4361	0.4361
CL 1138.2−1133a*	0.4546	0.4797	0.4797	0.4797	0.4797
CL 1059.2−1253	0.4564	0.4564	0.4564	0.4564	0.4564
3C 295	0.4593	0.4593	0.4593	0.4593	0.4593
CL 1018.8−1211	0.4736	0.4736	0.4736	0.4736	0.4736
CL 1138.2−1133	0.4797	0.4797	0.4797	0.4797	0.4797
CL 1301.7−1139	0.4832	0.4832	0.4824	0.4832	0.4832
RX J1117.4+0743	0.4857	0.4857	0.4857	0.4861	0.4857
CL 1420.3−1236	0.4961	0.4961	0.4960	0.4960	0.4961
CL 1411.1−1148	0.5196	0.5196	0.5197	0.5197	0.5196
CL 1601+42	0.5400	0.5400	0.5403	0.5400	0.5400
MS 0451.6−0305	0.5401	0.5398	0.5397	0.5403	0.5398
CL 1232.5−1250	0.5418	0.5418	0.5418	0.5418	0.5418
MS 0015.9+1609	0.5492	0.5479	0.5478	0.5481	0.5481
CL 1119.3−1129	0.5499	0.5500	0.5499	0.5500	0.5499
CL 0054−27	0.5608	0.5608	0.5608	0.5608	0.5608
CL 1037.9−1243	0.5784	0.5786	0.5786	0.5784	0.5786
CL 1353.0−1137	0.5878	0.5878	0.5881	0.5845	0.5877
CL 1354.2−1230a	0.5958	0.5958	0.5958	0.5958	0.5958
CL 1103.7−1245a	0.6261	0.6261	0.6261	0.6261	0.6261
CL 1054.4−1146	0.6976	0.6976	0.6976	0.6976	0.6976
CL 1103.7−1245b	0.7032	0.7031	0.7032	0.7032	0.7032
CL 1040.7−1155	0.7044	0.7044	0.7044	0.7044	0.7048
CL 1054.7−1245	0.7500	0.7501	0.7497	0.7501	0.7500
CL 1324+3011	0.7547	0.7547	0.7538	0.7556	0.7550
CL 1354.2−1230	0.7612	0.7609	0.7609	0.7612	0.7612
CL 1216.8−1201	0.7939	0.7940	0.7963	0.7940	0.7944
RX J1716+67	0.8065	0.8090	0.8090	0.8090	0.8090
MS 1054−03	0.8306	0.8307	0.8307	0.8307	0.8307
RX J0152.7−1357(1)	0.8357	0.8355	0.8344	0.8356	0.8355

RX J0152.7−1357	0.8359	0.8359	0.8325	0.8359	0.8359
CL 0023+0423	0.8453	0.8453	0.8453	0.8453	0.8452
RX J1226.9+3332	0.8910	0.8907	0.8904	0.8907	0.8906
CL 1604+4304	0.8978	0.8973	0.8958	0.8958	0.8967
CL 1604+4321	0.9219	0.9223	0.9216	0.9229	0.9226
CL 1103.7−1245	0.9578	0.9578	0.9578	0.9597	0.9586
XMMU J1230.3+1339	0.9737	0.9737	0.9737	0.9737	0.9737
AX J2016+1127	1.0044	1.0044	1.0044	0.9965	0.9965
RDCS J0910+54	1.0998	1.1014	1.0998	1.1014	1.1014
RDCS J1252.9−2927	1.2370	1.2370	1.2370	1.2370	1.2370
RX J0848.9+4452	1.2602	1.2602	1.2602	1.2602	1.2602
RX J0848.6+4453	1.2727	1.2735	1.2724	1.2724	1.2735
XMMU J2235.3−2557*	1.3905	1.3840	1.3907	1.3904	1.3905
XMMXCS J2215.9−1738*	1.4589	1.4592	1.4527	1.4626	1.4626

NOTE.− * Clusters for which at least two estimates of the mean redshift have a difference ≥ 0.01.

Table 9.2: Mean velocities according to P+G, ZHG, WG 2.5, WG 4 and WG4+YV

Cluster name	P+G $< cz_g >$ $\pm$ $\delta < cz_g >$ (km s^{-1})	ZHG $< cz_{zhg} >$ $\pm$ $\delta < cz_{zhg} >$ (km s^{-1})	WG 2.5 $< cz_{wg2.5} >$ $\pm$ $\delta < cz_{wg2.5} >$ (km s^{-1})	WG 4 $< cz_{wg4} >$ $\pm$ $\delta < cz_{wg4} >$ (km s^{-1})	WG4+YV $< cz_{wg4+yv} >$ $\pm$ $\delta < cz_{wg4+yv} >$ (km s^{-1})
CL 0024+16*	118026± 89	117979± 96	118430± 65	117931±103	117944± 99
CL 1301.7−1139a	118974± 98	118974± 98	118974± 98	118974± 97	118974± 98
CL 0939+47	121718±139	121718±139	121760±141	121734±154	121760±141
CL 0303+17*	125611±117	125611±117	125240± 70	125610±138	125604±137
CL 1202.7−1224	127116±113	127084±103	127116±113	127116±113	127116±113
MS 0302.5+1717	127161±129	127227±137	127268±150	127268±150	127227±137
MS 0302.7+1658	127362±136	127532±171	127532±171	127553±172	127532±171
CL 1037.9−1243a	127555± 82	127555± 82	127530± 77	127555± 82	127530± 77
MS 1621.5+2640	127935± 74	127935± 80	127956± 77	127943± 85	127943± 78
MACS J1206.2−0847(1B)	130412±206	130356±387	130356±387	130367±613	130367±613
MACS J1206.2−0847(2R)*	131425±151	131405±192	131935±156	131394±214	131405±192
MACS J1206.2−0847(2B)*	131553±126	131324±203	130481±166	131379±215	131379±206
MACS J1206.2−0847(1R)	131687±231	132094±353	132092±370	132092±370	132094±353
MACS J1206.2−0847*	131882± 45	131705± 70	142679± 7	130754± 32	130754± 32
CL 1138.2−1133a*	136276±143	143821±102	143821±102	143821±102	143821±102
CL 1059.2−1253	136811± 79	136811± 79	136811± 79	136811± 79	136811± 79
3C 295	137683±344	137683±344	137683±344	137683±344	137683±344
CL 1018.8−1211	141984± 84	141984± 84	141984± 84	141984± 84	141984± 84
CL 1138.2−1133	143821±102	143821±102	143821±102	143821±102	143821±102
CL 1301.7−1139	144849±108	144849±108	144625± 85	144849±108	144849±108
RX J1117.4+0743	145624±238	145624±238	145624±238	145719±302	145624±238
CL 1420.3−1236	148722± 50	148730± 48	148702± 53	148694± 55	148738± 44

CL 1411.1−1148	155769±157	155769±157	155804±172	155799±171	155769±157
CL 1601+42	161902± 97	161902± 97	161981± 87	161894±104	161902± 97
MS 0451.6−0305	161926±189	161842±208	161789±227	161975±286	161842±208
CL 1232.5−1250	162439±149	162439±149	162439±154	162440±166	162439±149
MS 0015.9+1609	164647±136	164258±179	164235±175	164314±195	164319±195
CL 1119.3−1129	164871± 43	164871± 43	164866± 37	164871± 43	164866± 37
CL 0054−27	168127±313	168117± 66	168117± 66	168127±313	168124±198
CL 1037.9−1243	173388±120	173446± 81	173446± 81	173388±120	173446± 81
CL 1353.0−1137*	176231±139	176231±139	176295±112	175240±344	176184±225
CL 1354.2−1230a	178615±141	178615±141	178615±141	178615±141	178615±141
CL 1103.7−1245a	187709± 90	187709± 90	187709± 90	187709± 90	187709± 90
CL 1054.4−1146	209148± 83	209148± 83	209148± 83	209148± 83	209148± 83
CL 1103.7−1245b	210815± 90	210793± 80	210815± 90	210815± 90	210815± 90
CL 1040.7−1155	211168± 77	211168± 77	211168± 77	211168± 77	211281± 89
CL 1054.7−1245	224853± 84	224870± 90	224748± 61	224870± 90	224853± 84
CL 1324+3011	226256±129	226256±129	225991± 93	226516±167	226350±147
CL 1354.2−1230	228196±148	228114±134	228114±134	228196±148	228196±148
CL 1216.8−1201*	238006±124	238046±124	238723± 97	238045±126	238156±133
RX J1716+67*	241792±229	242541±261	242541±261	242541±261	242541±261
MS 1054−03	249020± 93	249043± 94	249043± 95	249043± 95	249043± 94
RX J0152.7−1357(1)	250549±169	250482±193	250133±141	250494±193	250482±193
RX J0152.7−1357*	250598±119	250598±119	249581± 98	250587±125	250598±119
CL 0023+0423	253410± 65	253407± 66	253410± 65	253418± 75	253397± 59
RX J1226.9+3332	267108±145	267021±167	266927±155	267024±188	266982±161
CL 1604+4304	269155±171	269008±185	268563±382	268563±382	268831±341
CL 1604+4321	276393±108	276510±126	276285± 76	276674±140	276597±136
CL 1103.7−1245	287145±110	287145±110	287145±110	287716±416	287387±377
XMMU J1230.3+1339	291901±201	291901±201	291901±201	291901±201	291901±201
AX J2016+1127*	301109±384	301109±384	301109±384	298729±935	298729±935
RDCS J0910+54	329726±156	330188±224	329717±146	330197±224	330188±210
RDCS J1252.9−2927	370842±125	370842±125	370842±125	370842±125	370842±125
RX J0848.9+4452	377793±334	377793±334	377793±334	377793±334	377793±334
RX J0848.6+4453	381547±235	381772±191	381449±748	381460±977	381772±191
XMMU J2235.3−2557*	416851±136	414922±335	416917±128	416836±146	416851±136
XMMXCS J2215.9−1738*	437368±119	437454±137	435501± 22	438465±101	438465±101

NOTE.− * Clusters for which at least two estimates of the mean velocity have a difference $\geq 2\sigma$.

Table 9.3: Number of members according to P+G, ZHG, WG 2.5, WG 4 and WG4+YV

	P+G	ZHG	WG 2.5	WG 4	WG4+YV
Cluster name	N_g	N_{zhg}	$N_{wg2.5}$	N_{wg4}	N_{wg4+yv}
CL 0024+16[a]	100	104	77	107	105
CL 1301.7−1139a	17	17	17	18	17
CL 0939+47	70	70	71	74	71
CL 0303+17[a]	46	46	35	52	51
CL 1202.7−1224	21	20	21	21	21
MS 0302.5+1717	28	29	31	31	29
MS 0302.7+1658	34	38	38	40	38
CL 1037.9−1243a	47	47	46	47	46
MS 1621.5+2640	104	105	103	113	104
MACS J1206.2−0847(1B)	18	15	15	19	19
MACS J1206.2−0847(2R)[a]	75	76	64	81	76
MACS J1206.2−0847(2B)[a]	82	72	53	75	73
MACS J1206.2−0847(1R)	24	24	25	25	24
MACS J1206.2−0847[a]	599	547	15	203	203
CL 1138.2−1133a[a]	14	49	49	49	49
CL 1059.2−1253	42	42	42	42	42
3C 295	25	25	25	25	25
CL 1018.8−1211	34	34	34	34	34
CL 1138.2−1133	49	49	49	49	49
CL 1301.7−1139	37	37	32	37	37
RX J1117.4+0743	37	37	37	42	37
CL 1420.3−1236	27	26	28	29	24
CL 1411.1−1148	25	25	26	27	25
CL 1601+42	55	55	52	59	55
MS 0451.6−0305	44	47	49	54	47
CL 1232.5−1250	54	54	55	58	54
MS 0015.9+1609[a]	50	60	59	65	63
CL 1119.3−1129	20	20	19	20	19
CL 0054−27	12	9	9	12	11
CL 1037.9−1243	19	16	16	19	16
CL 1353.0−1137	21	21	19	31	25
CL 1354.2−1230a	17	17	17	17	17
CL 1103.7−1245a	15	15	15	15	15
CL 1054.4−1146	49	49	49	49	49
CL 1103.7−1245b	15	11	15	15	15
CL 1040.7−1155	30	30	30	30	25
CL 1054.7−1245	36	37	31	37	36
CL 1324+3011[a]	44	44	37	52	47
CL 1354.2−1230	23	22	22	23	23
CL 1216.8−1201[a]	66	67	50	68	61
RX J1716+67	31	37	37	37	37
MS 1054−03	143	144	145	145	144
RX J0152.7−1357(1)	27	29	25	31	29

RX J0152.7−1357[a]	125	125	93	129	125
CL 0023+0423	16	17	16	18	15
RX J1226.9+3332[a]	50	55	53	62	54
CL 1604+4304	16	17	24	24	23
CL 1604+4321	37	39	33	42	40
CL 1103.7−1245[a]	22	22	22	37	35
XMMU J1230.3+1339	13	13	13	13	13
AX J2016+1127	6	6	6	9	9
RDCS J0910+54	23	27	22	28	26
RDCS J1252.9−2927	38	38	38	38	38
RX J0848.9+4452	6	6	6	6	6
RX J0848.6+4453	9	8	11	12	8
XMMU J2235.3−2557[a]	30	44	29	31	30
XMMXCS J2215.9−1738[a]	41	43	12	25	25

NOTE.− [a] Clusters for which at least two estimates of the number of members are different for more than 10 galaxies.

Table 9.4: Robust velocity dispersions according to P+G, ZHG, WG 2.5, WG 4 and WG4+YV

	P+G	ZHG	WG 2.5	WG 4	WG4+YV
Cluster name	σ_v $\pm$ $\delta\sigma_v$ (km s^{-1})	σ_{zhg} $\pm$ $\delta\sigma_{zhg}$ (km s^{-1})	$\sigma_{wg2.5}$ $\pm$ $\delta\sigma_{wg2.5}$ (km s^{-1})	σ_{wg4} $\pm$ $\delta\sigma_{wg4}$ (km s^{-1})	σ_{wg4+yv} $\pm$ $\delta\sigma_{wg4+yv}$ (km s^{-1})
CL 0024+16[b]	888±75	978±105	564±65	1065±123	1010±108
CL 1301.7−1139a	388±75	388±75	388±75	397±76	388±75
CL 0939+47	1156±97	1156±97	1183±97	1319±136	1183±97
CL 0303+17[b]	785±114	785±114	406±70	986±229	969±219
CL 1202.7−1224	499±102	447±90	499±102	499±102	499±102
MS 0302.5+1717	666±74	722±87	819±136	819±136	722±87
MS 0302.7+1658	779±109	1041±183	1041±183	1072±187	1041±183
CL 1037.9−1243a	554±57	554±57	517±45	554±57	517±45
MS 1621.5+2640	749±44	819±61	781±50	906±81	798±54
MACS J1206.2−0847(1B)	840±146	1422±337	1422±337	2577±1120	2577±1120
MACS J1206.2−0847(2R)[b]	1305±143	1668±146	1241±104	1920±223	1668±146
MACS J1206.2−0847(2B)[b]	1139±117	1714±151	1198±151	1858±220	1754±146
MACS J1206.2−0847(1R)[b]	1103±173	1683±218	1804±329	1804±329	1683±218
MACS J1206.2−0847[b]	1105±33	1631±125	27±230	463±24	463±24
CL 1138.2−1133a[b]	510±57	710±73	710±73	710±73	710±73
CL 1059.2−1253	503±61	503±61	503±61	503±61	503±61
3C 295	1677±165	1677±165	1677±165	1677±165	1677±165
CL 1018.8−1211	484±64	484±64	484±64	484±64	484±64
CL 1138.2−1133	710±73	710±73	710±73	710±73	710±73
CL 1301.7−1139	648±81	648±81	472±38	648±81	648±81
RX J1117.4+0743	1426±162	1426±162	1426±162	1936±460	1426±162

CL 1420.3−1236	255±110	241±104	276±146	292±131	210±59
CL 1411.1−1148	764±121	764±121	856±159	871±167	764±121
CL 1601+42	715±84	715±84	623±72	794±120	715±84
MS 0451.6−0305[b]	1242±92	1414±127	1575±266	2082±313	1414±127
CL 1232.5−1250	1089±120	1089±120	1131±125	1255±198	1089±120
MS 0015.9+1609[b]	954±108	1380±163	1331±154	1564±202	1534±187
CL 1119.3−1129	185±52	185±52	157±34	185±52	157±34
CL 0054−27	1013±496	180±0	180±0	1013±496	607±271
CL 1037.9−1243	504±178	310±57	310±57	504±178	310±57
CL 1353.0−1137[b]	614±127	614±127	470±67	1880±552	1097±925
CL 1354.2−1230a	557±219	557±219	557±219	557±219	557±219
CL 1103.7−1245a	330±41	330±41	330±41	330±41	330±41
CL 1054.4−1146	579±73	579±73	579±73	579±73	579±73
CL 1103.7−1245b	330±132	246±92	330±132	330±132	330±132
CL 1040.7−1155	415±58	415±58	415±58	415±58	431±65
CL 1054.7−1245	499±81	539±92	331±31	539±92	499±81
CL 1324+3011[b]	844±124	844±124	559±61	1193±478	997±165
CL 1354.2−1230	689±100	608±70	608±70	689±100	689±100
CL 1216.8−1201[b]	1002±59	1013±68	681±69	1033±89	1034±73
RX J1716+67	1250±162	1566±153	1566±153	1566±153	1566±153
MS 1054−03	1112±73	1126±70	1145±76	1145±76	1126±70
RX J0152.7−1357(1)	859±169	1018±232	689±327	1056±238	1018±232
RX J0152.7−1357[b]	1330±68	1330±68	945±54	1425±96	1330±68
CL 0023+0423	248±102	260±131	248±102	306±204	218±36
RX J1226.9+3332	1019±110	1230±138	1121±109	1470±320	1172±121
CL 1604+4304	655±175	732±190	1826±1249	1826±1249	1589±919
CL 1604+4321	649±176	775±206	430±77	894±189	849±234
CL 1103.7−1245[b]	500±138	500±138	500±138	2495±917	2194±1755
XMMU J1230.3+1339	683±122	683±122	683±122	683±122	683±122
AX J2016+1127[b]	790±251	790±251	790±251	2540±689	2540±689
RDCS J0910+54	729±108	1137±250	663±114	1160±258	1047±213
RDCS J1252.9−2927	761±67	761±67	761±67	761±67	761±67
RX J0848.9+4452	689±547	689±547	689±547	689±547	689±547
RX J0848.6+4453	640±191	475±105	2290±1167	3163±1418	475±105
XMMU J2235.3−2557[b]	732±108	2199±319	677±87	799±158	732±108
XMMXCS J2215.9−1738[b]	753±102	889±123	71±0	490±246	490±246

NOTE.− [b] Clusters for which at least two estimates of the velocity dispersion differ for more than 2σ.

I consider the results of the P+G method as reference and I compare the estimates obtained using other procedures with these:

- **P+G vs ZHG**: there are 4 values of mean velocity with a significant difference. The number of members is not the same for 30/57 systems and clusters MACS J1206.2−0847, CL 1138.2−1133a and XMMU J2235.3−2557 differ for more than 10 galaxies. There are 6 objects for which estimates of velocity dispersion are different for more than 2σ.

9 Alternative member selection methods

- **P+G vs WG 2.5**: the estimates of mean velocity have a difference $\geq 2\sigma$ for 10 systems. The number of members differ for 37/57 objects and for 9 systems the difference is more than 10 members. Velocity dispersions disagree for 9 objects.

- **P+G vs WG 4**: the mean velocities aren't in agreement for 6 clusters. The number of members is not equal for 38/57 objects and for 7 systems the difference is more than 10 galaxies. In this case, there are 9 values of velocity dispersion with a relevant difference.

- **P+G vs WG4+YV**: for 5 clusters the values of mean velocity have a significant difference $\geq 2\sigma$. The number of members is not the same for 32/57 objects and 5 systems differ for more than 10 members. There are 9 systems with different velocity dispersions.

With regards to cluster CL 1138.2−1133a at $z = 0.45$, the methods ZHG, WG 2.5, WG 4 and WG4+YV aren't able to select its 14 member galaxies from the survey, but they capture the 49 galaxies of the cluster CL 1138.2−1133 at $z = 0.48$ and those belonging to the same sample. In Appendix A, figures A.3, A.4, A.5, A.6 and A.7 show the projected phase space for galaxy members resulting after the application of P+G, ZHG, WG 2.5, WG 4 and WG4+YV procedures for all 52 clusters and 5 subgroups.
In order to compare velocity dispersions and mean velocities obtained with the P+G method with those related to other procedures, I combine all values in five different velocity dispersion distributions and apply three statistical tests:

1. **t−test:** I use this test to compare mean velocities obtained by different methods. Table 9.5 lists the only relevant probabilities p that the mean velocities derived by methods ZHG, WG 2.5, WG 4 and WG4+YV are statistically diverse from those estimated by the P+G procedure. Only significant values of probability (i.e., $\geq$0.95) are written here. The symbol " − " represents a probability lower than 0.95. In Appendix F, Table F.1 reports all the probability values.

Table 9.5: Significant results of the t-test for the mean velocities obtained with P+G, ZHG, WG 2.5, WG 4 and WG4+YV

Cluster name	$\boldsymbol{p}\left(\begin{array}{c} < cz_g > \\ \text{vs} \\ < cz_{zhg} > \end{array}\right)$	$\boldsymbol{p}\left(\begin{array}{c} < cz_g > \\ \text{vs} \\ < cz_{wg2.5} > \end{array}\right)$	$\boldsymbol{p}\left(\begin{array}{c} < cz_g > \\ \text{vs} \\ < cz_{wg4} > \end{array}\right)$	$\boldsymbol{p}\left(\begin{array}{c} < cz_g > \\ \text{vs} \\ < cz_{wg4+yv} > \end{array}\right)$
CL 0024+16 *	−	0.9997	−	−
CL 1301.7−1139a	−	−	−	−
CL 0939+47	−	−	−	−
CL 0303+17*	−	0.9918	−	−
CL 1202.7−1224	−	−	−	−
MS 0302.5+1717	−	−	−	−
MS 0302.7+1658	−	−	−	−
CL 1037.9−1243a	−	−	−	−
MS 1621.5+2640	−	−	−	−
MACS J1206.2−0847(1B)	−	−	−	−
MACS J1206.2−0847(2R)*	−	0.9797	−	−
MACS J1206.2−0847(2B)*	−	1.0000	−	−
MACS J1206.2−0847(1R)	−	−	−	−
MACS J1206.2−0847*	0.9663	1.0000	1.0000	1.0000
CL 1138.2−1133a*	1.0000	1.0000	1.0000	1.0000
CL 1059.2−1253	−	−	−	−

3C 295	–	–	–	–
CL 1018.8−1211	–	–	–	–
CL 1138.2−1133	–	–	–	–
CL 1301.7−1139	–	–	–	–
RX J1117.4+0743	–	–	–	–
CL 1420.3−1236	–	–	–	–
CL 1411.1−1148	–	–	–	–
CL 1601+42	–	–	–	–
MS 0451.6−0305	–	–	–	–
CL 1232.5−1250	–	–	–	–
MS 0015.9+1609	–	–	–	–
CL 1119.3−1129	–	–	–	–
CL 0054−27	–	–	–	–
CL 1037.9−1243	–	–	–	–
CL 1353.0−1137*	–	–	0.9890	–
CL 1354.2−1230a	–	–	–	–
CL 1103.7−1245a	–	–	–	–
CL 1054.4−1146	–	–	–	–
CL 1103.7−1245b	–	–	–	–
CL 1040.7−1155	–	–	–	–
CL 1054.7−1245	–	–	–	–
CL 1324+3011	–	–	–	–
CL 1354.2−1230	–	–	–	–
CL 1216.8−1201*	–	1.0000	–	–
RX J1716+67*	0.9654	0.9654	0.9654	0.9654
MS 1054−03	–	–	–	–
RX J0152.7−1357(1)	–	–	–	–
RX J0152.7−1357*	–	1.0000	–	–
CL 0023+0423	–	–	–	–
RX J1226.9+3332	–	–	–	–
CL 1604+4304	–	–	–	–
CL 1604+4321	–	–	–	–
CL 1103.7−1245	–	–	–	–
XMMU J1230.3+1339	–	–	–	–
AX J2016+1127*	–	–	0.9607	0.9607
RDCS J0910+54	–	–	–	–
RDCS J1252.9−2927	–	–	–	–
RX J0848.9+4452	–	–	–	–
RX J0848.6+4453	–	–	–	–
XMMU J2235.3−2557*	1.0000	–	–	–
XMMXCS J2215.9−1738*	–	1.0000	1.0000	1.0000

NOTE.− * Clusters with one probability value larger than 0.95.

There are 4, 10, 6 and 5 systems with a probability larger than 0.95 for $< cz_g >$ vs $< cz_{zhg} >$, $< cz_g >$ vs $< cz_{wg2.5} >$, $< cz_g >$ vs $< cz_{wg4} >$ and $< cz_g >$ vs $< cz_{wg4+yv} >$, respectively.

9 Alternative member selection methods

In the following two statistical tests I compare velocity dispersion distributions and values only for those clusters with no significant difference in their redshift estimates between those obtained with the P+G procedure and those estimated with the other membership selection methods. Thus, for the comparison P+G vs ZHG, P+G vs WG 2.5, P+G vs WG 4 and P+G vs WG4+YV, I analyze 53, 47, 51 and 52 systems, respectively.

2. **Kolmogorov−Smirnov test:** applying the two−sample KS test and considering that a probability of about 95% means that the two samples are different, I obtain the following probabilities that the velocity dispersion distribution obtained with the P+G procedure is different from those of the other methods:

   - $\sigma_{\rm P+G}$ vs $\sigma_{\rm ZHG}$ for 53 systems, 13.41%: the two samples have a probability of about 87% to belong to the same population;
   - $\sigma_{\rm P+G}$ vs $\sigma_{\rm WG\ 2.5}$ for 47 systems, 53.38%: there isn't a significant difference;
   - $\sigma_{\rm P+G}$ vs $\sigma_{\rm WG\ 4}$ for 51 systems, 89.89%: the two distributions have a probability of about 90% to be different;
   - $\sigma_{\rm P+G}$ vs $\sigma_{\rm WG4+YV}$ for 52 systems, 73.83%: the probability that the two samples are of the same population is only 26%.

   In all cases there isn't a significant difference $> 95\%$. The comparison $\sigma_{\rm P+G}$ vs $\sigma_{\rm WG\ 4}$ has the highest value of probability of difference, then there are $\sigma_{\rm P+G}$ vs $\sigma_{\rm WG4+YV}$ and $\sigma_{\rm P+G}$ vs $\sigma_{\rm WG\ 2.5}$, and, finally, there is $\sigma_{\rm P+G}$ vs $\sigma_{\rm ZHG}$. Thus, the cluster member selection method that is in better agreement with P+G is the ZHG procedure, according to the KS test.
   Figures 9.1, 9.2, 9.3, 9.4 illustrate the cumulative distribution functions of velocity dispersions for 53, 47, 51 and 52 systems, respectively. The black, red, magenta, blue and green lines indicate the obtained velocity dispersion distributions using P+G, ZHG, WG 2.5, WG 4 and WG4+YV methods, respectively.
   In all figures the difference between the two considered distributions is stronger for high values of velocity dispersion. This fact is particularly true for the comparison between the P+G and the WG 4 methods. Applying the 3-σ clipping technique, this difference is reduced, as shown by the velocity dispersion distribution obtained with the WG4+YV procedure.
   With regards to the low values of velocity dispersion, only the WG 2.5 distribution is in disagreement with the P+G one. There are no relevant differences for the WG 4 and WG4+YV methods with the P+G estimates.

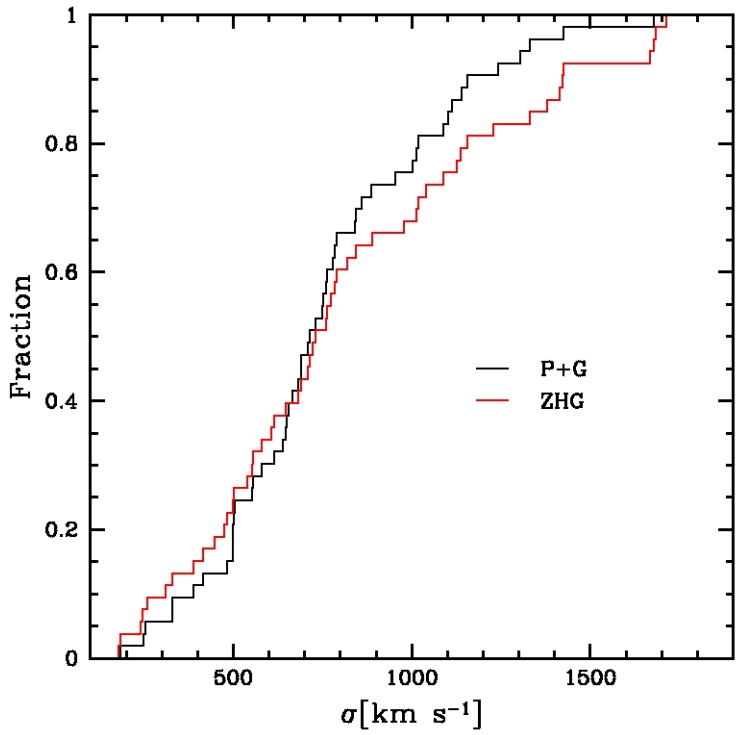

Figure 9.1: Cumulative distributions of velocity dispersion for 53 systems: $\sigma_{\mathrm{P+G}}$ vs σ_{ZHG}.

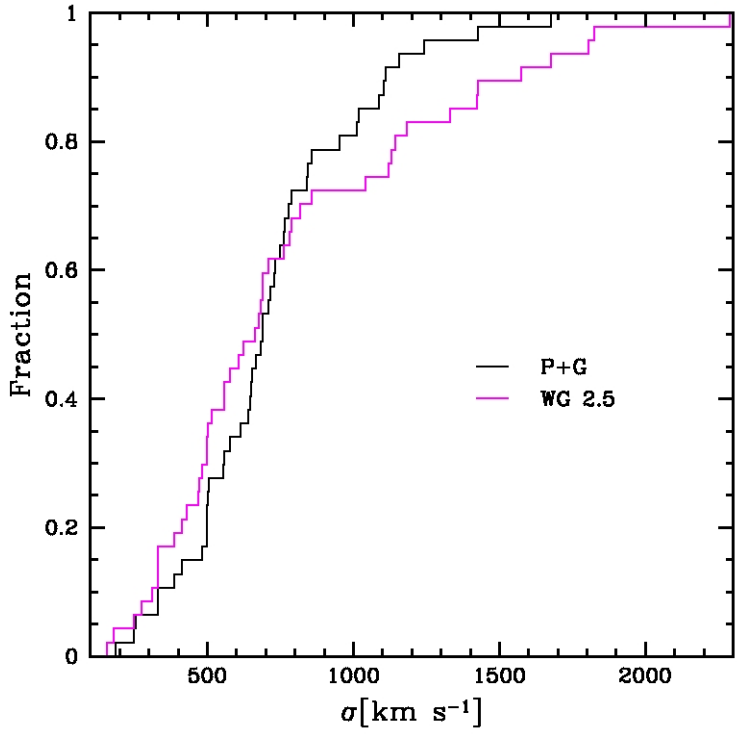

Figure 9.2: Cumulative distributions of velocity dispersion for 47 systems: $\sigma_{\mathrm{P+G}}$ vs $\sigma_{\mathrm{WG\ 2.5}}$.

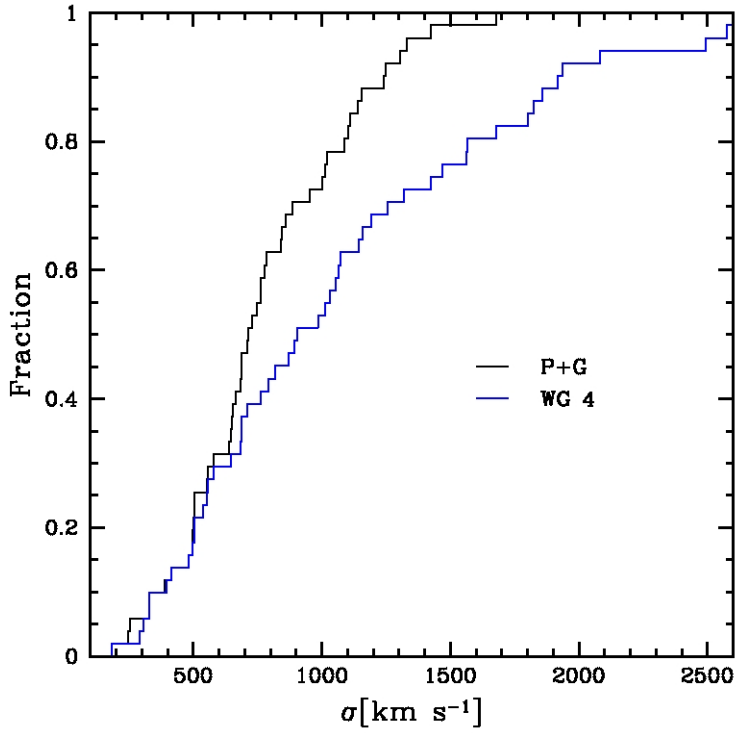

Figure 9.3: Cumulative distributions of velocity dispersion for 51 systems: $\sigma_{\mathrm{P+G}}$ vs $\sigma_{\mathrm{WG\ 4}}$.

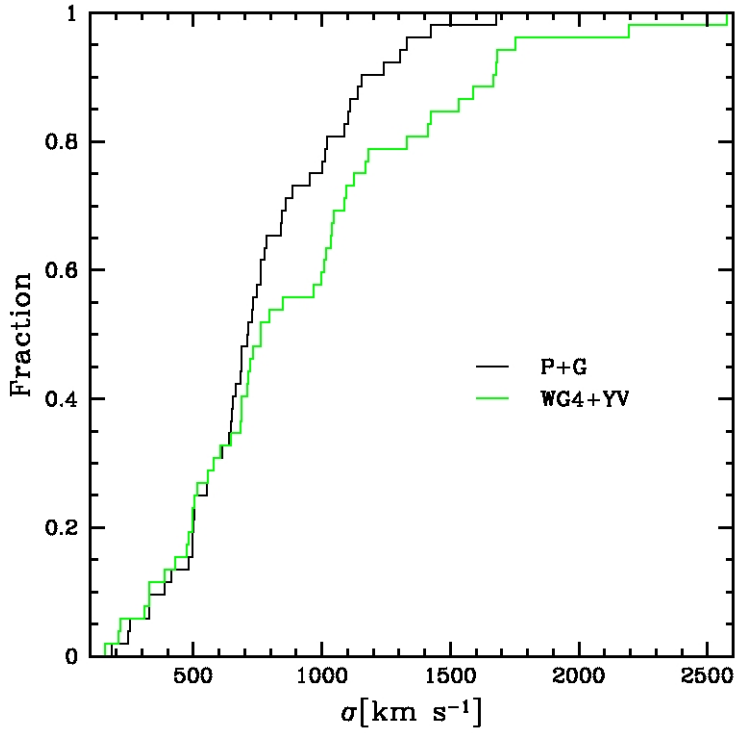

Figure 9.4: Cumulative distributions of velocity dispersion for 52 systems: $\sigma_{\mathrm{P+G}}$ vs $\sigma_{\mathrm{WG4+YV}}$.

3. **F−test:** I list in Table E.2 in Appendix E the probabilities P that velocity dispersions derived by methods P+G, ZHG, WG 2.5, WG 4 and WG4+YV are not statistically the same. When the value of probability is larger than 0.95, velocity dispersions are different. The relevant probabilities are reported in Table 9.6: the points "....." represent clusters which are excluded from the comparison because of redshifts in disagreement with the P+G ones, the symbol "−" indicates values lower than 0.95.
The significant differences in σ_v could be due to the fact that the procedures ZHG, WG 4 and WG4+YV are inclined to select more cluster members than the P+G method. Instead, the WG 2.5 procedure tends to identify only few members of the cluster and to divide the system. This fact means that for many clusters choosing a gap of 2.5 leads to an artificial fragmentation of the system.

Table 9.6: Significant results of the F-test for the velocity dispersions obtained with P+G, ZHG, WG 2.5, WG 4 and WG4+YV

Cluster name	$P(\sigma_v$ vs $\sigma_{zhg})$	$P(\sigma_v$ vs $\sigma_{wg2.5})$	$P(\sigma_v$ vs $\sigma_{wg4})$	$P(\sigma_v$ vs $\sigma_{wg4+yv})$
CL 0024+16	−	.....	−	−
CL 1301.7−1139a	−	−	−	−
CL 0939+47	−	−	−	−
CL 0303+17	−	.....	−	−
CL 1202.7−1224	−	−	−	−
MS 0302.5+1717	−	−	−	−
MS 0302.7+1658	−	−	−	−
CL 1037.9−1243a	−	−	−	−
MS 1621.5+2640	−	−	−	−
MACS J1206.2−0847(1B)*	0.9582	0.9582	1.0000	1.0000
MACS J1206.2−0847(2R)*	0.9642	.....	0.9991	0.9642
MACS J1206.2−0847(2B)*	0.9996	.....	1.0000	0.9998
MACS J1206.2−0847(1R)*	0.9519	0.9788	0.9788	0.9519
MACS J1206.2−0847	.....	.....	.....	.....
CL 1138.2−1133a	.....	.....	.....	.....
CL 1059.2−1253	−	−	−	−
3C 295	−	−	−	−
CL 1018.8−1211	−	−	−	−
CL 1138.2−1133	−	−	−	−
CL 1301.7−1139	−	−	−	−
RX J1117.4+0743	−	−	−	−
CL 1420.3−1236	−	−	−	−
CL 1411.1−1148	−	−	−	−
CL 1601+42	−	−	−	−
MS 0451.6−0305*	−	−	0.9993	−
CL 1232.5−1250	−	−	−	−
MS 0015.9+1609*	0.9913	0.9820	0.9996	0.9992
CL 1119.3−1129	−	−	−	−
CL 0054−27*	1.0000	1.0000	−	−
CL 1037.9−1243	−	−	−	−
CL 1353.0−1137*	−	−	.....	0.9894
CL 1354.2−1230a	−	−	−	−

CL 1103.7−1245a	–	–	–	–
CL 1054.4−1146	–	–	–	–
CL 1103.7−1245b	–	–	–	–
CL 1040.7−1155	–	–	–	–
CL 1054.7−1245*	–	0.9757	–	–
CL 1324+3011*	–	0.9872	0.9785	–
CL 1354.2−1230	–	–	–	–
CL 1216.8−1201	–	.....	–	–
RX J1716+67	.....	.....	.....	.....
MS 1054−03	–	–	–	–
RX J0152.7−1357(1)	–	–	–	–
RX J0152.7−1357	–	.....	–	–
CL 0023+0423	–	–	–	–
RX J1226.9+3332*	–	–	0.9911	–
CL 1604+4304*	–	0.9998	0.9998	0.9991
CL 1604+4321*	–	0.9798	–	–
CL 1103.7−1245*	–	–	1.0000	1.0000
XMMU J1230.3+1339	–	–	–	–
AX J2016+1127	–	–	.....	.....
RDCS J0910+54*	0.9623	–	0.9707	–
RDCS J1252.9−2927	–	–	–	–
RX J0848.9+4452	–	–	–	–
RX J0848.6+4453*	–	0.9986	0.9999	–
XMMU J2235.3−2557	.....	–	–	–
XMMXCS J2215.9−1738	–	.....	.....	.....

NOTE.− * Clusters with one probability value larger than 0.95.

There are 7, 9, 12 and 8 systems with a probability value of difference larger than 0.95 for σ_v vs σ_{zhg}, σ_v vs $\sigma_{wg2.5}$, σ_v vs σ_{wg4} and σ_v vs σ_{wg4+yv}, respectively.
Excluding the cluster MACS J1206.2−0847, only ∼10% of the systems show a significant difference between the values of σ_v for all the compared cases.
Figures 9.5, 9.6, 9.7 and 9.8 show graphically the comparisons. I plot velocity dispersions with their jackknife errors and I draw the bisector line as reference.

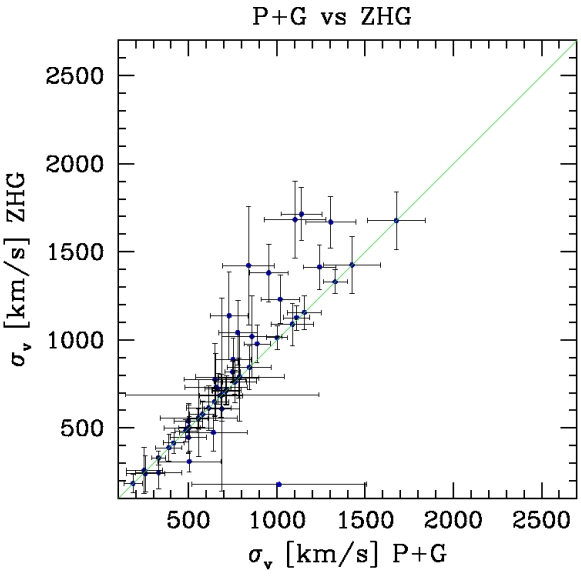

Figure 9.5: σ_v vs σ_{zhg} for 53 systems.

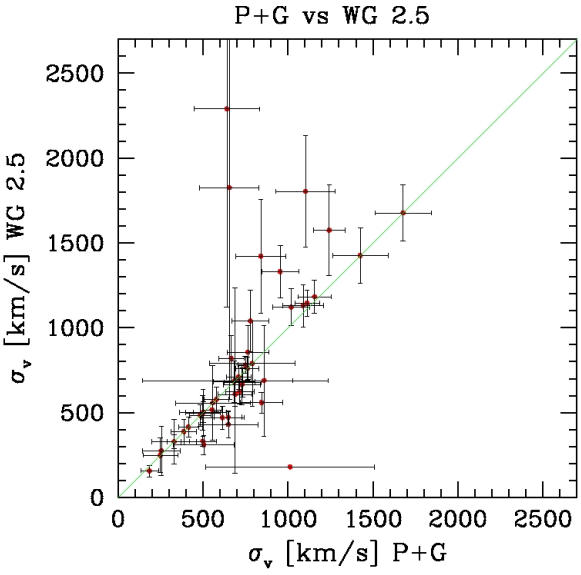

Figure 9.6: σ_v vs $\sigma_{wg2.5}$ for 47 systems.

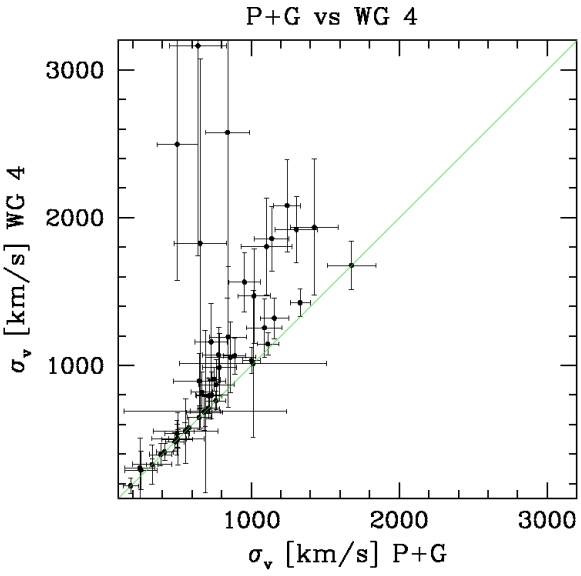

Figure 9.7: σ_v vs σ_{wg4} for 51 systems.

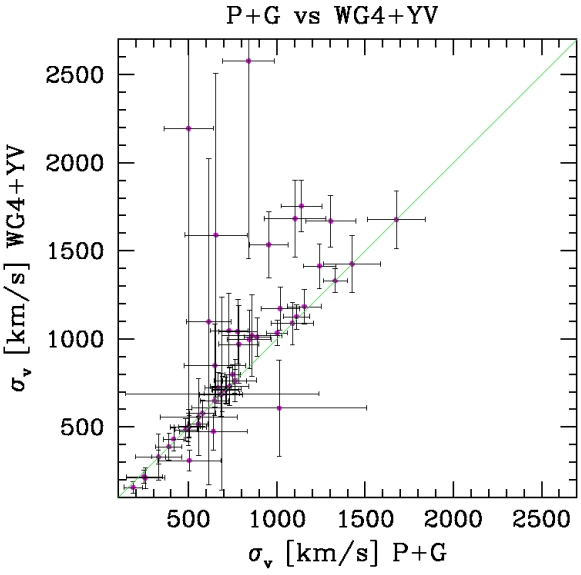

Figure 9.8: σ_v vs σ_{wg4+yv} for 52 systems.

There is a better agreement between the velocity dispersion estimates obtained with the different methods when these velocity dispersions are small than when they are large. In particular, the alternative methods are characterized by estimates of velocity dispersions larger than those of the P+G procedure. This fact can be due to the fixed gap of 1000 kms^{-1} that I use in the P+G method and that decreases the velocity dispersion.
To investigate the effect of the fixed gap of 1000 kms^{-1} in the P+G procedure, I consider the values of velocity dispersion after the peak detection of galaxies in the velocity distribution (P step) but before the "shifting gapper".
Table 9.7 lists the robust velocity dispersions obtained by P, P+G, ZHG, WG 2.5, WG 4 and WG4+YV procedures, with jackknife errors. For each alternative method I exclude clusters with redshifts in disagreement with the P+G ones and I represent them with points ".....".
In the comparisons between the P values and those estimated with all other methods, I also don't consider cluster CL 0023+0423, because the error on its velocity dispersion calculated with only the P procedure is larger than the measurement.
The P estimates are larger or equal to the P+G ones, according to the "shifting gapper" which removes or not other galaxies. The P step is somewhat in better agreement with the alternative methods than the complete P+G procedure.

Table 9.7: Robust velocity dispersions according to the procedures P, P+G, ZHG, WG 2.5, WG 4 and WG4+YV

	P	P+G	ZHG	WG 2.5	WG 4	WG4+YV
Cluster name	σ_p $\pm$ $\delta\sigma_p$	σ_v $\pm$ $\delta\sigma_v$	σ_{zhg} $\pm$ $\delta\sigma_{zhg}$	$\sigma_{wg2.5}$ $\pm$ $\delta\sigma_{wg2.5}$	σ_{wg4} $\pm$ $\delta\sigma_{wg4}$	σ_{wg4+yv} $\pm$ $\delta\sigma_{wg4+yv}$
	($\mathrm{km\ s}^{-1}$)	($\mathrm{km\ s}^{-1}$)	($\mathrm{km\ s}^{-1}$)	($\mathrm{km\ s}^{-1}$)	($\mathrm{km\ s}^{-1}$)	($\mathrm{km\ s}^{-1}$)
CL 0024+16	1065±123	888±75	978±105	.....	1065±123	1010±108
CL 1301.7−1139a	388±75	388±75	388±75	388±75	397±76	388±75
CL 0939+47	1237±111	1156±97	1156±97	1183±97	1319±136	1183±97
CL 0303+17	835±139	785±114	785±114	.....	986±229	969±219
CL 1202.7−1224	499±102	499±102	447±90	499±102	499±102	499±102
MS 0302.5+1717	806±125	666±74	722±87	819±136	819±136	722±87
MS 0302.7+1658	1041±183	779±109	1041±183	1041±183	1072±187	1041±183
CL 1037.9−1243a	554±57	554±57	554±57	517±45	554±57	517±45
MS 1621.5+2640[a,c,e]	992±80	749±44	819±61	781±50	906±81	798±54
MACS J1206.2−0847(1B)[a]	1894±362	840±146	1422±337	1422±337	2577±1120	2577±1120
MACS J1206.2−0847(2R)[a]	2108±255	1305±143	1668±146	.....	1920±223	1668±146
MACS J1206.2−0847(2B)[a]	1717±152	1139±117	1714±151	.....	1858±220	1754±146
MACS J1206.2−0847(1R)	1652±238	1103±173	1683±218	1804±329	1804±329	1683±218
MACS J1206.2−0847	1127±31	1105±33	.....	.....	.....	.....
CL 1138.2−1133a	510±57	510±57	.....	.....	.....	.....
CL 1059.2−1253	503±61	503±61	503±61	503±61	503±61	503±61
3C 295	1677±165	1677±165	1677±165	1677±165	1677±165	1677±165
CL 1018.8−1211	484±64	484±64	484±64	484±64	484±64	484±64
CL 1138.2−1133	710±73	710±73	710±73	710±73	710±73	710±73
CL 1301.7−1139[c]	743±110	648±81	648±81	472±38	648±81	648±81
RX J1117.4+0743	1426±162	1426±162	1426±162	1426±162	1936±460	1426±162
CL 1420.3−1236	266±118	255±110	241±104	276±146	292±131	210±59
CL 1411.1−1148	856±159	764±121	764±121	856±159	871±167	764±121

CL 1601+42	794±120	715±84	715±84	623±72	794±120	715±84
MS 0451.6−0305[a]	2005±309	1242±92	1414±127	1575±266	2082±313	1414±127
CL 1232.5−1250	1179±146	1089±120	1089±120	1131±125	1255±198	1089±120
MS 0015.9+1609[a]	1534±187	954±108	1380±163	1331±154	1564±202	1534±187
CL 1119.3−1129	201±56	185±52	185±52	157±34	185±52	157±34
CL 0054−27[b,c]	1013±496	1013±496	180±0	180±0	1013±496	607±271
CL 1037.9−1243	504±178	504±178	310±57	310±57	504±178	310±57
CL 1353.0−1137	614±127	614±127	614±127	470±67	.....	1097±925
CL 1354.2−1230a	717±178	557±219	557±219	557±219	557±219	557±219
CL 1103.7−1245a	330±41	330±41	330±41	330±41	330±41	330±41
CL 1054.4−1146	579±73	579±73	579±73	579±73	579±73	579±73
CL 1103.7−1245b	330±132	330±132	246±92	330±132	330±132	330±132
CL 1040.7−1155	415±58	415±58	415±58	415±58	415±58	431±65
CL 1054.7−1245[c]	539±92	499±81	539±92	331±31	539±92	499±81
CL 1324+3011	1125±442	844±124	844±124	559±61	1193±478	997±165
CL 1354.2−1230	689±100	689±100	608±70	608±70	689±100	689±100
CL 1216.8−1201	1013±68	1002±59	1013±68	.....	1033±89	1034±73
RX J1716+67	1566±153	1250±162	.....	.....	.....	.....
MS 1054−03	1145±76	1112±73	1126±70	1145±76	1145±76	1126±70
RX J0152.7−1357(1)	1018±232	859±169	1018±232	689±327	1056±238	1018±232
RX J0152.7−1357[a,b,e]	1687±153	1330±68	1330±68	.....	1425±96	1330±68
CL 0023+0423	688±1081	248±102	260±131	248±102	306±204	218±36
RX J1226.9+3332	1397±202	1019±110	1230±138	1121±109	1470±320	1172±121
CL 1604+4304	1589±919	655±175	732±190	1826±1249	1826±1249	1589±919
CL 1604+4321	920±239	649±176	775±206	430±77	894±189	849±234
CL 1103.7−1245[d]	539±161	500±138	500±138	500±138	2495±917	2194±1755
XMMU J1230.3+1339	683±122	683±122	683±122	683±122	683±122	683±122
AX J2016+1127	790±251	790±251	790±251	790±251	.....	.....
RDCS J0910+54	1145±246	729±108	1137±250	663±114	1160±258	1047±213
RDCS J1252.9−2927	761±67	761±67	761±67	761±67	761±67	761±67
RX J0848.9+4452	689±547	689±547	689±547	689±547	689±547	689±547
RX J0848.6+4453	640±191	640±191	475±105	2290±1167	3163±1418	475±105
XMMU J2235.3−2557	799±158	732±108	.....	677±87	799±158	732±108
XMMXCS J2215.9−1738	875±121	753±102	889±123	.....	.....	.....

NOTE.
[a] Clusters for which σ_p and σ_v differ more than 2σ.
[b] Clusters for which σ_p and σ_{zhg} differ more than 2σ.
[c] Clusters for which σ_p and $\sigma_{wg2.5}$ differ more than 2σ.
[d] Clusters for which σ_p and σ_{wg4} differ more than 2σ.
[e] Clusters for which σ_p and σ_{wg4+yv} differ more than 2σ.

Comparing the P velocity dispersions with the estimates of the alternative methods, I obtain:

- **P vs P+G**: there are 7 systems for which σ_p and σ_v differ more than 2σ;
- **P vs ZHG**: only for the 2 clusters CL 0054−27 and RX J0152.7−1357 there is a significant difference;
- **P vs WG 2.5**: 4 systems have $\sigma_{wg2.5}$ that differs from σ_p more than 2σ;

- **P vs WG 4**: these procedures are in better agreement and only 1 cluster, CL 1103.7−1245, is characterized by a significant difference;
- **P vs WG4+YV**: σ_p and σ_{wg4+yv} differ more than 2σ for the 2 clusters MS 1621.5+2640 and RX J0152.7−1357.

I plot these comparisons in the following figures 9.9, 9.10, 9.11, 9.12 and 9.13, excluding CL 0023+0423 and clusters for which redshift estimates obtained by the different methods disagree. Comparing with the previous plots, the velocity dispersions estimated by alternative methods are not much larger than the P values and there is a better agreement with respect to the P+G ones. In particular, the estimates determined by the P and the WG 4 methods are very similar and most points are along the bisector line.
This means that the fixed gap of 1000 kms^{-1} in the P+G procedure is able to reduce the velocity dispersion by rejecting more galaxies as interlopers.
Deciding which is the best member selection method is beyond of the aims of this thesis and, indeed, an ad hoc study based on simulations would be needed. I note that the alternative methods to P+G provide σ_v values up to $1500-2000\ \mathrm{kms}^{-1}$ which have never been found for very well studied clusters and would imply implausible high masses, inconsistent with alternative estimates (e.g., gravitational lensing), while the P+G procedure is able to avoid these cases. On the other hand, it is possible that the fixed value for the gap of $1000\ \mathrm{kms}^{-1}$ might not be the best for all clusters. In fact, the adopted gap would be smaller, e.g. $800\ \mathrm{kms}^{-1}$ if the cluster is much more sampled, as for the cluster MACS J1206.2−0847, in order to reject possible interlopers.

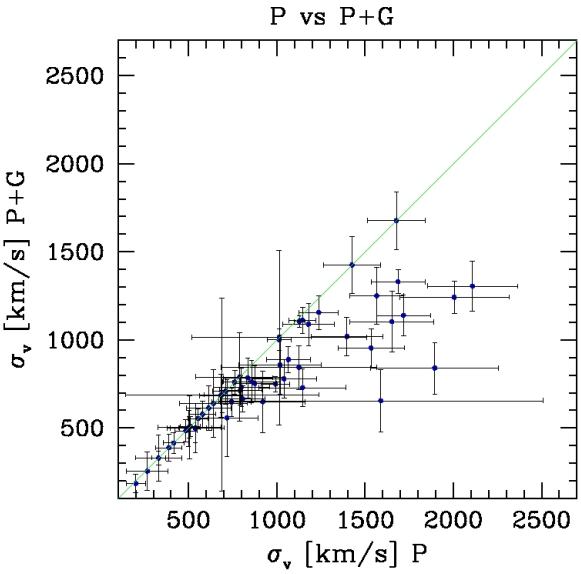

Figure 9.9: σ_p vs σ_v for 56 systems: the P+G values are equal or lower than the P ones.

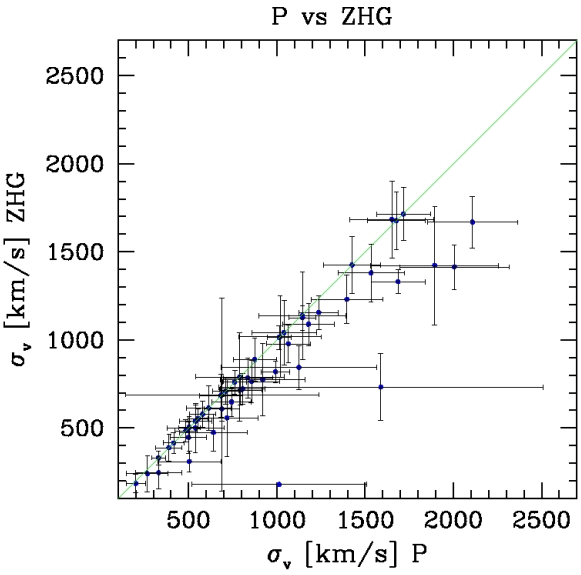

Figure 9.10: σ_p vs σ_{zhg} for 52 systems: the P estimates are larger than the ZHG ones for high values of velocity dispersion.

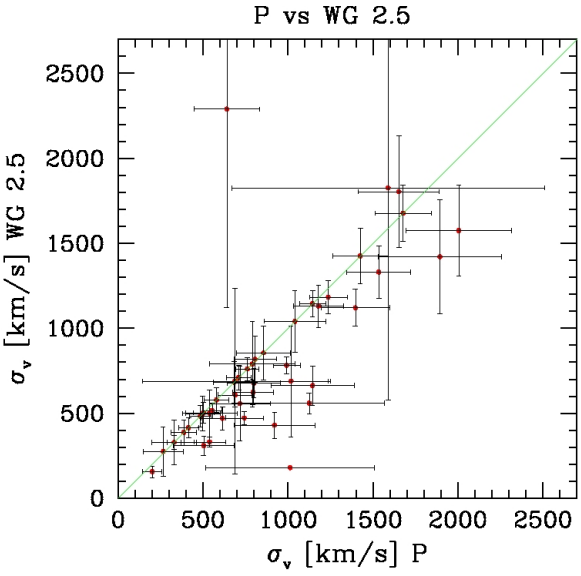

Figure 9.11: σ_p vs $\sigma_{wg2.5}$ for 46 systems.

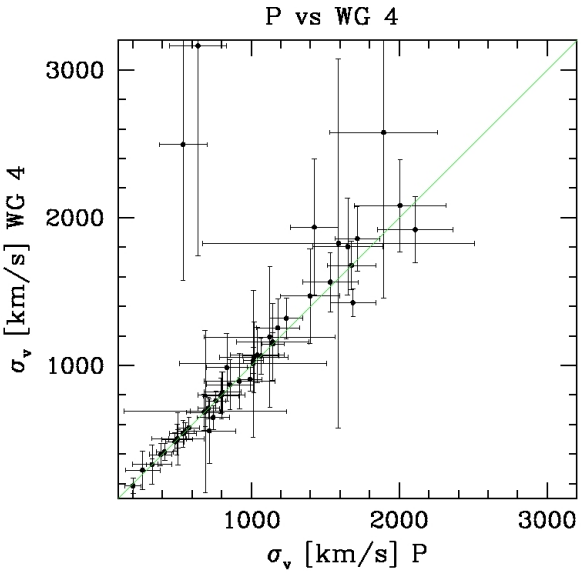

Figure 9.12: σ_p vs σ_{wg4} for 50 systems: most points are located along the bisector line.

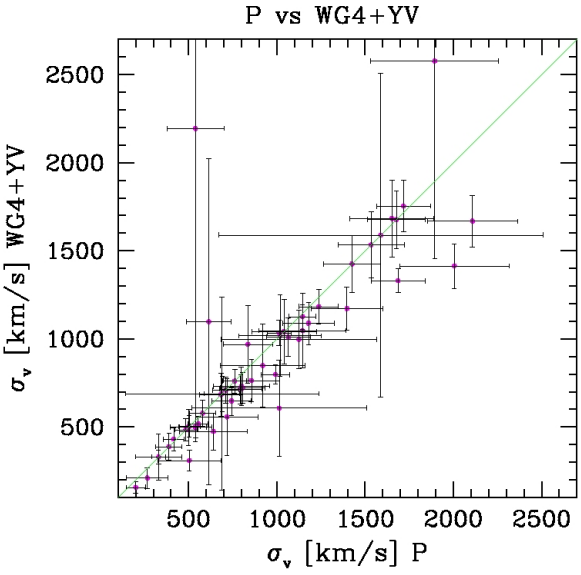

Figure 9.13: σ_p vs σ_{wg4+yv} for 51 systems.

Chapter 10

Blue and red member galaxies

In order to study the kinematics of different galaxy populations, I carry out the analysis of photometric data drawing the color-magnitude (CM) diagram for the cluster members to separate galaxies belonging to the red sequence from the blue ones characterized by active star formation. When it is not possible to employ this procedure, I use the equivalent width of the spectral line [OII] to divide passive from star-forming galaxies. Finally, for clusters with both this spectral information and the CM diagram, I investigate the agreement between spectroscopic and photometric classification of galaxies. In this chapter and in the following ones, red galaxies are synonymous of passive/early-type, while blue galaxies indicate those star-forming/late-type.

10.1 Color-Magnitude diagram

The color-magnitude diagram is a useful tool to separate different galaxy populations in clusters. This diagram shows a color, which is the difference between two magnitudes, as a function of a given magnitude. Plotting cluster members, it is possible to identify three different zones which correspond to three diverse galaxy populations: the red sequence, the green valley, and the blue cloud.
The red sequence includes most red galaxies which are generally ellipticals. The blue cloud contains most blue member galaxies which are generally spirals. In between the two distributions there is an underpopulated space known as the green valley which includes a number of red spirals.
Recent results suggest that the green valley is actually composed of two different populations of galaxies: one of late-type galaxies, where star formation has been quenched due to their gas supplies being shut off followed by exhaustion of their gas reservoirs for several billion years, and another of early-type galaxies where both the gas supplies and gas reservoirs have been destroyed very quickly, likely because of mergers with other galaxies and/or the presence of an active galactic nucleus. Figure 10.1 shows a representation of a CM diagram and highlights the three different populations.
In this thesis, where the number of galaxies per cluster is small, I consider only red and blue galaxy populations in order to compare their kinematics.

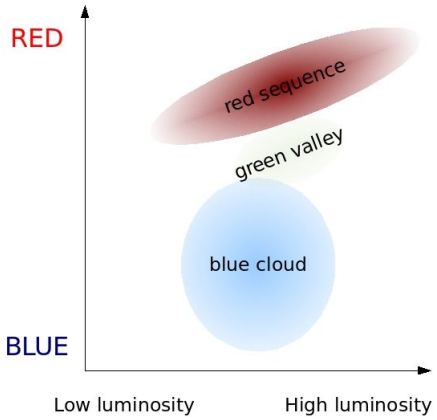

Figure 10.1: Color–magnitude diagram with three galaxy populations: the top red sequence, the mid green valley and the bottom blue cloud.

10.2 Selection of red and blue populations: color cuts

For all 57 systems (52 clusters, 4 subgroups of MACS J1206.2−0847 and 1 subgroup of RX J0152.7−1357) I draw a CM diagram. When it is possible, for each cluster the used color and magnitude are selected among those available according to figure 10.2 of Westra et al. (2010), which displays the normalized bandpasses for SDSS *ugriz* bands (*top*) and Johnson-Cousins $UBVRI$ bands (*bottom*) as a function of wavelength and redshift. The plot shows which are the more appropriate bands to use in order to see the division between the red and blue populations at any given cluster redshift.

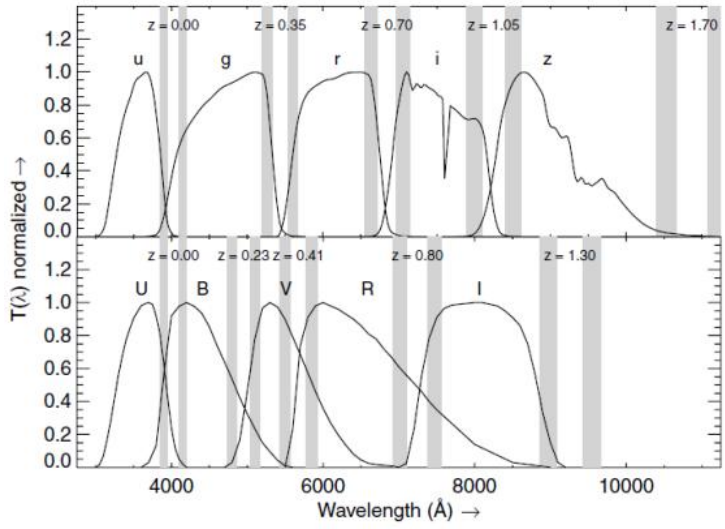

Figure 10.2: Normalized bandpasses for SDSS *ugriz* bands (*top*) and Johnson-Cousins $UBVRI$ bands (*bottom*) as a function of wavelength and redshift. The vertical bands indicate the observed wavelength ranges where the Balmer break would roughly be between filters (from Westra et al., 2010).

10 Blue and red member galaxies

To separate red members from blue ones, I perform a color cut considering red the galaxies above a color threshold and blue those below. I obtain the cut limit using the KMM software, implemented by Ashman et al. (1994), which investigates the bi-modality of the color distribution and is able to separate it into two groups. In order to illustrate graphically the results of KMM, I report as an example in figure 10.3 the $g - r$ color histogram for the cluster MS 1621.5+2640. The two Gaussian distributions are the two different cluster populations and the intersection point between these represents the color cut. In particular, the blue Gaussian indicates the star-forming members, whereas the red Gaussian fitted on points above the color cut is formed by passive galaxies.

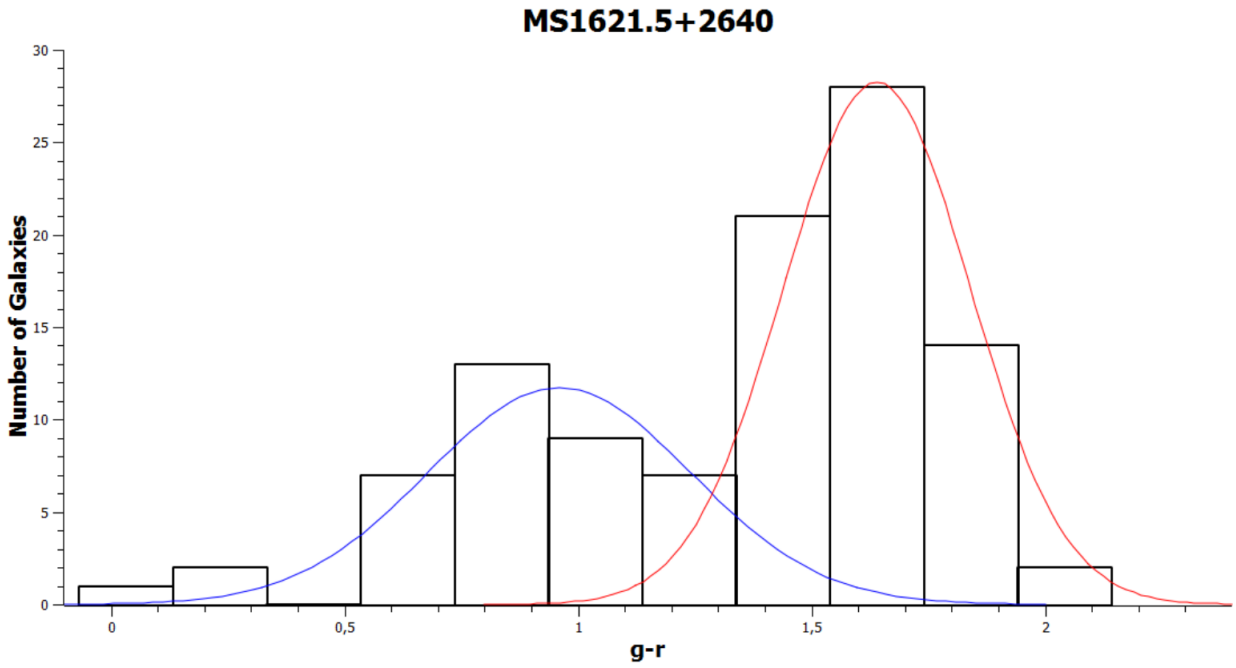

Figure 10.3: Bi-modality in color g-r for MS 1621.5+2640: the blue Gaussian indicates the star-forming population, whereas the red Gaussian is formed by passive galaxies. The intersection point indicates the color cut.

When very few data are available, KMM fails. In this case, I use a theoretical cut limit as reference obtained by redshifting the typical $z = 0$ colors of red and blue galaxies at the cluster redshift, according to the study of Fukugita et al. (1995).
In the case of 5 clusters at high z or with large uncertainties on magnitudes, I prefer to employ an alternative procedure based on the equivalent width of [OII] (see the next section 10.3: *Selection of red and blue populations: equivalent widths of the spectral line [OII]*).
For each system Table 10.1 lists colors and magnitudes used in the corresponding CM diagrams, and the obtained color cuts. With regards to the clusters for which I do not use the color cut procedure, I write only colors and magnitudes. In addition, for the subgroups of MACS J1206.2−0847 I employ the same color cut of the whole cluster.

Table 10.1: Color cuts

Cluster name	Color	Magnitude	Color cut
CL 0024+16	$g-r$	r	1.200
CL 1301.7−1139a	$B-I$	I	3.025
CL 0939+47	$g-r$	r	1.130
CL 0303+17	$g-r$	r	1.370
CL 1202.7−1224	$B-I$	I	2.700
MS 0302.5+1717	$R-I$	I	0.760
MS 0302.7+1658	$g-r$	r	1.265
CL 1037.9−1243a	$V-I$	I	1.600
MS 1621.5+2640	$g-r$	r	1.275
MACS J1206.2−0847(1B)	$B-R_c$	R_c	1.440
MACS J1206.2−0847(2R)	$B-R_c$	R_c	1.440
MACS J1206.2−0847(2B)	$B-R_c$	R_c	1.440
MACS J1206.2−0847(1R)	$B-R_c$	R_c	1.440
MACS J1206.2−0847	$B-R_c$	R_c	1.440
CL 1138.2−1133a	$V-I$	I	1.880
CL 1059.2−1253	$B-I$	I	3.200
3C 295	$g-r$	r	1.400
CL 1018.8−1211	$B-I$	I	2.940
CL 1138.2−1133	$V-I$	I	1.695
CL 1301.7−1139	$B-I$	I	3.200
RX J1117.4+0743	$g'-r'$	r'	1.780
CL 1420.3−1236	$B-I$	I	3.475
CL 1411.1−1148	$B-I$	I	3.580
CL 1601+42	$g-r$	r	1.200
MS 0451.6−0305	$g'-r'$	r'_{tot}	1.758
CL 1232.5−1250	$B-I$	I	3.785
MS 0015.9+1609	$g-r$	r	1.200
CL 1119.3−1129	$V-I$	I	2.070
CL 0054−27	$V-I$	I	2.000
CL 1037.9−1243	$V-R$	R	1.085
CL 1353.0−1137	$V-I$	I	2.160
CL 1354.2−1230a	$V-R$	R	1.100
CL 1103.7−1245a	$V-I$	I	2.200
CL 1054.4−1146	$R-I$	I	2.150
CL 1103.7−1245b	$V-I$	I	2.085
CL 1040.7−1155	$R-I$	I	1.020
CL 1054.7−1245	$R-I$	I	1.115
CL 1324+3011	$R-I$	I	1.215
CL 1354.2−1230	$V-I$	I	2.115
CL 1216.8−1201	$R-I$	I	1.280
RX J1716+67	$i-z$	z	.....
MS 1054−03	$V-i$	i	1.430
RX J0152.7−1357(1)	$i'-z'$	z'_{tot}	0.718
RX J0152.7−1357	$r-K_s$	K_s	2.520
CL 0023+0423	$R-I$	I	.....

RX J1226.9+3332	$i' - z'$	z'_{tot}	0.630
CL 1604+4304	$B - R$	R	1.050
CL 1604+4321	$B - R$	R	2.000
CL 1103.7−1245	$R - I$	I	1.200
XMMU J1230.3+1339	$i - z$	z	0.370
AX J2016+1127	$R - I$	I	1.700
RDCS J0910+54	$i - z$	z	0.820
RDCS J1252.9−2927	$R - K_s$	K_s	.....
RX J0848.9+4452	$R - K$	K	5.800
RX J0848.6+4453	$J - K$	K	1.985
XMMU J2235.3−2557	$J - K$	K	.....
XMMXCS J2215.9−1738	$I - K_s$	K_s	.....

Figure 16.6 shows the CM diagram for each cluster: the green line is the color cut adopted in this study, the red integer line represents the CM relation and the two red dashed lines indicate the locus of the red sequence within the standard deviation (calculated and used in the first check of this procedure, see next paragraph 10.4: *First check: color-magnitude relations and rectified color cuts*). With regards to the 5 clusters for which the analysis of photometric data fails, I draw only the CM diagrams without a color cut or a CM straight line. The cluster name is written at the top of each plot.
One could wonder whether a magnitude-dependent color cut (following the CM relation) would do a better job in separating red and blue galaxies, and we will explore this in the following section.

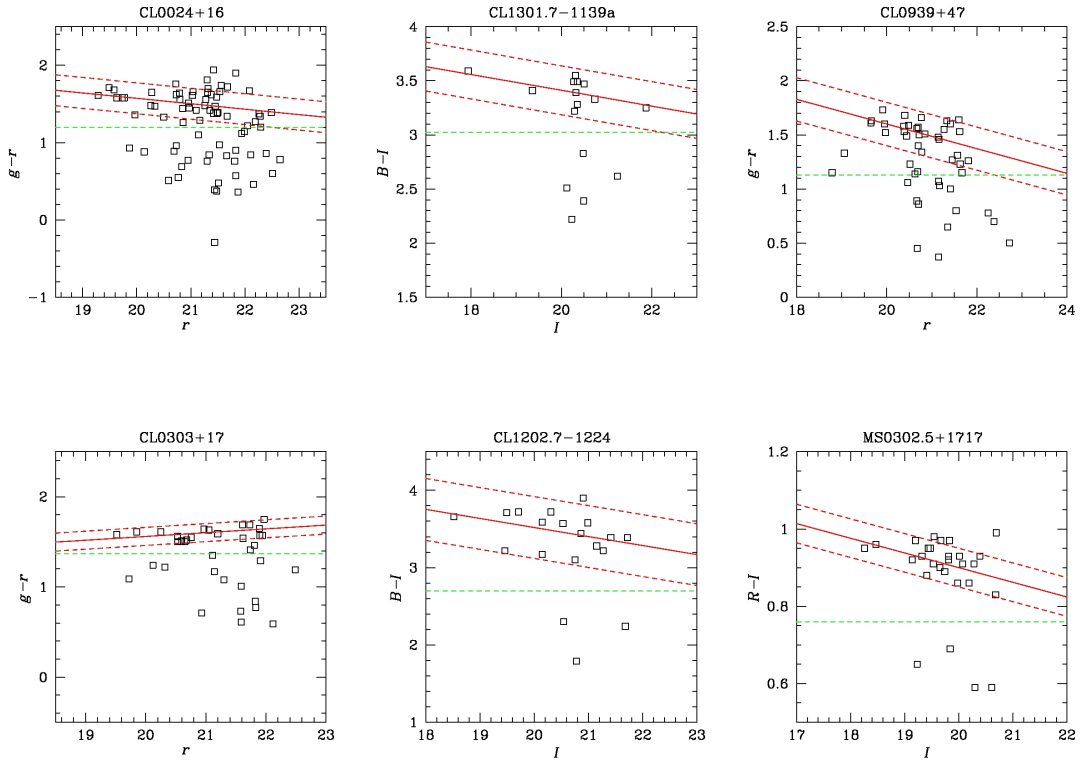

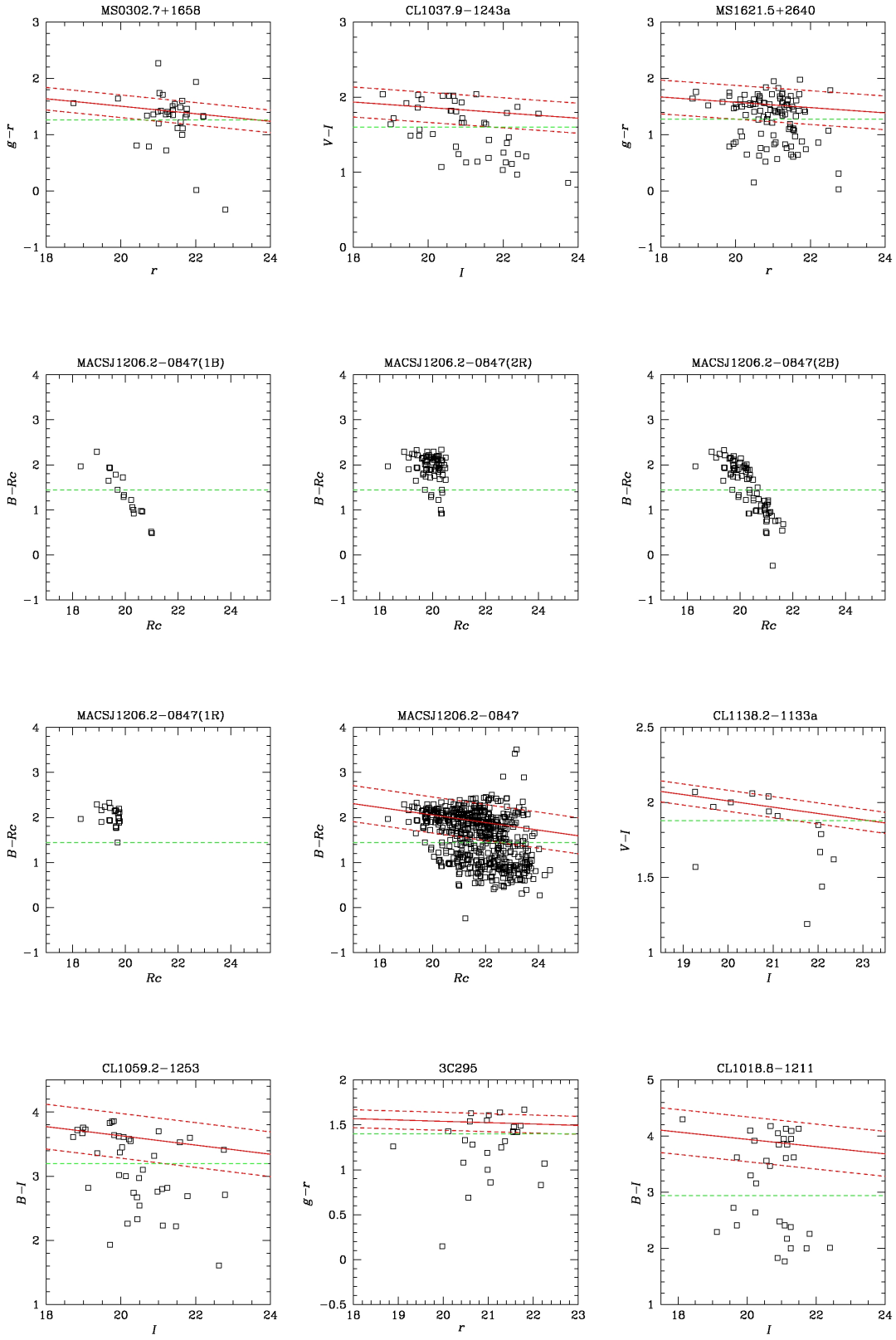
MS0302.7+1658
g−r
r
CL1037.9−1243a
V−I
I
MS1621.5+2640
g−r
r
MACSJ1206.2−0847(1B)
B−Rc
Rc
MACSJ1206.2−0847(2R)
B−Rc
Rc
MACSJ1206.2−0847(2B)
B−Rc
Rc
MACSJ1206.2−0847(1R)
B−Rc
Rc
MACSJ1206.2−0847
B−Rc
Rc
CL1138.2−1133a
V−I
I
CL1059.2−1253
B−I
I
3C295
g−r
r
CL1018.8−1211
B−I
I

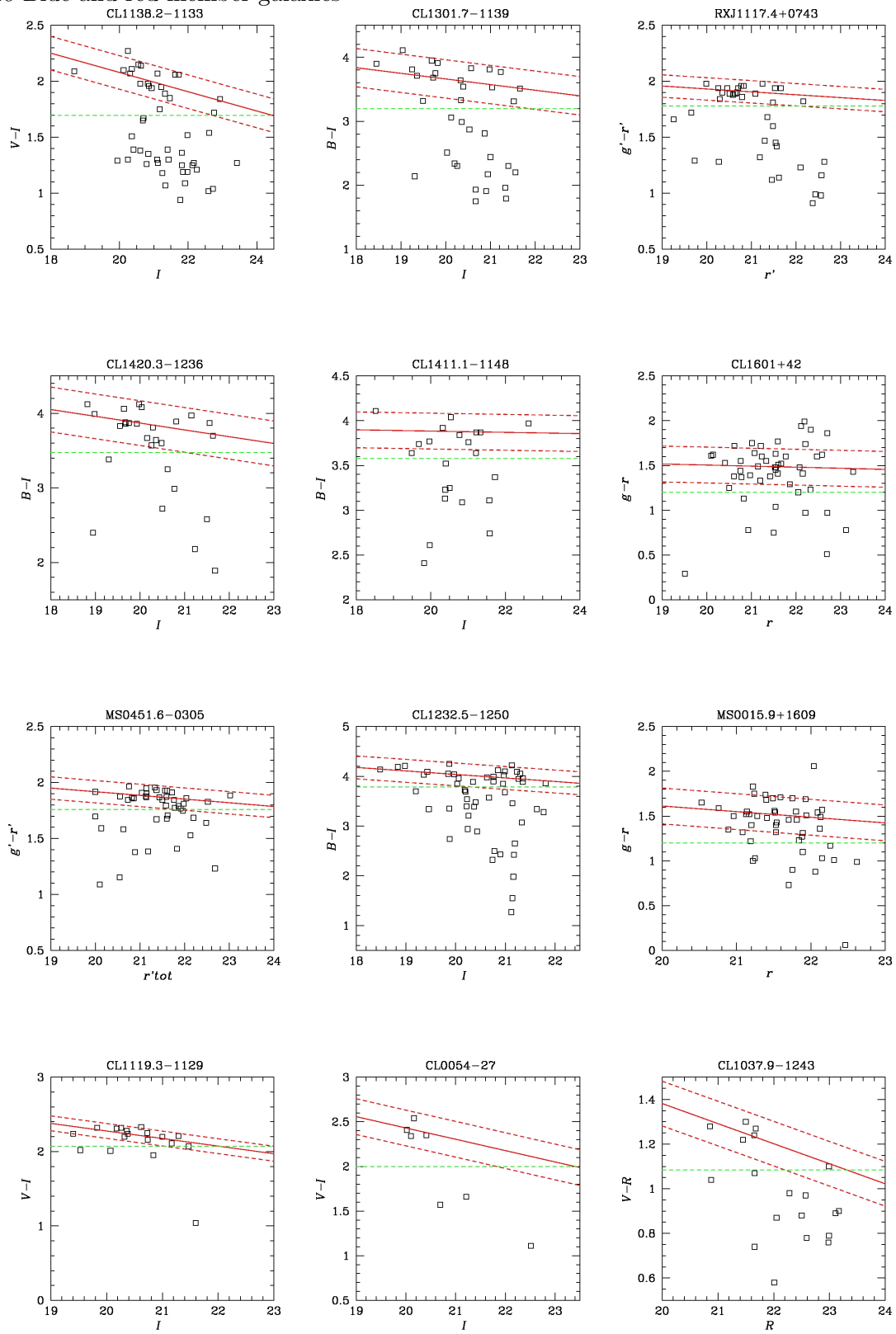
CL1138.2−1133
V−I
I
CL1301.7−1139
B−I
I
RXJ1117.4+0743
g'−r'
r'
CL1420.3−1236
B−I
I
CL1411.1−1148
B−I
I
CL1601+42
g−r
r
MS0451.6−0305
g'−r'
r'tot
CL1232.5−1250
B−I
I
MS0015.9+1609
g−r
r
CL1119.3−1129
V−I
I
CL0054−27
V−I
I
CL1037.9−1243
V−R
R

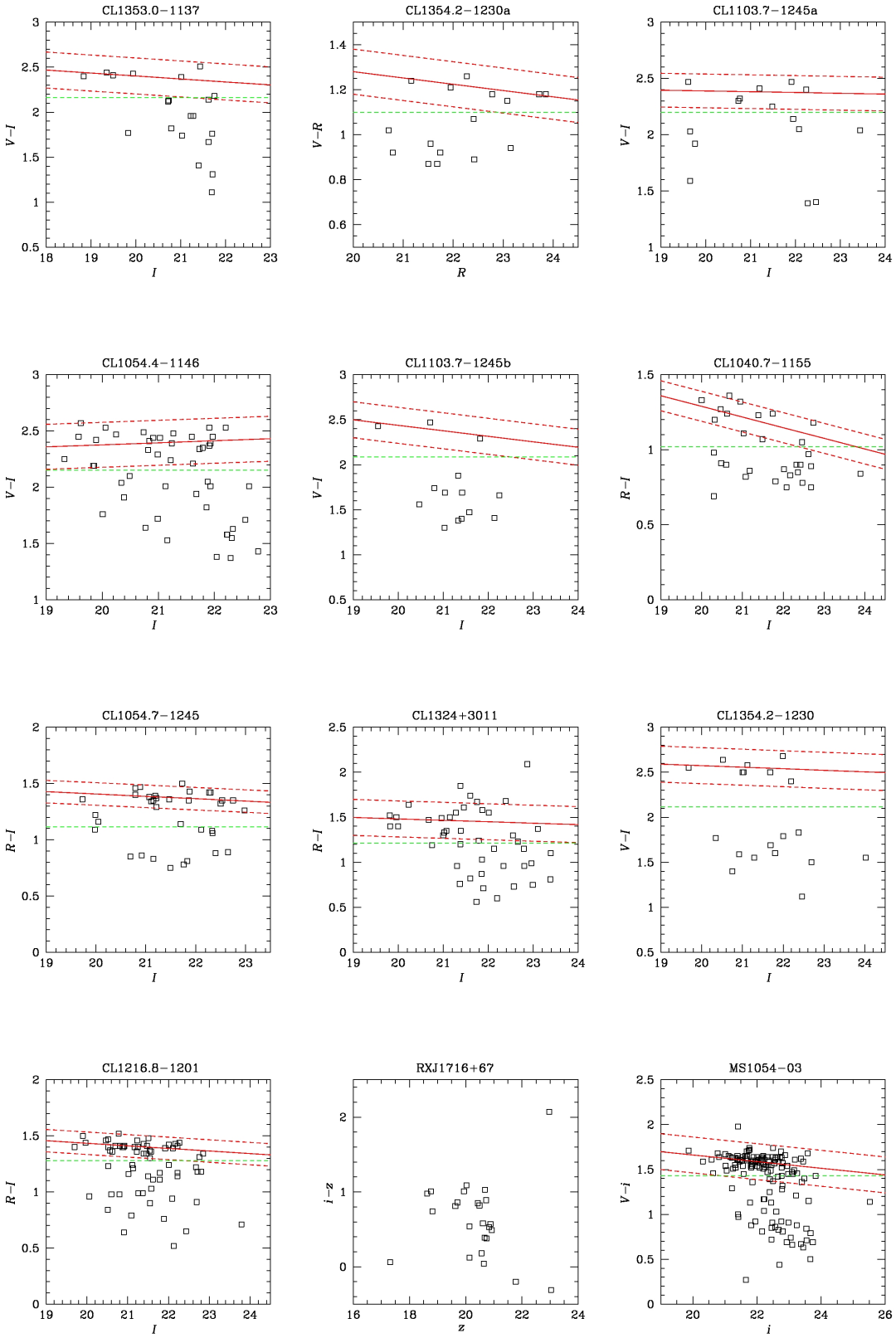
CL1353.0−1137
V−I
I
CL1354.2−1230a
V−R
R
CL1103.7−1245a
V−I
I
CL1054.4−1146
V−I
I
CL1103.7−1245b
V−I
I
CL1040.7−1155
R−I
I
CL1054.7−1245
R−I
I
CL1324+3011
R−I
I
CL1354.2−1230
V−I
I
CL1216.8−1201
R−I
I
RXJ1716+67
i−z
z
MS1054−03
V−i
i

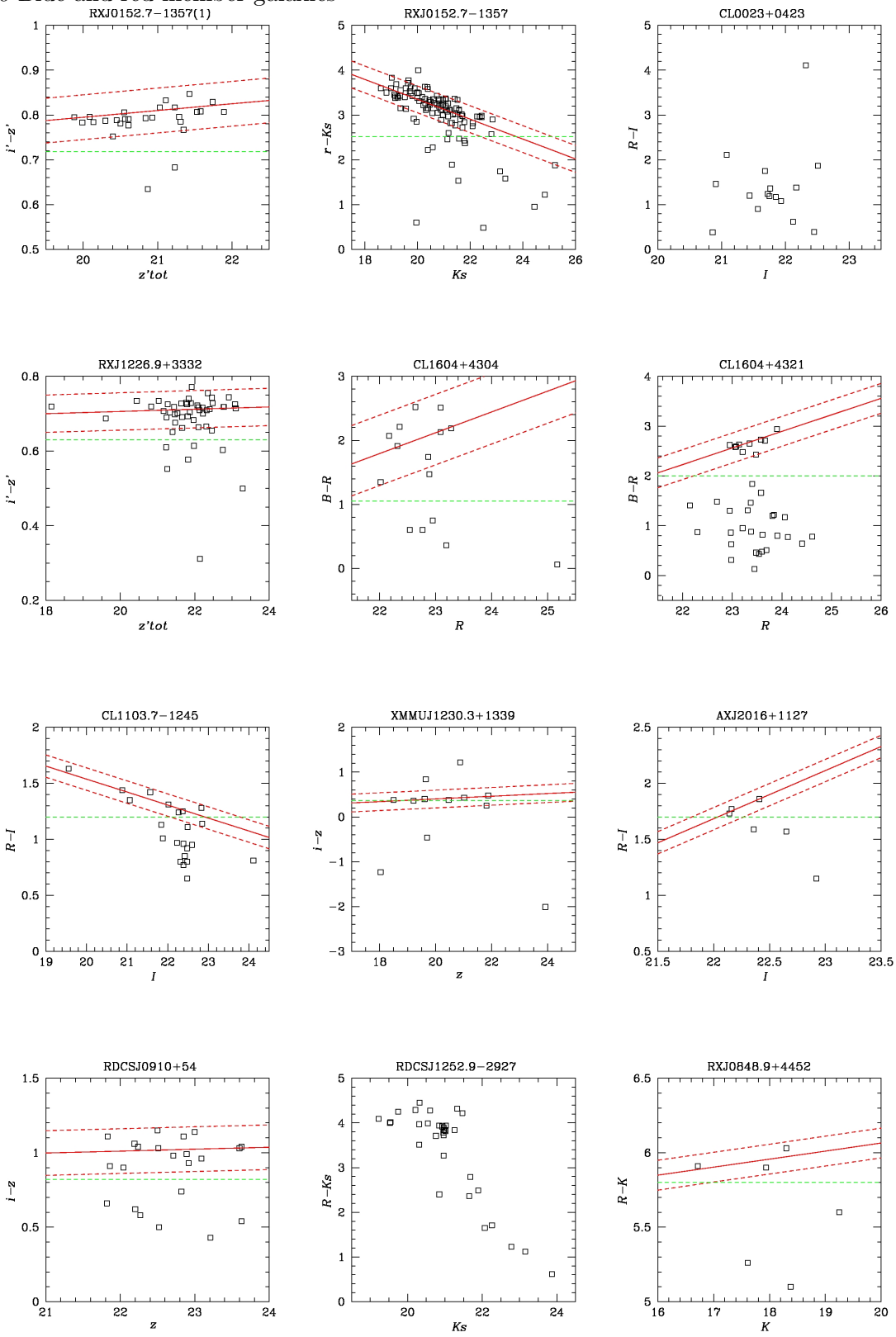
RXJ0152.7−1357(1)
i'−z'
z'tot
RXJ0152.7−1357
r−Ks
Ks
CL0023+0423
R−I
I
RXJ1226.9+3332
i'−z'
z'tot
CL1604+4304
B−R
R
CL1604+4321
B−R
R
CL1103.7−1245
R−I
I
XMMUJ1230.3+1339
i−z
z
AXJ2016+1127
R−I
I
RDCSJ0910+54
i−z
z
RDCSJ1252.9−2927
R−Ks
Ks
RXJ0848.9+4452
R−K
K

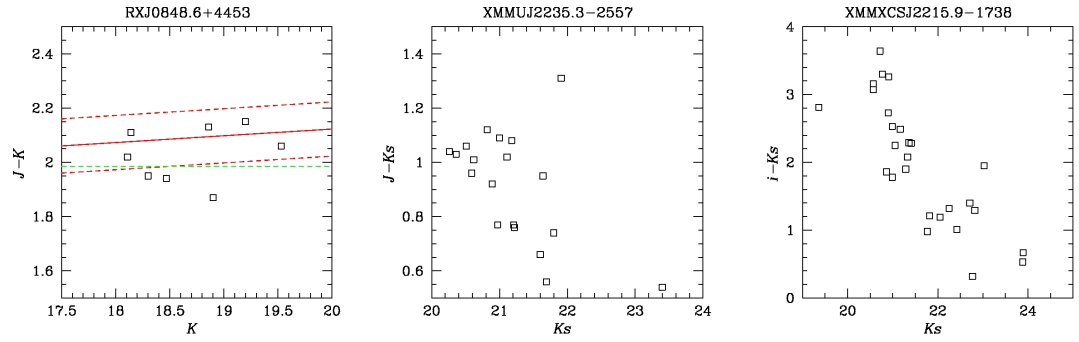

Figure 10.4: Color-magnitude diagrams for cluster members: the green line is the color cut adopted in this thesis, the red solid line represents the CM relation and the two red dashed lines indicate the locus of the red sequence within the standard deviation. In addition, the CM diagrams are shown without color cuts for the 5 clusters for which this method is not employed.

10.3 Selection of red and blue populations: equivalent widths of the spectral line [OII]

I prefer to adopt an alternative procedure to that based on color cuts for the 5 distant clusters for which it is not possible to separate the blue population from the red one because of the large uncertainties on the magnitudes (RX J1716+67, CL 0023+0423, RDCS J1252.9−2927, XMMU J2235.3−2557 and XMMXCS J2215.9−1738).
For these clusters I use the equivalent width of the spectral line [OII], which is an important indicator of star formation in a galaxy, to separate passive from star-forming galaxies. In particular, I consider a galaxy with EW[OII]$\geq$15Å as star-forming and with EW[OII]$<$15Å as passive. Sometimes measurements of EW are not available. The only known information is the presence or absence of the [OII] emission line in the galaxy spectrum, which I use to identify it as blue or red galaxy, respectively.

10.4 First check: color-magnitude relations and rectified color cuts

In order to check the color cuts applied in the section above, I compute the CM relations and I apply the rectified color cuts, which are obtained by using the CM relation as the reference color at any given magnitude (see equation 10.1). However, this more complex second step does not change a lot the previous results about the separation of red and blue galaxies and I decide to not apply it.
After the selection using color cuts, I fit the red sequence estimating the color-magnitude relation which is a linear equation, $y = ax + b$, where a is the angular coefficient and b is the intercept. Table 10.2 reports colors and magnitudes used in the CM diagrams, obtained color cuts and the coefficients of CM relations with their standard deviations (SD) for the red population. The clusters for which I use the procedure based on EW[OII] are not listed. For the subgroups of MACS J1206.2−0847 I employ the same color cut of the whole cluster but I don't fit the partial red sequences. The CM relations are drawn in figure 16.6: the red integer line is the CM equation and the two red dashed lines indicate the locus of the red sequence within the standard deviation.

Table 10.2: Results of color-magnitude relations

Cluster name	Color	Magnitude	Color cut	a	SD(a)	b	SD(b)
CL 0024+16	$g-r$	r	1.200	−0.070	0.022	2.973	0.462
CL 1301.7−1139a	$B-I$	I	3.025	−0.073	0.012	4.872	0.226
CL 0939+47	$g-r$	r	1.130	−0.114	0.035	3.881	0.722
CL 0303+17	$g-r$	r	1.370	+0.042	0.021	0.720	0.437
CL 1202.7−1224	$B-I$	I	2.700	−0.117	0.041	5.859	0.853
MS 0302.5+1717	$R-I$	I	0.760	−0.038	0.012	1.660	0.228
MS 0302.7+1658	$g-r$	r	1.265	−0.067	0.019	2.846	0.402
CL 1037.9−1243a	$V-I$	I	1.600	−0.036	0.025	2.584	0.524
MS 1621.5+2640	$g-r$	r	1.275	−0.047	0.020	2.517	0.409
MACS J1206.2−0847(1B)	$B-R_c$	R_c	1.440	.....	.....	.....	.....
MACS J1206.2−0847(2R)	$B-R_c$	R_c	1.440	.....	.....	.....	.....
MACS J1206.2−0847(2B)	$B-R_c$	R_c	1.440	.....	.....	.....	.....
MACS J1206.2−0847(1R)	$B-R_c$	R_c	1.440	.....	.....	.....	.....
MACS J1206.2−0847	$B-R_c$	R_c	1.440	−0.084	0.010	3.736	0.216
CL 1138.2−1133a	$V-I$	I	1.880	−0.042	0.026	2.851	0.527
CL 1059.2−1253	$B-I$	I	3.200	−0.072	0.017	5.070	0.349
3C 295	$g-r$	r	1.400	−0.015	0.055	1.840	1.168
CL 1018.8−1211	$B-I$	I	2.940	−0.065	0.072	5.244	1.499
CL 1138.2−1133	$V-I$	I	1.695	−0.086	0.023	3.799	0.488
CL 1301.7−1139	$B-I$	I	3.200	−0.088	0.052	5.422	1.064
RX J1117.4+0743	$g'-r'$	r'	1.780	−0.026	0.023	2.452	0.477
CL 1420.3−1236	$B-I$	I	3.475	−0.091	0.036	5.688	0.718
CL 1411.1−1148	$B-I$	I	3.580	−0.007	0.048	4.024	1.012
CL 1601+42	$g-r$	r	1.200	−0.012	0.034	1.745	0.734
MS 0451.6−0305	$g'-r'$	r'_{tot}	1.758	−0.033	0.014	2.578	0.305
CL 1232.5−1250	$B-I$	I	3.785	−0.071	0.015	5.458	0.300
MS 0015.9+1609	$g-r$	r	1.200	−0.063	0.035	2.873	0.746
CL 1119.3−1129	$V-I$	I	2.070	−0.102	0.034	4.317	0.696
CL 0054−27	$V-I$	I	2.000	−0.127	0.114	4.971	2.319
CL 1037.9−1243	$V-R$	R	1.085	−0.090	0.015	3.182	0.322
CL 1353.0−1137	$V-I$	I	2.160	−0.033	0.040	3.062	0.788
CL 1354.2−1230a	$V-R$	R	1.100	−0.028	0.006	1.840	0.131
CL 1103.7−1245a	$V-I$	I	2.200	−0.007	0.036	2.529	0.765
CL 1054.4−1146	$R-I$	I	2.150	+0.018	0.027	2.017	0.575
CL 1103.7−1245b	$V-I$	I	2.085	−0.061	0.023	3.658	0.479
CL 1040.7−1155	$R-I$	I	1.020	−0.071	0.024	2.709	0.508
CL 1054.7−1245	$R-I$	I	1.115	−0.021	0.015	1.827	0.326
CL 1324+3011	$R-I$	I	1.215	−0.016	0.029	1.802	0.608
CL 1354.2−1230	$V-I$	I	2.115	−0.017	0.037	2.913	0.773
CL 1216.8−1201	$R-I$	I	1.280	−0.023	0.010	1.894	0.205
MS 1054−03	$V-i$	i	1.430	−0.037	0.009	2.402	0.193
RX J0152.7−1357(1)	$i'-z'$	z'_{tot}	0.718	+0.015	0.004	0.495	0.078
RX J0152.7−1357	$r-K_s$	K_s	2.520	−0.222	0.017	7.790	0.343
RX J1226.9+3332	$i'-z'$	z'_{tot}	0.630	+0.003	0.003	0.646	0.061
CL 1604+4304	$B-R$	R	1.050	+0.325	0.229	−5.357	5.203

CL 1604+4321	$B-R$	R	2.000	+0.333	0.081	−5.098	1.882
CL 1103.7−1245	$R-I$	I	1.200	−0.116	0.015	3.858	0.315
XMMU J1230.3+1339	$i-z$	z	0.370	+0.030	0.005	−0.198	0.108
AX J2016+1127	$R-I$	I	1.700	+0.430	0.043	−7.776	0.957
RDCS J0910+54	$i-z$	z	0.820	+0.013	0.032	0.725	0.736
RX J0848.9+4452	$R-K$	K	5.800	+0.054	0.028	4.985	0.471
RX J0848.6+4453	$J-K$	K	1.985	+0.025	0.039	1.623	0.726

In order to obtain a better separation between passive and star-forming member galaxies, I can employ a second step after drawing CM plots. This second step consists in the rectification of the CM diagrams: I represent the rectified color C_{rect} as function of the magnitude m, where the rectified color is the difference between the observed color C and the corrected color C_{cor} given by the estimated CM relation:

$$C_{rect} = C - C_{cor}, \tag{10.1}$$

with $C_{cor} = am + b$.
In this context, I complete my analysis computing color-magnitude relations and applying a color-magnitude cut rather than a single color cut to separate red and blue members. However, I decide not to consider the results of this more complex procedure because in some cases data are too poor to obtain reliable color-magnitude relations, as for examples in the cases of CL 1604+4304 and CL 1604+4321, where the slope of the relation is inverted probably because of the small data sample and the limited magnitude range. Moreover, this complicated second step does not change the previous results about the separation of red and blue galaxies in a significant way.
To show this, I consider the most numerous cluster MACS J1206.2−0847 and I draw the CM and $C_{rect}M$ diagrams in figure 10.5.

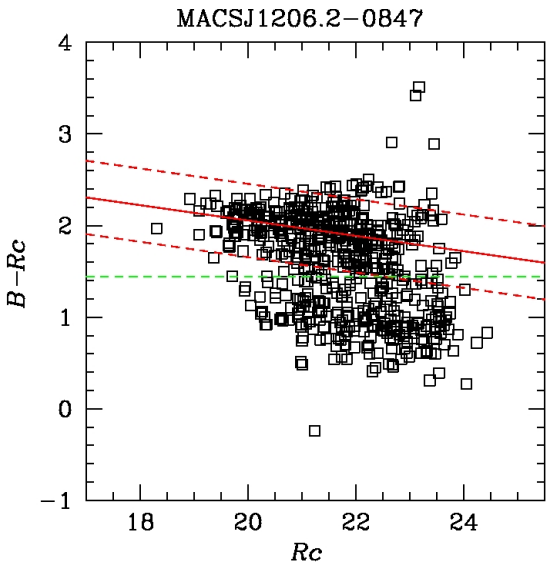

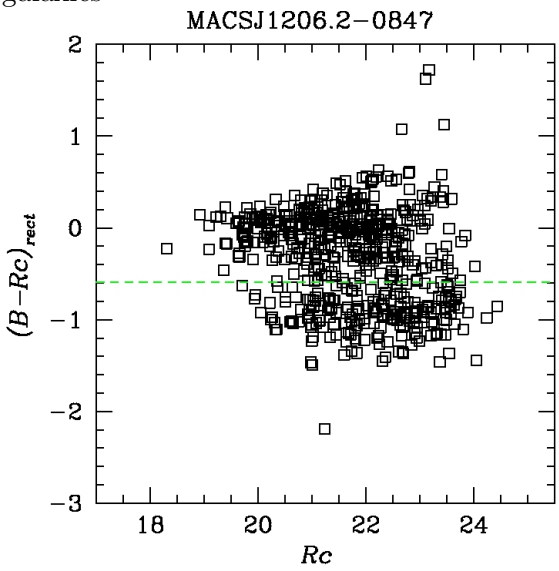

Figure 10.5: CM and $C_{rect}M$ diagrams for member galaxies of the most numerous cluster MACS J1206.2−0847.

In Table 10.3 for MACS J1206.2−0847 I list cuts, total number of members N_g, number of galaxies with no measures of magnitudes N_{noM}, number of red/passive galaxies N_{red} and number of blue/star-forming members N_{blue}.
Comparing the results of the 1st step with that of the 2nd one, I obtain that for a sample of 597 member galaxies the difference in the number of red and blue members is 29 galaxies: N_{red} increases of 29 galaxies while N_{blue} decreases of the same number.
The difference in the number of galaxies between the two steps is negligible for the other clusters which are less numerous than MACS J1206.2−0847, too. As a consequence of this, I consider only the results obtained with the magnitude-independent color cuts as numbers of red and blue galaxies belonging to the respective clusters (see next section 10.6: *Number of red and blue member galaxies*).
Note that the rectification procedure of the CM relation is iterative and this 2nd step is only the 2nd phase. However, the difference in the number of galaxies does not change in a significant way.

Table 10.3: Results of CM and $C_{rect}M$ diagrams for MACS J1206.2−0847

Diagram	Cut	N_g	N_{noM}	N_{red}	N_{blue}
CM	1.440	599	2	369	228
$C_{rect}M$	−0.592	599	2	398	199

10.5 Second check: agreement between EWs[OII] and color cuts

The spectral information about the EW[OII] is available for several clusters for which the separation between galaxy populations is estimated using color cuts. In this context, I compare the results obtained with a photometric separation with those related to a spectroscopic division and I find that the populations separated by color cuts are in agreement with a division based on EW[OII]: galaxies belonging to the red sequence have no emission of [OII] or small values of EW, instead spectra of blue members, which are located below the red sequence, are featured by a strong emission line [OII].
For 11 clusters, I display their CM diagrams where the point sizes are weighted on EW[OII] in figure 10.6: a larger square means a higher value of EW[OII]. I plot cluster members for which this information is available. Blue/star-forming members are larger squares while red/passive galaxies are represented by smaller ones. The plots illustrate that most of the passive galaxies are located above the color cut and, in particular, along the red sequence while most star-forming galaxies lie below it.
This second check verifies that the use of the color cut procedure is quite efficient to separate passive/red from star-forming/blue galaxies.

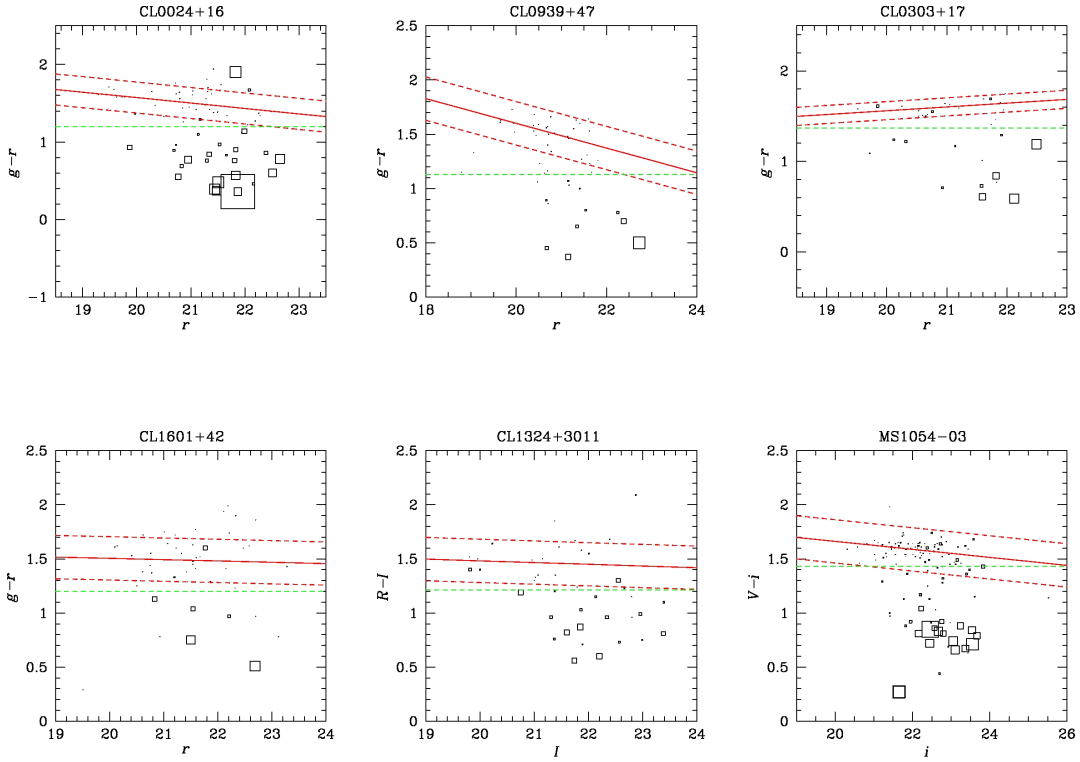

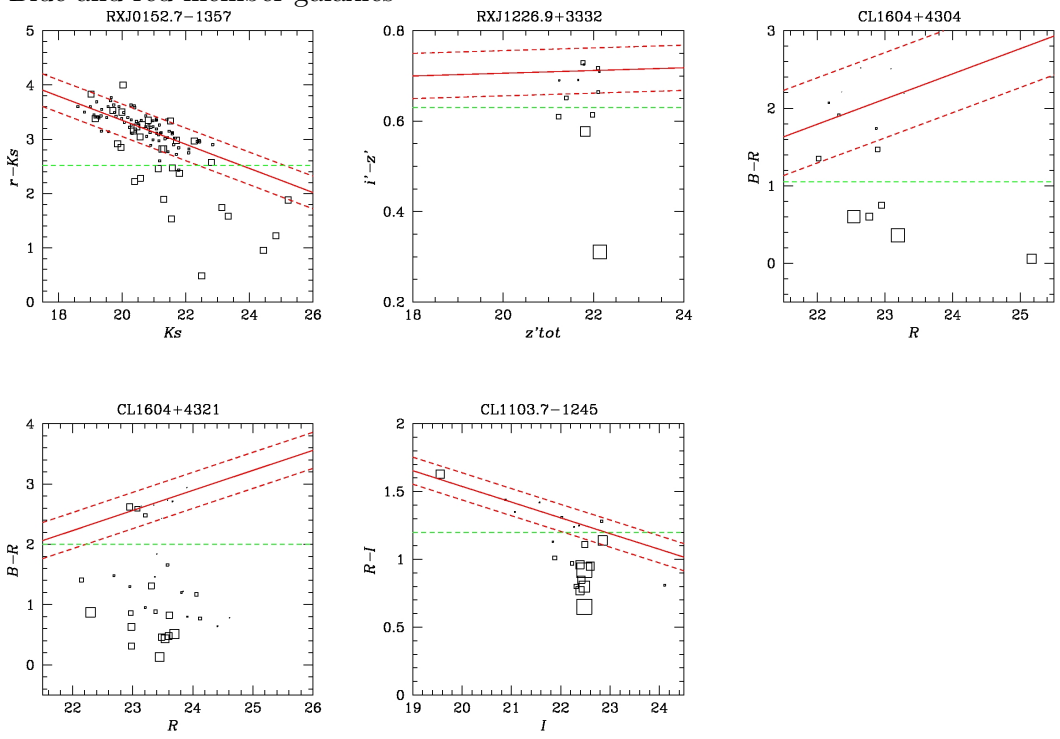

Figure 10.6: Examples of CM diagrams weighted on EW[OII]: most smaller squares, which indicate small values of EW[OII] and passive galaxies, populate the red sequence, while large ones, which represent high values of EW[OII] and strong star formation, lie below it.

10.6 Number of red and blue member galaxies

Using color cuts for 47 clusters and EW[OII] for 5 ones, I obtain the following numbers of red/passive members, N_{red}, and blue/star-forming galaxies, N_{blue}. Table 10.4 lists also the total number of cluster members, N_g, and the number of galaxies with no measures of magnitudes, N_{noM}, or with no values of EW[OII], $N_{no\mathrm{EW[OII]}}$, according to the used procedure to select different populations. The symbol "–" indicates that the corresponding method is not used.

Table 10.4: Number of red and blue member galaxies for all 52 clusters

Cluster name	N_g	N_{noM}	$N_{no\mathrm{EW[OII]}}$	N_{red}	N_{blue}
CL 0024+16	100	22	–	49	29
CL 1301.7−1139a	17	0	–	12	5
CL 0939+47	70	22	–	34	14
CL 0303+17	46	9	–	21	16
CL 1202.7−1224	21	0	–	18	3
MS 0302.5+1717	28	0	–	24	4
MS 0302.7+1658	34	0	–	24	10
CL 1037.9−1243a	47	0	–	26	21
MS 1621.5+2640	104	0	–	66	38
MACS J1206.2−0847	599	2	–	369	228
CL 1138.2−1133a	14	0	–	7	7

CL 1059.2−1253	42	1	–	22	19
3C 295	25	0	–	12	13
CL 1018.8−1211	34	0	–	19	15
CL 1138.2−1133	49	0	–	20	29
CL 1301.7−1139	37	0	–	20	17
RX J1117.4+0743	37	0	–	19	18
CL 1420.3−1236	27	0	–	19	8
CL 1411.1−1148	25	0	–	14	11
CL 1601+42	55	5	–	41	9
MS 0451.6−0305	44	0	–	28	16
CL 1232.5−1250	54	0	–	26	28
MS 0015.9+1609	50	0	–	39	11
CL 1119.3−1129	20	0	–	16	4
CL 0054−27	12	5	–	4	3
CL 1037.9−1243	19	0	–	6	13
CL 1353.0−1137	21	0	–	8	13
CL 1354.2−1230a	17	0	–	7	10
CL 1103.7−1245a	15	0	–	7	8
CL 1054.4−1146	49	0	–	28	21
CL 1103.7−1245b	15	1	–	3	11
CL 1040.7−1155	30	0	–	12	18
CL 1054.7−1245	36	1	–	23	12
CL 1324+3011	44	0	–	25	19
CL 1354.2−1230	23	1	–	11	11
CL 1216.8−1201	66	0	–	35	31
RX J1716+67	31	–	0	18	13
MS 1054−03	143	1	–	96	46
RX J0152.7−1357	125	19	–	91	15
CL 0023+0423	16	–	0	6	10
RX J1226.9+3332	50	0	–	43	7
CL 1604+4304	16	1	–	10	5
CL 1604+4321	37	0	–	11	26
CL 1103.7−1245	22	0	–	8	14
XMMU J1230.3+1339	13	0	–	8	5
AX J2016+1127	6	0	–	3	3
RDCS J0910+54	23	0	–	16	7
RDCS J1252.9−2927	38	–	0	21	17
RX J0848.9+4452	6	0	–	3	3
RX J0848.6+4453	9	1	–	5	3
XMMU J2235.3−2557	30	–	1	19	10
XMMXCS J2215.9−1738	41	–	0	13	28

Chapter 11

Velocity dispersions of cluster galaxy populations

I calculate velocity dispersions of red/passive galaxies and blue/star-forming members separately, using the robust estimator (ROSTAT routines; see Beers et al., 1990). In this way it is possible to investigate the kinematics of the cluster blue population with respect to the red component.
In Table 11.1 for all 52 clusters I write the galaxy number and the respective velocity dispersion for the red/passive members (N_{red}, σ_{red}) and for the blue/star-forming galaxies (N_{blue}, σ_{blue}). Values of velocity dispersions are characterized by bootstrap errors at 68% c.l., but I also list their jackknife errors ($\delta\sigma_{red}$, $\delta\sigma_{blue}$).

Table 11.1: Robust velocity dispersions for red/passive and blue/star-forming cluster galaxy populations

Cluster name	N_{red}	σ_{red} (km s^{-1})	$\delta\sigma_{red}$ (km s^{-1})	N_{blue}	σ_{blue} (km s^{-1})	$\delta\sigma_{blue}$ (km s^{-1})
CL 0024+16	49	1042^{+115}_{-110}	114	29	889^{+108}_{-116}	118
CL 1301.7−1139a	12	331^{+89}_{-52}	83	5	586^{+176}_{-193}	233
CL 0939+47	34	1212^{+147}_{-117}	139	14	996^{+207}_{-156}	192
CL 0303+17	21	690^{+309}_{-320}	618	16	284^{+132}_{-150}	271
CL 1202.7−1224*	18	351^{+85}_{-62}	74	3	.....	...
MS 0302.5+1717	24	638^{+63}_{-82}	90	4	900^{+482}_{-420}	773
MS 0302.7+1658	24	669^{+166}_{-113}	150	10	906^{+623}_{-282}	346
CL 1037.9−1243a	26	555^{+133}_{-63}	90	21	560^{+76}_{-54}	71
MS 1621.5+2640	66	734^{+78}_{-61}	71	38	781^{+71}_{-54}	69
MACS J1206.2−0847	369	1061^{+38}_{-48}	43	228	1176^{+49}_{-55}	48
CL 1138.2−1133a	7	418^{+131}_{-50}	134	7	486^{+657}_{-57}	208
CL 1059.2−1253	22	401^{+71}_{-54}	70	19	613^{+81}_{-75}	86
3C 295	12	1354^{+168}_{-228}	141	13	1686^{+310}_{-190}	236
CL 1018.8−1211	19	449^{+85}_{-54}	71	15	493^{+180}_{-85}	119
CL 1138.2−1133	20	484^{+123}_{-79}	104	29	867^{+133}_{-40}	97
CL 1301.7−1139	20	543^{+187}_{-81}	127	17	778^{+143}_{-65}	106
RX J1117.4+0743	19	1066^{+441}_{-227}	433	18	1654^{+248}_{-156}	218
CL 1420.3−1236	19	249^{+80}_{-55}	73	8	439^{+463}_{-65}	183
CL 1411.1−1148	14	665^{+112}_{-73}	106	11	741^{+264}_{-135}	214
CL 1601+42	41	727^{+108}_{-97}	112	9	764^{+169}_{-107}	175

MS 0451.6−0305	28	1269^{+124}_{-102}	128	16	1115^{+161}_{-169}	189
CL 1232.5−1250	26	1025^{+235}_{-91}	156	28	1062^{+147}_{-129}	143
MS 0015.9+1609	39	994^{+138}_{-87}	114	11	809^{+538}_{-140}	307
CL 1119.3−1129	16	181^{+62}_{-43}	64	4	209^{+91}_{-135}	206
CL 0054−27*	4	1061^{+135}_{-54}	134	3	.....	...
CL 1037.9−1243	6	347^{+113}_{-72}	141	13	594^{+231}_{-274}	170
CL 1353.0−1137	8	277^{+62}_{-19}	60	13	810^{+182}_{-96}	148
CL 1354.2−1230a	7	627^{+502}_{-246}	221	10	501^{+277}_{-111}	167
CL 1103.7−1245a	7	341^{+163}_{-97}	124	8	317^{+71}_{-35}	40
CL 1054.4−1146	28	447^{+114}_{-75}	108	21	715^{+112}_{-67}	97
CL 1103.7−1245b*	3	.....	...	11	757^{+224}_{-107}	103
CL 1040.7−1155	12	383^{+89}_{-45}	79	18	450^{+82}_{-59}	90
CL 1054.7−1245	23	545^{+130}_{-76}	105	12	469^{+330}_{-68}	161
CL 1324+3011	25	723^{+128}_{-102}	125	19	1028^{+248}_{-203}	264
CL 1354.2−1230	11	455^{+91}_{-63}	75	11	575^{+236}_{-176}	200
CL 1216.8−1201	35	976^{+122}_{-78}	99	31	959^{+117}_{-71}	105
RX J1716+67	18	1288^{+237}_{-166}	236	13	1261^{+162}_{-454}	266
MS 1054−03	96	1050^{+76}_{-74}	78	46	1268^{+203}_{-148}	184
RX J0152.7−1357	91	1270^{+85}_{-68}	86	15	1750^{+396}_{-289}	294
CL 0023+0423	6	483^{+166}_{-204}	237	10	174^{+58}_{-58}	63
RX J1226.9+3332	43	926^{+127}_{-101}	124	7	1199^{+698}_{-258}	490
CL 1604+4304	10	500^{+110}_{-125}	162	5	1158^{+339}_{-84}	536
CL 1604+4321	11	591^{+188}_{-162}	294	26	722^{+289}_{-144}	220
CL 1103.7−1245	8	653^{+219}_{-151}	247	14	353^{+99}_{-125}	164
XMMU J1230.3+1339	8	768^{+192}_{-71}	142	5	605^{+279}_{-60}	322
AX J2016+1127*	3	.....	...	3	.....	...
RDCS J0910+54	16	721^{+153}_{-131}	150	7	819^{+356}_{-87}	208
RDCS J1252.9−2927	21	787^{+110}_{-108}	107	17	752^{+145}_{-87}	120
RX J0848.9+4452*	3	.....	...	3	.....	...
RX J0848.6+4453 *	5	724^{+201}_{-192}	360	3	.....	...
XMMU J2235.3−2557	19	786^{+179}_{-136}	171	10	698^{+148}_{-98}	158
XMMXCS J2215.9−1738	13	676^{+177}_{-227}	217	28	762^{+141}_{-103}	150

NOTE.− * Clusters with small values of N_{red} or N_{blue} (i.e., ≤ 3) and which are excluded from later analyses.

The following 6 clusters CL 1202.7−1224, CL 0054−27, CL 1103.7−1245b, AX J2016+1127, RX J0848.9+4452 and RX J0848.6+4453 are characterized by very few red or blue galaxies (i.e., N_{red} or $N_{blue} \leq 3$) and for these populations it is not possible to estimate the velocity dispersion. I will exclude these clusters in the comparison of velocity dispersion values and profiles of the blue/star-forming population with respect to that of red/passive. Thus, in the following Chapter 12, I will consider the remaining 46 galaxy clusters.

Chapter 12

Kinematics comparison between cluster galaxy populations

12.1 Results for all the 46 clusters: σ_{blue} vs σ_{red} distributions

I investigate the kinematics of the blue population with respect to the red one, comparing their distributions of velocity dispersion. For this purpose I apply a series of statistical tests (see the Appendix D for their descriptions) to the sample formed by the 46 clusters for which each galaxy population contains more than 3 galaxies. For all the tests, a probability value $\geq 95\%$ represents a significant difference.
I collect the velocity dispersion estimates of the blue populations in one distribution and that of red populations in a second distribution. These distributions obtained collecting cluster data are shown in the two different histograms 12.1 and 12.2:

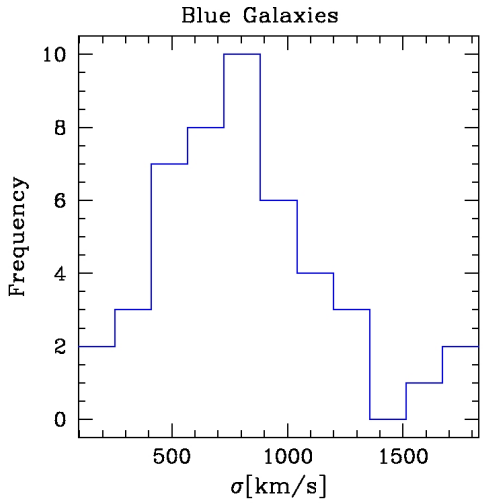

Figure 12.1: Velocity dispersion histogram for star-forming member galaxies.

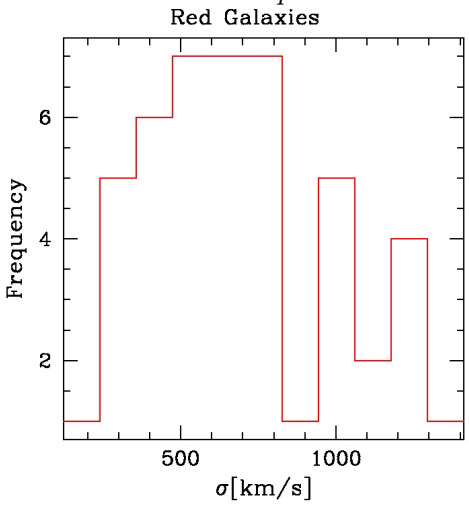

Figure 12.2: Velocity dispersion histogram for passive member galaxies.

1. **Kolmogorov−Smirnov test:** the probability that the two velocity dispersion distributions are different is only 80.08% according to the KS test. Thus, it is acceptable that σ_{blue} and σ_{red} values are part of the same parent population.
   From the visual inspection of figure 12.3, I obtain that the formal difference between the cumulative distributions of σ_{blue} and σ_{red} estimates is $\delta\sigma = 95\,\mathrm{kms}^{-1}$ at fraction=0.5, in the sense that blue galaxy populations are characterized by a higher σ_v than the red galaxy populations. Dividing $\delta\sigma$ by the median of all the velocity dispersions, which is 721.50 kms^{-1}, I find that **the velocity dispersion of blue/star-forming galaxies is, on average, about 13% larger than that of red/passive galaxies.**

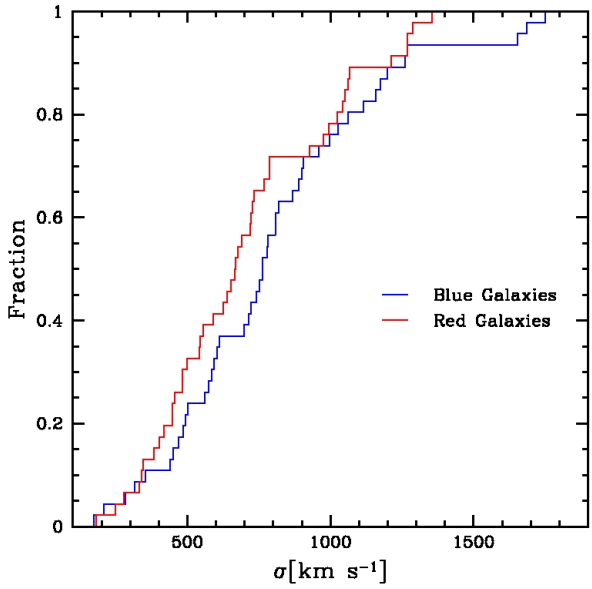

Figure 12.3: Cumulative distributions of velocity dispersion: σ_{blue} vs σ_{red}.

2. **Sign test:** there are 31/46 clusters with $\sigma_{blue} > \sigma_{red}$. **The two distributions are different at 98.70% confidence level.**

3. **Wilcoxon test:** the probability forthe velocity dispersion distribution of star-forming members to be higher than that of passive galaxies is **99.55%** according to this test.

12.2 Results for all the 46 clusters: σ_{blue} vs σ_{red} values

I apply the F-test in order to compare the individual σ_{blue} estimates with the σ_{red} ones for the same cluster considering also the uncertainties on the velocity dispersions.

- **F-test:** I compare the velocity dispersion values of different cluster galaxy populations for each individual cluster. I list in Table 12.1 only the significant probabilities, i.e. those larger than 0.95, (all the values are reported in Table E.3 in Appendix E).

Table 12.1: Significant results of F-test for velocity dispersions related to different galaxy populations

Cluster name	$P(\sigma_{blue}$ vs $\sigma_{red})$
CL 0024+16	–
CL 1301.7−1139a	–
CL 0939+47	–
CL 0303+17	0.9990
MS 0302.5+1717	–
MS 0302.7+1658	–
CL 1037.9−1243a	–
MS 1621.5+2640	–
MACS J1206.2−0847	–
CL 1138.2−1133a	–
CL 1059.2−1253	–
3C 295	–
CL 1018.8−1211	–
CL 1138.2−1133	0.9895
CL 1301.7−1139	–
RX J1117.4+0743	–
CL 1420.3−1236	0.9505
CL 1411.1−1148	–
CL 1601+42	–
MS 0451.6−0305	–
CL 1232.5−1250	–
MS 0015.9+1609	–
CL 1119.3−1129	–
CL 1037.9−1243	–
CL 1353.0−1137	0.9913
CL 1354.2−1230a	–
CL 1103.7−1245a	–
CL 1054.4−1146	0.9762
CL 1040.7−1155	–
CL 1054.7−1245	–

CL 1324+3011	–
CL 1354.2−1230	–
CL 1216.8−1201	–
RX J1716+67	–
MS 1054−03	–
RX J0152.7−1357	–
CL 0023+0423	0.9910
RX J1226.9+3332	–
CL 1604+4304	0.9654
CL 1604+4321	–
CL 1103.7−1245	–
XMMU J1230.3+1339	–
RDCS J0910+54	–
RDCS J1252.9−2927	–
XMMU J2235.3−2557	–
XMMXCS J2215.9−1738	–

I obtain that the σ_{blue} value differs significantly from the σ_{red} one for 7 clusters.
Figure 12.4 shows the comparison σ_{blue} vs σ_{red}: the values are plotted with their jackknife errors and the bisector line is drown as a reference. Most of the velocity dispersions of star-forming cluster members are larger than the respective estimates for the passive populations.

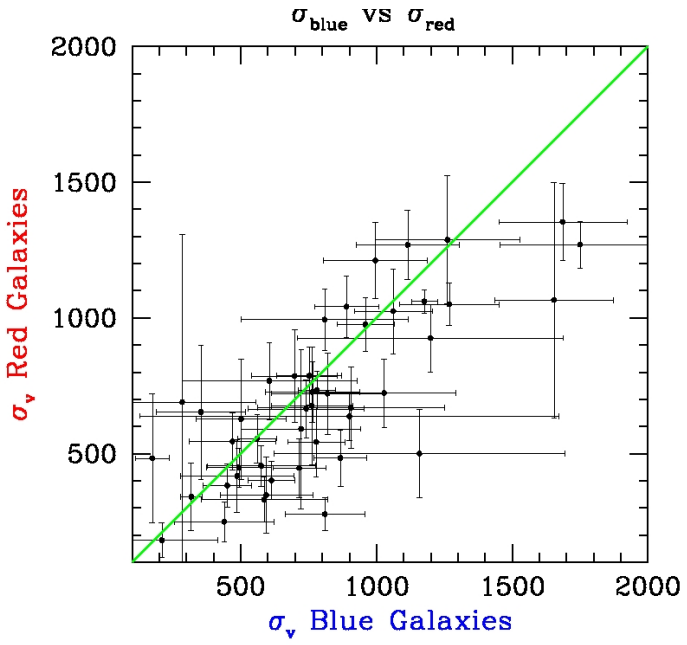

Figure 12.4: σ_{blue} vs σ_{red}: most of the σ_{blue} values are larger than the respective σ_{red} estimates.

12.3 Statistical results for the 30 well sampled clusters

I select only clusters for which both blue and red galaxy populations have at least 10 members (see Table 11.1). These 30 clusters form the high-statistics sample since their values of velocity dispersions are more reliable. The results of the statistical tests are reported below and confirm those obtained by the analysis for all the 46 clusters.

1. **Kolmogorov−Smirnov test:** the probability for the two velocity dispersion distributions to be different is $\sim 66\%$ and thus, the two distributions belong to the same population.
   As shown in figure 12.5, when the fraction value is 0.5, the two distributions have a difference in velocity dispersion of 75 kms^{-1}. Dividing this estimate for the median of all the velocity dispersions, which is 779.50 kms^{-1}, I obtain that the velocity dispersion of star-forming galaxies is, on average, about 10% larger than that of passive galaxies.

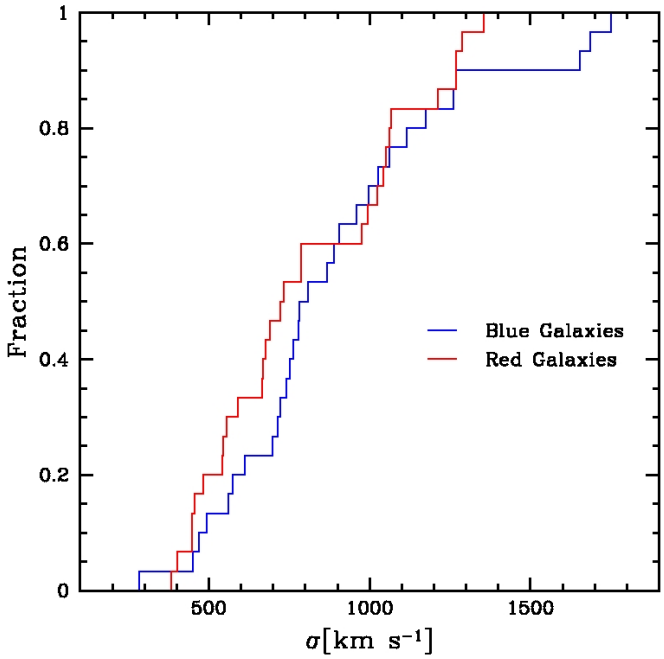

Figure 12.5: Cumulative distributions of velocity dispersion: σ_{blue} vs σ_{red} for the high-statistic cluster sample.

2. **Sign test:** in this case $\sigma_{blue} > \sigma_{red}$ for 20/30 clusters. The two distributions are different at the 95.06% confidence level.

3. **Wilcoxon test:** the probability for the velocity dispersion distribution of star-forming members to be higher than that of passive galaxies is 98.38%.

4. **F-test:** from Table 12.1 there are 3/30 clusters with $P(\sigma_{blue}$ vs $\sigma_{red}) > 0.95$.

12.4 Statistical results for the 32 intermediate-z clusters

In order to investigate about a possible evolution of the relative velocity dispersions of red and blue galaxies, I apply the statistical tests only to the 32 intermediate-z clusters in the range $0.39 \leq z < 0.79$ listed in the Table 12.2 below:

Table 12.2: Intermediate-redshift clusters

Cluster name	$< z >$
CL 0024+16	0.3937
CL 1301.7−1139a	0.3969
CL 0939+47	0.4060
CL 0303+17	0.4190
MS 0302.5+1717	0.4242
MS 0302.7+1658	0.4248
CL 1037.9−1243a	0.4255
MS 1621.5+2640	0.4267
MACS J1206.2−0847	0.4399
CL 1138.2−1133a	0.4546
CL 1059.2−1253	0.4564
3C 295	0.4593
CL 1018.8−1211	0.4736
CL 1138.2−1133	0.4797
CL 1301.7−1139	0.4832
RX J1117.4+0743	0.4857
CL 1420.3−1236	0.4961
CL 1411.1−1148	0.5196
CL 1601+42	0.5400
MS 0451.6−0305	0.5401
CL 1232.5−1250	0.5418
MS 0015.9+1609	0.5492
CL 1119.3−1129	0.5499
CL 1037.9−1243	0.5784
CL 1353.0−1137	0.5878
CL 1354.2−1230a	0.5958
CL 1103.7−1245a	0.6261
CL 1054.4−1146	0.6976
CL 1040.7−1155	0.7044
CL 1054.7−1245	0.7500
CL 1324+3011	0.7547
CL 1354.2−1230	0.7612

The following statistical results indicate that blue and red galaxies are segregated in velocity with $\sigma_{blue} > \sigma_{red}$:

1. **Kolmogorov−Smirnov test:** the probability that the two velocity dispersion distributions are not part of the same population is 86.85%. The difference is not significant and figure 12.6 illustrates the cumulative distribution functions for the intermediate-z cluster galaxy populations.

For fraction=0.5, the difference in velocity dispersion between the two profiles is 137 kms^{-1}. Dividing this estimate for the median of all the velocity dispersions, which is 651.50 kms^{-1}, I find that the velocity dispersion of blue members in medium-z clusters is, on average, about 21% higher than that of red ones.

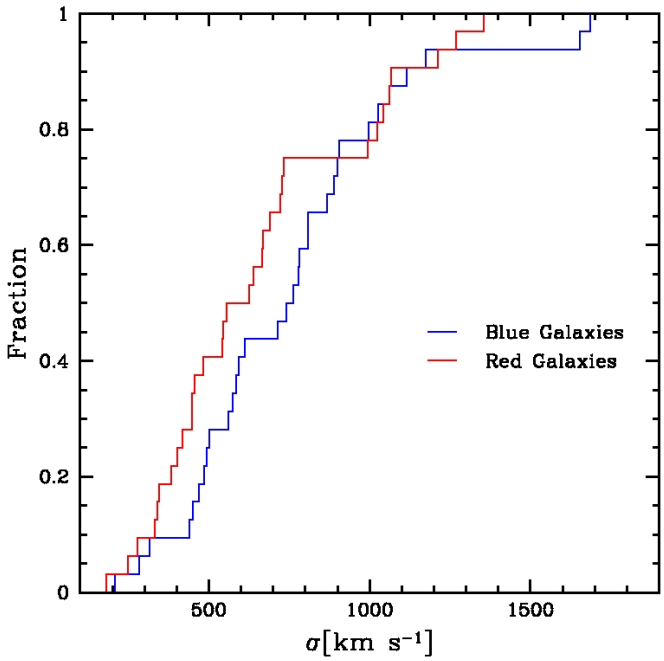

Figure 12.6: Cumulative distributions of velocity dispersion: σ_{blue} vs σ_{red} for the intermediate-z clusters.

2. **Sign test:** I obtain $\sigma_{blue} > \sigma_{red}$ for 24/32 clusters: the two distributions are different at the **99.65%** confidence level.

3. **Wilcoxon test:** the probability for the velocity dispersion distribution of blue members to be larger than that of red populations is **99.62%** in intermediate-z clusters.

4. **F-test:** from Table 12.1 the different values of velocity dispersion are significant for 5/32 medium-z clusters.

12.5 Statistical results for the 14 high-redshift clusters

I consider only the 14 clusters with high-redshift in the range $0.79 \leq z \leq 1.46$ listed in the following Table 12.3:

Table 12.3: High-redshift clusters

Cluster name	$< z >$
CL 1216.8−1201	0.7939
RX J1716+67	0.8065
MS 1054−03	0.8306
RX J0152.7−1357	0.8359

CL 0023+0423	0.8453
RX J1226.9+3332	0.8910
CL 1604+4304	0.8978
CL 1604+4321	0.9219
CL 1103.7−1245	0.9578
XMMU J1230.3+1339	0.9737
RDCS J0910+54	1.0998
RDCS J1252.9−2927	1.2370
XMMU J2235.3−2557	1.3905
XMMXCS J2215.9−1738	1.4589

The results indicate that, at variance with what I found in the lower-z sample of clusters, **there is not significant difference between the kinematics of star-forming and passive populations for distant clusters**.

1. **Kolmogorov−Smirnov test:** the probability that the two velocity dispersion distributions don't belong to the same population is 13.08% according to the KS test. Thus, there isn't a relevant difference and I plot the cumulative distribution functions for high-z cluster galaxy populations in figure 12.7.
   When the fraction value is 0.5, the difference in velocity dispersion between the two profiles is 33 kms^{-1}. Dividing this estimate for the median of all the velocity dispersions, which is 777 kms^{-1}, I obtain that the velocity dispersion of star-forming galaxies within distant clusters is, on average, about 4% larger than that of passive members.

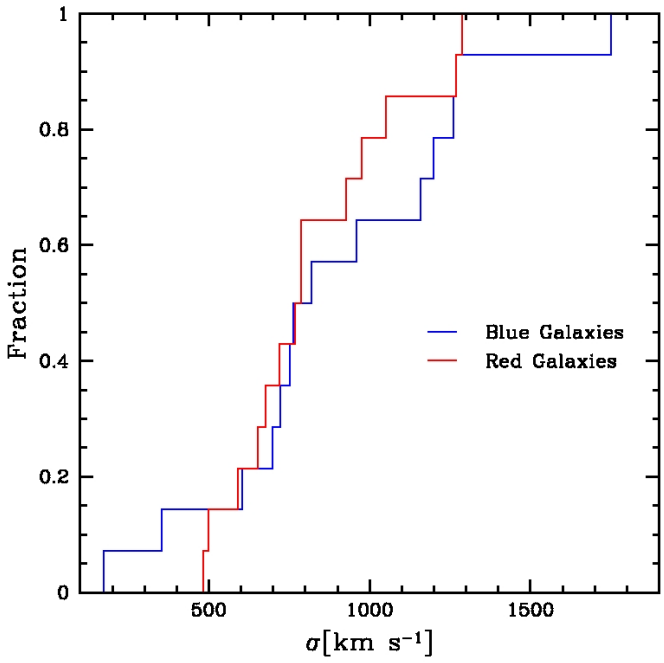

Figure 12.7: Cumulative distributions of velocity dispersion: σ_{blue} vs σ_{red} for the high-z clusters.

2. **Sign test:** I find $\sigma_{blue} > \sigma_{red}$ for 7/14 couples: the two distributions are not significantly different (50% c.l.).

3. **Wilcoxon test:** the probability for the velocity dispersion profile of star-forming galaxies to be higher than that of passive populations is 74.92% for distant clusters.

4. **F-test:** from Table 12.1 I obtain that the velocity dispersion values of the two galaxy populations differ significantly for 2/14 high-z clusters.

12.6 Velocity segregation vs cluster properties

In order to check if the kinematical differences are related to σ_v, which is connected to the cluster mass, I analyze the ratio $\sigma_{blue}/\sigma_{red}$ as function of σ_v in figure 12.8. The green line marks the unit value. Most points are located above this line indicating the velocity dispersion of the star-forming galaxies is higher than that of passive ones.
I calculate the following correlation coefficients which are described in Appendix G:

- corr. coeff. of Spearman: -0.1021 (75.01%)
- corr. coeff. of Kendall: -0.0763 (77.28%)

The probability values indicate that there is not significant correlation between $\sigma_{blue}/\sigma_{red}$ and σ_v.

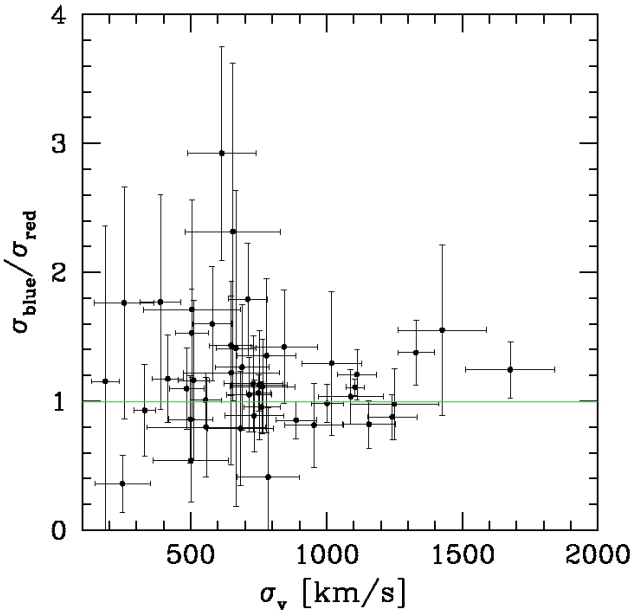

Figure 12.8: $\sigma_{blue}/\sigma_{red}$ vs σ_v: the uncertainties on σ_v are jackknife errors and those on $\sigma_{blue}/\sigma_{red}$ are obtained with the error propagation formula for repeated measurements. The green line signs when the velocity dispersions of blue and red populations are equal. Most of the $\sigma_{blue}/\sigma_{red}$ values are larger than 1. Moreover, there isn't a significant correlation between $\sigma_{blue}/\sigma_{red}$ and σ_v.

I also investigate a possible correlation between the ratio $\sigma_{blue}/\sigma_{red}$ and the cluster redshift. Figure 12.9 displays only the uncertainties on $\sigma_{blue}/\sigma_{red}$, since in comparison the errors on redshifts are negligible.
For the correlation coefficients I obtain the following values:

- corr. coeff. of Spearman: -0.1216 (78.95%)
- corr. coeff. of Kendall: -0.0841 (79.49%)

The coefficients are near to zero and confirm that the variables $\sigma_{blue}/\sigma_{red}$ and $z_{cluster}$ are independent. However, in this case the absolute values of the correlation coefficients are higher than in the previous comparison.

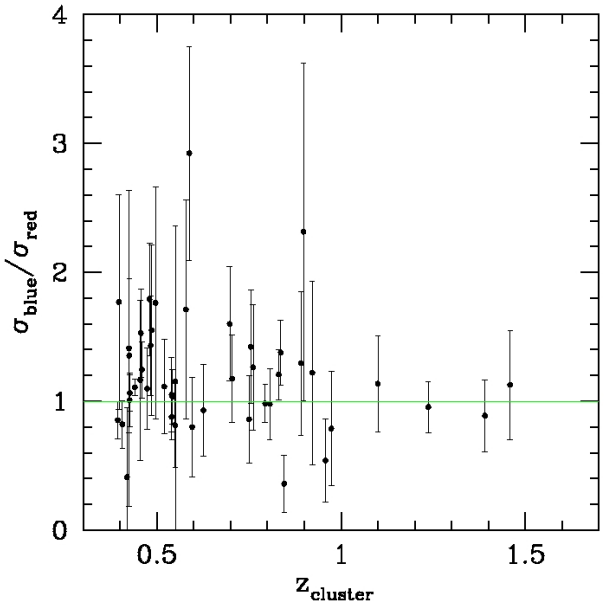

Figure 12.9: $\sigma_{blue}/\sigma_{red}$ vs $z_{cluster}$: the green line signs when the velocity dispersions of blue and red populations are equal. Many points are located upper this line and for all of them $\sigma_{blue} > \sigma_{red}$. There isn't a significant correlation between $\sigma_{blue}/\sigma_{red}$ and $z_{cluster}$.

12.7 Stacking clusters and the projected phase space

In order to understand better the connection between position and velocity of cluster galaxy populations I draw the projected phase space diagrams in normalized units: v_{rf}/σ_v vs R/R_{200} and $|v_{rf}|/\sigma_v$ vs R/R_{200}. The line-of-sight velocity, v_{rf}, in the cluster rest frame is:

$$v_{rf} = \frac{v - cz_{cluster}}{(1 + z_{cluster})} \tag{12.1}$$

for which $z_{cluster}$ is the cluster redshift and $(1+z_{cluster})$ is the cosmological correction. Moreover, R_{200} is the radius of a sphere enclosing a mean density which is 200 times the critical cosmic density at redshift z.

12 Kinematics comparison between cluster galaxy populations

Most members are located within $2R_{200}$ (see Table 8.1 in Chapter 8 for the R_{max} values) and the points which are isolated with respect to the main cluster body are possible interlopers, i.e foreground or background galaxies, unidentified by the P+G procedure of cluster membership. Figure 12.10 shows the projected phase space within $5R_{200}$ and with the caustic curves indicating the escape velocity of the cluster galaxies (den Hartog and Katgert, 1996). These two outer curved lines (symmetric with respect to the mean velocity represented by the horizontal line) sign the minimum and the maximum of the allowed line-of-sight velocities for cluster members, determining the border between the bound and not bound galaxies, i.e. the cluster members and interlopers. For drawing the caustics, I assume a typical cluster mass distribution described by a density profile of Navarro, Frenk and White with the concentration parameter c=3.4, which is typical at $z \sim 0.6$ out to $2R_{200}$ (Dolag et al., 2004).

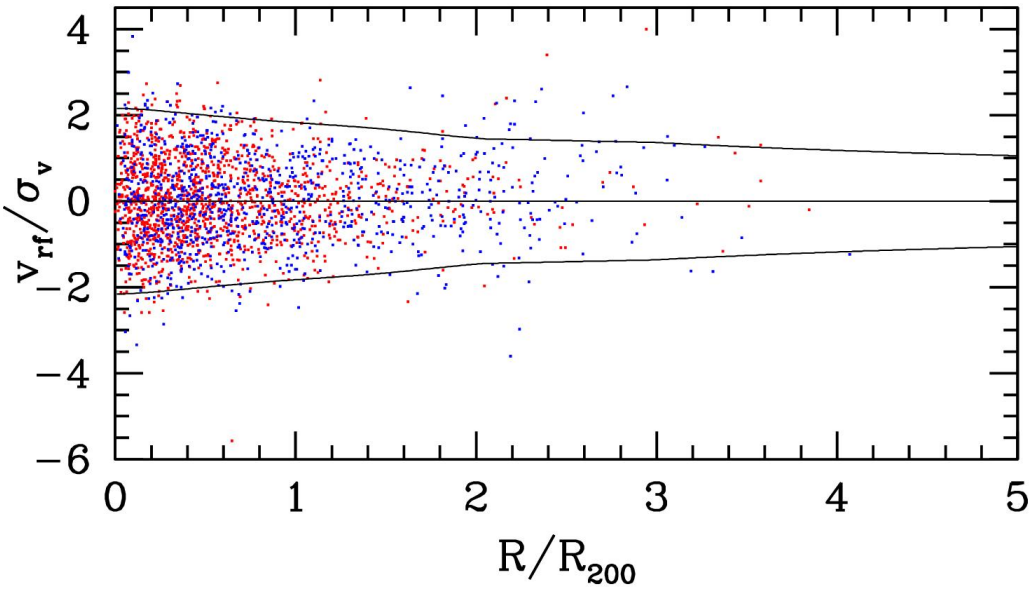

Figure 12.10: Caustic curves: they indicate the border between the cluster members and the interloper galaxies in the projected phase space. The purpose of this plot is to show that the cluster member selection procedure works well. However, determining a precise mass density profile is out of the aims of this thesis.

I represent the projected phase space diagrams in normalized units in figure 12.11.
The *top panel* shows the distributions of star-forming (blue points) and passive (red points) galaxies for all the 46 clusters. The units are normalized in both position and velocity axes to take into account the fact that I am combining clusters of different masses: the rest-frame velocity is divided by the velocity dispersion whereas the clustercentric distance is normalized by R_{200}. The horizontal line marks the zero point for the galaxy velocities, that is the mean cluster velocity in the rest frame. The plot displays a clear spatial separation between early- and late-type members: the passive populations dominate the inner regions of the clusters while the star-forming ones are more common towards the outskirts.
The *bottom panel* illustrates the absolute value of the rest-frame velocity as a function of the projected clustercentric distance in normalized units. This panel shows that the estimates of blue galaxies are higher than that for red galaxies and that the velocity dispersions of both populations decrease from the cluster center to $2R_{200}$. For larger values of the projected clustercentric distance, the velocity dispersions start to rise possibly because of the presence of possible background and foreground galaxies.

In order to eliminate a possible statistic effect I also draw the projected phase space diagrams without the most sampled cluster MACS 1206.2−0847 in figure 12.12. This plot displays the same results of figure 12.11, indicating that the well sampled and rich cluster MACS 1206.2−0847 does not dominate the statistics.

Figure 12.13 is a zoom of the projected phase space diagrams from 0 to $2R_{200}$ in order to focus the attention on the interesting cluster regions. **Applying the χ^2 test to the $|v_{rf}|/\sigma_v$ vs R/R_{200} data within $2R_{200}$ I find χ^2=23.37 and the probability that the two distributions are described by the same curve is 0.001%.**

Finally, all the *bottom panels* are binned in radius and the band uncertainties are bootstrap errors at 68% confidence level.

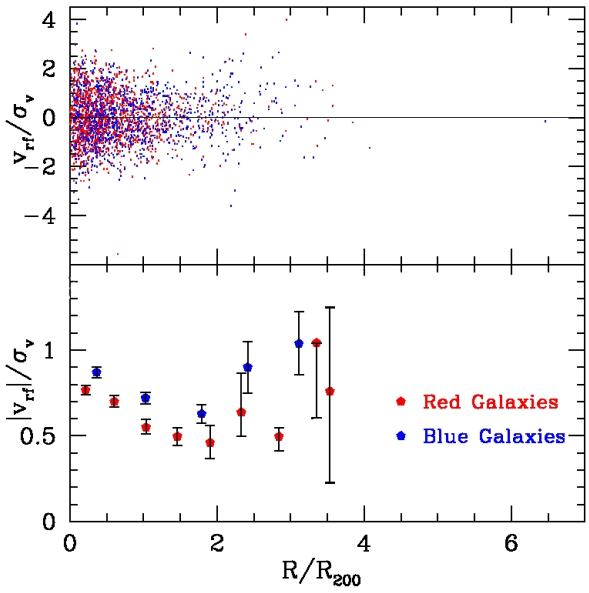

Figure 12.11: Projected phase space diagrams in normalized units. *Top panel*: the rest-frame velocity vs projected clustercentric distance shows the spatial segregation between early- and late-type members. *Bottom panel*: the absolute value of the rest-frame velocity vs projected clustercentric distance highlights that the blue galaxies have a σ_v larger than the red ones. Moreover, it shows the presence of possible interlopers for $R > 2R_{200}$, which would explain the unphysical increase of $|v_{rf}|/\sigma_v$ at large radii.

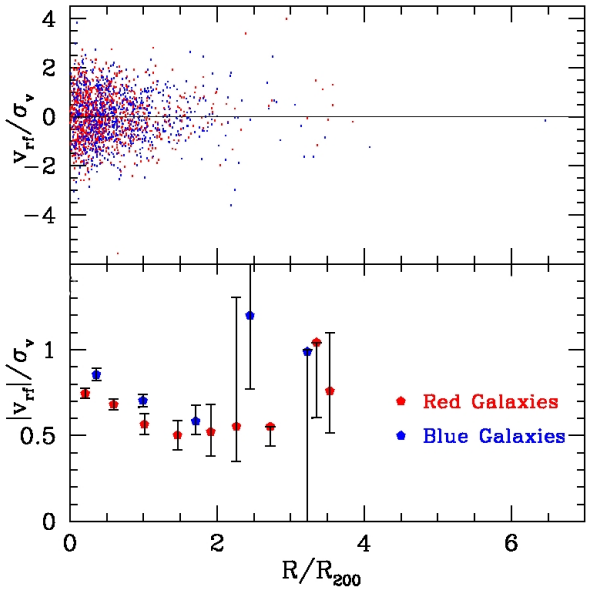

Figure 12.12: Projected phase space diagrams in normalized units without the most sampled cluster MACS 1206.2−0847: the results are the same of figure 12.11 and so they are not dominated by the well sampled and rich cluster MACS 1206.2−0847.

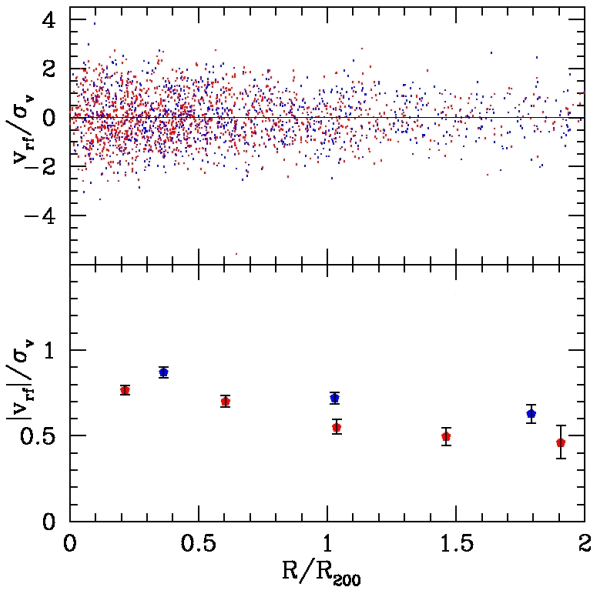

Figure 12.13: A zoom within $2R_{200}$ of figure 12.11 focused on the interesting cluster regions.

12.8 Intermediate- vs high-z clusters

In order to understand the differences and similarities between medium-z and distant clusters I plot the projected phase space diagrams within $4R_{200}$ for intermediate- and high-redshift clusters separately in figure 12.14 and 12.15, respectively. The redshift which divides clusters in these two categories is 0.8, which corresponds to the lower limit value above which the Euclid spectroscopic observations will be possible. The intermediate-z clusters are characterized by the redshift range $0.4 \leq z < 0.8$ and are 32 systems, whereas there are 14 high-z clusters with $0.8 \leq z \leq 1.5$.

For intermediate-z clusters there is a clear velocity segregation between passive and star-forming galaxies, while in distant clusters the two populations do not show a significant difference in velocity. Applying the χ^2 test to the $|v_{rf}|/\sigma_v$ vs R/R_{200} data within $2R_{200}$ I obtain χ^2=21.53 and 3.48, and the probability that the two distributions are fitted by the same curve is 0.008% and 17.542%, for the intermediate- and high-z clusters, respectively.

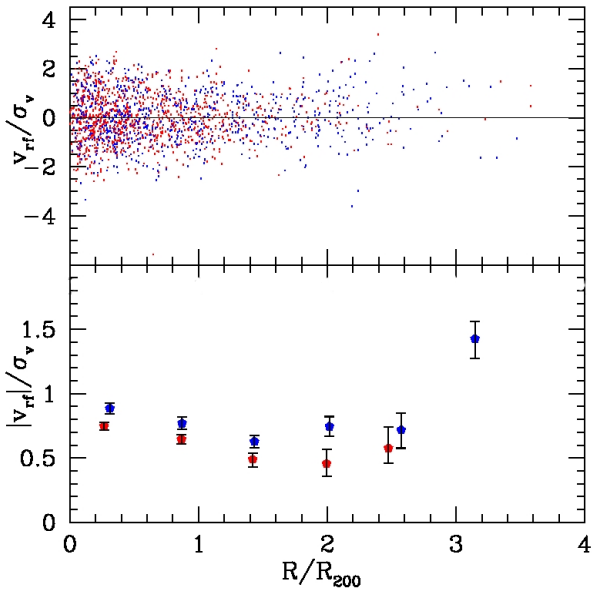

Figure 12.14: Projected phase space diagrams in normalized units for the 32 intermediate-z clusters ($0.4 \leq z < 0.8$). *Top panel*: the red members dominate the inner regions of the clusters while the blue ones are more common towards the outskirts. *Bottom panel*: the velocity dispersion profile of star-forming galaxies is higher than that of passive members.

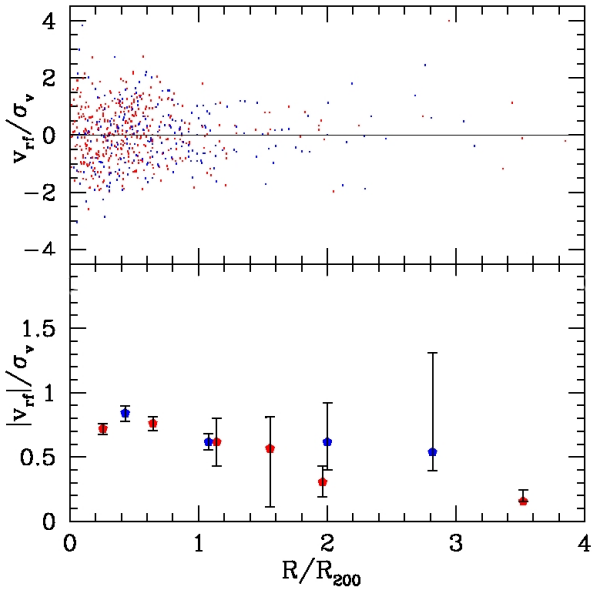

Figure 12.15: Projected phase space diagrams in normalized units for the 14 high-z clusters ($0.8 \leq z \leq 1.5$). *Top panel*: many star-forming galaxies are contained in the inner regions of the clusters. *Bottom panel*: there is no a clear velocity segregation between passive and star-forming galaxies.

12.9 Comparison of the kinematical results with previous studies

I compare the obtained kinematical results for the red and blue populations with previous studies focused on low- and intermediate-redshift clusters.
Studying the ESO Nearby Abell Cluster Survey (ENACS), Biviano et al. (1997) investigated 75 clusters with $< z > \leq 0.1$ and combining the data, they found that the emission-line galaxies (ELG) are characterized by a velocity dispersion which is, on average, 20% larger than that of the other galaxies. This result is qualitatively and quantitatively in agreement with the formal result of the KS test for the 32 intermediate-z clusters in the sample of my study, according to which the velocity dispersion of blue members is, on average, about 21% higher than that of red ones. Moreover, I consider the kinematics of the total cluster members with respect to that of the blue galaxies and I compare the cumulative distribution functions for the intermediate-z clusters with those obtained by Biviano et al. (1997) in the *bottom plot* and in the *top panel* of figure 12.16, respectively. Applying the Wilcoxon test I find that the probability for the velocity dispersion distribution of the total members to be higher than that of red galaxies is 99.93%, in agreement with the result obtained by Biviano et al. (1997), which indicates that the ELG+non-ELG σ_v distribution is different from that of the non-ELG at the $> 99.90\%$ c.l., and that σ_v of ELG+non-ELG is, on average, larger than σ_v of the non-ELG.
My results are also in agreement with the study of Carlberg et al. (1997), who analyzed the $< z > \sim 0.3$ Canadian Network for Observational Cosmology (CNOC) cluster sample, finding that the red galaxies have a smaller velocity dispersion.

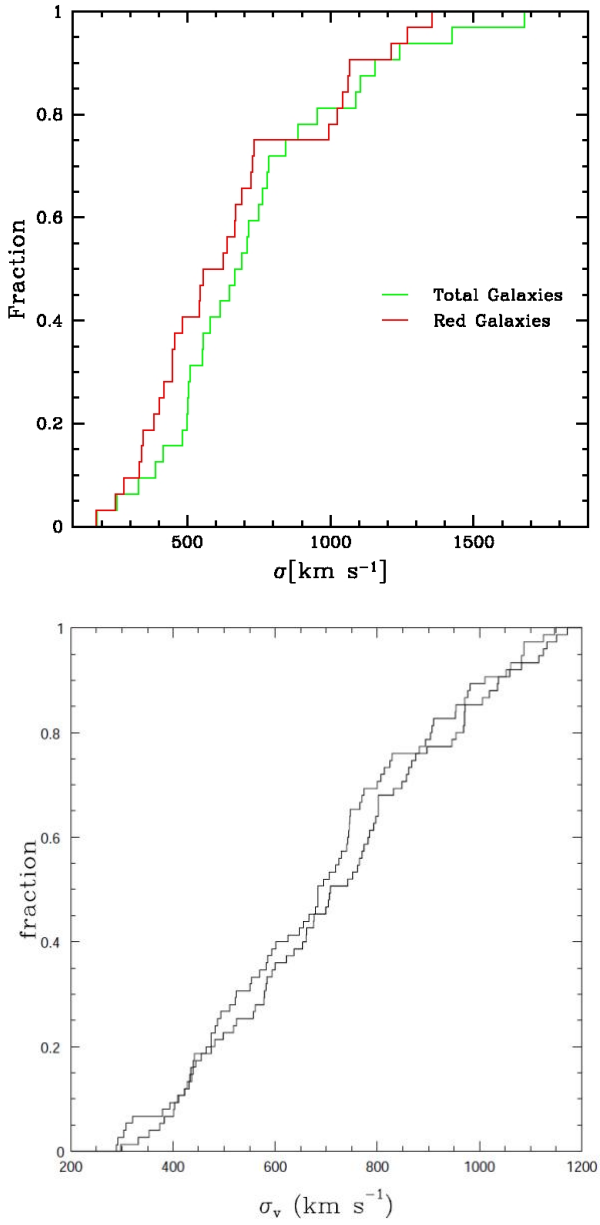

Figure 12.16: *Top panel*: the cumulative σ_v distributions for the red and total member galaxies in the 32 intermediate-z clusters analyzed in my study. *Bottom panel*: the cumulative distributions for the non-ELG only (thin line), and for all the galaxies (ELG+non-ELG, thick line) in the 75 ENACS clusters with at least 20 members (from Biviano et al., 1997).

I also compare my results about the velocity dispersion profiles with the literature. Figure 12.17 illustrates the comparison of the velocity dispersion profiles obtained by Carlberg et al. (1997) *(right panel)* and in this thesis *(left panel)*. I plot my data (without the most sampled cluster MACS 1206.2−0847) in the projected phase space and I fit the data of red and blue galaxies separately. The coefficients of the least-squares linear fits are the following:

- y=−0.20x+0.92 for blue galaxies;
- y=−0.14x+0.75 for red galaxies.

In both panels the velocity dispersion profile of blue galaxies is higher than that of red galaxies. Moreover, the line fitting the blue galaxies is steeper than that related to the red points, and this fact agrees with both the results of Carlberg et al. (1997) (see *right panel* of figure 12.17) and the findings of Biviano and Katgert (2004) for the ENACS sample.

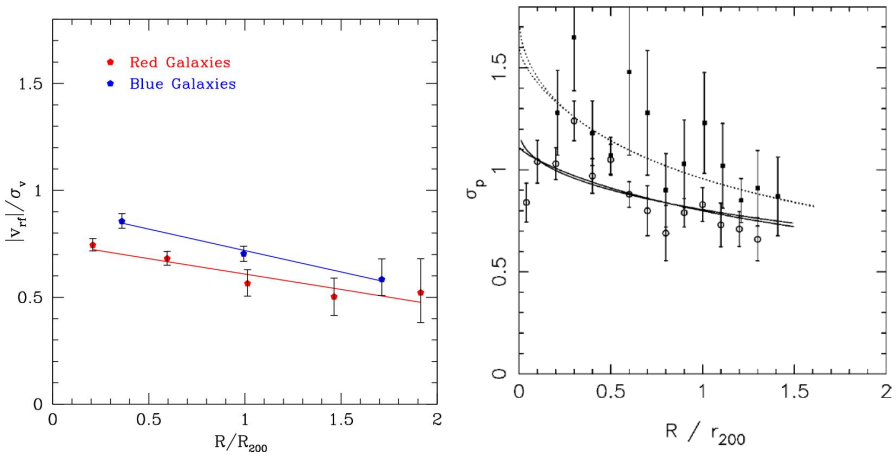

Figure 12.17: Velocity segregation of cluster galaxy populations: comparison between this study *(left panel)* and Carleberg et al. (1997) *(right panel)* results. The blue galaxies *(filled squares and blue points)* have a larger σ_v than the red ones *(open circles and red points)*.

In figure12.18 I consider my results without MACS 1206.2−0847 *(left panel)* compared to those related to the very well sampled cluster MACS 1206.2−0847 at $z = 0.44$ *(right panel)*, for which Girardi et al. (2015) found that values of σ_v computed for the emission-line galaxy population are higher than those of the passive population at comparable radii. Note that the enhancement of the $|v_{rf}|/\sigma_v$ profile at $R > R_{200}$ is likely due to the presence of some remaining interlopers (see previous section 12.7).

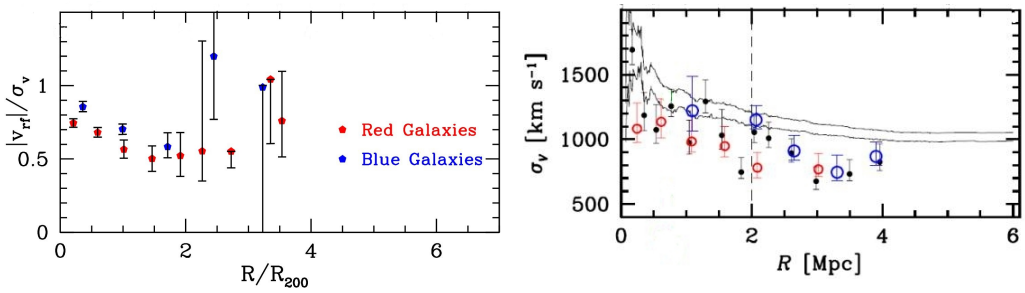

Figure 12.18: Velocity segregation for MACS 1206.2−0847 obtained by Girardi et al. (2015) *(right panel)* in comparison with the projected phase space in normalized units obtained in this thesis without MACS 1206.2−0847 *(left panel)*. Small black dots, small red circles, and blue circles show the different profiles for total, passive, and star-forming galaxies.

Finally, with regards to the high-z clusters, I do not find evidence of a significant segregation in velocity (see figure 12.15 in section 12.8). In fact, the blue and red populations are characterized by similar kinematics properties. Moreover, many star-forming galaxies populate the inner region of the clusters (see figure 12.15).
These outcomes agree with the pioneering study of Biviano and Poggianti (2009), who analyzed separately low-redshift clusters ($< z >\sim 0.07$) and intermediate-redshift clusters ($< z >\sim 0.6$). They found that the emission-line galaxies (ELGs) do not avoid the central cluster regions as in the low-z clusters. In addition, the segregation in the velocity space is not so strong. In fact, the σ_v-profiles of ELGs and not ELGs are not very different (see figure 2 of Biviano and Poggianti, 2009). However, the high-z cluster sample considered in this thesis is characterized by larger redshift values than that of Biviano and Poggianti (2009) and the absence of the velocity and space segregations is more evident. By contrast, the results for the galaxy populations in the intermediate-z cluster sample selected in this study show significant differences in space and velocity, in agreement with the results for low-z clusters.
In conclusion, these comparisons show that the kinematical segregation between red and blue galaxies that I detect at intermediate redshift agree with the results of the literature for nearby and $< z >\sim 0.3$ clusters. The differences in the velocity dispersion profiles of red/passive and blue/star-forming galaxies are explained by the different spatial galaxy distributions and galaxy orbits, both red and blue galaxies being in dynamical equilibrium with the cluster and having isotropic or somewhat more radial orbits (see Biviano and Katgert, 2004). However, the precise analysis of the galaxy orbits is out of the aims of this thesis and it will be the subject of a future study.

12.10 Luminosity segregation in velocity space and the dynamical friction effect

In order to investigate the evidence of luminosity segregation in velocity space, I analyze the $|v_{rf}|/\sigma_v$ vs $m - m_3$ plot in figure 12.19, where m is the apparent magnitude and m_3 is the magnitude of the third brightest cluster galaxy. The magnitude is a negative measurement of the galaxy luminosity, which is connected with the galaxy mass. Thus, lower magnitudes imply higher luminosities and larger galaxy masses.
Since the luminosity segregation is likely associated to secondary relaxation processes (e.g. dynamical friction; see section 3.2: *Environmental processes*), I consider only galaxies located within $1R_{200}$ from the cluster center. There are 40 clusters with at least 3 blue and red cluster members within R_{200}. I draw the blue and red points for the blue and red populations, respectively. Only very luminous ($m \leq m_3$) red galaxies, which are also very massive, show a marginal evidence of velocity segregation: the more luminous galaxies are slower than the less luminous ones. This is in agreement with a scenario where the gravitational force produces a frictional force which slows down the orbital motions of the most massive galaxies (Biviano et al., 1992; Adami et al., 1998; Goto et al., 2011).
For illustrating graphically the trend of the more bright red galaxies with respect to the less bright ones, I fit the velocity-magnitude relation separately for the members with $m \leq m_3$ and those with $m > m_3$. In particular, I obtain that the red galaxies with $m \leq m_3$ are fitted by a line with a positive slope, while those with $m > m_3$ are fitted by a constant line, indicating that these latter are not affected by the velocity segregation. The coefficients of the linear fits are the following:

- y=0.14x+0.77 for red galaxies with $m \leq m_3$;
- y=0.78 for red galaxies with $m > m_3$.

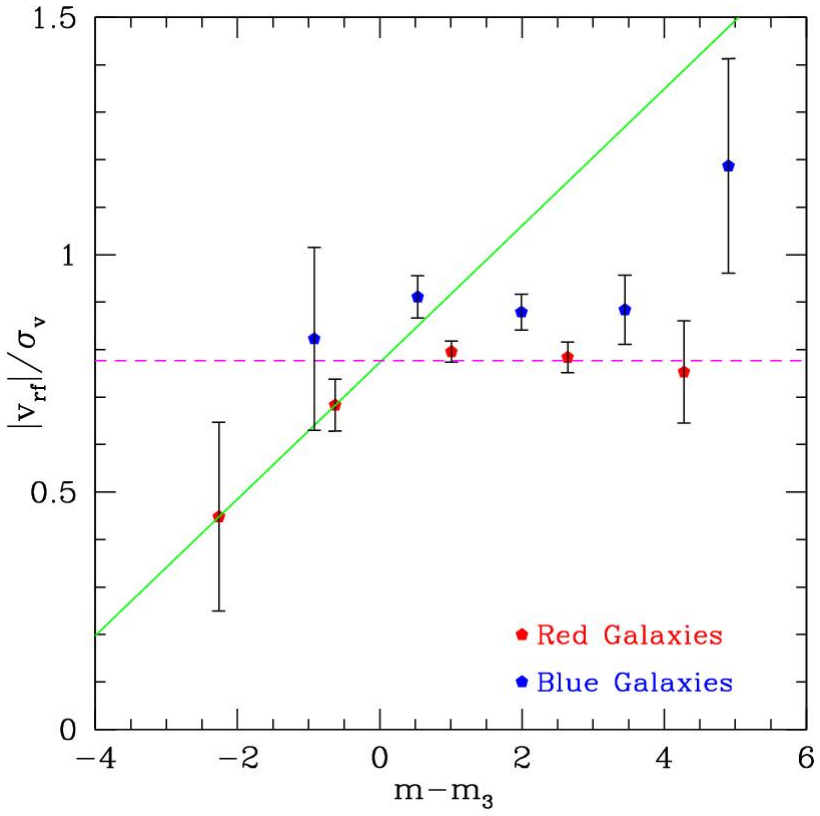

Figure 12.19: $|v_{rf}|/\sigma_v$ vs $m-m_3$ plot within $1R_{200}$ for galaxies of 40 clusters, where m_3 is the magnitude of the third brightest cluster galaxy. The red and blue members are shown separately and their error bars are the standard deviations of the arithmetic averages. The green line fits the less luminous and massive red galaxies with $m > m_3$, while the magenta dotted line fits the more luminous and massive ones with $m \leq m_3$, which are the segregated galaxies.

In order to analyze the effect of dynamical friction as a function of cluster redshift, I plot in figure 12.20 and 12.21 the results for red and blue galaxies in intermediate- and high-z clusters, respectively.
As for the red galaxies in intermediate-z clusters, only the most luminous ones with $m \leq m_3$ show a marginal evidence of segregation. Instead, the effect of dynamical friction is not present in high-z clusters.

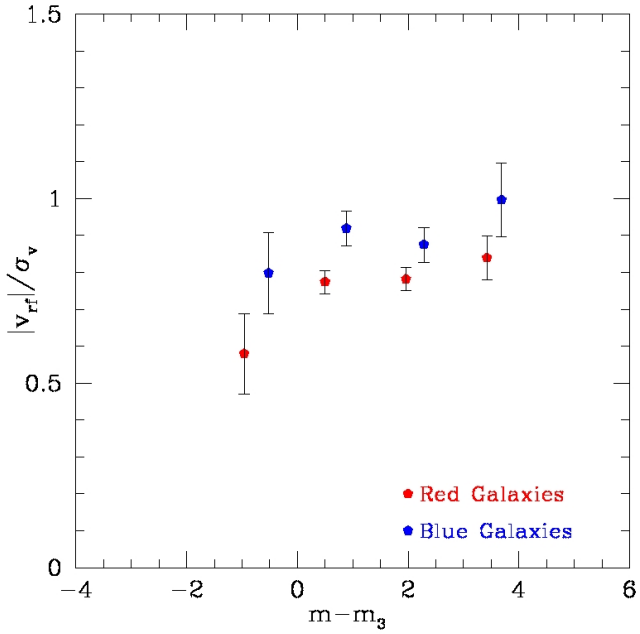

Figure 12.20: $|v_{rf}|/\sigma_v$ vs $m - m_3$ plot within $1R_{200}$ for the 28 intermediate-z clusters ($0.4 \leq z < 0.8$): the trend for the red component decreases for $m \leq m_3$ and the early-type galaxies with $m \leq m_3$ suffer the effect of dynamical friction.

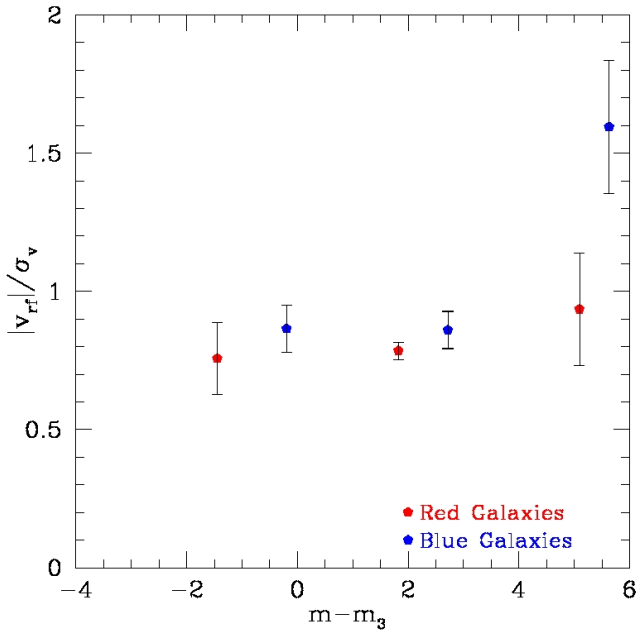

Figure 12.21: $|v_{rf}|/\sigma_v$ vs $m - m_3$ plot within $1R_{200}$ for the 12 high-z clusters ($0.8 \leq z \leq 1.5$): the trend for the red component remains constant and the process of dynamical friction does not seem to be present.

12 Kinematics comparison between cluster galaxy populations

The comparison between the red populations of intermediate- and high-z clusters is illustrated in figure 12.22: the trend for the red population in the high-z clusters remains approximately constant, whereas for the red members in the intermediate-z clusters there is a marginal evidence of a decrease of velocity when considering more and more luminous galaxies.

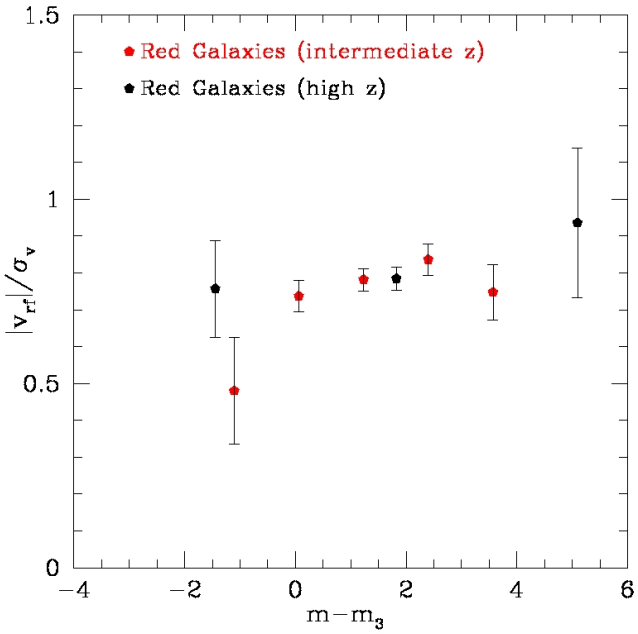

Figure 12.22: $|v_{rf}|/\sigma_v$ vs $m - m_3$ plot within $1R_{200}$ for red galaxies of intermediate- and high-z clusters: the trend for the red population in high-z clusters remains approximately constant, whereas that in intermediate-z clusters decreases for $m \leq m_3$.

Finally, I directly compare the results of this study about the effect of dynamical friction for intermediate- and high-z clusters with those obtained by Biviano et al. (1992) for nearby clusters and by Girardi et al. (2003) for nearby poor groups. Figure 12.23 shows the red component of intermediate- and high-z clusters analyzed in this thesis, the total members of clusters with $< z >= 0.15$ and considered by Biviano et al. (1992), and the elliptical galaxies belonging to nearby groups with at least 5 members and studied by Girardi et al. (2003).

In agreement with previous studies about nearby clusters and groups, I find some evidence of kinematical segregation of galaxies of different luminosity belonging to intermediate-z clusters, and luminosity segregation seems to be related only to the most luminous galaxies. The velocity-magnitude relation for nearby groups and low- and intermediate-z clusters first rapidly increases and then flattens out at faint magnitudes at $m \sim m_3$. According to Biviano et al. (1992), this trend can be explained if galaxies brighter than m_3 have achieved the energy-equipartition status, maybe due to dynamical friction or galaxy merging, while fainter galaxies still lie in the velocity-equipartition status generated by violent relaxation.

On the other hand, my results for distant clusters with $0.8 \leq z \leq 1.5$ indicate that the velocity-magnitude relation remains flat and that there is not segregation in velocity not even for the most luminous early-type galaxies: this is the first study concerning high-z clusters.

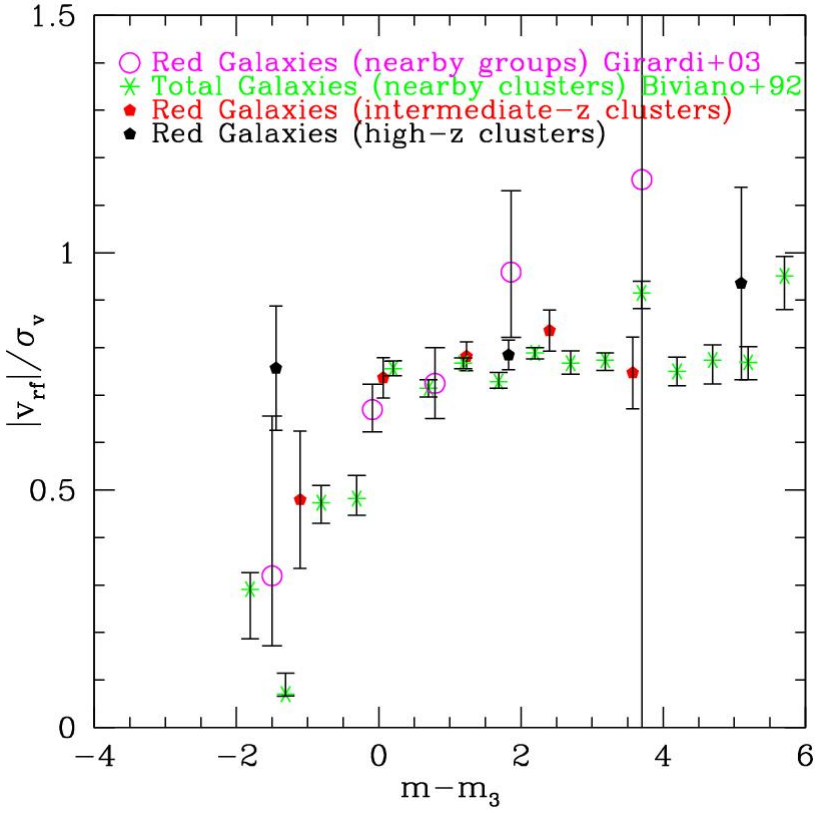

Figure 12.23: $|v_{rf}|/\sigma_v$ vs $m - m_3$ plot in comparison with previous studies: the most luminous red galaxies in the intermediate-z clusters are likely affected by the process of dynamical friction which lowers their velocity dispersion, in agreement with the results obtaining for the early-type galaxies in nearby groups (Girardi et al., 2003) and low-z clusters (Biviano et al., 1992). By contrast, the velocity-magnitude relation remains flat for the red galaxies in distant clusters.

Chapter 13

Euclid-like spectroscopic observations

13.1 Hα emitters

In the context of the preparatory science for the ESA Euclid space mission, many studies have been focused on Hα emitters in galaxy clusters. In fact, spectroscopic observations with Euclid will be possible only for star-forming galaxies through the detection of the Hα line at $z \geq 0.9$. The Hα line has a wavelength of 6562.8 Å and it is a specific deep-red visible spectral line in the Balmer series. Moreover, it is a typical strong emission line of a star-forming galaxies and it is used as star formation indicator (see previous section 2.3: *Hα and [OII] spectral lines as star formation tracers.*)
It is widely recognized that galaxy properties such as star formation rate (SFR) and morphology depend on the environment in which the galaxies reside. Local galaxy clusters are dominated by red quiescent ellipticals and S0s, and their tight color–magnitude relation suggests very old stellar populations. This means that many present-day cluster galaxies must have formed their stars in the early universe at $z >> 1$, and therefore distant clusters are an ideal site for studying this early evolutionary stage.
Earlier studies have identified a high fraction of star-forming population in distant clusters and the number of Hα emitters declines towards the cluster center (Koyama et al., 2014), whereas those with redder color tend to be located in high density clumps (Hayashi et al., 2012). In the very rich cluster cores, however, the star-forming galaxy fraction is still very low up to $z \sim 1$ suggesting that the major phase of star formation for galaxies in these regions must be occurring at an even earlier epoch. Some recent studies have suggested a reversal of the star formation-density relation at $z \sim 1$ in high-density environments in the distant universe (Elbaz et al., 2007; Cooper et al., 2008). As evidence of this, Santos et al. (2015) find that the amount of star formation in the core of the cluster XDCP J0044.0−2033 at $z = 1.58$, the most massive cluster at $z > 1.5$, is four times higher than that in the cluster outskirts. Therefore, the next challenge must be to study directly the site of cluster galaxy formation at high redshift (Koyama et al., 2013).

13.2 Data sample

In order to mimic the future spectroscopic observations of Euclid with the instrument NISP, I analyze a data sample of 17 clusters in the redshift range $0.79 \leq z \leq 1.46$ reported in Table 13.1. I consider clusters with $z \sim 0.80$ to increase the statistical significance of my results.

Table 13.1: Euclid high-redshift clusters

Cluster name	$< z >$
CL 1216.8−1201	0.7939
RX J1716+67	0.8065
MS 1054−03	0.8306
RX J0152.7−1357(1)*	0.8359
CL 0023+0423	0.8453
RX J1226.9+3332	0.8910
CL 1604+4304	0.8978
CL 1604+4321	0.9219
CL 1103.7−1245	0.9578
XMMU J1230.3+1339	0.9737
AX J2016+1127	1.0044
RDCS J0910+54	1.0998
RDCS J1252.9−2927	1.2370
RX J0848.9+4452	1.2602
RX J0848.9+4453	1.2727
XMMU J2235.3−2557	1.3905
XMMXCS J2215.9−1738	1.4589

NOTE.− * I take into account the subgroup RX J0152.7−1357(1) studied by Jorgensen et al. (2005) of the cluster RX J0152.7−1357 because in this case there are more numerous available magnitudes for the non member galaxies.

Since Euclid will be able to detect only star-forming galaxies, I define and consider the samples of blue/star-forming galaxies. For each cluster I take into account two alternative galaxy samples (sample A and sample B) and in order to mimic Euclid observations, I consider all galaxies, i.e. both members and not members.
Sample A is formed by galaxies selected in the same way I select blue/star-forming galaxies among the member galaxies (see Chapter 10: *Blue and red member galaxies*), but now the selection procedure is applied to all galaxies. Considering the whole cluster sample, the total number of star-forming galaxies is 930 and the median value for each cluster is 46.
Sample B is formed by all galaxies with the exception of those identified as red/passive member galaxies in Chapter 10. The total number of star-forming galaxies is 1155 and the median value for each cluster is 61.
In order to reproduce the Euclid NISP observations:

- I estimate the Hα fluxes of the star-forming galaxies;
- I select only galaxies with a Hα flux larger than the predicted Hα limit flux for the Euclid satellite;
- I apply several selection methods to obtain cluster members;
- finally, I calculate the velocity dispersion of the cluster members, comparing the different values obtained by the diverse procedures.

Chapter 14

Estimate of the Hα fluxes

The procedure through which I estimate the Hα fluxes of the star-forming galaxies is organized in the following steps:

1. **I make conversion from apparent to absolute magnitudes**, using the relations of Poggianti (1997) and Schlafly and Finkbeiner (2011);
2. **I utilize absolute magnitudes and colors to compute stellar masses**, using the relations of Bell and de Jong (2001) and Bell et al. (2003);
3. **I employ stellar masses to obtain star formation rates**, using the relations of Whitaker et al. (2014);
4. **finally, from star formation rates I derive Hα fluxes**, using the relations of Kewley et al. (2004) and Calzetti et al. (2000).

14.1 From apparent to absolute magnitudes

To estimate the absolute magnitude from the apparent magnitude for a fixed band λ, I consider the following relation:

$$\mathrm{M}(\lambda) = \mathrm{m}(\lambda) - 25 - 5 \times \log[D_L(z)] - k(\lambda; z) - \mathrm{A}(\lambda; \alpha, \delta),$$

where $\mathrm{M}(\lambda)$ is the absolute magnitude, $\mathrm{m}(\lambda)$ is the apparent magnitude, $D_L(z)$ is the luminosity distance measured in Mpc, $k(\lambda; z)$ is the k-correction and $\mathrm{A}(\lambda; \alpha, \delta)$ is the correction for the galactic extinction. The luminosity distance and the k-correction are functions of redshift, and I adopt the correction of the galactic extinction at the position (α, δ) of the cluster center.
Table 14.1 lists the cluster redshift, the luminosity distance and the center coordinates for all 17 clusters.

Table 14.1: Redshift, luminosity distance and coordinates

Cluster name	$< z >$	D_L (Mpc)	R.A. (J2000)	Decl. (J2000)
CL 1216.8−1201	0.794	4974.275	12 16 44.582	−12 01 18.67
RX J1716+67	0.806	5071.751	17 16 51.116	−67 08 25.78
MS 1054−03	0.831	5258.958	10 57 00.424	−03 37 31.84
RX J0152.7−1357(1)	0.836	5298.756	01 52 42.255	−13 57 53.21
CL 0023+0423	0.845	5373.378	00 23 51.631	+04 22 02.39
RX J1226.9+3332	0.891	5733.661	12 26 58.504	+33 32 51.66

CL 1604+4304	0.898	5787.918	16 04 24.690	+43 04 56.24
CL 1604+4321	0.922	5980.598	16 04 34.070	+43 20 56.80
CL 1103.7−1245	0.958	6269.225	11 03 46.334	−12 45 30.71
XMMU J1230.3+1339	0.974	6397.783	12 30 15.819	+13 39 26.69
AX J2016+1127	1.004	6648.160	20 19 18.279	+11 27 15.70
RDCS J0910+54	1.099	7438.246	09 10 43.478	+54 22 02.16
RDCS J1252.9−2927	1.237	8602.489	12 52 55.040	−29 27 08.91
RX J0848.9+4452	1.260	8802.428	08 48 58.615	+44 51 49.70
RX J0848.9+4453	1.273	8910.778	08 48 34.813	+44 53 47.00
XMMU J2235.3−2557	1.390	9941.194	22 35 20.729	−25 57 32.26
XMMXCS J2215.9−1738	1.459	10549.100	22 15 58.373	−17 37 58.58

NOTE.−Units of right ascension (R.A.) are hours, minutes and seconds, and units of declination (Decl.) are degrees, arcminutes and arcseconds.

The k-correction allows a measurement of a quantity of light from an object at a redshift z which is lost in the observation, in such way to obtain the rest-frame measurement of the light. It depends on the galaxy morphological type. The need for a k-correction arises because an astronomical measurement through a single filter or a single bandpass only sees a fraction of the total spectrum, redshifted into the frame of the observer. In this thesis the adapted k-correction values are those calculated by Poggianti (1997) for star-forming galaxies and the adopted estimates are reported in the following Table 14.2.
The galactic extinction is due to the absorption by the dust in the Milky Way and the correction values by Schlafly and Finkbeiner (2011) are listed in Table 14.2 for each cluster.

14.2 From colors to stellar masses

There is a strong correlation between the stellar mass-to-light (M_*/L) ratio and the colors of star-forming galaxies. The color index (or color) is defined as the difference between two magnitudes in different bands. Adopting a mass-dependent formation epoch model with bursts and a scaled Salpeter IMF, Bell and de Jong (2001) found the following $Color-(M_*/L)$ equation for a spiral galaxy population:

$$\log[(M_*/L)] = a_\lambda + b_\lambda \times Color,$$

where the fit coefficients a_λ and b_λ calculated by Bell and de Jong (2001) for the Johnson filters and by Bell et al. (2003) for the Sloan system are presented in figure H.1 of Appendix H.
These fits can be used to estimate the stellar M_*/L ratio for a star-forming galaxy of a given color for a fixed band. In order to calculate the stellar mass M_* in solar masses $M_\odot$, I evaluate the luminosity L in the chosen band from the relation:

$$L(\lambda) = 10^{-0.4[\mathrm{M}(\lambda)-\mathrm{M}_\odot(\lambda)]},$$

where $M_\odot(\lambda)$ is the solar absolute magnitude. The solar values $M_\odot(\lambda)$ estimated by Binney and Merrifield (1998) for the Johnson filters and by Sparke and Gallagher (2007) for the Sloan system are reported in Table H.1 in Appendix H.

The bands considered for magnitudes and colors are listed for each cluster in Table 14.2, which also reports the applied k-corrections and the corrections for the galactic extinction. The symbol "−" indicates that the correction for the galactic extinction was already applied by the authors from whom I collect the data.

Table 14.2: Used bands of colors and magnitudes, k and galactic extinction corrections

Cluster name	Color($\lambda_1 - \lambda_2$)	Mag(λ)	$k(\lambda_1)$	$k(\lambda_2)$	$k(\lambda)$	A(λ_1)	A(λ_2)	A(λ)
CL 1216.8−1201	$V-I$	R	1.154	0.283	0.810	0.107	0.059	0.085
RX J1716+67	$r-i$	r	0.950	0.434	0.950	0.080	0.059	0.080
MS 1054−03*	$V-I$	I	1.182	0.313	0.313	0.097	0.053	0.053
RX J0152.7−1357(1)	$r-i$	r	1.010	0.485	1.010	0.033	0.024	0.033
CL 0023+0423	$V-I$	R	1.182	0.313	0.873	0.059	0.032	0.047
RX J1226.9+3332	$r-i$	r	1.058	0.553	1.058	0.044	0.033	0.044
CL 1604+4304	$V-I$	R	1.199	0.349	0.930	0.031	0.017	0.024
CL 1604+4321	$V-I$	R	1.216	0.386	0.987	0.036	0.020	0.029
CL 1103.7−1245	$V-I$	R	1.228	0.432	1.036	0.095	0.052	0.075
XMMU J1230.3+1339	$r-i$	r	1.137	0.701	1.137	0.071	0.053	0.071
AX J2016+1127*	$r-i$	r	1.167	0.781	1.167	0.527	0.392	1.167
RDCS J0910+54	$V-K$	R	1.251	−0.565	1.177	−	−	−
RDCS J1252.9−2927	$B-R$	R	0.673	1.238	1.238	−	−	−
RX J0848.9+4452*	$R-J$	J	1.260	0.010	0.010	0.060	0.020	0.020
RX J0848.9+4453	$B-R$	R	0.620	1.282	1.282	0.097	0.058	0.058
XMMU J2235.3−2557*	$J-K$	J	0.070	−0.599	0.070	0.014	0.006	0.014
XMMXCS J2215.9−1738	$I-K$	I	1.049	−0.602	1.049	0.347	0.070	0.347

NOTE.− * Clusters for which magnitude transformations are applied.

For four clusters, galaxies are characterized by colors for which Bell and de Jong (2001) and Bell et al. (2003) do not list the respective fit coefficients. In this case, I apply the magnitude transformation relations of Windhorst et al. (1991) between the Johnson filters and the Sloan systems:

$$R = r - 0.51 - 0.15 \times (g - r)$$
$$I = i - 0.75$$
$$J = g + 0.39 + 0.37 \times (g - r)$$
$$K = r - 0.25 + 0.17 \times (g - r).$$

In this way it is possible to obtain I magnitude for MS 1054−03, r and i for AX J2016+1127, g and r for RX J0848.9+4452 and XMMU J2235.3−2557. Moreover, for AX J2016+1127 I assume the typical value of $(g - r)$=0.96 for a spiral galaxy at $z \sim 1$ from Fukugita et al. (1995).

14.3 From stellar masses to star formation rates

Following the study of Whitaker et al. (2014), I estimate the star formation rate from the stellar mass using a broken power law to independently quantify the behavior of the low-mass galaxies and the high-mass galaxies. The SFR$-M_*$ relation is parametrized as:

$$\log(\mathrm{SFR}) = a[\log(M_*/M_\odot) - 10.2] + b,$$

where the SFR is estimated in $M_\odot yr^{-1}$. The values of a and b are functions of the redshift and are listed in figure H.2 in Appendix H. Furthermore, the coefficient a is different above and below the characteristic mass of $\log(M_*/M_\odot) = 10.2$. In this study, I use the estimates of a and b for the redshift ranges $0.5 < z < 1.0$ and $1.0 < z < 1.5$.

14.4 From star formation rates to Hα fluxes

The model adopted by Bell and de Jong (2001) and Whitaker et al. (2014) takes into account the correction due to the absorption by dust. Thus, the obtained values of SFR, using the above equations, are intrinsic estimates. However, the Euclid Hα limit flux is an observational quantity. In this context, I have to decorrect (i.e. add) for the dust component in order to obtain the observational Hα fluxes.
The intrinsic SFR and luminosity in Hα are bound by the following relation of Kennicutt (1998):

$$L(\mathrm{H}\alpha)(\mathrm{erg\ s^{-1}}) = \mathrm{SFR}(M_\odot yr^{-1})/7.9 \times 10^{-42}.$$

To decorrect for the dust component, I evaluate from the intrinsic SFR the intrinsic luminosity in [OII], using the relation of Kewley et al. (2004):

$$L[\mathrm{OII}](\mathrm{erg\ s^{-1}}) = \mathrm{SFR}(M_\odot yr^{-1})/6.6 \times 10^{-42},$$

and from L[OII] I estimate the color excess $E(B-V)$, using the best-fit relation of Kewley et al. (2004):

$$E(B-V) = 0.174 \times \log(L[\mathrm{OII}]) - 6.84.$$

In this way it is possible to calculate the observational Hα luminosity $L(\mathrm{H}\alpha)_{\mathrm{obs}}$ from the following equation of Calzetti et al. (2000):

$$L(\mathrm{H}\alpha)_{\mathrm{obs}} = \mathrm{L(H}\alpha)/10^{0.4\times 3.326\times \mathrm{E(B-V)}}.$$

Finally, I estimate the observational Hα flux $F(\mathrm{H}\alpha)_{\mathrm{obs}}$ for each star-forming galaxy:

$$F(\mathrm{H}\alpha)_{\mathrm{obs}}(\mathrm{erg\ cm^{-2}\ s^{-1}}) = \frac{L(\mathrm{H}\alpha)_{\mathrm{obs}}(\mathrm{erg\ s^{-1}})}{4\pi D_L^2(\mathrm{cm^2})},$$

to be compared with the Hα flux limit expected for the instrument NISP of the Euclid satellite.

Chapter 15

Cuts in the Hα fluxes

After the estimate of the Hα fluxes for the star-forming galaxies, I select only the late-type galaxies with a Hα flux larger than the limit expected for Euclid, $F(\mathrm{H}\alpha)_{\mathrm{lim}} = 2\times10^{-16}$ erg cm^{-2} s^{-1}. Applying this threshold, most of the star-forming galaxies cannot be considered, having lower values of the Hα flux. However, the cluster sample of this thesis is not the best one to mimic Euclid results, since most clusters are known for their X-ray emission, i.e. they are probably dynamically more evolved than the typical cluster population at those z. Moreover, the clusters of my data sample have $z < 1.5$ and there are observational evidences of a reversal of the star formation-density relation at $z \sim 1.5$ (Elbaz et al., 2007; Cooper et al., 2008; Santos et al., 2015). Thus, I expect that many Euclid cluster galaxies will have larger Hα fluxes than those of the galaxies here studied.
Although it is obvious that a full reliable study mimicking the Euclid observations should consider a different cluster sample or, better, a Hα based galaxy survey (still not present in the literature), in order to take into account the above drawbacks, I decide to also consider a lower Hα flux limit, i.e. $F(\mathrm{H}\alpha)_{\mathrm{lim}} = 1\times10^{-16}$ erg cm^{-2} s^{-1}, which increases the number of Hα selected galaxies per cluster.
Table 15.1 and 15.2 list the number of star-forming galaxies in each cluster, N_{SF}, and the numbers resulting after the application of the cuts according to the two limiting fluxes, $N_{\geq1\times10^{-16}}$ for $F(\mathrm{H}\alpha)_{\mathrm{lim}} = 1\times10^{-16}$ erg cm^{-2} s^{-1} and $N_{\geq2\times10^{-16}}$ for $F(\mathrm{H}\alpha)_{\mathrm{lim}} = 2\times10^{-16}$ erg cm^{-2} s^{-1}, for both samples A and B.
I restrict the following analysis to the $F(\mathrm{H}\alpha)_{\mathrm{lim}} = 1\times10^{-16}$ erg cm^{-2} s^{-1} case and I call the selected galaxies, i.e those having $F(\mathrm{H}\alpha)_{\mathrm{obs}} \geq 1\times10^{-16}$ erg cm^{-2} s^{-1}, as Hα bright galaxies hereafter.
The samples related to the clusters RX J0848.9+4452, XMMU J2235.3−2557 and XMMXCS J2215.9−1738, which have no galaxies with $F(\mathrm{H}\alpha)_{\mathrm{obs}} \geq 1\times10^{-16}$ erg cm^{-2} s^{-1}, cannot be considered and so my final sample is composed of 14 clusters.

Table 15.1: Sample A: results after the Hα flux cuts

Cluster name	N_{SF}	$N_{\geq1\times10^{-16}}(=N_{\mathrm{H}\alpha})$	$N_{\geq2\times10^{-16}}$
CL 1216.8−1201	76	51	0
RX J1716+67	14	13	0
MS 1054−03	47	27	0
RX J0152.7−1357(1)	11	11	0
CL 0023+0423	51	8	0
RX J1226.9+3332	55	35	0
CL 1604+4304	46	4	0

CL 1604+4321	111	14	0
CL 1103.7−1245	141	10	0
XMMU J1230.3+1339	6	4	0
AX J2016+1127	26	25	25
RDCS J0910+54	133	15	0
RDCS J1252.9−2927	145	88	45
RX J0848.9+4452	5	0	0
RX J0848.9+4453	3	3	3
XMMU J2235.3−2557	42	0	0
XMMXCS J2215.9−1738	18	0	0

Table 15.2: Sample B: results after the Hα flux cuts

Cluster name	N_{SF}	$N_{\geq 1\times10^{-16}}(= N_{\mathrm{H}\alpha})$	$N_{\geq 2\times10^{-16}}$
CL 1216.8−1201	83	58	0
RX J1716+67	19	17	0
MS 1054−03	48	28	0
RX J0152.7−1357(1)	16	16	0
CL 0023+0423	94	22	0
RX J1226.9+3332	76	51	0
CL 1604+4304	86	27	2
CL 1604+4321	123	23	0
CL 1103.7−1245	169	30	0
XMMU J1230.3+1339	7	5	0
AX J2016+1127	26	25	25
RDCS J0910+54	140	19	0
RDCS J1252.9−2927	181	105	54
RX J0848.9+4452	5	0	0
RX J0848.9+4453	3	3	3
XMMU J2235.3−2557	61	0	0
XMMXCS J2215.9−1738	18	0	0

Chapter 16

Selection of Hα bright galaxy members and velocity dispersions

In order to select the cluster members among the Hα bright galaxies, I apply the selection methods described in Chapter 7 and Chapter 9 which are shown to be the most reliable, i.e. the procedures: P+G, ZHG and WG4+YV.

16.1 Results for the sample A

First, I apply to all galaxies a radial cut of 3 Mpc from the cluster center and a velocity cut of $\pm 10\,000$ kms^{-1} (in the appropriate cluster rest frame) from the cluster velocity center. The clusters CL 1604+4304, CL 1103.7−1245 and RDCS J0910+54 do not have Hα bright galaxies within 3 Mpc and $\pm 10\,000$ kms^{-1}, and for the remaining sample of 11 clusters I employ the following member selection procedures.
Note that when the mean redshift of a selected population is far from the real cluster redshift, $| < z_{\mathrm{H}\alpha} > - < z > | \geq 0.01$ (where $< z >$ is the cluster redshift obtained in Chapter 7), I do not consider that system. In fact, from Euclid photometric data the cluster redshift will be known with an uncertainty of the order of 0.01, since the uncertainty of Euclid on the photometric redshift for a single galaxy is $\Delta z/(1+z) = (z_{photo} - z_{spect})/(1+z) \sim 0.05$, e.g $\Delta z = 0.1$ for $z = 0.95$ which is the mean redshift of my cluster sample, and the error on the cluster redshift, which is the mean galaxy redshift and scales with $1/\sqrt{N}$ where N is the number of galaxies, will be generally based on many tens of galaxies having photometry (likely 50 or more galaxies: see figure 1 of Sartoris et al. 2015).

- **P+G:** I apply the 1D-DEDICA procedure and I find 4 clusters where there is a significant peak at the cluster redshift and 7 clusters without a peak at the cluster redshift that is characterized by only field galaxies. For the 4 significant cluster peaks, I employ the "shifting gapper" technique. The number of members per cluster is $\geq$6.

- **ZHG:** I perform the procedure of Zabludoff et al. (1990) on the 11 clusters, finding 8 clusters with at least 3 members.

- **WG4+YV:** I employ the WG4+YV procedure, obtaining 5 clusters with at least 3 members.

The number of Hα galaxy members for the 11 clusters surviving the application of the radial and velocity cuts are shown in Table 16.1. In order to compare these results with those derived by the blue galaxy population, I also write in Table 16.1 the number of blue galaxies, N_{blue}, (see Chapter 10: *Blue and red member galaxies*).
For the clusters RDCS J1252.9−2927 and RX J0848.9+4453 all the member selection procedures agree in finding no members.
Table 16.2 reports the mean redshifts and the comparison between $< z_{\mathrm{H}\alpha} >$ and $< z >$ is shown in figure 16.1. I do not report the errors on redshifts since they are 4 orders of magnitude smaller than the measurements.

Table 16.1: Sample A: number of Hα bright galaxy members for P+G, ZHG and WG4+YV

Cluster name	$N_{\mathrm{H}\alpha,\mathrm{P+G}}$	$N_{\mathrm{H}\alpha,\mathrm{ZHG}}$	$N_{\mathrm{H}\alpha,\mathrm{WG4+YV}}$	N_{blue}
CL 1216.8−1201	22	22	22	31
RX J1716+67	13	13	13	13
MS 1054−03	25	27	27	46
RX J0152.7−1357(1)	−	3	−	2
CL 0023+0423	−	3	3	10
RX J1226.9+3332	6	6	6	7
CL 1604+4321	−	−	−	26
XMMU J1230.3+1339	−	3	−	5
AX J2016+1127	−	3	−	3
RDCS J1252.9−2927	−	−	−	17
RX J0848.9+4453	−	−	−	3

NOTE.− * The symbol " − " indicates that the number of the selected Hα bright members is zero.

Table 16.2: Sample A: redshift comparison

Cluster name	$< z >$	$< z_{\mathrm{H}\alpha,\mathrm{P+G}} >$	$< z_{\mathrm{H}\alpha,\mathrm{ZHG}} >$	$< z_{\mathrm{H}\alpha,\mathrm{WG4+YV}} >$
CL 1216.8−1201	0.7939	0.7929	0.7929	0.7929
RX J1716+67	0.8065	0.8074	0.8074	0.8074
MS 1054−03	0.8306	0.8311	0.8302	0.8302
RX J0152.7−1357(1)	0.8359	−	0.8413	−
CL 0023+0423	0.8453	−	0.8455	0.8455
RX J1226.9+3332	0.8910	0.8862	0.8862	0.8862
XMMU J1230.3+1339	0.9737	−	0.9744	−
AX J2016+1127	1.0044	−	1.0115	−

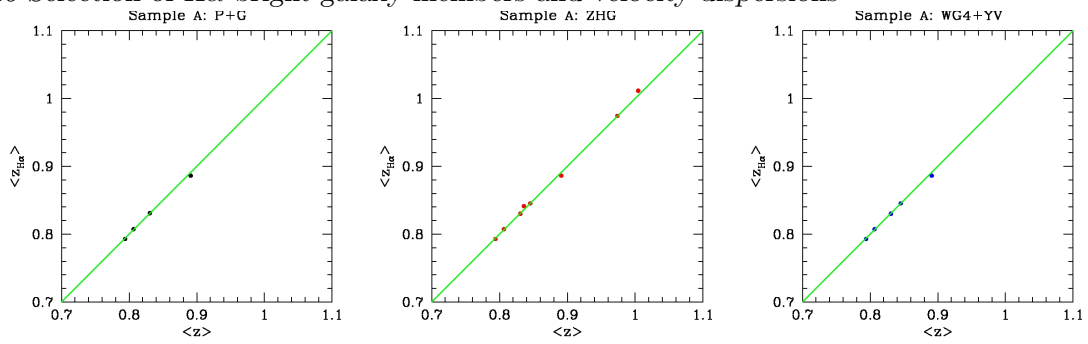

Figure 16.1: Sample A: $< z >$ vs $< z_{\mathrm{H}\alpha} >$ for P+G, ZHG and WG4+YV.

Finally, I estimate the robust velocity dispersions for the cluster samples having at least 5 Hα bright members. I write their values and jackknife errors in Table 16.3. This table also displays the velocity dispersions and the relative uncertainties of the blue cluster members (see Chapter 11: *Velocity dispersions of cluster galaxy populations*). The visual inspection of Table 16.3 shows that the velocity dispersion estimates computed on Hα bright cluster members are similar, considering the large uncertainties, to those estimated on the blue population σ_{blue}. The F-test confirms that there are not significant differences (see Tables E.4 in the Appendix E) and I plot the comparison between $\sigma_{\mathrm{H}\alpha}$ and σ_{blue} for all the four clusters in figure 16.2. Moreover, figure 16.3 illustrates $\sigma_{\mathrm{H}\alpha}$ vs σ_v, which is the velocity dispersion of all the cluster members found with the P+G procedure (see Chapter 6: *Velocity dispersion estimates*).
Since the cluster sample is formed by only 4 clusters, I do not apply any test involving the velocity dispersion distributions.

Table 16.3: Sample A: robust velocity dispersions of the Hα bright cluster members

Cluster name	$\sigma_{\mathrm{H}\alpha,\mathrm{P+G}} \pm \delta\sigma_{\mathrm{H}\alpha,\mathrm{P+G}}$ (km s^{-1})	$\sigma_{\mathrm{H}\alpha,\mathrm{ZHG}} \pm \delta\sigma_{\mathrm{H}\alpha,\mathrm{ZHG}}$ (km s^{-1})	$\sigma_{\mathrm{H}\alpha,\mathrm{WG4+YV}} \pm \delta\sigma_{\mathrm{H}\alpha,\mathrm{WG4+YV}}$ (km s^{-1})	$\sigma_{blue} \pm \delta\sigma_{blue}$ (km s^{-1})
CL 1216.8−1201	966±92	966±92	966±92	959±105
RX J1716+67	1470±298	1470±298	1470±298	1261±266
MS 1054−03	1243±169	1442±215	1442±215	1268±184
RX J1226.9+3332	1333±491	1333±491	1333±491	1199±490

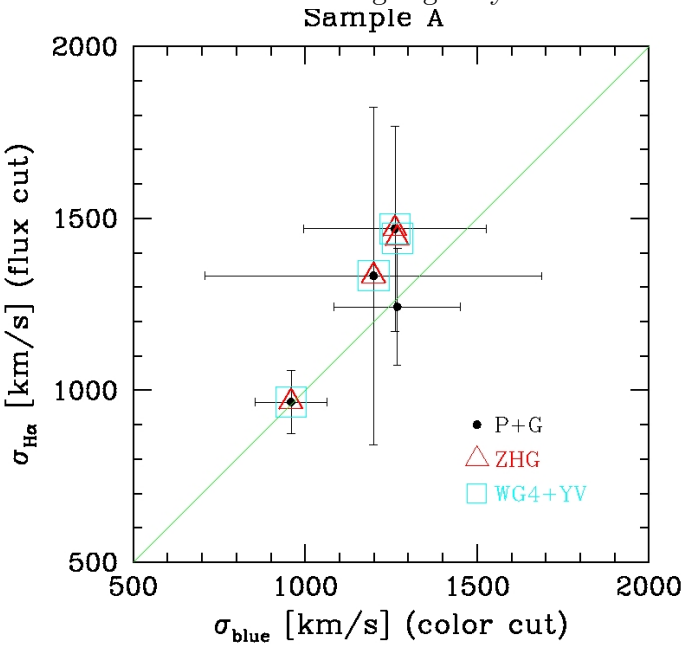

Figure 16.2: Sample A: $\sigma_{\mathrm{H}\alpha}$ vs σ_{blue} for the selection procedures P+G, ZHG and WG4+YV. Only the errors on the estimates of $\sigma_{\mathrm{H}\alpha,\mathrm{P+G}}$ are shown.

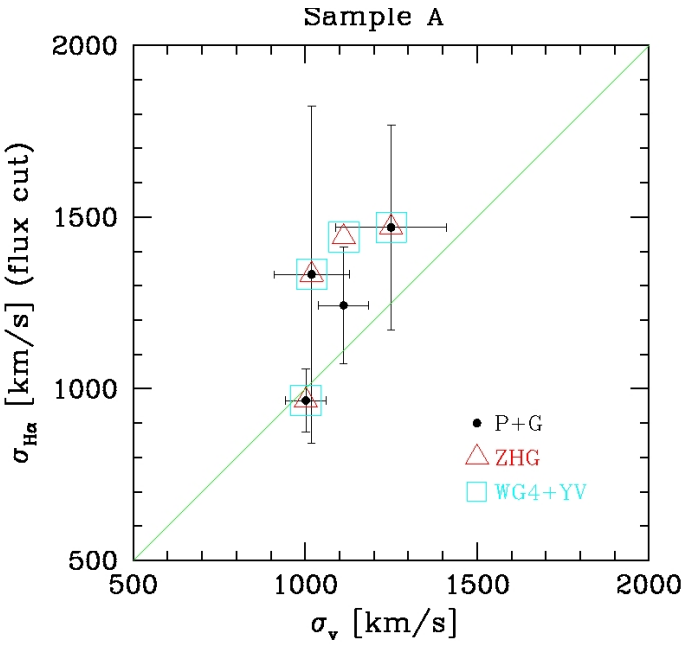

Figure 16.3: Sample A: $\sigma_{\mathrm{H}\alpha}$ vs σ_v for the selection procedures P+G, ZHG and WG4+YV. Only the errors on the estimates of $\sigma_{\mathrm{H}\alpha,\mathrm{P+G}}$ are shown.

16 Selection of Hα bright galaxy members and velocity dispersions

Comparing the selected Hα bright galaxies with the cluster members, I find that all the procedures correctly identify only Hα bright galaxies which are cluster members. Only in the case of the cluster RX J1716+67 all the procedures identify one Hα bright galaxy which is an interloper. Thus, the member selection procedures are efficient and the calculated velocity dispersions of the Hα bright galaxies are reliable. This suggest that the velocity dispersion computed using Hα bright galaxies can be an useful mass proxy after an appropriate calibration. This will be possible on a data-set at least 3-5 times larger than the one I analyzed.

In this context, I compare the velocity dispersion values estimated with different cluster populations: the red galaxies, the blue galaxies and the Hα bright galaxies, which are a subgroup of the blue galaxies and are the most blue galaxies. Figures 16.4 and 16.5 show $\sigma_{\mathrm{H}\alpha,\mathrm{P+G}}$ and $\sigma_{\mathrm{H}\alpha,\mathrm{ZHG}}$ ($=\sigma_{\mathrm{H}\alpha,\mathrm{WG4+YV}}$) in comparison with σ_{blue} and σ_{red}, respectively. In the case of the cluster MS 1054−03 the methods ZHG and WG4+YV select a larger number of cluster members than the P+G procedure, and so they find a more reliable estimate of $\sigma_{\mathrm{H}\alpha}$. From a visual inspection of these figures $\sigma_{\mathrm{H}\alpha} > \sigma_{blue}$ typically and **there is a marginal evidence of a possible velocity segregation between the blue and the Hα bright galaxies in the high-z clusters** which do not show a segregation between the red and the blue galaxies (see Chapter 12: *Kinematics comparison between cluster galaxy populations*).

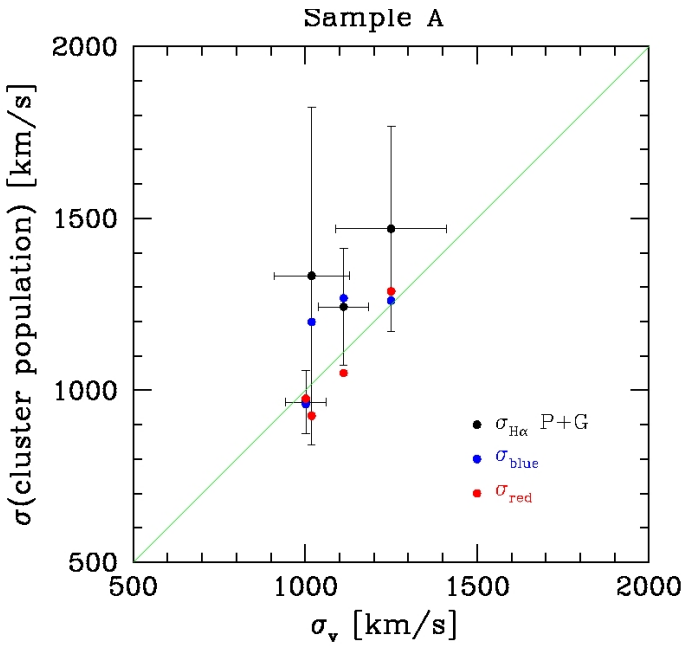

Figure 16.4: Sample A: $\sigma_{\mathrm{H}\alpha,\mathrm{P+G}}$ vs σ_{blue} vs σ_{red}. Only the errors on the estimates of $\sigma_{\mathrm{H}\alpha,\mathrm{P+G}}$ are shown.

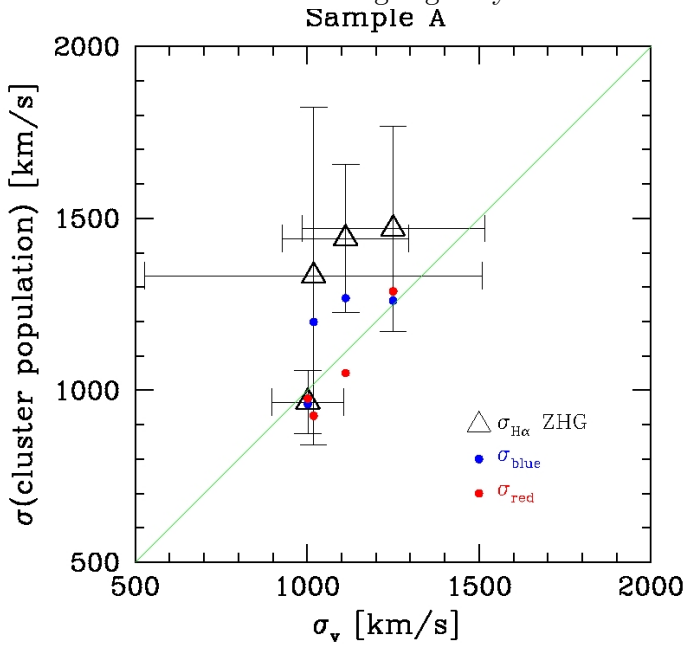

Figure 16.5: Sample A: $\sigma_{\mathrm{H}\alpha,\mathrm{ZHG}}$ vs σ_{blue} vs σ_{red}. Only the errors on the estimates of $\sigma_{\mathrm{H}\alpha,\mathrm{ZHG}}$ are shown.

16.2 Results for the sample B

For the 14 clusters characterized by Hα bright galaxies with $F(\mathrm{H}\alpha)_{\mathrm{obs}} \geq 1 \times 10^{-16}$ erg cm^{-2} s^{-1} I apply to all galaxies a radial cut of 3 Mpc from the cluster center and a velocity cut of $\pm$10 000 kms^{-1} (in the appropriate cluster rest frame), obtaining no Hα bright galaxies only for the cluster RDCS J0910+54. Then, I employ the following cluster member selection methods, excluding the systems with $| < z_{\mathrm{H}\alpha} > - < z > | \geq 0.01$:

- **P+G:** I apply the 1D-DEDICA procedure and I find 4 clusters where there is a significant peak at the cluster redshift and 7 clusters without a peak at the cluster redshift that is characterized by only field galaxies. For the 4 significant cluster peaks, I employ the "shifting gapper" technique. The number of members per cluster is ≥9.
- **ZHG:** I perform the procedure of Zabludoff et al. (1990) on the 11 clusters, finding 7 clusters with at least 2 members.
- **WG4+YV:** I employ the WG4+YV procedure, obtaining 5 clusters with at least 6 members.

I write in Table 16.4 the numbers of the Hα bright galaxy members obtained with the different methods, $N_{\mathrm{H}\alpha}$, and the number of blue galaxies, N_{blue}, (see Chapter 10: *Blue and red member galaxies*). For the 6 clusters CL 1604+4304, CL 1604+4321, CL 1103.7−1245, XMMU J1230.3+1339, RDCS J1252.9−2927 and RX J0848.9+4453 all the member selection procedures agree in finding no members.
Table 16.5 reports the mean redshifts and figure 16.6 shows the comparison between $< z >$ and $< z_{\mathrm{H}\alpha} >$ without the errors on redshifts, since they are 4 orders of magnitude smaller than the measurements.

Table 16.4: Sample B: number of Hα bright galaxy members for P+G, ZHG and WG4+YV

Cluster name	$N_{\mathrm{H}\alpha,\mathrm{P+G}}$	$N_{\mathrm{H}\alpha,\mathrm{ZHG}}$	$N_{\mathrm{H}\alpha,\mathrm{WG4+YV}}$	N_{blue}
CL 1216.8−1201	23	23	25	31
RX J1716+67	12	17	17	13
MS 1054−03	25	27	28	46
RX J0152.7−1357(1)	–	2	6	2
CL 0023+0423	–	4	–	10
RX J1226.9+3332	9	7	–	7
CL 1604+4304	–	–	–	5
CL 1604+4321	–	–	–	26
CL 1103.7−1245	–	–	–	14
XMMU J1230.3+1339	–	–	–	5
AX J2016+1127	–	3	6	3
RDCS J1252.9−2927	–	–	–	17
RX J0848.9+4453	–	–	–	3

NOTE.− * The symbol " − " indicates that the number of the selected Hα bright members is zero.

Table 16.5: Sample B: redshift comparison

Cluster name	$< z >$	$< z_{\mathrm{H}\alpha,\mathrm{P+G}} >$	$< z_{\mathrm{H}\alpha,\mathrm{ZHG}} >$	$< z_{\mathrm{H}\alpha,\mathrm{WG4+YV}} >$
CL 1216.8−1201	0.7939	0.7933	0.7933	0.7933
RX J1716+67	0.8065	0.8062	0.8110	0.8110
MS 1054−03	0.8306	0.8311	0.8302	0.8299
RX J0152.7−1357(1)	0.8359	–	0.8303	0.8309
CL 0023+0423*	0.8453	–	0.8453	–
RX J1226.9+3332*	0.8910	0.8855	0.8889	–
AX J2016+1127	1.0044	–	1.0115	0.9905

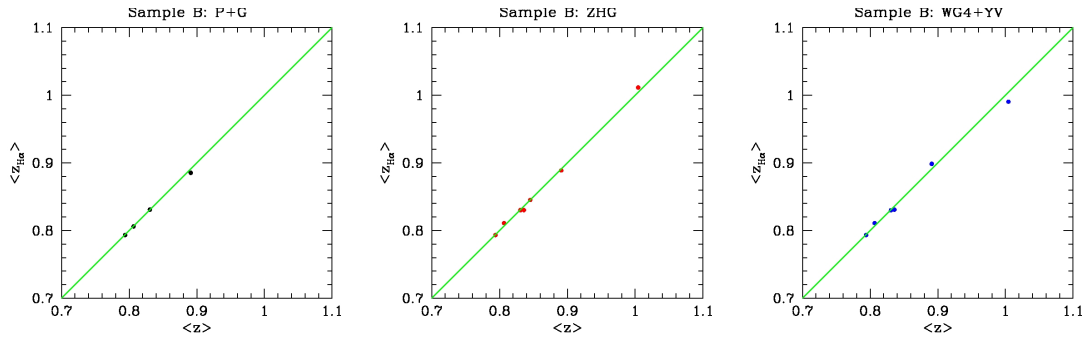

Figure 16.6: Sample B: $< z >$ vs $< z_{\mathrm{H}\alpha} >$ for P+G, ZHG and WG4+YV.

Finally, I estimate the robust velocity dispersions for the cluster samples having at least 5 Hα bright members. I write their values and jackknife errors in Table 16.6. This table also displays the velocity dispersions and the relative uncertainties of the blue cluster members (see Chapter 11: *Velocity dispersions of cluster galaxy populations*). The visual inspection of Table 16.6 shows that the velocity dispersion estimates computed on Hα bright cluster members are similar, considering the large uncertainties, to those estimated on the blue population σ_{blue}. The F-test confirms that there are not significant differences (see Tables E.5 in the Appendix E) and I plot the comparison between $\sigma_{\rm H\alpha}$ and σ_{blue} for all the four clusters in figure 16.7. Moreover, figure 16.8 illustrates $\sigma_{\rm H\alpha}$ vs σ_v, which is the velocity dispersion of all the cluster members found with the P+G procedure (see Chapter 6: *Velocity dispersion estimates*).
Since the cluster sample is formed by only 4 clusters, I do not apply any test involving the velocity dispersion distributions.
The velocity dispersions estimated for the sample B are larger than those calculated in the case of the sample A and this is due to the fact that the procedure used to select star-forming galaxies to form the sample B is more affected by interlopers than that applied to collect the sample A. Note that the sample B is that based on the most pessimistic case in which all non red cluster member galaxies are considered to be star-forming, thus possibly including in the Hα sample also galaxies not really star-forming.
Table 16.7 lists for each cluster the number of interlopers, n_i, according to the selection method. The P+G method is more efficient in selecting true member galaxies.

Table 16.6: Sample B: robust velocity dispersions of the Hα bright cluster members

Cluster name	$\sigma_{\rm H\alpha,P+G} \pm \delta\sigma_{\rm H\alpha,P+G}$ (km s^{-1})	$\sigma_{\rm H\alpha,ZHG} \pm \delta\sigma_{\rm H\alpha,ZHG}$ (km s^{-1})	$\sigma_{\rm H\alpha,WG4+YV} \pm \delta\sigma_{\rm H\alpha,WG4+YV}$ (km s^{-1})	$\sigma_{blue} \pm \delta\sigma_{blue}$ (km s^{-1})
CL 1216.8−1201	1014±112	1014±112	1169±213	959±105
RX J1716+67	1326±262	1712±278	1712±278	1261±266
MS 1054−03	1243±169	1442±215	1576±270	1268±184
RX J1226.9+3332	1687±385	1585±357	–	1199±490

Table 16.7: Sample B: number of interlopers

Cluster name	$n_{i,\rm P+G}$	$n_{i,\rm ZHG}$	$n_{i,\rm WG4+YV}$
CL 1216.8−1201	1	1	3
RX J1716+67	0	5	5
MS 1054−03	0	0	2
RX J1226.9+3332	3	1	–

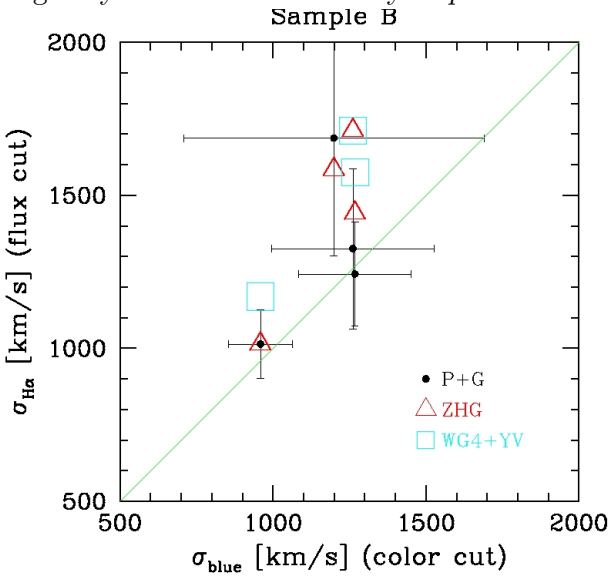

Figure 16.7: Sample B: $\sigma_{\mathrm{H}\alpha}$ vs σ_{blue} for P+G, ZHG and WG4+YV. Only the errors on the estimates of $\sigma_{\mathrm{H}\alpha,\mathrm{P+G}}$ are shown.

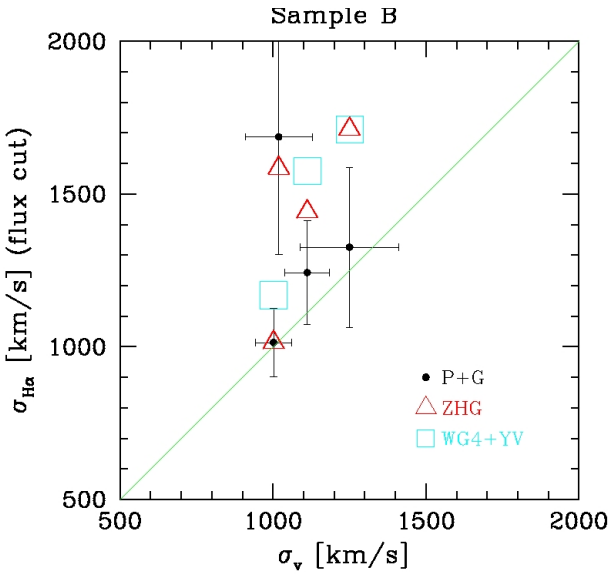

Figure 16.8: Sample B: $\sigma_{\mathrm{H}\alpha}$ vs σ_v for P+G, ZHG and WG4+YV. Only the errors on the estimates of $\sigma_{\mathrm{H}\alpha,\mathrm{P+G}}$ are shown.

Chapter 17

Summary, conclusions and future perspectives

The results presented in Chapter 12 about the kinematics comparison between the cluster galaxy populations extend to intermediate-z the results found in the literature for nearby clusters. For a sample of 32 intermediate-z clusters ($0.40 \leq z < 0.80$) my findings can be summarized as follows:

1. the blue and red galaxies are segregated in the velocity space with the related velocity dispersions $\sigma_{blue} > \sigma_{red}$. The sign test and the Wilcoxon test show that the probability for the velocity dispersion distribution of blue members to be larger than that of red galaxies is 99.65% and 99.62%, respectively;

2. the brightest galaxies are segregated in velocity in agreement with a scenario characterized by the dynamical friction process.

The most plausible explanation for these findings is that in nearby and intermediate-z clusters blue galaxies represent a very recently accreted population, while red galaxies, which belong to the cluster since a longer time, have become a more relaxed population.
On the other hand, according to my analysis for a sample of 14 high-z clusters ($0.80 \leq z \leq 1.46$):

1. *there is no evidence of velocity and luminosity segregations in distant clusters: this is the most important finding of my study.*

I interpret this latter result as a consequence of the fact that high-redshift clusters are observed closer to their formation epoch with both red and blue galaxies being accreted recently and thus having similar kinematical properties. In particular, the dynamical friction had no time to affect galaxy kinematics yet. This scenario can be acceptable in the case that red galaxies infall into clusters together with blue ones (e.g., if both of them belong to small groups), and/or in the case that a possible morphological transformation from the blue to the red type is very fast with a characteristic time much smaller than the time involved in the kinematical segregation.
In conclusion, it is known that in nearby clusters, although the relation between velocity dispersion and cluster mass is different for the diverse cluster populations, both galaxy populations are good tracers of the gravitational potential. By contrast, for distant clusters, my thesis provides the first observational evidence that the kinematics of blue/star-forming galaxies is not different from that of red/passive galaxies. Future studies are needed to clarify how much both the populations can be used to trace the cluster dynamics and to calibrate the velocity dispersion-cluster mass relation.

17 Summary, conclusions and future perspectives

My study about high-redshift clusters ($0.80 \leq z \leq 1.46$) continues in the first analysis devoted to the Euclid-like spectroscopic observations in order to determinate the robustness of σ_v estimates, and described in Chapter 16. The results I have obtained can be summarized as follows:

1. the threshold in the Hα flux limit strongly limit the number of NISP spectroscopic observable clusters and the number of cluster members; this problem has already been suggested also by previous studies (e.g., Sartoris et al., 2015);

2. applying the F-test for each of the remaining four clusters I analyzed, I do not find significant difference between the velocity dispersion of the Hα bright galaxies, $\sigma_{\mathrm{H}\alpha}$, and the velocity dispersion of the blue galaxies, σ_{blue}, within the respective uncertainties;

3. qualitatively, my results suggest that typically $\sigma_{\mathrm{H}\alpha} > \sigma_{blue}$, i.e. there is a level of velocity segregation between Hα bright galaxies and blue galaxies. However, I cannot give a precise statistical result based on four clusters.

The efficiency of the member selection procedures in the case of the Hα bright samples (in particular, the P+G method) suggests that the estimates of velocity dispersions based on NISP spectroscopic data can be a useful mass proxy after an appropriate calibration.
Moreover, the above evidence (3rd point), although very marginal, seems to fit in a more global scenario where the phenomenon of the velocity segregation occurs among different galaxy types, taking into account that Hα bright galaxies are likely the bluest in the blue galaxy population. Considering the first part of my thesis, the color threshold between segregated and non segregated galaxies is bluer at higher redshift, or - using the time axis - the color threshold between segregated and non segregated galaxies is redder at lower redshift. Thus, my results can have interesting implications for the dynamical processes regulating the evolution of galaxies in combination with the cluster evolution. However, a larger cluster sample is obviously needed to confirm my results for the Hα bright galaxies in the distant clusters.
The natural following step in this research project will be to study the relation between the velocity dispersion and the mass of intermediate and high-z clusters, where velocity dispersions are computed using different populations - in particular blue and Hα bright galaxies - and masses are obtained using other mass proxies or working with appropriate simulated clusters at known mass. This work will be useful both to calibrate the velocity dispersion - mass relation and to better interpret my results about velocity segregation.

Chapter 18

Bibliography

C. Adami, A. Mazure, P. Katgert, and A. Biviano. The ESO nearby Abell cluster survey. VII. Galaxy density profiles of rich clusters of galaxies. *Astronomy & Astrophysics*, 336:63–82, August 1998.

L. Anderson, É. Aubourg, S. Bailey, F. Beutler, V. Bhardwaj, M. Blanton, and al. The clustering of galaxies in the SDSS-III Baryon Oscillation Spectroscopic Survey: baryon acoustic oscillations in the Data Releases 10 and 11 Galaxy samples. *Monthly Notices of the Royal Astronomical Society*, 441:24–62, June 2014.

A. Aragon-Salamanca, R. S. Ellis, and R. M. Sharples. Optical-infrared studies of the rich cluster of galaxies Abell 370 at $z = 0.37$. *Monthly Notices of the Royal Astronomical Society*, 248:128–138, January 1991.

A. Aragon-Salamanca, R. S. Ellis, W. J. Couch, and D. Carter. Evidence for systematic evolution in the properties of galaxies in distant clusters. *Monthly Notices of the Royal Astronomical Society*, 262:764–794, June 1993.

M. Arnaud, G. W. Pratt, R. Piffaretti, H. Böhringer, J. H. Croston, and E. Pointecouteau. The universal galaxy cluster pressure profile from a representative sample of nearby systems (REXCESS) and the Y_{SZ} - M_{500} relation. *Astronomy & Astrophysics*, 517:A92, July 2010.

K. M. Ashman, C. M. Bird, and S. E. Zepf. Detecting bimodality in astronomical datasets. *The Astronomical Journal*, 108:2348–2361, December 1994.

M. L. Balogh, S. L. Morris, H. K. C. Yee, R. G. Carlberg, and E. Ellingson. Star Formation in Cluster Galaxies at $0.2 \leq z \leq 0.55$. *The Astrophysical Journal, Letters*, 488:L75–L78, October 1997.

T. C. Beers, K. Flynn, and K. Gebhardt. Measures of location and scale for velocities in clusters of galaxies - A robust approach. *The Astronomical Journal*, 100:32–46, July 1990.

E. F. Bell and R. S. de Jong. Stellar Mass-to-Light Ratios and the Tully-Fisher Relation. *The Astrophysical Journal*, 550:212–229, March 2001.

E. F. Bell, D. H. McIntosh, N. Katz, and M. D. Weinberg. The Optical and Near-Infrared Properties of Galaxies. I. Luminosity and Stellar Mass Functions. *The Astrophysical Journal, Supplement*, 149:289–312, December 2003.

B. A. Benson, T. de Haan, J. P. Dudley, C. L. Reichardt, K. A. Aird, and et al. Cosmological Constraints from Sunyaev-Zel'dovich-selected Clusters with X-Ray Observations in the First

178 deg^2 of the South Pole Telescope Survey. *The Astrophysical Journal*, 763:147, February 2013.

M. Betoule, R. Kessler, J. Guy, J. Mosher, D. Hardin, R. Biswas, and et al. Improved cosmological constraints from a joint analysis of the SDSS-II and SNLS supernova samples. *Astronomy & Astrophysics*, 568:A22, August 2014.

B. Binggeli, G. A. Tammann, and A. Sandage. Studies of the Virgo cluster. VI - Morphological and kinematical structure of the Virgo cluster. *The Astronomical Journal*, 94:251–277, August 1987.

J. Binney and M. Merrifield. *Galactic Astronomy*. 1998.

J. Binney and S. Tremaine. *Galactic dynamics*. 1987.

A. Biviano and P. Katgert. The ESO Nearby Abell Cluster Survey. XIII. The orbits of the different types of galaxies in rich clusters. *Astronomy & Astrophysics*, 424:779–791, September 2004.

A. Biviano and B. M. Poggianti. The orbital velocity anisotropy of cluster galaxies: evolution. *Astronomy & Astrophysics*, 501:419–427, July 2009.

A. Biviano, M. Girardi, G. Giuricin, F. Mardirossian, and M. Mezzetti. Velocity segregation in galaxy clusters. *The Astrophysical Journal*, 396:35–44, September 1992.

A. Biviano, G. Giuricin, P. Katgert, A. Mazure, R. den Hartog, P. Dubath, E. Escalera, P. Focardi, D. Gerbal, B. Jones, PerePerea J. O. Le Fevre, Moles, and G. Rhee. The ESO Nearby Abell Clusters Survey (ENACS): Velocity Dispersion Distribution for a Complete Cluster Sample. *Astrophysical Letters and Communications*, 33:157, February 1996.

A. Biviano, P. Katgert, A. Mazure, M. Moles, R. den Hartog, J. Perea, and P. Focardi. The ESO Nearby Abell Cluster Survey. III. Distribution and kinematics of emission-line galaxies. *Astronomy & Astrophysics*, 321:84–104, May 1997.

A. Biviano, G. Murante, S. Borgani, A. Diaferio, K. Dolag, and M. Girardi. On the efficiency and reliability of cluster mass estimates based on member galaxies. *Astronomy & Astrophysics*, 456:23–36, September 2006.

A. Biviano, P. Rosati, I. Balestra, A. Mercurio, M. Girardi, M. Nonino, C. Grillo, M. Scodeggio, D. Lemze, D. Kelson, K. Umetsu, M. Postman, A. Zitrin, O. Czoske, S. Ettori, A. Fritz, M. Lombardi, C. Maier, E. Medezinski, S. Mei, V. Presotto, V. Strazzullo, P. Tozzi, B. Ziegler, M. Annunziatella, M. Bartelmann, N. Benitez, L. Bradley, M. Brescia, T. Broadhurst, D. Coe, R. Demarco, M. Donahue, H. Ford, R. Gobat, G. Graves, A. Koekemoer, U. Kuchner, P. Melchior, M. Meneghetti, J. Merten, L. Moustakas, E. Munari, E. Regős, B. Sartoris, S. Seitz, and W. Zheng. CLASH-VLT: The mass, velocity-anisotropy, and pseudo-phase-space density profiles of the $z = 0.44$ galaxy cluster MACS J1206.2-0847. *Astronomy & Astrophysics*, 558: A1, October 2013.

A. W. Blain, I. Smail, R. J. Ivison, and J.-P. Kneib. The history of star formation in dusty galaxies. *Monthly Notices of the Royal Astronomical Society*, 302:632–648, February 1999.

H. Böhringer and P. Schuecker. The Construction of X-ray Cluster Surveys and Their Spatial Analysis. In A. J. Banday, S. Zaroubi, and M. Bartelmann, editors, *Mining the Sky*, page 171, 2001.

H. Böhringer and N. Werner. X-ray spectroscopy of galaxy clusters: studying astrophysical processes in the largest celestial laboratories. *Astronomy & Astrophysics Reviews*, 18:127–196, February 2010.

S. Borgani and L. Guzzo. X-ray clusters of galaxies as tracers of structure in the Universe. *Nature*, 409:39–45, January 2001.

S. Borgani and A. Kravtsov. Cosmological Simulations of Galaxy Clusters. *Advanced Science Letters*, 4:204–227, February 2011.

S. Borgani, P. Rosati, P. Tozzi, S. A. Stanford, P. R. Eisenhardt, C. Lidman, B. Holden, R. Della Ceca, C. Norman, and G. Squires. Measuring Ω_m with the ROSAT Deep Cluster Survey. *The Astrophysical Journal*, 561:13–21, November 2001.

M. Brodwin, S. A. Stanford, A. H. Gonzalez, G. R. Zeimann, G. F. Snyder, C. L. Mancone, A. Pope, P. R. Eisenhardt, D. Stern, S. Alberts, M. L. N. Ashby, M. J. I. Brown, R.-R. Chary, A. Dey, A. Galametz, D. P. Gettings, B. T. Jannuzi, E. D. Miller, J. Moustakas, and L. A. Moustakas. The Era of Star Formation in Galaxy Clusters. *The Astrophysical Journal*, 779: 138, December 2013.

G. Bruzual A. and S. Charlot. Spectral evolution of stellar populations using isochrone synthesis. *The Astrophysical Journal*, 405:538–553, March 1993.

D. A. Buote. X-Ray Observations of Cluster Mergers: Cluster Morphologies and Their Implications. In L. Feretti, I. M. Gioia, and G. Giovannini, editors, *Merging Processes in Galaxy Clusters*, volume 272 of *Astrophysics and Space Science Library*, pages 79–107, June 2002.

R. A. Burenin and A. A. Vikhlinin. Cosmological parameters constraints from galaxy cluster mass function measurements in combination with other cosmological data. *Astronomy Letters*, 38:347–363, June 2012.

H. Butcher and A. Oemler, Jr. The evolution of galaxies in clusters. I - ISIT photometry of CL 0024+1654 and 3C 295. *The Astrophysical Journal*, 219:18–30, January 1978.

D. Calzetti, L. Armus, R. C. Bohlin, A. L. Kinney, J. Koornneef, and T. Storchi-Bergmann. The Dust Content and Opacity of Actively Star-forming Galaxies. *The Astrophysical Journal*, 533:682–695, April 2000.

R. G. Carlberg, H. K. C. Yee, E. Ellingson, S. L. Morris, R. Abraham, P. Gravel, C. J. Pritchet, T. Smecker-Hane, F. D. A. Hartwick, J. E. Hesser, J. B. Hutchings, and J. B. Oke. The Dynamical Equilibrium of Galaxy Clusters. *The Astrophysical Journal, Letters*, 476:L7–L10, February 1997.

J. E. Carlstrom, P. A. R. Ade, K. A. Aird, B. A. Benson, L. E. Bleem, S. Busetti, C. L. Chang, and al. The 10 Meter South Pole Telescope. *Publications of the Astronomical Society of the Pacific*, 123:568–581, May 2011.

E. R. Carrasco, E. S. Cypriano, G. B. L. Neto, H. Cuevas, L. Sodré, Jr., C. M. de Oliveira, and A. Ramirez. Witnessing the Formation of a Galaxy Cluster at $z = 0.485$: Optical and X-Ray Properties of RX J1117.4+0743 ([VMF 98] 097). *The Astrophysical Journal*, 664:777–790, August 2007.

N. Clerc, T. Sadibekova, M. Pierre, F. Pacaud, J.-P. Le Fèvre, C. Adami, B. Altieri, and I. Valtchanov. The cosmological analysis of X-ray cluster surveys - II. Application of the CR-HR method to the XMM archive. *Monthly Notices of the Royal Astronomical Society*, 423:3561–3583, July 2012.

S. Cole, C. G. Lacey, C. M. Baugh, and C. S. Frenk. Hierarchical galaxy formation. *Monthly Notices of the Royal Astronomical Society*, 319:168–204, November 2000.

M. Colless and A. M. Dunn. Structure and Dynamics of the Coma Cluster. *The Astrophysical Journal*, 458:435, February 1996.

M. C. Cooper, J. A. Newman, B. J. Weiner, R. Yan, C. N. A. Willmer, K. Bundy, A. L. Coil, C. J. Conselice, M. Davis, S. M. Faber, B. F. Gerke, P. Guhathakurta, D. C. Koo, and K. G. Noeske. The DEEP2 Galaxy Redshift Survey: the role of galaxy environment in the cosmic star formation history. *Monthly Notices of the Royal Astronomical Society*, 383:1058–1078, January 2008.

O. Cucciati, G. De Lucia, E. Zucca, A. Iovino, S. de la Torre, L. Pozzetti, J. Blaizot, G. Zamorani, M. Bolzonella, D. Vergani, S. Bardelli, L. Tresse, and A. Pollo. Comparison of the VIMOS-VLT Deep Survey with the Munich semi-analytical model. II. The colour - density relation up to $z \sim 1.5$. *Astronomy & Astrophysics*, 548:A108, December 2012.

L. Danese, G. de Zotti, and G. di Tullio. On velocity dispersions of galaxies in rich clusters. *Astronomy & Astrophysics*, 82:322–327, February 1980.

H. Dannerbauer, C. de Breuck, G. Miley, B. Emonts, H. Rottgering, J. Kurk, D. Wylezalek, J. Santos, Y. Koyama, M. Tanaka, B. Altieri, D. Coia, A. Galametz, M. Lehnert, T. Matiz, T. Kodama, M. Sanchez-Portal, I. Valtchanov, B. Venemans, B. Ziegler, and N. Seymour. Characterizing Dusty Starbursts at $z = 2.2$ in a High Density Field. ATNF Proposal, October 2014.

R. Demarco, P. Rosati, C. Lidman, N. L. Homeier, E. Scannapieco, N. Benítez, V. Mainieri, M. Nonino, M. Girardi, S. A. Stanford, P. Tozzi, S. Borgani, J. Silk, G. Squires, and T. J. Broadhurst. A VLT spectroscopic survey of RX J0152.7-1357, a forming cluster of galaxies at $z = 0.837$. *Astronomy & Astrophysics*, 432:381–394, March 2005.

R. Demarco, P. Rosati, C. Lidman, M. Girardi, M. Nonino, A. Rettura, V. Strazzullo, A. van der Wel, H. C. Ford, V. Mainieri, B. P. Holden, S. A. Stanford, J. P. Blakeslee, R. Gobat, M. Postman, P. Tozzi, R. A. Overzier, A. W. Zirm, N. Benítez, N. L. Homeier, G. D. Illingworth, L. Infante, M. J. Jee, S. Mei, F. Menanteau, V. Motta, W. Zheng, M. Clampin, and G. Hartig. VLT and ACS Observations of RDCS J1252.9-2927: Dynamical Structure and Galaxy Populations in a Massive Cluster at $z = 1.237$. *The Astrophysical Journal*, 663: 164–182, July 2007.

R. Demarco, R. Gobat, P. Rosati, C. Lidman, A. Rettura, M. Nonino, A. van der Wel, M. J. Jee, J. P. Blakeslee, H. C. Ford, and M. Postman. Star Formation Histories in a Cluster Environment at $z \sim 0.84$. *The Astrophysical Journal*, 725:1252–1276, December 2010.

R. den Hartog and P. Katgert. On the dynamics of the cores of galaxy clusters. *Monthly Notices of the Royal Astronomical Society*, 279:349–388, March 1996.

K. Dolag, M. Bartelmann, F. Perrotta, C. Baccigalupi, L. Moscardini, M. Meneghetti, and G. Tormen. Numerical study of halo concentrations in dark-energy cosmologies. *Astronomy & Astrophysics*, 416:853–864, March 2004.

M. Domínguez, H. Muriel, and D. G. Lambas. Galaxy Morphological Segregation in Clusters: Local versus Global Conditions. *The Astronomical Journal*, 121:1266–1274, March 2001.

A. Dressler. A catalog of morphological types in 55 rich clusters of galaxies. *The Astrophysical Journal, Supplement*, 42:565–609, April 1980.

A. Dressler and J. E. Gunn. Spectroscopy of galaxies in distant clusters. IV - A catalog of photometry and spectroscopy for galaxies in seven clusters with z in the range of 0.35 to 0.55. *The Astrophysical Journal, Supplement*, 78:1–60, January 1992.

A. Dressler, A. Oemler, Jr., W. J. Couch, I. Smail, R. S. Ellis, A. Barger, H. Butcher, B. M. Poggianti, and R. M. Sharples. Evolution since $z = 0.5$ of the Morphology-Density Relation for Clusters of Galaxies. *The Astrophysical Journal*, 490:577–591, December 1997.

A. Dressler, I. Smail, B. M. Poggianti, H. Butcher, W. J. Couch, R. S. Ellis, and A. Oemler, Jr. A Spectroscopic Catalog of 10 Distant Rich Clusters of Galaxies. *The Astrophysical Journal, Supplement*, 122:51–80, May 1999.

A. Dressler, A. Oemler, Jr., B. M. Poggianti, I. Smail, S. Trager, S. A. Shectman, W. J. Couch, and R. S. Ellis. Studying the Star Formation Histories of Galaxies in Clusters from Composite Spectra. *The Astrophysical Journal*, 617:867–878, December 2004.

D. Elbaz, E. Daddi, D. Le Borgne, M. Dickinson, D. M. Alexander, R.-R. Chary, J.-L. Starck, W. N. Brandt, M. Kitzbichler, E. MacDonald, M. Nonino, P. Popesso, D. Stern, and E. Vanzella. The reversal of the star formation-density relation in the distant universe. *Astronomy & Astrophysics*, 468:33–48, June 2007.

E. Ellingson, H. K. C. Yee, R. G. Abraham, S. L. Morris, R. G. Carlberg, and T. A. Smecker-Hane. The CNOC Cluster Redshift Survey Catalogs. III. MS 1621.5+2640 and MS 0302.7+1658. *The Astrophysical Journal, Supplement*, 113:1–21, 1997.

E. Ellingson, H. K. C. Yee, R. G. Abraham, S. L. Morris, and R. G. Carlberg. The CNOC Cluster Redshift Survey Catalogs. VI. MS 0015.9+1609 and MS 0451.5-0305. *The Astrophysical Journal, Supplement*, 116:247–262, June 1998.

R. S. Ellis, I. Smail, A. Dressler, W. J. Couch, A. Oemler, Jr., H. Butcher, and R. M. Sharples. The Homogeneity of Spheroidal Populations in Distant Clusters. *The Astrophysical Journal*, 483:582–596, July 1997.

S. Ettori. The generalized scaling relations for X-ray galaxy clusters: the most powerful mass proxy. *Monthly Notices of the Royal Astronomical Society*, 435:1265–1277, October 2013.

S. Ettori, S. De Grandi, and S. Molendi. Gravitating mass profiles of nearby galaxy clusters and relations with X-ray gas temperature, luminosity and mass. *Astronomy and Astrophysics*, 391:841–855, September 2002.

A. E. Evrard and I. M. Gioia. Clusters, Cosmology and Mergers. In L. Feretti, I. M. Gioia, and G. Giovannini, editors, *Merging Processes in Galaxy Clusters*, volume 272 of *Astrophysics and Space Science Library*, pages 253–304, June 2002.

G. Evrard. The Future of Cosmology with Galaxy Clusters. In *KITP Program: Galaxy-Intergalactic Medium Interactions*, page 6, October 2004.

D. G. Fabricant, M. W. Bautz, and J. E. McClintock. Galaxy evolution in distant, X-ray selected clusters of galaxies. II: CL 0303+1658 and CL 0303+1717. *The Astronomical Journal*, 107: 8–23, January 1994.

D. Fadda, M. Girardi, G. Giuricin, F. Mardirossian, and M. Mezzetti. The Observational Distribution of Internal Velocity Dispersions in Nearby Galaxy Clusters. *The Astrophysical Journal*, 473:670, December 1996.

R. Fassbender, H. Böhringer, J. S. Santos, G. W. Pratt, R. Šuhada, J. Kohnert, M. Lerchster, E. Rovilos, D. Pierini, G. Chon, A. D. Schwope, G. Lamer, M. Mühlegger, P. Rosati, H. Quintana, A. Nastasi, A. de Hoon, S. Seitz, and J. J. Mohr. A pan-chromatic view of the galaxy cluster XMMU J1230.3+1339 at $z = 0.975$. Observing the assembly of a massive system. *Astronomy and Astrophysics*, 527:A78, March 2011.

R. Fassbender, A. Nastasi, J. S. Santos, C. Lidman, M. Verdugo, Y. Koyama, P. Rosati, D. Pierini, N. Padilla, A. D. Romeo, N. Menci, A. Bongiorno, M. Castellano, P. Cerulo, A. Fontana, A. Galametz, A. Grazian, A. Lamastra, L. Pentericci, V. Sommariva, V. Strazzullo, R. Šuhada, and P. Tozzi. Galaxy population properties of the massive X-ray luminous galaxy cluster XDCP J0044.0-2033 at $z = 1.58$. Red-sequence formation, massive galaxy assembly, and central star formation activity. *Astronomy & Astrophysics*, 568:A5, August 2014.

M. Fukugita, K. Shimasaku, and T. Ichikawa. Galaxy Colors in Various Photometric Band Systems. *Publications of the Astronomical Society of the Pacific*, 107:945, October 1995.

J. S. Gallagher, III, D. A. Hunter, and H. Bushouse. Evolutionary status of luminous blue galaxies. *Publications of the Astronomical Society of the Pacific*, 96:788, October 1984.

B. Gerken, B. Ziegler, M. Balogh, D. Gilbank, A. Fritz, and K. Jäger. Star formation activity of intermediate redshift cluster galaxies out to the infall regions. *Astronomy & Astrophysics*, 421:59–70, July 2004.

I. M. Gioia, J. P. Henry, C. R. Mullis, H. Ebeling, and A. Wolter. RX J1716.6+6708: A Young Cluster at $z = 0.81$. *The Astronomical Journal*, 117:2608–2616, June 1999.

M. Girardi and A. Biviano. Optical Analysis of Cluster Mergers. In L. Feretti, I. M. Gioia, and G. Giovannini, editors, *Merging Processes in Galaxy Clusters*, volume 272 of *Astrophysics and Space Science Library*, pages 39–77, June 2002.

M. Girardi and M. Mezzetti. Evolution of the Internal Dynamics of Galaxy Clusters. *The Astrophysical Journal*, 548:79–96, February 2001.

M. Girardi, A. Biviano, G. Giuricin, F. Mardirossian, and M. Mezzetti. Velocity dispersions in galaxy clusters. *The Astrophysical Journal*, 404:38–50, February 1993.

M. Girardi, D. Fadda, G. Giuricin, F. Mardirossian, M. Mezzetti, and A. Biviano. Galaxy Clusters: X-ray Temperature vs. Galaxy Velocity Dispersion. *Astrophysical Letters and Communications*, 33:163, February 1996.

M. Girardi, G. Giuricin, F. Mardirossian, M. Mezzetti, and W. Boschin. Optical Mass Estimates of Galaxy Clusters. *The Astrophysical Journal*, 505:74–95, September 1998.

M. Girardi, E. Rigoni, F. Mardirossian, and M. Mezzetti. Morphology and luminosity segregation of galaxies in nearby loose groups. *Astronomy & Astrophysics*, 406:403–414, August 2003.

M. Girardi, R. Demarco, P. Rosati, and S. Borgani. Internal dynamics of the $z \sim 0.8$ cluster RX J0152.7-1357. *Astronomy & Astrophysics*, 442:29–41, October 2005.

M. Girardi, S. Bardelli, R. Barrena, W. Boschin, F. Gastaldello, and M. Nonino. Internal dynamics of Abell 2254: a merging galaxy cluster with a clumpy, diffuse radio emission. *Astronomy & Astrophysics*, 536:A89, December 2011.

M. Girardi, A. Mercurio, I. Balestra, M. Nonino, A. Biviano, C. Grillo, P. Rosati, M. Annunziatella, R. Demarco, A. Fritz, R. Gobat, D. Lemze, V. Presotto, M. Scodeggio, P. Tozzi, G. Bartosch Caminha, M. Brescia, D. Coe, D. Kelson, A. Koekemoer, M. Lombardi, E. Medezinski, M. Postman, B. Sartoris, K. Umetsu, A. Zitrin, W. Boschin, O. Czoske, G. De Lucia, U. Kuchner, C. Maier, M. Meneghetti, P. Monaco, A. Monna, E. Munari, S. Seitz, M. Verdugo, and B. Ziegler. CLASH-VLT: Substructure in the galaxy cluster MACS J1206.2-0847 from kinematics of galaxy populations. *Astronomy & Astrophysics*, 579:A4, July 2015.

T. Goto, S. Arnouts, M. Malkan, T. Takagi, H. Inami, C. Pearson, T. Wada, H. Matsuhara, C. Yamauchi, T. T. Takeuchi, T. Nakagawa, S. Oyabu, D. Ishihara, D. B. Sanders, E. Le Floc'h, H. M. Lee, W.-S. Jeong, S. Serjeant, and C. Sedgwick. Infrared luminosity functions of AKARI Sloan Digital Sky Survey galaxies. *Monthly Notices of the Royal Astronomical Society*, 414:1903–1913, July 2011.

G. L. Granato, C. Ragone-Figueroa, R. Domínguez-Tenreiro, A. Obreja, S. Borgani, G. De Lucia, and G. Murante. The early phases of galaxy clusters formation in IR: coupling hydrodynamical simulations with GRASIL-3D. *Monthly Notices of the Royal Astronomical Society*, 450:1320–1332, June 2015.

J. E. Gunn and J. R. Gott, III. On the Infall of Matter Into Clusters of Galaxies and Some Effects on Their Evolution. *The Astrophysical Journal*, 176:1, August 1972.

C. Halliday, B. Milvang-Jensen, S. Poirier, B. M. Poggianti, P. Jablonka, A. Aragón-Salamanca, R. P. Saglia, G. De Lucia, R. Pelló, L. Simard, D. I. Clowe, G. Rudnick, J. J. Dalcanton, S. D. M. White, and D. Zaritsky. Spectroscopy of clusters in the ESO Distant Cluster Survey (EDisCS). Redshifts, velocity dispersions and substructure for 5 clusters. *Astronomy & Astrophysics*, 427:397–413, November 2004.

M. Hayashi, T. Kodama, Y. Koyama, K.-I. Tadaki, and I. Tanaka. Properties of star-forming galaxies in a cluster and its surrounding structure at $z = 1.46$. *Monthly Notices of the Royal Astronomical Society*, 415:2670–2687, August 2011.

M. Hayashi, T. Kodama, K.-i. Tadaki, Y. Koyama, and I. Tanaka. A Starbursting Proto-cluster in Making Associated with a Radio Galaxy at $z = 2.53$ Discovered by Hα Imaging. *The Astrophysical Journal*, 757:15, September 2012.

M. Hilton, E. Lloyd-Davies, S. A. Stanford, J. P. Stott, C. A. Collins, A. K. Romer, M. Hosmer, B. Hoyle, S. T. Kay, A. R. Liddle, N. Mehrtens, C. J. Miller, M. Sahlén, and P. T. P. Viana. The XMM Cluster Survey: Active Galactic Nuclei and Starburst Galaxies in XMMXCS J2215.9-1738 at $z = 1.46$. *The Astrophysical Journal*, 718:133–147, July 2010.

G. Hinshaw, D. Larson, E. Komatsu, D. N. Spergel, C. L. Bennett, J. Dunkley, M. R. Nolta, M. Halpern, R. S. Hill, N. Odegard, L. Page, K. M. Smith, J. L. Weiland, B. Gold, N. Jarosik, A. Kogut, M. Limon, S. S. Meyer, G. S. Tucker, E. Wollack, and E. L. Wright. Nine-year Wilkinson Microwave Anisotropy Probe (WMAP) Observations: Cosmological Parameter Results. *The Astrophysical Journal, Supplement*, 208:19, October 2013.

H. Hoekstra. How well can we determine cluster mass profiles from weak lensing? *Monthly Notices of the Royal Astronomical Society*, 339:1155–1162, March 2003.

G. Hütsi. Power spectrum of the maxBCG sample: detection of acoustic oscillations using galaxy clusters. *Monthly Notices of the Royal Astronomical Society*, 401:2477–2489, February 2010.

I. Jørgensen and K. Chiboucas. Stellar Populations and Evolution of Early-type Cluster Galaxies: Constraints from Optical Imaging and Spectroscopy of $z = 0.5 - 0.9$ Galaxy Clusters. *The Astronomical Journal*, 145:77, March 2013.

I. Jørgensen, M. Bergmann, R. Davies, J. Barr, M. Takamiya, and D. Crampton. RX J0152.7-1357: Stellar Populations in an X-Ray Luminous Galaxy Cluster at $z = 0.83$. *The Astronomical Journal*, 129:1249–1286, March 2005.

P. Katgert, A. Biviano, and A. Mazure. The ESO Nearby Abell Cluster Survey. XII. The Mass and Mass-to-Light Ratio Profiles of Rich Clusters. *The Astrophysical Journal*, 600:657–669, January 2004.

G. Kauffmann. The age of elliptical galaxies and bulges in a merger model. *Monthly Notices of the Royal Astronomical Society*, 281:487–492, July 1996.

G. Kauffmann, J. M. Colberg, A. Diaferio, and S. D. M. White. Clustering of galaxies in a hierarchical universe - II. Evolution to high redshift. *Monthly Notices of the Royal Astronomical Society*, 307:529–536, August 1999.

R. C. Kennicutt, Jr. The rate of star formation in normal disk galaxies. *The Astrophysical Journal*, 272:54–67, September 1983.

R. C. Kennicutt, Jr. The Birth of Stars in Galaxies. In J. M. Shull and H. A. Thronson, editors, *The Environment and Evolution of Galaxies*, volume 188 of *Astrophysics and Space Science Library*, page 533, 1993.

R. C. Kennicutt, Jr. Star Formation in Galaxies Along the Hubble Sequence. *Annual Review of Astronomy & Astrophysics*, 36:189–232, 1998.

R. C. Kennicutt, Jr., P. Tamblyn, and C. E. Congdon. Past and future star formation in disk galaxies. *The Astrophysical Journal*, 435:22–36, November 1994.

L. J. Kewley, M. J. Geller, and R. A. Jansen. [O II] as a Star Formation Rate Indicator. *The Astronomical Journal*, 127:2002–2030, April 2004.

T. D. Kitching, A. F. Heavens, J. Alsing, T. Erben, C. Heymans, H. Hildebrandt, H. Hoekstra, A. Jaffe, A. Kiessling, Y. Mellier, L. Miller, L. van Waerbeke, J. Benjamin, J. Coupon, L. Fu, M. J. Hudson, M. Kilbinger, K. Kuijken, B. T. P. Rowe, T. Schrabback, E. Semboloni, and M. Velander. 3D cosmic shear: cosmology from CFHTLenS. *Monthly Notices of the Royal Astronomical Society*, 442:1326–1349, August 2014.

B. P. Koester, T. A. McKay, J. Annis, R. H. Wechsler, A. Evrard, L. Bleem, M. Becker, D. Johnston, E. Sheldon, R. Nichol, C. Miller, R. Scranton, N. Bahcall, J. Barentine, H. Brewington, J. Brinkmann, M. Harvanek, S. Kleinman, J. Krzesinski, D. Long, A. Nitta, D. P. Schneider, S. Sneddin, W. Voges, and D. York. A MaxBCG Catalog of 13,823 Galaxy Clusters from the Sloan Digital Sky Survey. *The Astrophysical Journal*, 660:239–255, May 2007.

Y. Koyama, T. Kodama, K.-i. Tadaki, M. Hayashi, M. Tanaka, I. Smail, I. Tanaka, and J. Kurk. Massive starburst galaxies in a $z = 2.16$ proto-cluster unveiled by panoramic Hα mapping. *Monthly Notices of the Royal Astronomical Society*, 428:1551–1564, January 2013.

Y. Koyama, T. Kodama, K.-i. Tadaki, M. Hayashi, I. Tanaka, and R. Shimakawa. The Environmental Impacts on the Star Formation Main Sequence: An Hα Study of the Newly Discovered Rich Cluster at $z = 1.52$. *The Astrophysical Journal*, 789:18, July 2014.

A. V. Kravtsov and S. Borgani. Formation of Galaxy Clusters. *Annual Review of Astronomy & Astrophysics*, 50:353–409, September 2012.

A. V. Kravtsov, A. Vikhlinin, and D. Nagai. A New Robust Low-Scatter X-Ray Mass Indicator for Clusters of Galaxies. *The Astrophysical Journal*, 650:128–136, October 2006.

R. Laureijs, J. Amiaux, S. Arduini, J. . Augueres, J. Brinchmann, R. Cole, M. Cropper, C. Dabin, L. Duvet, A. Ealet, and et al. Euclid Definition Study Report. *ArXiv e-prints*, October 2011.

M. Lerchster, S. Seitz, F. Brimioulle, R. Fassbender, M. Rovilos, H. Böhringer, D. Pierini, M. Kilbinger, A. Finoguenov, H. Quintana, and R. Bender. The massive galaxy cluster XMMU J1230.3+1339 at $z \sim 1$: colour-magnitude relation, Butcher-Oemler effect, X-ray and weak lensing mass estimates. *Monthly Notices of the Royal Astronomical Society*, 411: 2667–2694, March 2011.

S. J. Lilly, O. Le Fevre, F. Hammer, and D. Crampton. The Canada-France Redshift Survey: The Luminosity Density and Star Formation History of the Universe to z approximately 1. *The Astrophysical Journal, Letters*, 460:L1, March 1996.

L. M. Lubin. The Palomar Distant Cluster Survey. III. The Colors of the Cluster Galaxy. *The Astronomical Journal*, 112:23, July 1996.

L. M. Lubin, J. B. Oke, and M. Postman. Evidence for Cluster Evolution from an Improved Measurement of the Velocity Dispersion and Morphological Fraction of Cluster 1324+3011 at $z = 0.76$. *The Astronomical Journal*, 124:1905–1917, October 2002.

P. Madau, H. C. Ferguson, M. E. Dickinson, M. Giavalisco, C. C. Steidel, and A. Fruchter. High-redshift galaxies in the Hubble Deep Field: colour selection and star formation history to $z \sim 4$. *Monthly Notices of the Royal Astronomical Society*, 283:1388–1404, December 1996.

P. Madau, L. Pozzetti, and M. Dickinson. The Star Formation History of Field Galaxies. *The Astrophysical Journal*, 498:106–116, May 1998.

A. Mana, T. Giannantonio, J. Weller, B. Hoyle, G. Hütsi, and B. Sartoris. Combining clustering and abundances of galaxy clusters to test cosmology and primordial non-Gaussianity. *Monthly Notices of the Royal Astronomical Society*, 434:684–695, September 2013.

A. B. Mantz, S. W. Allen, R. G. Morris, R. W. Schmidt, A. von der Linden, and O. Urban. Cosmology and astrophysics from relaxed galaxy clusters - I. Sample selection. *Monthly Notices of the Royal Astronomical Society*, 449:199–219, May 2015.

T. A. Marriage, J. Baptiste Juin, Y.-T. Lin, and al. The Atacama Cosmology Telescope: Extragalactic Sources at 148 GHz in the 2008 Survey. *The Astrophysical Journal*, 731:100, April 2011.

N. Mehrtens, A. K. Romer, M. Hilton, E. J. Lloyd-Davies, C. J. Miller, S. A. Stanford, M. Hosmer, B. Hoyle, C. A. Collins, A. R. Liddle, P. T. P. Viana, R. C. Nichol, J. P. Stott, E. N. Dubois, S. T. Kay, M. Sahlén, O. Young, C. J. Short, L. Christodoulou, W. A. Watson, M. Davidson, C. D. Harrison, L. Baruah, M. Smith, C. Burke, J. A. Mayers, P.-J. Deadman, P. J. Rooney, E. M. Edmondson, M. West, H. C. Campbell, A. C. Edge, R. G. Mann, K. Sabirli, D. Wake, C. Benoist, L. da Costa, M. A. G. Maia, and R. Ogando. The XMM Cluster Survey: optical analysis methodology and the first data release. *Monthly Notices of the Royal Astronomical Society*, 423:1024–1052, June 2012.

S. Mei, B. P. Holden, J. P. Blakeslee, H. C. Ford, M. Franx, N. L. Homeier, G. D. Illingworth, M. J. Jee, R. Overzier, M. Postman, P. Rosati, A. Van der Wel, and J. G. Bartlett. Evolution of the Color-Magnitude Relation in Galaxy Clusters at $z \sim 1$ from the ACS Intermediate Redshift Cluster Survey. *The Astrophysical Journal*, 690:42–68, January 2009.

A. Merloni, P. Predehl, W. Becker, H. Böhringer, T. Boller, H. Brunner, M. Brusa, K. Dennerl, M. Freyberg, P. Friedrich, A. Georgakakis, F. Haberl, G. Hasinger, N. Meidinger, J. Mohr, K. Nandra, A. Rau, T. H. Reiprich, J. Robrade, M. Salvato, A. Santangelo, M. Sasaki, A. Schwope, J. Wilms, and t. German eROSITA Consortium. eROSITA Science Book: Mapping the Structure of the Energetic Universe. *ArXiv e-prints*, September 2012.

B. Milvang-Jensen, S. Noll, C. Halliday, B. M. Poggianti, P. Jablonka, A. Aragón-Salamanca, R. P. Saglia, N. Nowak, A. von der Linden, G. De Lucia, R. Pelló, J. Moustakas, S. Poirier, S. P. Bamford, D. I. Clowe, J. J. Dalcanton, G. H. Rudnick, L. Simard, S. D. M. White, and D. Zaritsky. Spectroscopy of clusters in the ESO distant cluster survey (EDisCS). II.. Redshifts, velocity dispersions, and substructure for clusters in the last 15 fields. *Astronomy & Astrophysics*, 482:419–449, May 2008.

B. Moore, N. Katz, G. Lake, A. Dressler, and A. Oemler. Galaxy harassment and the evolution of clusters of galaxies. *Nature*, 379:613–616, February 1996.

C. Moss and R. J. Dickens. Redshifts of galaxies in the cluster Abell 262, and in the region of the Pisces group /centred on NGC 383/. *Monthly Notices of the Royal Astronomical Society*, 178:701–715, March 1977.

E. Munari, A. Biviano, S. Borgani, G. Murante, and D. Fabjan. The relation between velocity dispersion and mass in simulated clusters of galaxies: dependence on the tracer and the baryonic physics. *Monthly Notices of the Royal Astronomical Society*, 430:2638–2649, April 2013.

E. Munari, A. Biviano, and G. A. Mamon. Mass, velocity anisotropy, and pseudo phase-space density profiles of Abell 2142. *Astronomy & Astrophysics*, 566:A68, June 2014.

J. B. Oke, J. E. Gunn, and J. G. Hoessel. The Evolution of Red Galaxies in Clusters T $z = 0.5$. *The Astronomical Journal*, 111:29, January 1996.

A. Pisani. A Non-Parametric and Scale-Independent Method for Cluster Analysis - Part One - the Univariate Case. *Monthly Notices of the Royal Astronomical Society*, 265:706, December 1993.

A. Pisani. A non-parametric and scale-independent method for cluster analysis - II. The multivariate case. *Monthly Notices of the Royal Astronomical Society*, 278:697–726, February 1996.

Planck Collaboration. Planck early results. XXVI. Detection with Planck and confirmation by XMM-Newton of PLCK G266.6-27.3, an exceptionally X-ray luminous and massive galaxy cluster at $z \sim 1$. *Astronomy & Astrophysics*, 536:A26, December 2011.

Planck Collaboration, P. A. R. Ade, N. Aghanim, C. Armitage-Caplan, M. Arnaud, M. Ashdown, F. Atrio-Barandela, J. Aumont, H. Aussel, C. Baccigalupi, and et al. Planck 2013 results. XXIX. The Planck catalogue of Sunyaev-Zeldovich sources. *Astronomy & Astrophysics*, 571:A29, November 2014a.

Planck Collaboration, P. A. R. Ade, N. Aghanim, C. Armitage-Caplan, M. Arnaud, M. Ashdown, F. Atrio-Barandela, J. Aumont, C. Baccigalupi, A. J. Banday, and et al. Planck 2013 results. XXX. Cosmic infrared background measurements and implications for star formation. *Astronomy & Astrophysics*, 571:A30, November 2014b.

B. M. Poggianti. K and evolutionary corrections from UV to IR. *Astronomy & Astrophysics, Supplement*, 122:399–407, May 1997.

B. M. Poggianti and G. Barbaro. Starbursts and the Butcher-Oemler effect in galaxy clusters. *Astronomy & Astrophysics*, 314:379–392, October 1996.

B. M. Poggianti, I. Smail, A. Dressler, W. J. Couch, A. J. Barger, H. Butcher, R. S. Ellis, and A. Oemler, Jr. The Star Formation Histories of Galaxies in Distant Clusters. *The Astrophysical Journal*, 518:576–593, June 1999.

M. Postman and M. J. Geller. The morphology-density relation - The group connection. *The Astrophysical Journal*, 281:95–99, June 1984.

M. Postman, L. M. Lubin, and J. B. Oke. A Study of Nine High-Redshift Clusters of Galaxies. II. Photometry, Spectra, and Ages of Clusters 0023+0423 and 1604+4304. *The Astronomical Journal*, 116:560–583, August 1998.

M. Postman, L. M. Lubin, and J. B. Oke. A Study of Nine High-Redshift Clusters of Galaxies. IV. Photometry and Spectra of Clusters 1324+3011 and 1604+4321. *The Astronomical Journal*, 122:1125–1150, September 2001.

K. D. Rakos and J. M. Schombert. Color evolution from $z = 0$ to $z = 1$. *The Astrophysical Journal*, 439:47–59, January 1995.

D. Rapetti, S. W. Allen, A. Mantz, R. G. Morris, H. Ebeling, R. Schmidt, and A. C. Fabian. Constraining Dark Energy and Gravity with X-Ray Galaxy Clusters. In H. V. Klapdor-Kleingrothaus and I. V. Krivosheina, editors, *Dark Matter in Astrophysics and Particle Physics, Dark 2009*, pages 426–439, December 2010.

A. Reichert, H. Böhringer, R. Fassbender, and M. Mühlegger. Observational constraints on the redshift evolution of X-ray scaling relations of galaxy clusters out to $z \sim 1.5$. *Astronomy & Astrophysics*, 535:A4, November 2011.

K. Rines, M. J. Geller, M. J. Kurtz, and A. Diaferio. CAIRNS: The Cluster and Infall Region Nearby Survey. III. Environmental Dependence of Hα Properties of Galaxies. *The Astronomical Journal*, 130:1482–1501, October 2005.

K. Rines, M. J. Geller, A. Diaferio, and M. J. Kurtz. Measuring the Ultimate Halo Mass of Galaxy Clusters: Redshifts and Mass Profiles from the Hectospec Cluster Survey (HeCS). *The Astrophysical Journal*, 767:15, April 2013.

P. Rosati, S. A. Stanford, P. R. Eisenhardt, R. Elston, H. Spinrad, D. Stern, and A. Dey. An X-Ray-Selected Galaxy Cluster at $z = 1.26$. *The Astronomical Journal*, 118:76–85, July 1999.

P. Rosati, P. Tozzi, R. Gobat, J. S. Santos, M. Nonino, R. Demarco, C. Lidman, C. R. Mullis, V. Strazzullo, H. Böhringer, R. Fassbender, K. Dawson, M. Tanaka, J. Jee, H. Ford, G. Lamer, and A. Schwope. Multi-wavelength study of XMMU J2235.3-2557: the most massive galaxy cluster at $z > 1$. *Astronomy & Astrophysics*, 508:583–591, December 2009.

P. Rosati, I. Balestra, C. Grillo, A. Mercurio, M. Nonino, A. Biviano, M. Girardi, E. Vanzella, and Clash-VLT Team. CLASH-VLT: A VIMOS Large Programme to Map the Dark Matter Mass Distribution in Galaxy Clusters and Probe Distant Lensed Galaxies. *The Messenger*, 158:48–53, December 2014.

E. Rozo, R. H. Wechsler, E. S. Rykoff, J. T. Annis, M. R. Becker, A. E. Evrard, J. A. Frieman, S. M. Hansen, J. Hao, D. E. Johnston, B. P. Koester, T. A. McKay, E. S. Sheldon, and D. H. Weinberg. Cosmological Constraints from the Sloan Digital Sky Survey maxBCG Cluster Catalog. *The Astrophysical Journal*, 708:645–660, January 2010.

E. Rozo, E. Rykoff, B. Koester, B. Nord, H.-Y. Wu, A. Evrard, and R. Wechsler. Extrinsic Sources of Scatter in the Richness-mass Relation of Galaxy Clusters. *The Astrophysical Journal*, 740:53, October 2011.

E. Rozo, J. G. Bartlett, A. E. Evrard, and E. S. Rykoff. Closing the loop: a self-consistent model of optical, X-ray and Sunyaev-Zel'dovich scaling relations for clusters of Galaxies. *Monthly Notices of the Royal Astronomical Society*, 438:78–96, February 2014.

E. S. Rykoff, B. P. Koester, E. Rozo, J. Annis, A. E. Evrard, S. M. Hansen, J. Hao, D. E. Johnston, T. A. McKay, and R. H. Wechsler. Robust Optical Richness Estimation with Reduced Scatter. *The Astrophysical Journal*, 746:178, February 2012.

A. Sandage. Star formation rates, galaxy morphology, and the Hubble sequence. *Astronomy & Astrophysics*, 161:89–101, June 1986.

J. S. Santos, R. Fassbender, A. Nastasi, H. Böhringer, P. Rosati, R. Šuhada, D. Pierini, M. Nonino, M. Mühlegger, H. Quintana, A. D. Schwope, G. Lamer, A. de Hoon, and V. Strazzullo. Discovery of a massive X-ray luminous galaxy cluster at $z = 1.579$. *Astronomy & Astrophysics*, 531:L15, July 2011.

J. S. Santos, B. Altieri, P. Popesso, V. Strazzullo, I. Valtchanov, S. Berta, H. Böhringer, L. Conversi, R. Demarco, A. C. Edge, C. Lidman, D. Lutz, L. Metcalfe, C. R. Mullis, I. Pintos-Castro, M. Sánchez-Portal, T. D. Rawle, P. Rosati, A. M. Swinbank, and M. Tanaka. Dust-obscured star formation in the outskirts of XMMU J2235.3-2557, a massive galaxy cluster at $z = 1.4$. *Monthly Notices of the Royal Astronomical Society*, 433:1287–1299, August 2013.

J. S. Santos, B. Altieri, M. Tanaka, I. Valtchanov, A. Saintonge, M. Dickinson, S. Foucaud, T. Kodama, T. D. Rawle, and K. Tadaki. Star formation in the cluster CLG0218.3-0510 at $z = 1.62$ and its large-scale environment: the infrared perspective. *Monthly Notices of the Royal Astronomical Society*, 438:2565–2577, March 2014.

J. S. Santos, B. Altieri, I. Valtchanov, A. Nastasi, H. Böhringer, G. Cresci, D. Elbaz, R. Fassbender, P. Rosati, P. Tozzi, and M. Verdugo. The reversal of the SF-density relation in a massive, X-ray-selected galaxy cluster at $z = 1.58$: results from Herschel. *Monthly Notices of the Royal Astronomical Society*, 447:L65–L69, February 2015.

C. L. Sarazin. X-ray emission from clusters of galaxies. *Reviews of Modern Physics*, 58:1–115, January 1986.

A. Saro, J. J. Mohr, G. Bazin, and K. Dolag. Toward Unbiased Galaxy Cluster Masses from Line-of-sight Velocity Dispersions. *The Astrophysical Journal*, 772:47, July 2013.

B. Sartoris, A. Biviano, C. Fedeli, J. G. Bartlett, S. Borgani, M. Costanzi, C. Giocoli, L. Moscardini, J. Weller, B. Ascaso, S. Bardelli, S. Maurogordato, and P. T. P Viana. Next Generation Cosmology: Constraints from the Euclid Galaxy Cluster Survey. *ArXiv e-prints*, May 2015.

E. F. Schlafly and D. P. Finkbeiner. Measuring Reddening with Sloan Digital Sky Survey Stellar Spectra and Recalibrating SFD. *The Astrophysical Journal*, 737:103, August 2011.

P. Schuecker, R. R. Caldwell, H. Böhringer, C. A. Collins, L. Guzzo, and N. N. Weinberg. Observational constraints on general relativistic energy conditions, cosmic matter density and dark energy from X-ray clusters of galaxies and type-Ia supernovae. *Astronomy & Astrophysics*, 402:53–63, April 2003.

L. Sodre, H. V. Capaleto, J. E. Steiner, and A. Mazure. On the kinematical behaviour of galaxies in clusters. In M. J. Fitchett and W. R. Oegerle, editors, *Clusters of Galaxies*, page 239, May 1989.

R. S. Somerville, J. R. Primack, and S. M. Faber. The nature of high-redshift galaxies. *Monthly Notices of the Royal Astronomical Society*, 320:504–528, February 2001.

G. Soucail, J.-P. Kneib, A. O. Jaunsen, J. Hjorth, M. Hattori, and T. Yamada. Spectroscopic confirmation of a cluster of galaxies at $z = 1$ in the field of the gravitational lens MG 2016+112. *Astronomy & Astrophysics*, 367:741–747, March 2001.

L. S. Sparke and J. S. Gallagher, III. *Galaxies in the Universe*. February 2007.

S. A. Stanford, P. R. M. Eisenhardt, and M. Dickinson. Evolution of Infrared-selected Galaxies in z approximately 0.4 Clusters. *The Astrophysical Journal*, 450:512, September 1995.

S. A. Stanford, P. Eisenhardt, and M. Dickinson. Color Evolution in Moderate Redshift Galaxy Clusters. In N. R. Tanvir, A. Aragon-Salamanca, and J. V. Wall, editors, *The Hubble Space Telescope and the High Redshift Universe*, page 225, 1997.

Z. Staniszewski, P. A. R. Ade, K. A. Aird, B. A. Benson, and et al. Galaxy Clusters Discovered with a Sunyaev-Zel'dovich Effect Survey. *The Astrophysical Journal*, 701:32–41, August 2009.

V. Strazzullo, P. Rosati, M. Pannella, R. Gobat, J. S. Santos, M. Nonino, R. Demarco, C. Lidman, M. Tanaka, C. R. Mullis, C. Nuñez, A. Rettura, M. J. Jee, H. Böhringer, R. Bender, R. J. Bouwens, K. Dawson, R. Fassbender, M. Franx, S. Perlmutter, and M. Postman. Cluster galaxies in XMMU J2235-2557: galaxy population properties in most massive environments at $z \sim 1.4$. *Astronomy & Astrophysics*, 524:A17, December 2010.

G. A. Tammann. Remarks on the Radial Velocities of Galaxies in the Virgo Cluster. *Astronomy & Astrophysics*, 21:355, December 1972.

M. Tanaka, A. Finoguenov, T. Kodama, T. Morokuma, P. Rosati, S. A. Stanford, P. Eisenhardt, B. Holden, and S. Mei. The environmental dependence of properties of galaxies around the RDCSJ0910+54 cluster at $z = 1.1$. *Astronomy & Astrophysics*, 489:571–581, October 2008.

K.-V. H. Tran, M. Franx, G. D. Illingworth, P. van Dokkum, D. D. Kelson, J. P. Blakeslee, and M. Postman. A Keck Spectroscopic Survey of MS 1054-03 ($z = 0.83$): Forming the Red Sequence. *The Astrophysical Journal*, 661:750–767, June 2007.

K.-V. H. Tran, C. Papovich, A. Saintonge, M. Brodwin, J. S. Dunlop, D. Farrah, K. D. Finkelstein, S. L. Finkelstein, J. Lotz, R. J. McLure, I. Momcheva, and C. N. A. Willmer. Reversal of Fortune: Confirmation of an Increasing Star Formation-Density Relation in a Cluster at $z = 1.62$. *The Astrophysical Journal, Letters*, 719:L126–L129, August 2010.

T. Treu, R. S. Ellis, J.-P. Kneib, A. Dressler, I. Smail, O. Czoske, A. Oemler, and P. Natarajan. A Wide-Field Hubble Space Telescope Study of the Cluster Cl 0024+16 at $z = 0.4$. I. Morphological Distributions to 5 Mpc Radius. *The Astrophysical Journal*, 591:53–78, July 2003.

A. Vikhlinin, A. V. Kravtsov, R. A. Burenin, H. Ebeling, W. R. Forman, A. Hornstrup, C. Jones, S. S. Murray, D. Nagai, H. Quintana, and A. Voevodkin. Chandra Cluster Cosmology Project III: Cosmological Parameter Constraints. *The Astrophysical Journal*, 692:1060–1074, February 2009.

B. Vulcani, A. Aragón-Salamanca, B. M. Poggianti, B. Milvang-Jensen, A. von der Linden, J. Fritz, P. Jablonka, O. Johnson, and D. Zaritsky. Cl 1103.7-1245 at $z = 0.96$: the highest redshift galaxy cluster in the EDisCS survey. *Astronomy & Astrophysics*, 544:A104, August 2012.

E. Westra, M. J. Geller, M. J. Kurtz, D. G. Fabricant, and I. Dell'Antonio. Empirical Optical k-Corrections for Redshifts ≤ 0.7. *Publications of the Astronomical Society of the Pacific*, 122:1258–1284, November 2010.

K. E. Whitaker, M. Franx, J. Leja, P. G. van Dokkum, A. Henry, R. E. Skelton, M. Fumagalli, I. G. Momcheva, G. B. Brammer, I. Labbé, E. J. Nelson, and J. R. Rigby. Constraining the Low-mass Slope of the Star Formation Sequence at $0.5 < z < 2.5$. *The Astrophysical Journal*, 795:104, November 2014.

M. White, M. Blanton, A. Bolton, D. Schlegel, J. Tinker, A. Berlind, L. da Costa, E. Kazin, Y.-T. Lin, M. Maia, C. K. McBride, N. Padmanabhan, J. Parejko, W. Percival, F. Prada, B. Ramos, E. Sheldon, F. de Simoni, R. Skibba, D. Thomas, D. Wake, I. Zehavi, Z. Zheng, R. Nichol, D. P. Schneider, M. A. Strauss, B. A. Weaver, and D. H. Weinberg. The Clustering of Massive Galaxies at $z \sim 0.5$ from the First Semester of BOSS Data. *The Astrophysical Journal*, 728:126, February 2011.

S. D. M. White, D. I. Clowe, L. Simard, G. Rudnick, G. De Lucia, A. Aragón-Salamanca, R. Bender, P. Best, M. Bremer, S. Charlot, J. Dalcanton, M. Dantel, V. Desai, B. Fort, C. Halliday, P. Jablonka, G. Kauffmann, Y. Mellier, B. Milvang-Jensen, R. Pelló, B. Poggianti, S. Poirier, H. Rottgering, R. Saglia, P. Schneider, and D. Zaritsky. EDisCS - the ESO distant cluster survey. Sample definition and optical photometry. *Astronomy & Astrophysics*, 444: 365–379, December 2005.

B. C. Whitmore, D. M. Gilmore, and C. Jones. What determines the morphological fractions in clusters of galaxies? *The Astrophysical Journal*, 407:489–509, April 1993.

R. A. Windhorst, D. Burstein, D. F. Mathis, L. W. Neuschaefer, F. Bertola, L. M. Buson, D. C. Koo, K. Matthews, P. D. Barthel, and K. C. Chambers. The discovery of a young radio galaxy at $z = 2.390$ - Probing initial star formation at z less than approximately 3.0. *The Astrophysical Journal*, 380:362–383, October 1991.

A. Yahil and N. V. Vidal. The Velocity Distribution of Galaxies in Clusters. *The Astrophysical Journal*, 214:347–350, June 1977. doi: 10.1086/155257.

A. I. Zabludoff and M. Franx. Morphology and kinematics in clusters of galaxies. *The Astronomical Journal*, 106:1314–1323, October 1993.

A. I. Zabludoff, J. P. Huchra, and M. J. Geller. The kinematics of Abell clusters. *The Astrophysical Journal, Supplement*, 74:1–36, September 1990.

F. Zwicky. On the Masses of Nebulae and of Clusters of Nebulae. *The Astrophysical Journal*, 86:217, October 1937.

Appendix A

Other plots of projected phase space

I show the plots of the projected phase space for galaxy members resulting after the application of the P+G(3Mpc), P+G(1Mpc), P+G with subgroups, ZHG, WG 2.5, WG 4 and WG4+YV methods. The same plots obtained using the P+G procedure are illustrated for only the clusters in figures 7.6 of Chapter 7.
Note that small black crosses indicate the cluster member galaxies, whereas bigger circles represent galaxies of the survey belonging to the field.

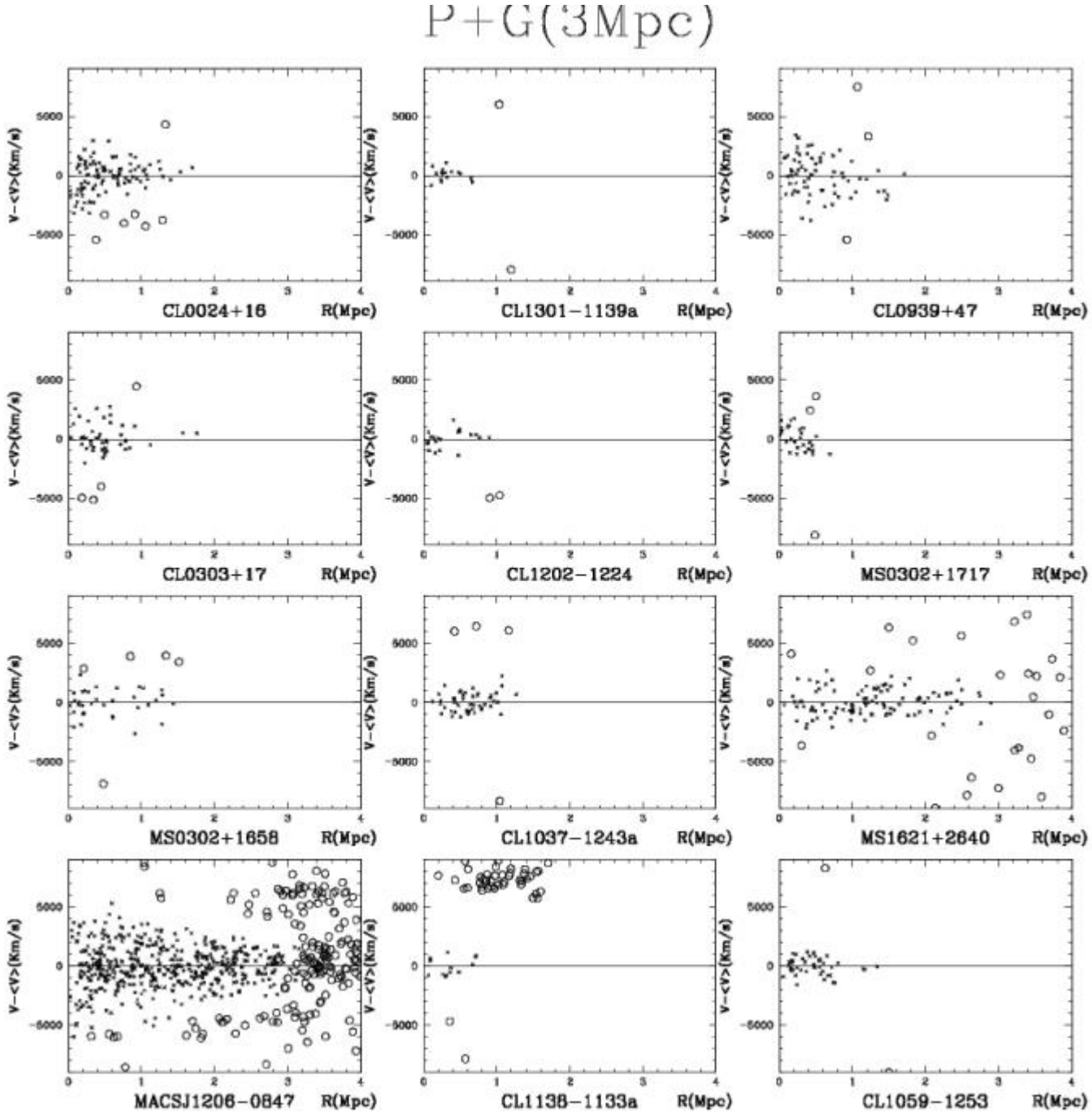
P+G(3Mpc)
V−<V>(Km/s)
R(Mpc)
CL0024+16
CL1301−1139a
CL0939+47
CL0303+17
CL1202−1224
MS0302+1717
MS0302+1658
CL1037−1243a
MS1621+2640
MACSJ1206−0847
CL1138−1133a
CL1059−1253

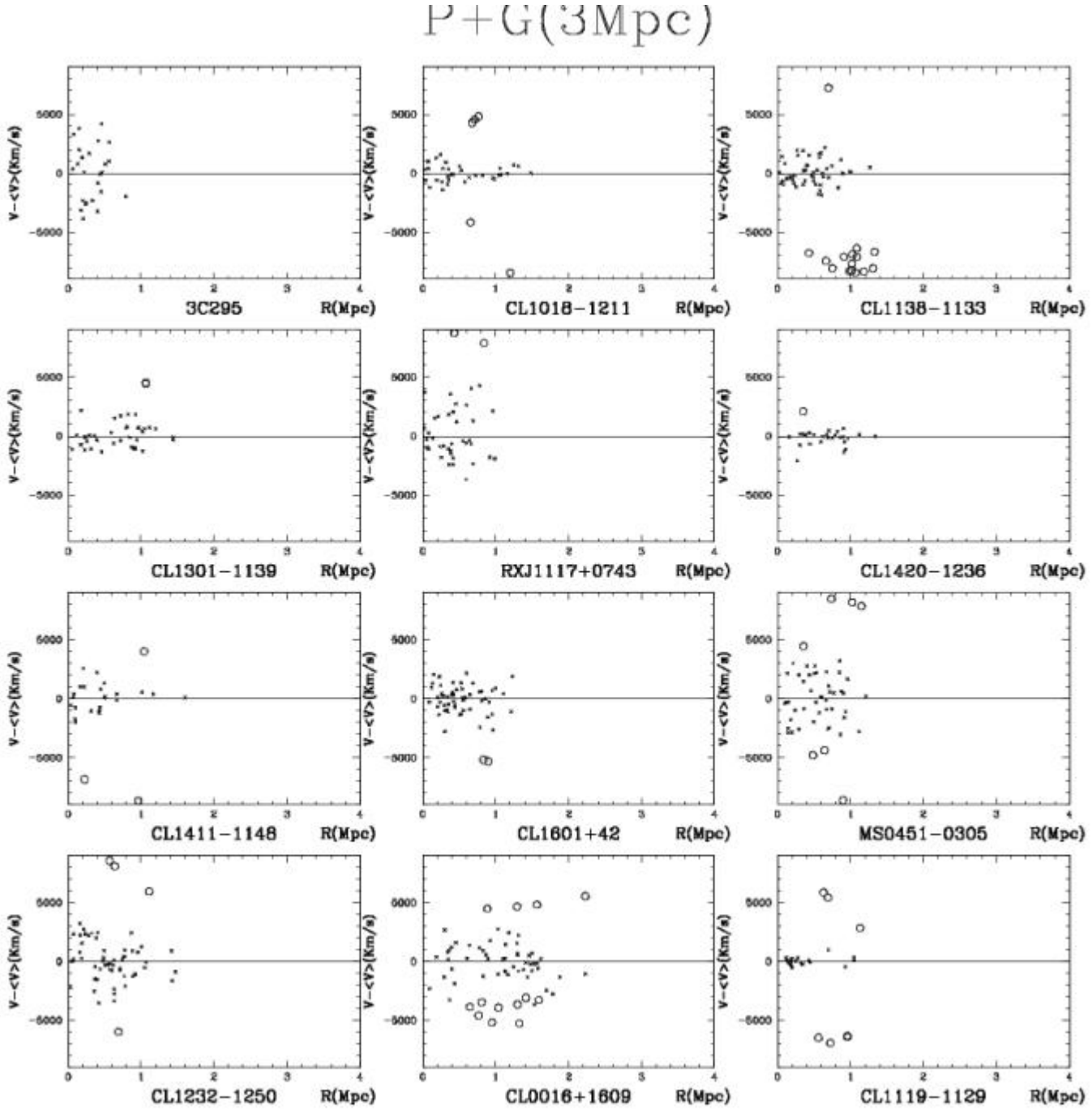
P+G(3Mpc)
V−<V>(Km/s)
R(Mpc)
3C295
CL1018−1211
CL1138−1133
CL1301−1139
RXJ1117+0743
CL1420−1236
CL1411−1148
CL1601+42
MS0451−0305
CL1232−1250
CL0016+1609
CL1119−1129

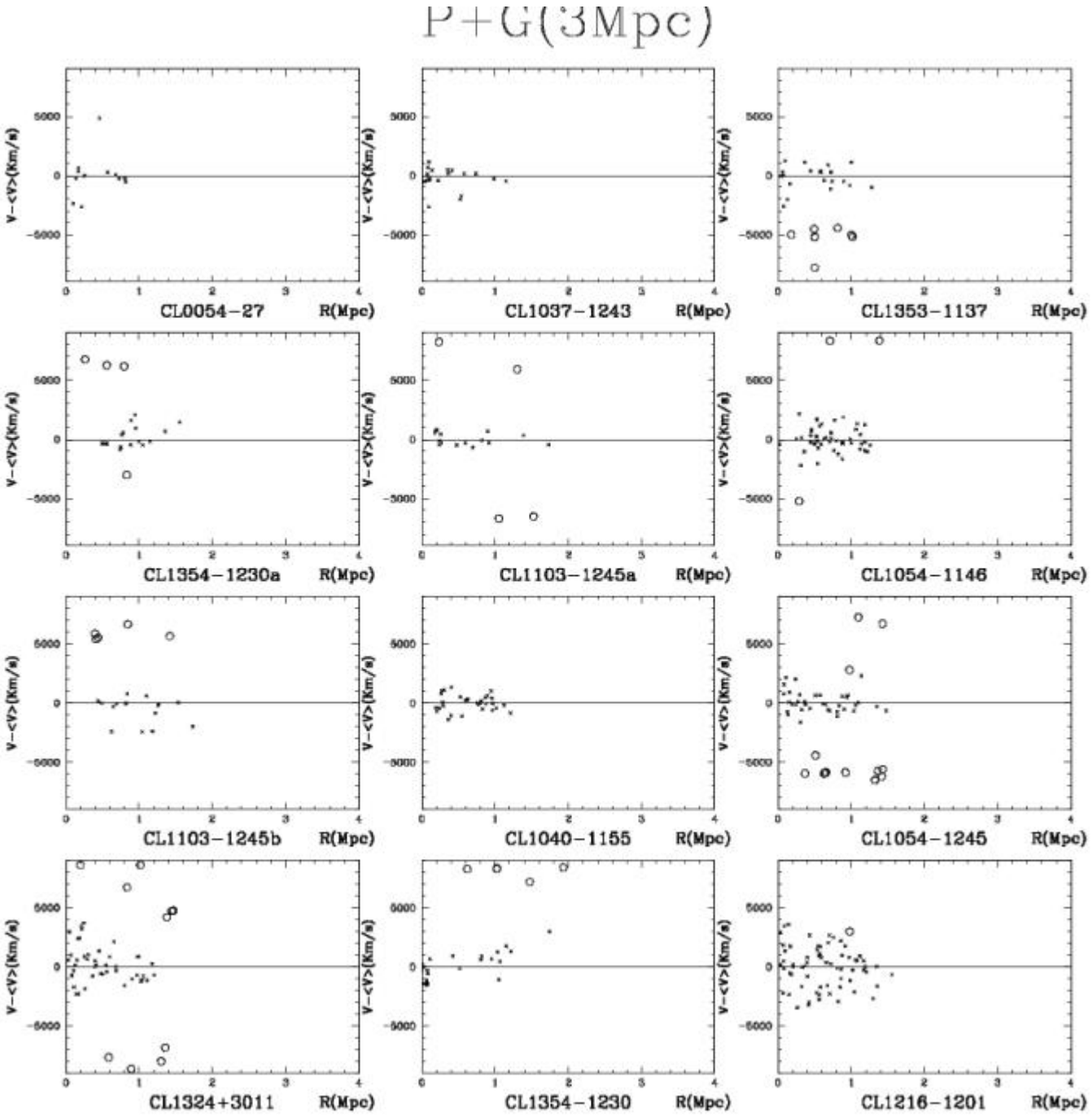
P+G(3Mpc)
V−<V>(Km/s)
R(Mpc)
CL0054−27
CL1037−1243
CL1353−1137
CL1354−1230a
CL1103−1245a
CL1054−1146
CL1103−1245b
CL1040−1155
CL1054−1245
CL1324+3011
CL1354−1230
CL1216−1201

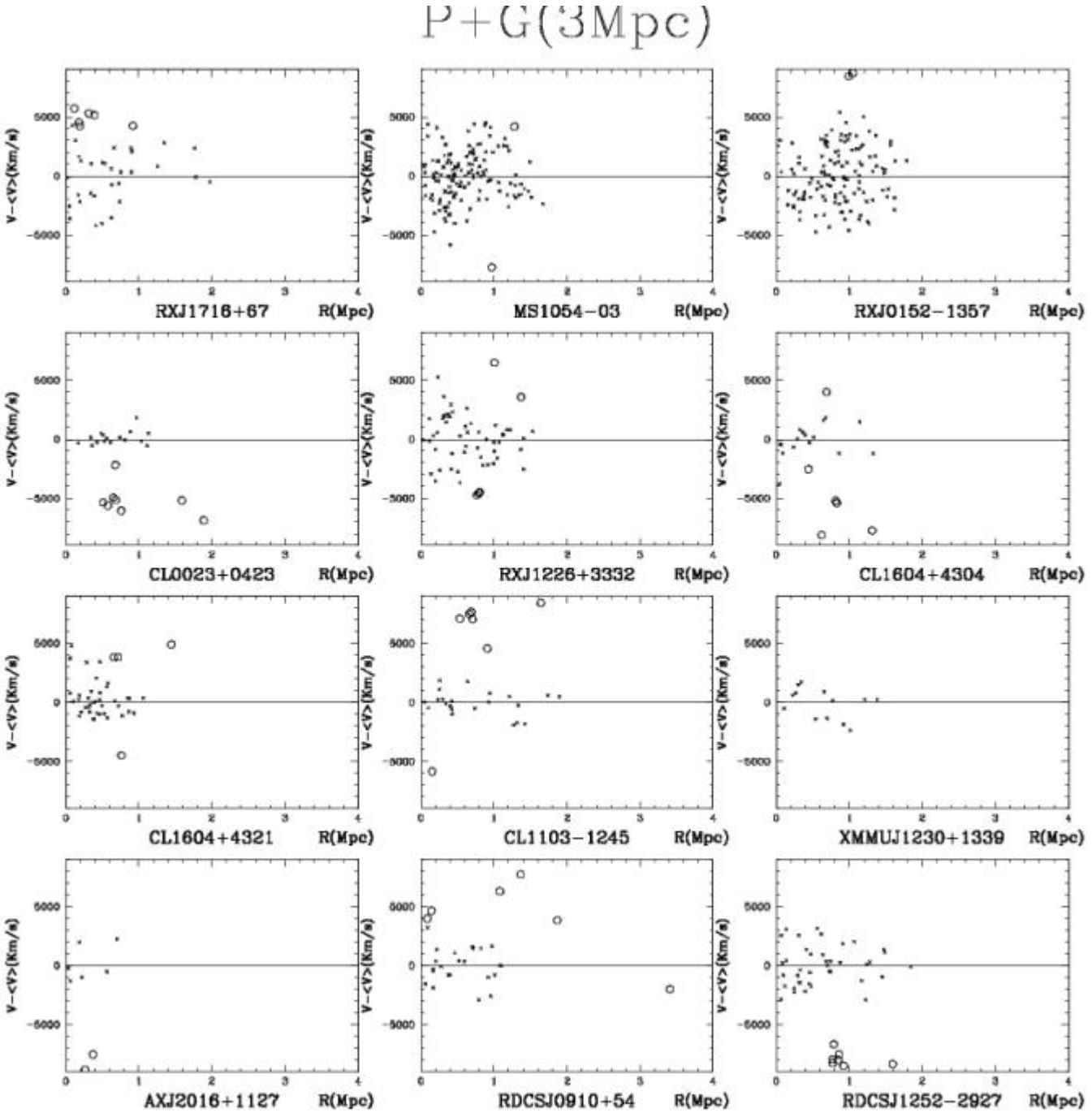
P+G(3Mpc)
V−<V>(Km/s)
R(Mpc)
RXJ1716+67
MS1054−03
RXJ0152−1357
CL0023+0423
RXJ1226+3332
CL1604+4304
CL1604+4321
CL1103−1245
XMMUJ1230+1339
AXJ2016+1127
RDCSJ0910+54
RDCSJ1252−2927

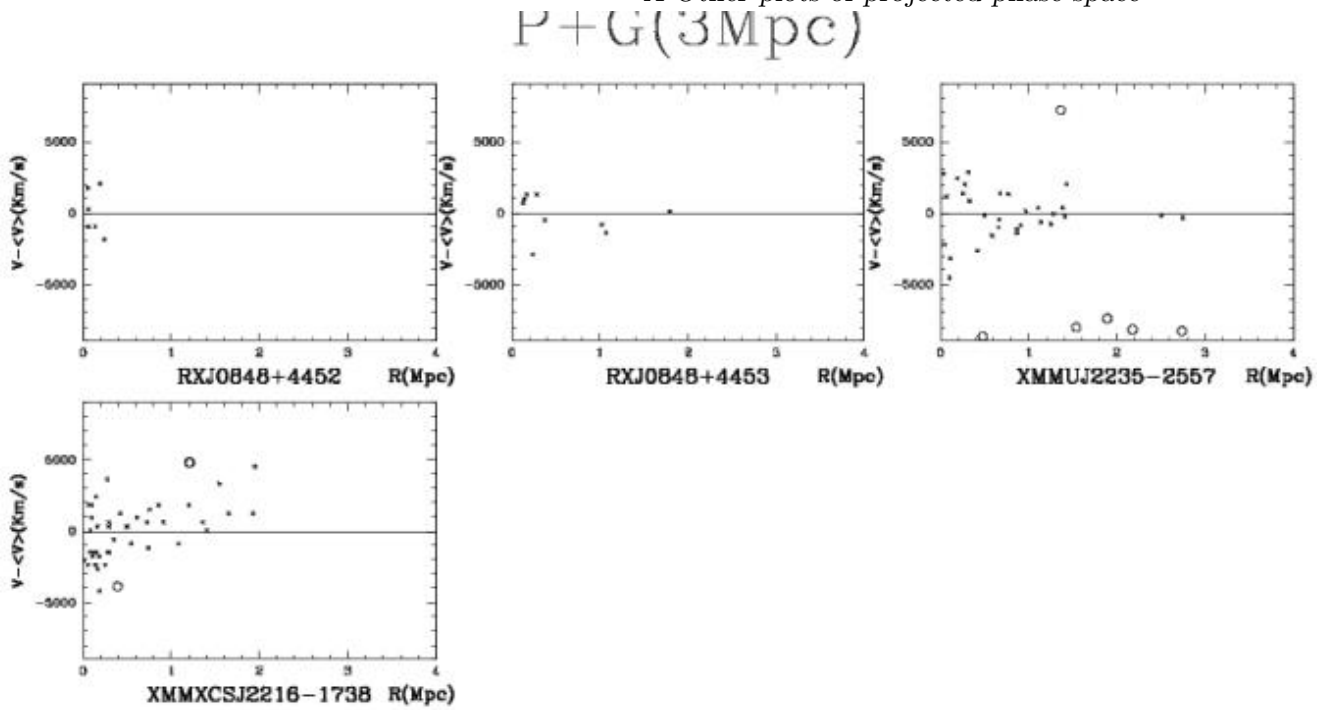

Figure A.1: Projected phase space - P+G(3Mpc): velocity distribution of galaxies vs projected cluster-centric distance, according to the P+G(3Mpc) procedure.

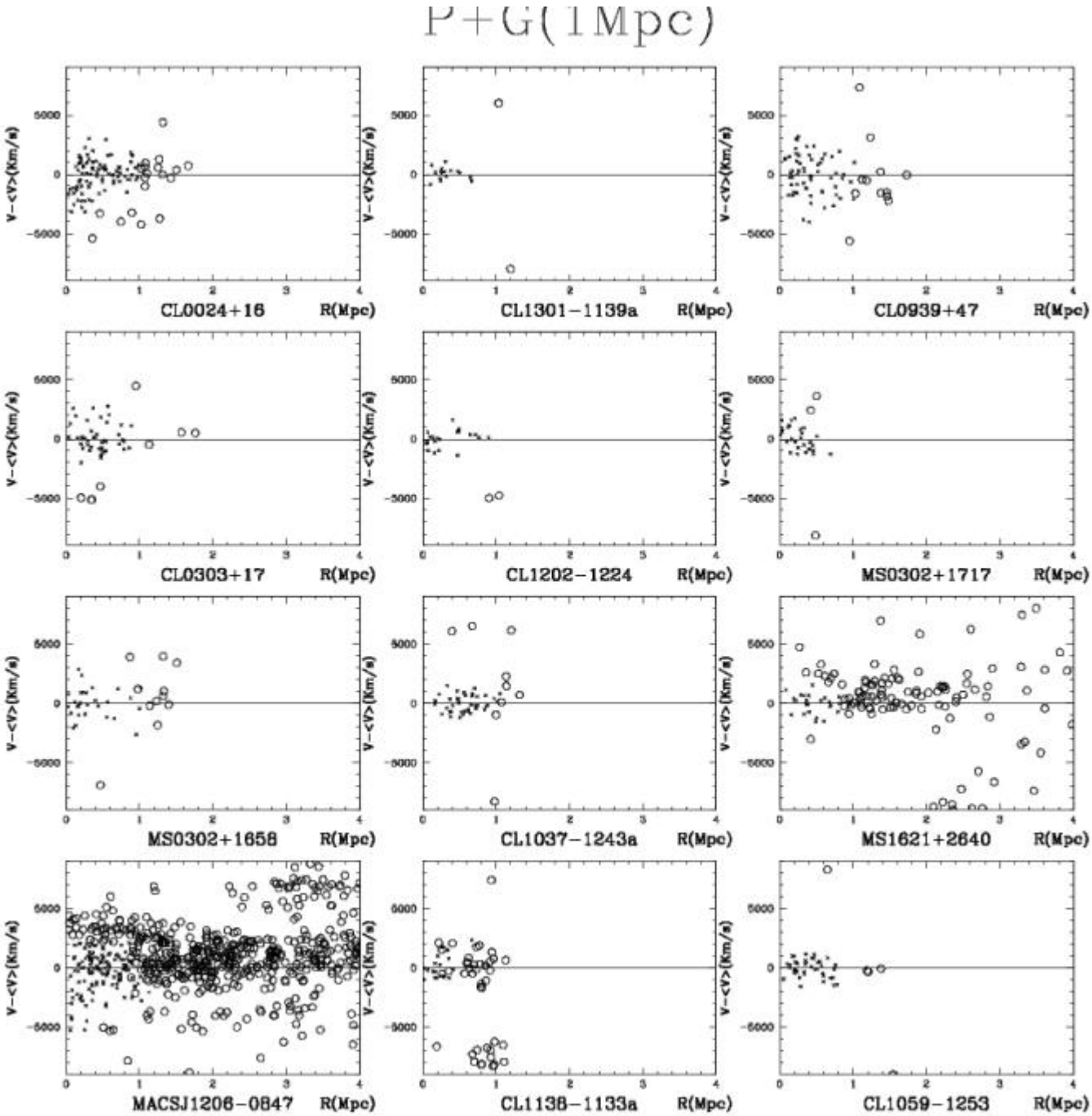
P+G(1Mpc)
V−<V>(Km/s)
R(Mpc)
CL0024+16
CL1301−1139a
CL0939+47
CL0303+17
CL1202−1224
MS0302+1717
MS0302+1658
CL1037−1243a
MS1621+2640
MACSJ1206−0847
CL1138−1133a
CL1059−1253

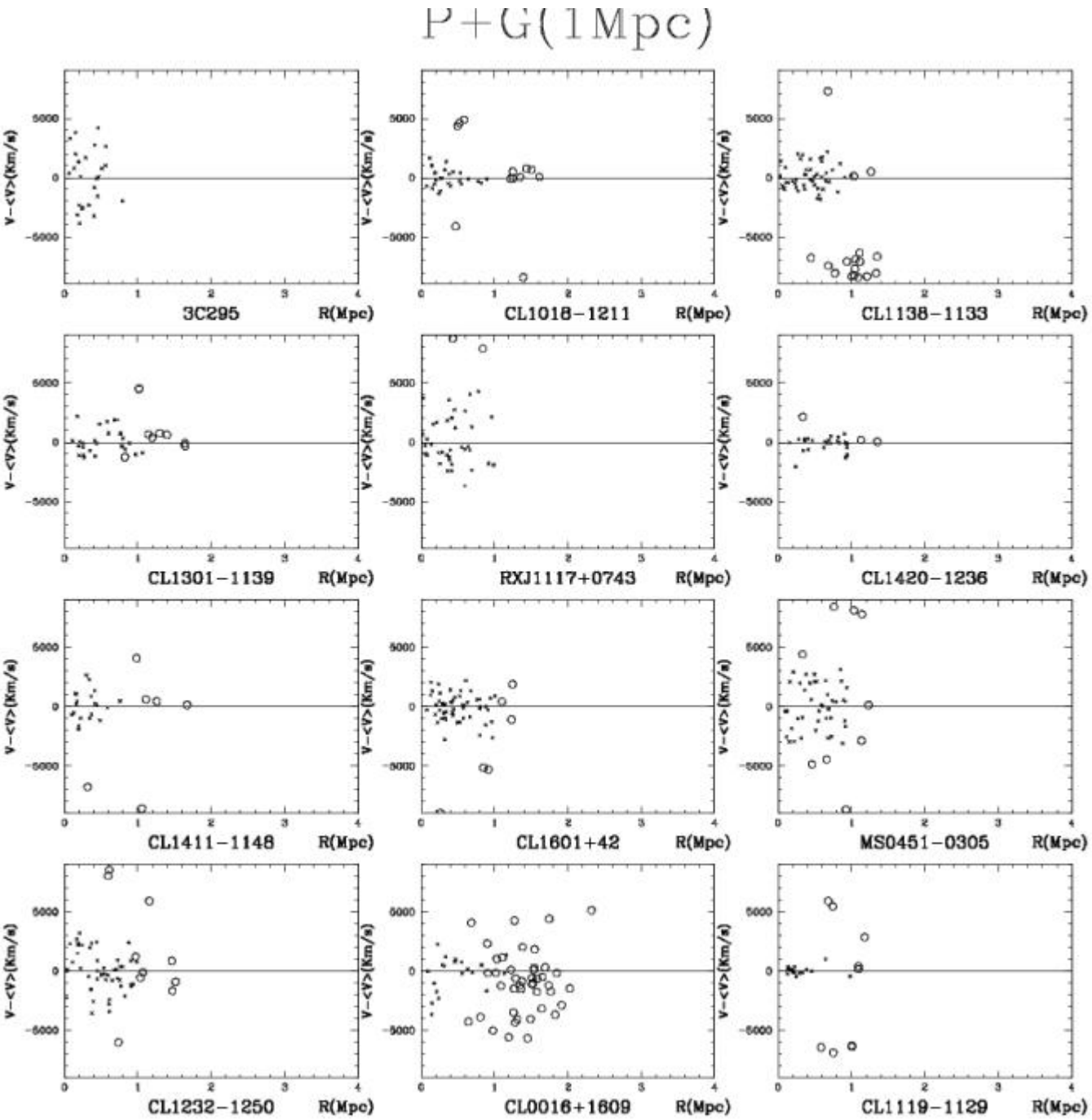
P+G(1Mpc)
V−<V>(Km/s)
R(Mpc)
3C295
CL1018−1211
CL1138−1133
CL1301−1139
RXJ1117+0743
CL1420−1236
CL1411−1148
CL1601+42
MS0451−0305
CL1232−1250
CL0016+1609
CL1119−1129

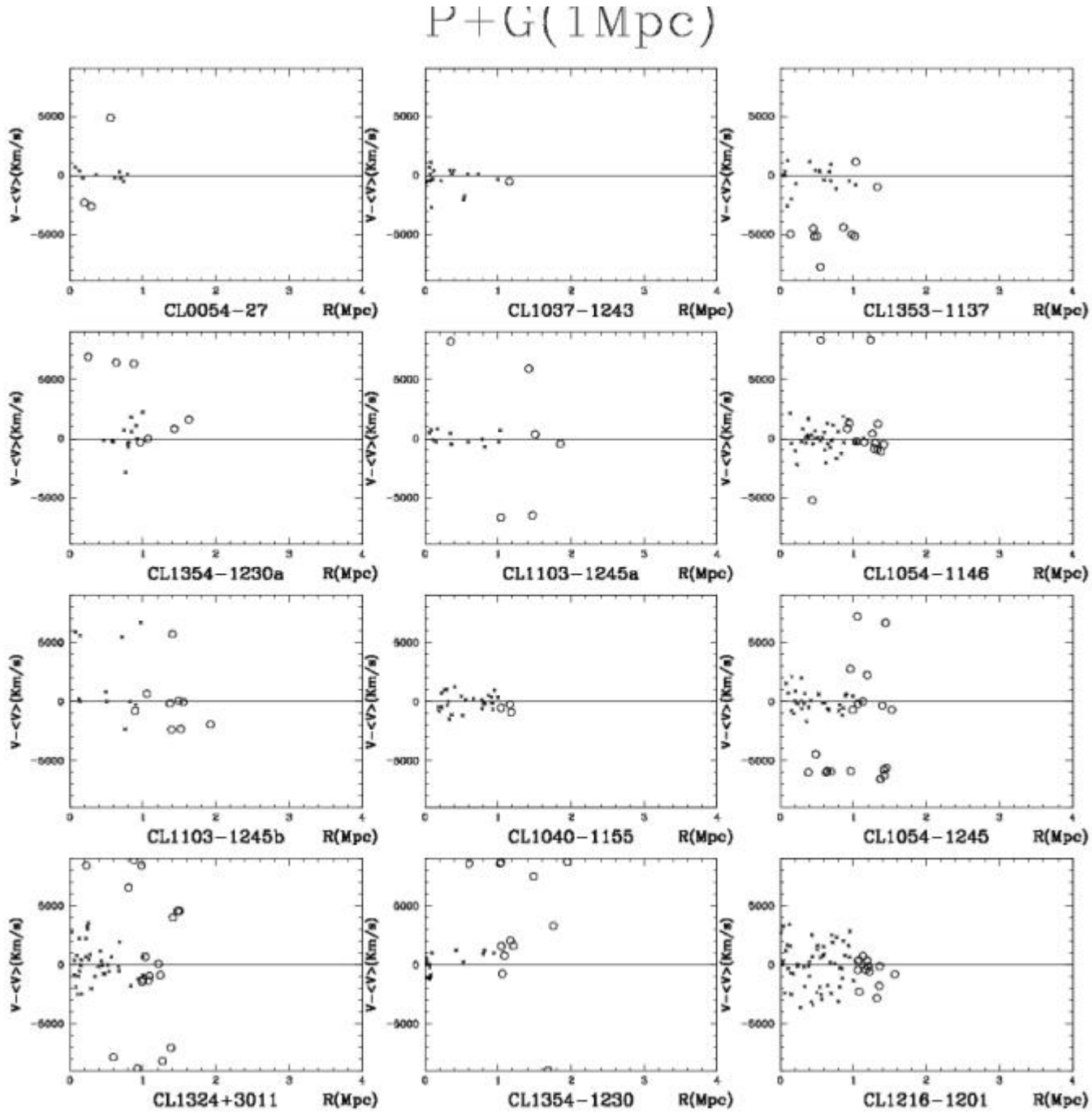
P+G(1Mpc)
V−<V>(Km/s)
R(Mpc)
CL0054−27
CL1037−1243
CL1353−1137
CL1354−1230a
CL1103−1245a
CL1054−1146
CL1103−1245b
CL1040−1155
CL1054−1245
CL1324+3011
CL1354−1230
CL1216−1201

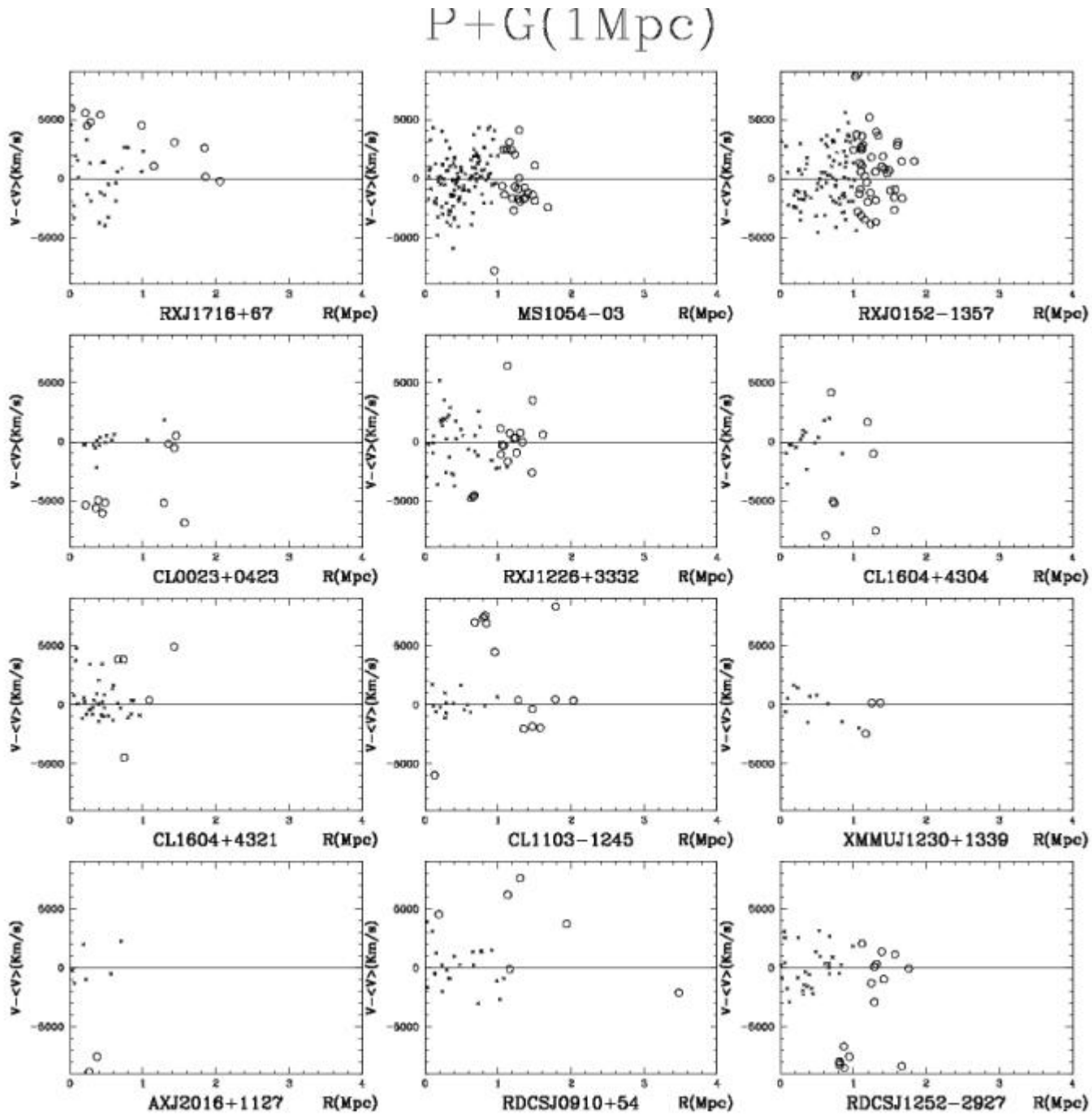
P+G(1Mpc)
V−<V>(Km/s)
R(Mpc)
RXJ1716+67
MS1054−03
RXJ0152−1357
CL0023+0423
RXJ1226+3332
CL1604+4304
CL1604+4321
CL1103−1245
XMMUJ1230+1339
AXJ2016+1127
RDCSJ0910+54
RDCSJ1252−2927

A Other plots of projected phase space

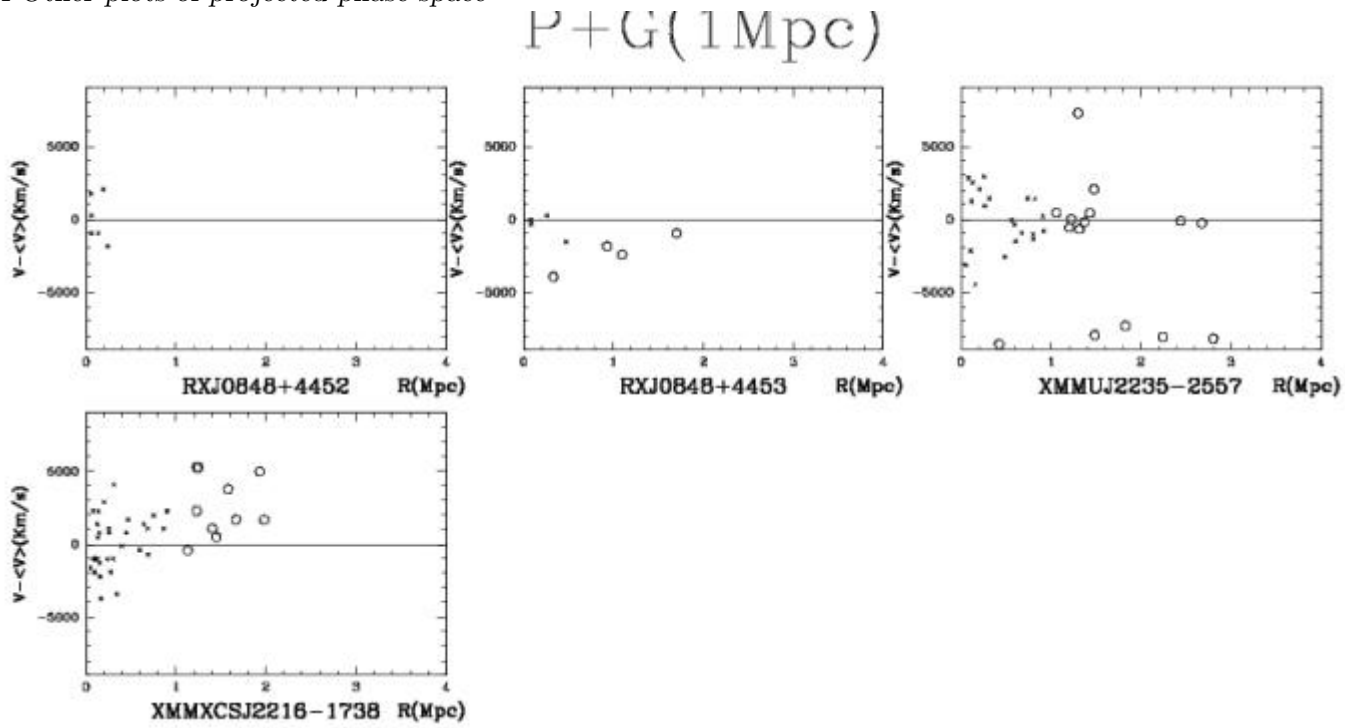

Figure A.2: Projected phase space - P+G(1Mpc): velocity distribution of galaxies vs projected cluster-centric distance, according to the P+G(1Mpc) procedure.

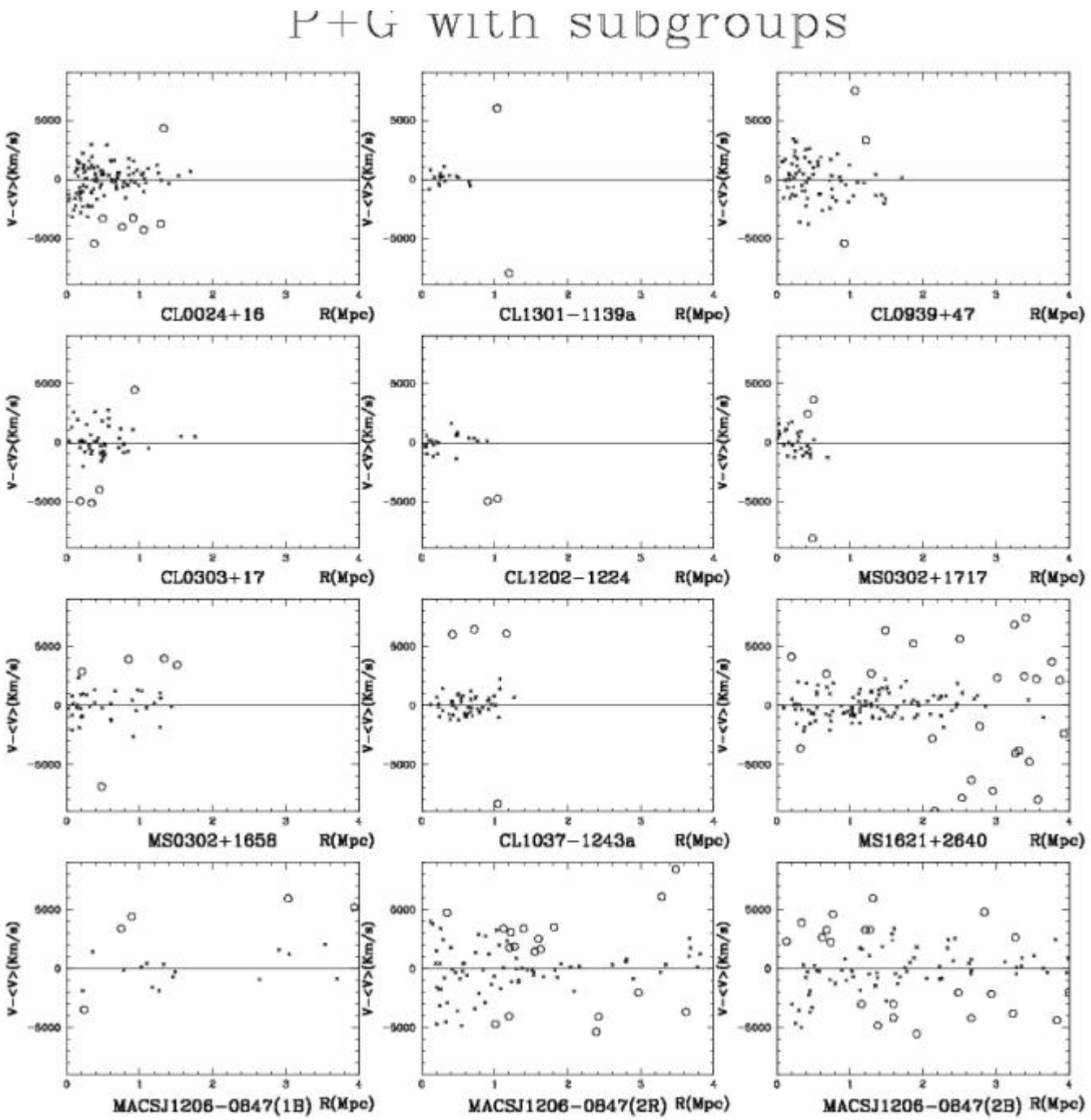
P+G with subgroups
V−<V>(Km/s)
R(Mpc)
CL0024+16
CL1301−1139a
CL0939+47
CL0303+17
CL1202−1224
MS0302+1717
MS0302+1658
CL1037−1243a
MS1621+2640
MACSJ1206−0847(1B)
MACSJ1206−0847(2R)
MACSJ1206−0847(2B)

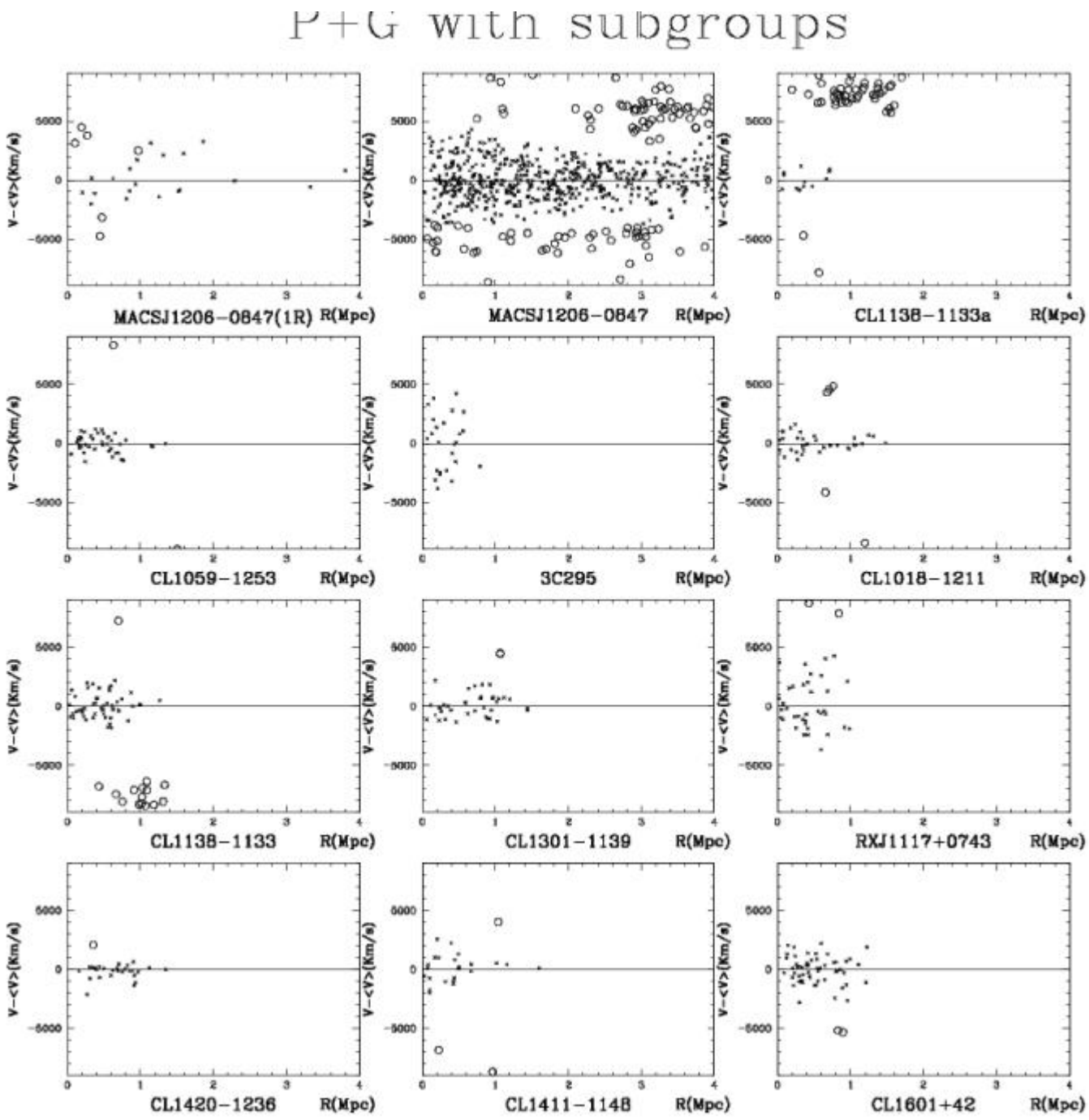
P+G with subgroups
MACSJ1206−0847(1R)
MACSJ1206−0847
CL1138−1133a
CL1059−1253
3C295
CL1018−1211
CL1138−1133
CL1301−1139
RXJ1117+0743
CL1420−1236
CL1411−1148
CL1601+42
V−<V>(Km/s)
R(Mpc)

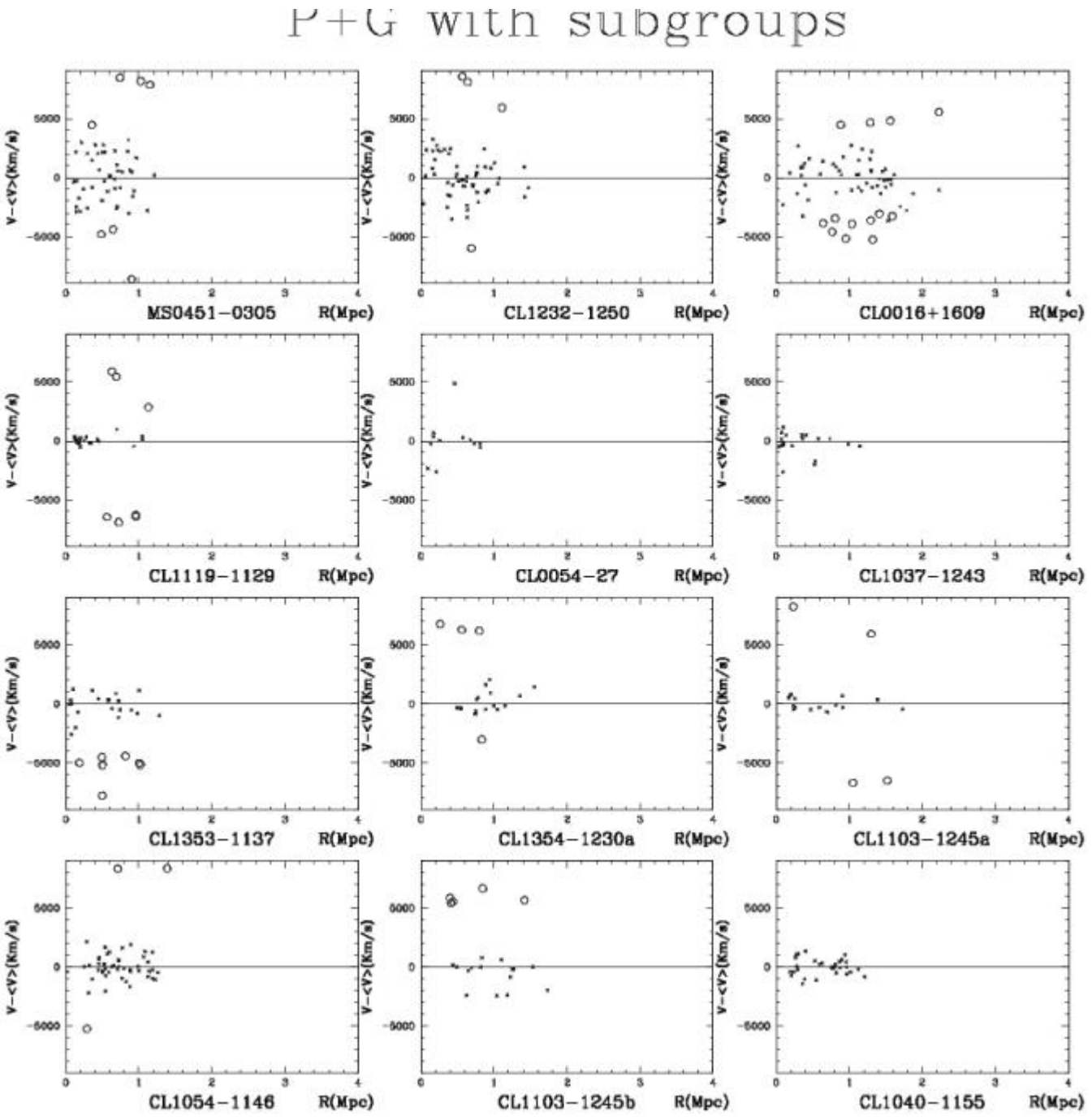
P+G with subgroups
MS0451−0305
CL1232−1250
CL0016+1609
CL1119−1129
CL0054−27
CL1037−1243
CL1353−1137
CL1354−1230a
CL1103−1245a
CL1054−1146
CL1103−1245b
CL1040−1155
V−<V>(Km/s)
R(Mpc)

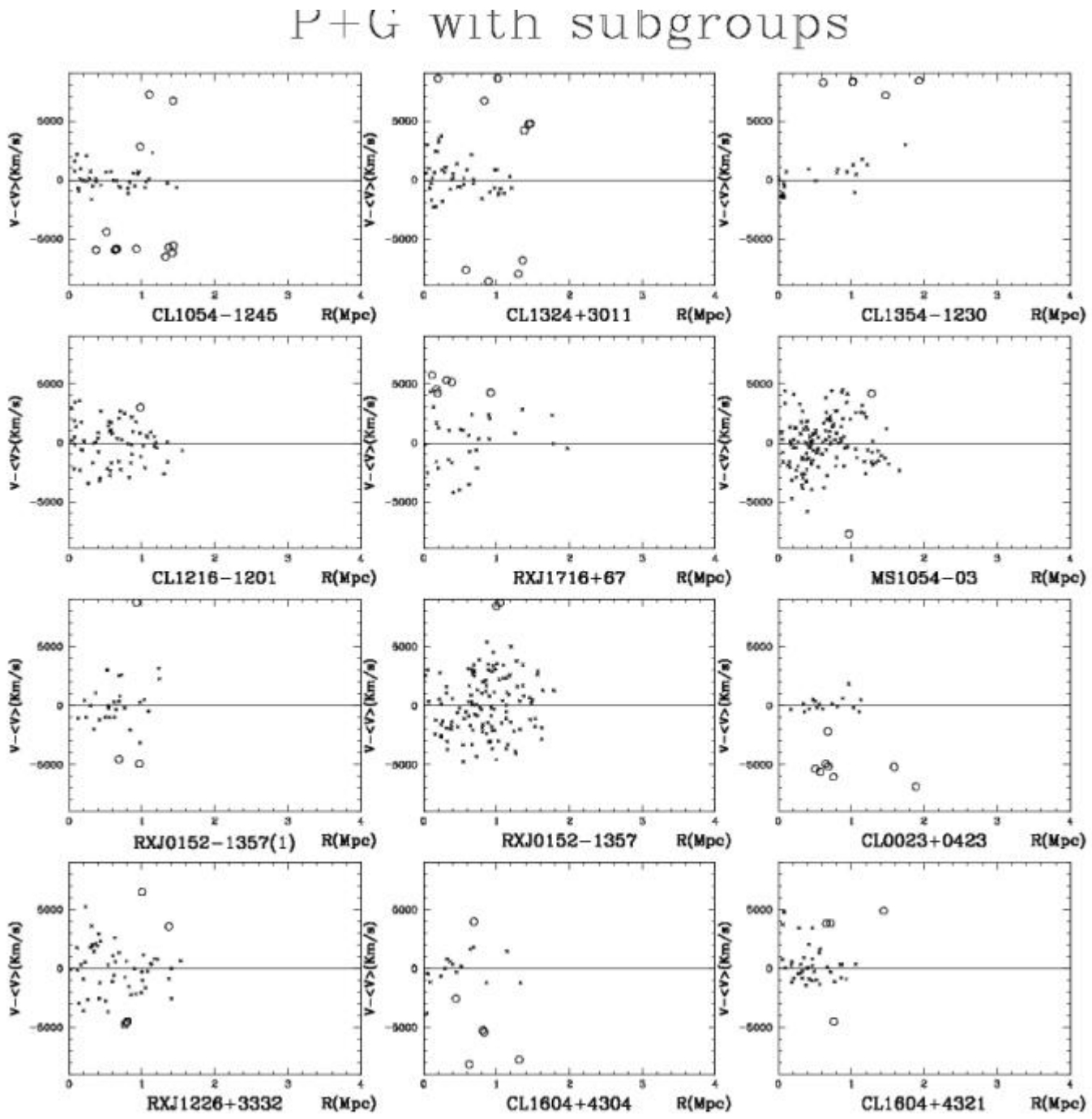
P+G with subgroups
V−<V>(Km/s)
R(Mpc)
CL1054−1245
CL1324+3011
CL1354−1230
CL1216−1201
RXJ1716+67
MS1054−03
RXJ0152−1357(1)
RXJ0152−1357
CL0023+0423
RXJ1226+3332
CL1604+4304
CL1604+4321

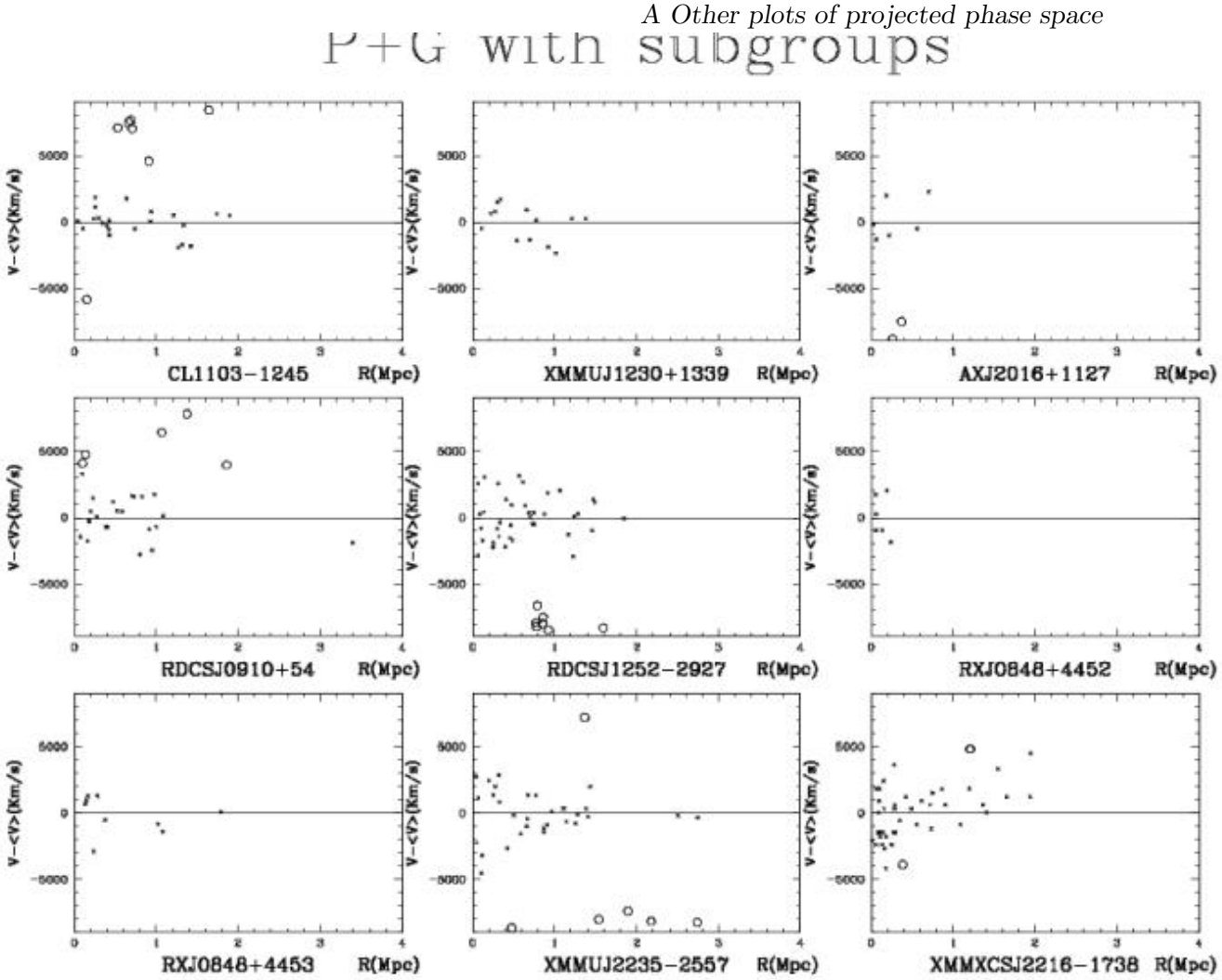

Figure A.3: Projected phase space for clusters and subgroups derived by the P+G procedure.

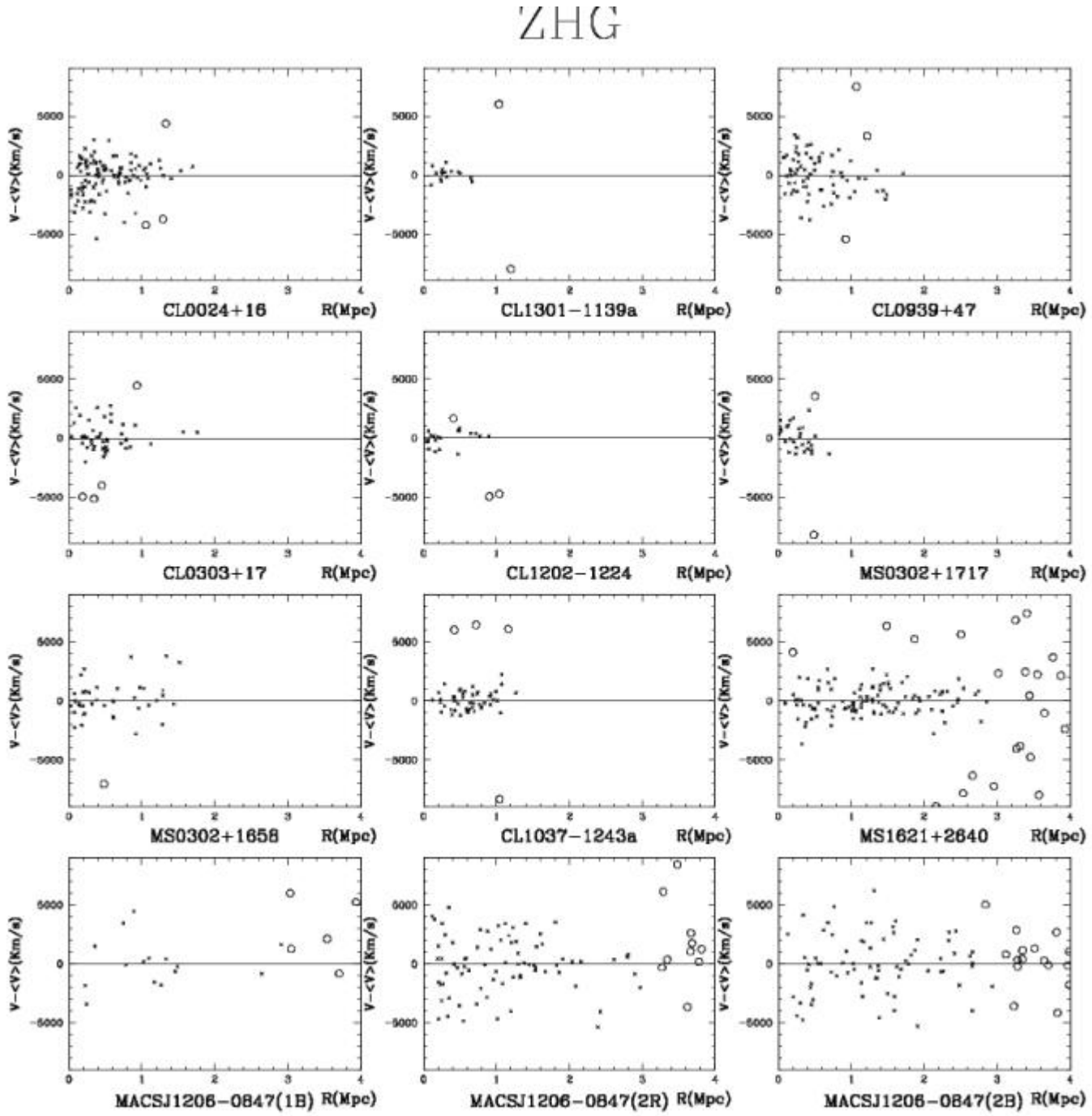
ZHG
V−<V>(Km/s)
R(Mpc)
CL0024+16
CL1301−1139a
CL0939+47
CL0303+17
CL1202−1224
MS0302+1717
MS0302+1658
CL1037−1243a
MS1621+2640
MACSJ1206−0847(1B)
MACSJ1206−0847(2R)
MACSJ1206−0847(2B)

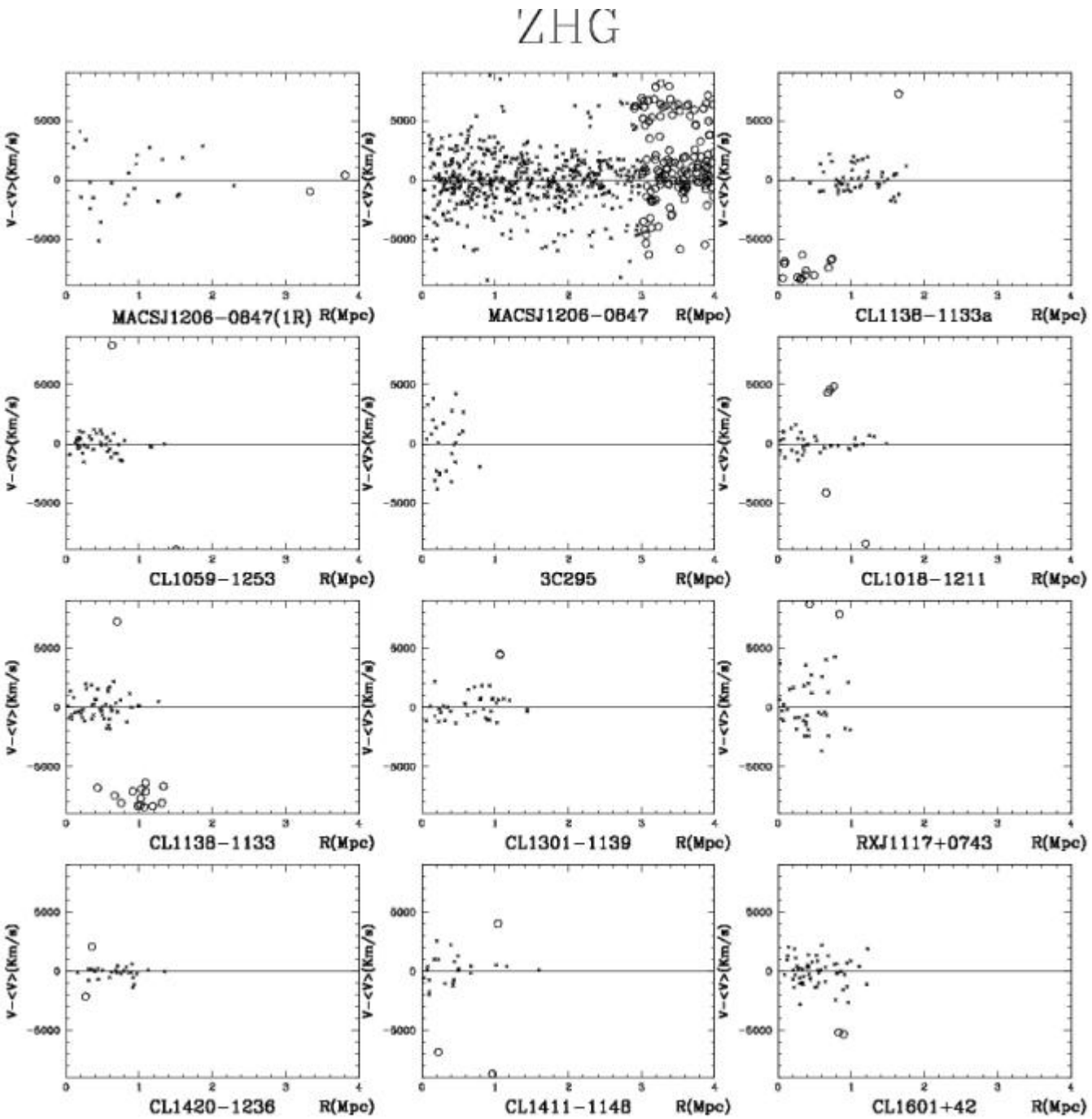
ZHG
V−<V>(Km/s)
R(Mpc)
MACSJ1206−0847(1R)
MACSJ1206−0847
CL1138−1133a
CL1059−1253
3C295
CL1018−1211
CL1138−1133
CL1301−1139
RXJ1117+0743
CL1420−1236
CL1411−1148
CL1601+42

A Other plots of projected phase space

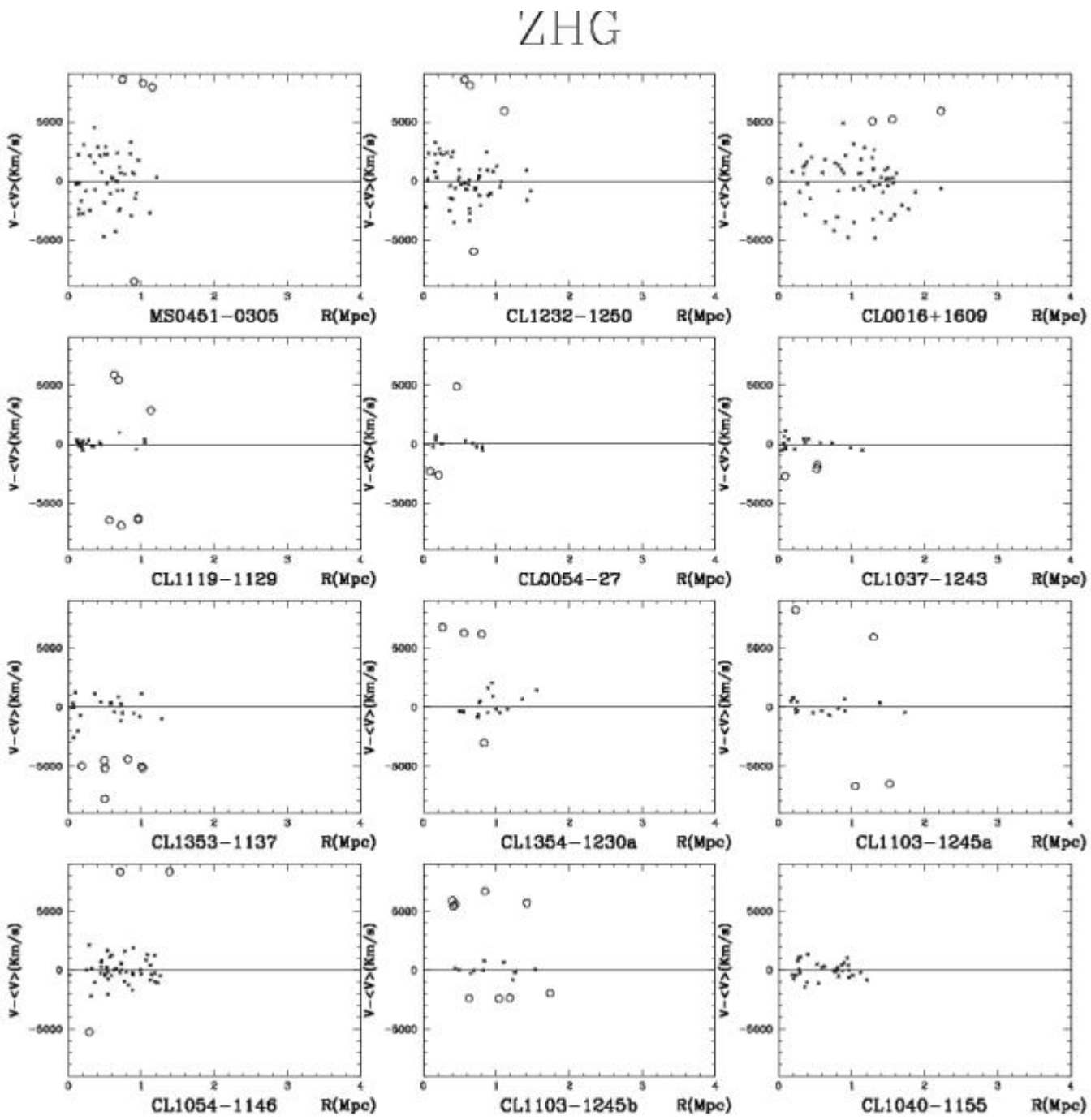

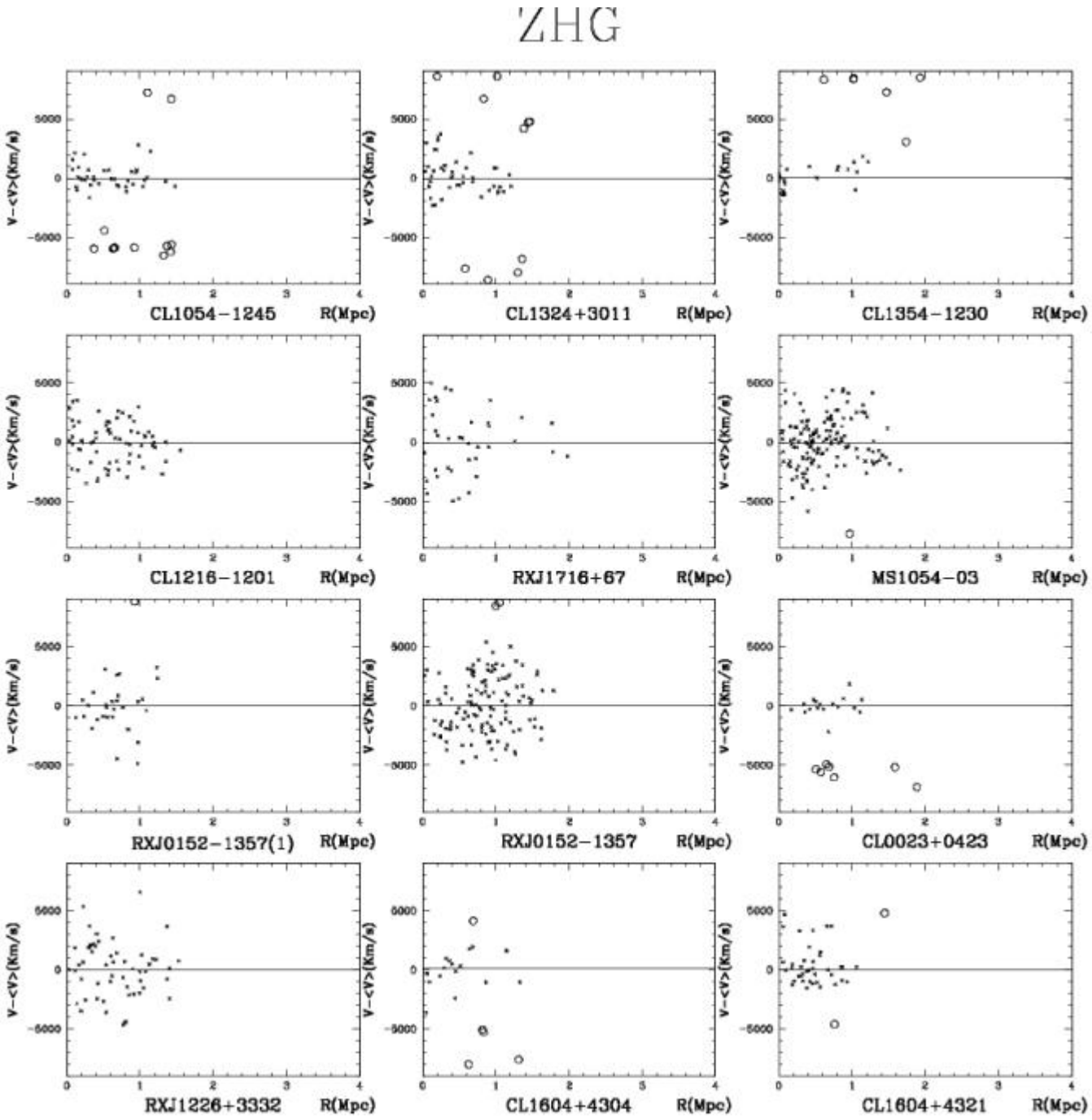
ZHG
V−<V>(Km/s)
R(Mpc)
CL1054−1245
CL1324+3011
CL1354−1230
CL1216−1201
RXJ1716+67
MS1054−03
RXJ0152−1357(1)
RXJ0152−1357
CL0023+0423
RXJ1226+3332
CL1604+4304
CL1604+4321

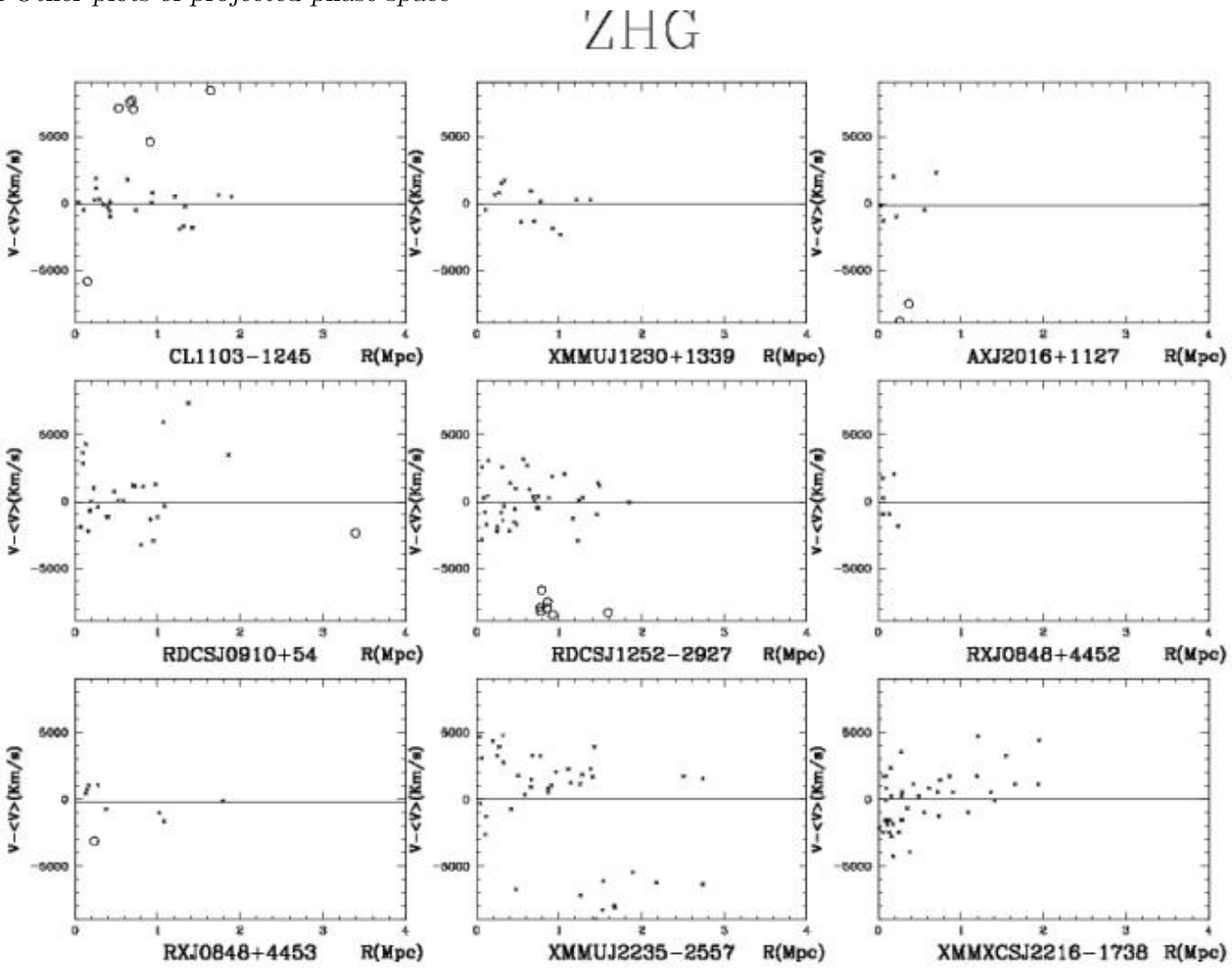

Figure A.4: Projected phase space derived by the ZHG procedure.

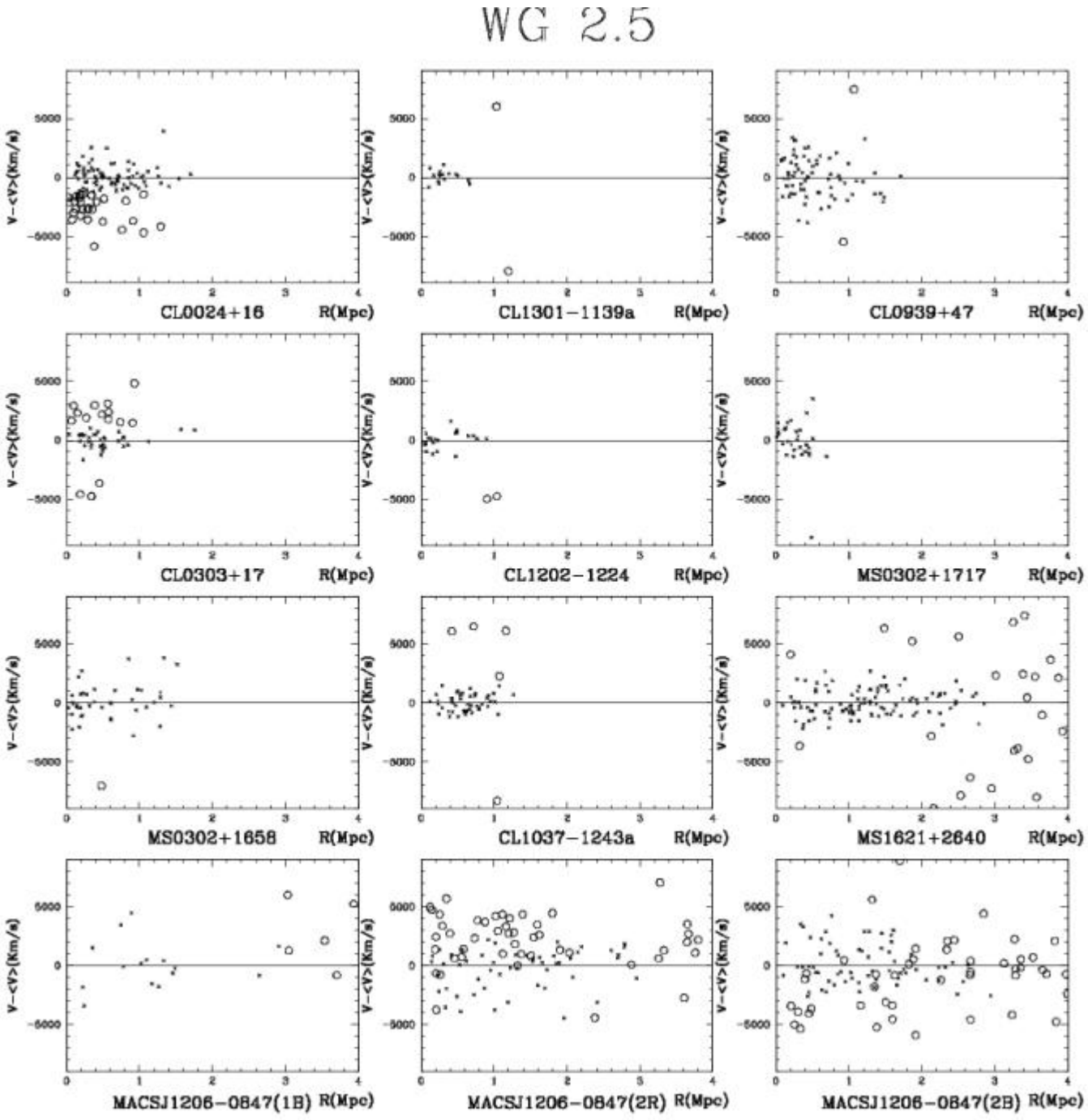
WG 2.5
V−<V>(Km/s)
R(Mpc)
CL0024+16
CL1301−1139a
CL0939+47
CL0303+17
CL1202−1224
MS0302+1717
MS0302+1658
CL1037−1243a
MS1621+2640
MACSJ1206−0847(1B)
MACSJ1206−0847(2R)
MACSJ1206−0847(2B)

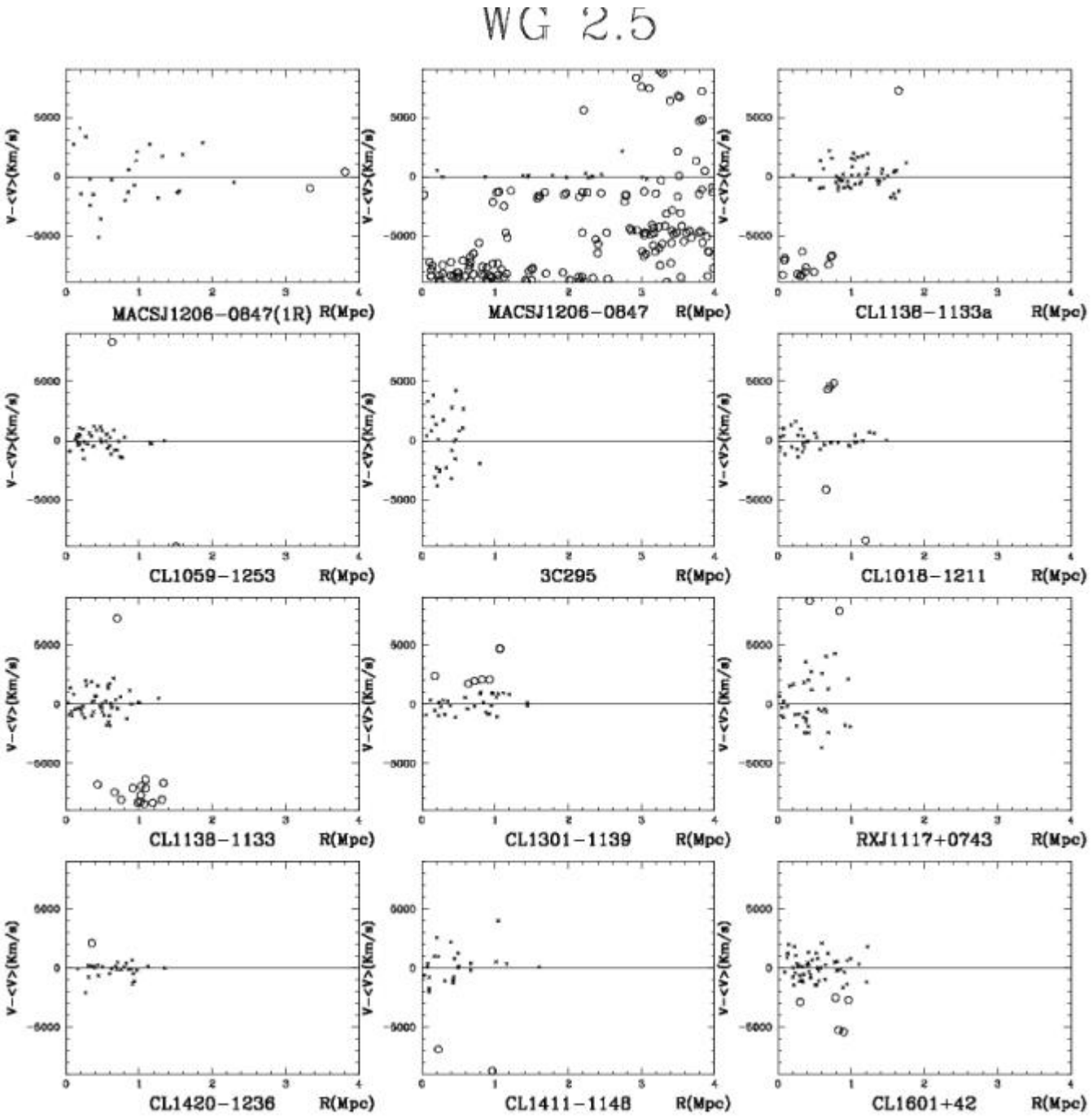
WG 2.5
MACSJ1206−0847(1R)
MACSJ1206−0847
CL1138−1133a
CL1059−1253
3C295
CL1018−1211
CL1138−1133
CL1301−1139
RXJ1117+0743
CL1420−1236
CL1411−1148
CL1601+42
V−<V>(Km/s)
R(Mpc)

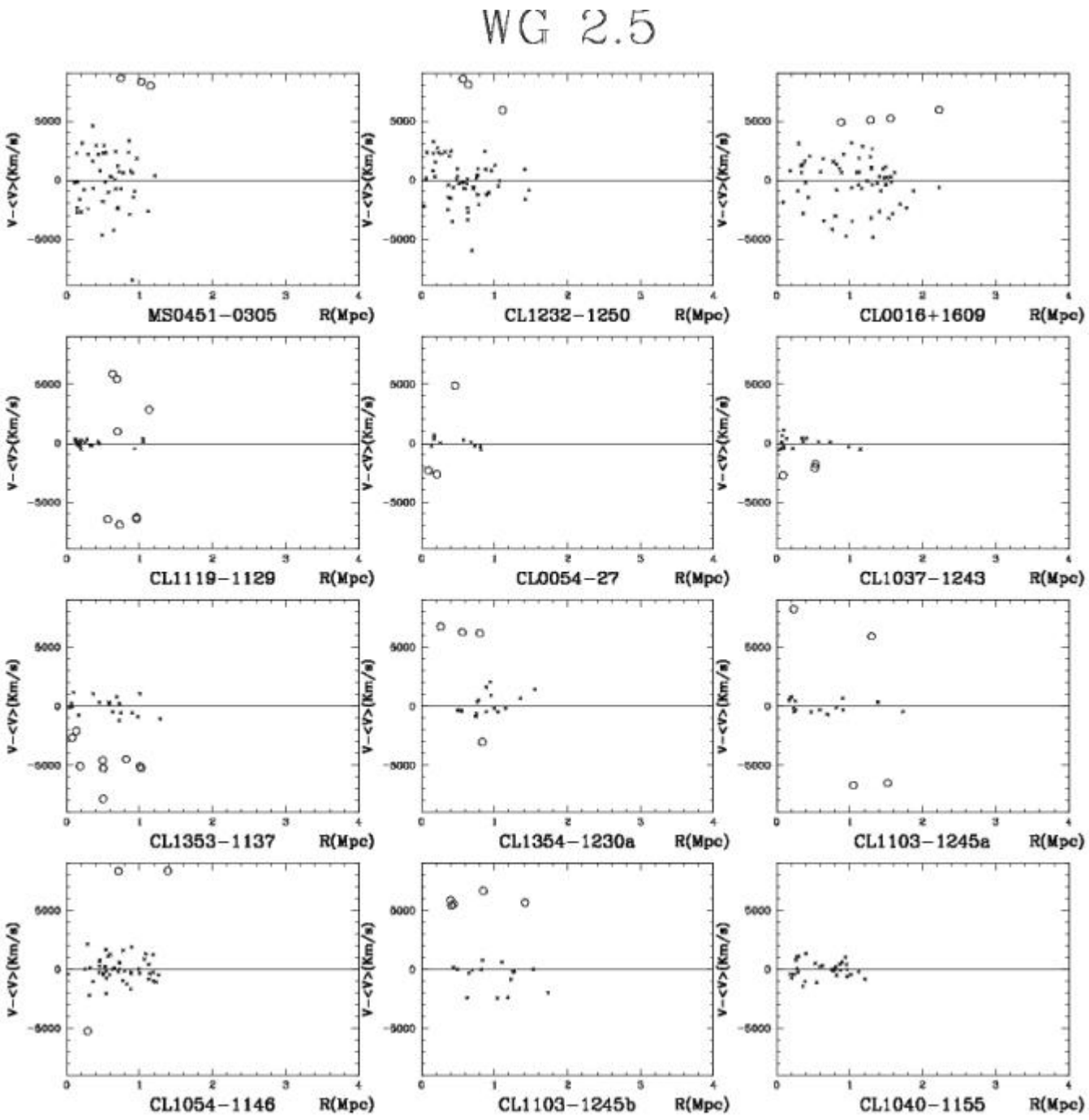
WG 2.5
V−<V>(Km/s)
R(Mpc)
MS0451−0305
CL1232−1250
CL0016+1609
CL1119−1129
CL0054−27
CL1037−1243
CL1353−1137
Cl1354−1230a
CL1103−1245a
CL1054−1146
CL1103−1245b
CL1040−1155

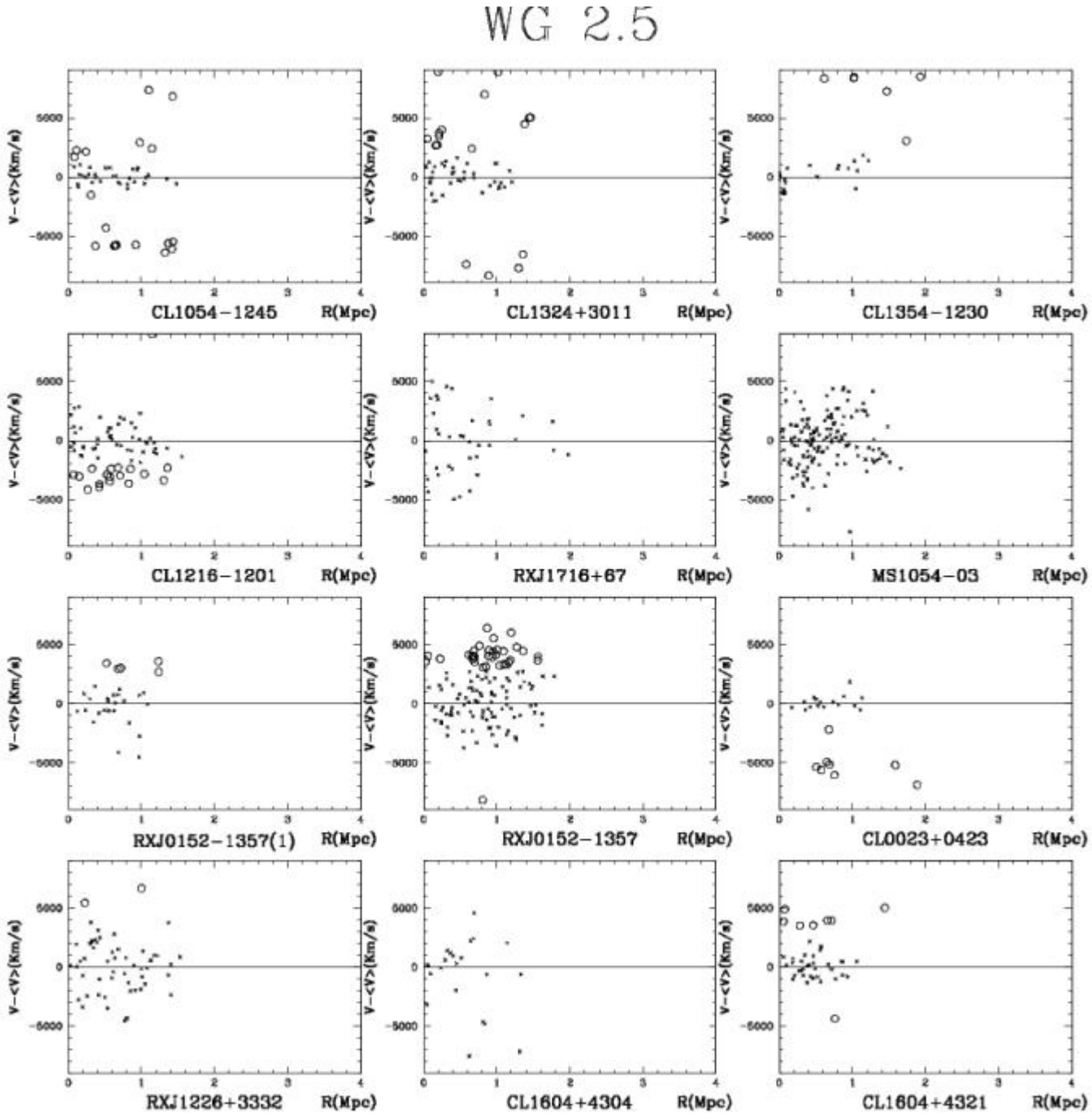
WG 2.5
V−<V>(Km/s)
R(Mpc)
CL1054−1245
CL1324+3011
CL1354−1230
CL1216−1201
RXJ1716+67
MS1054−03
RXJ0152−1357(1)
RXJ0152−1357
CL0023+0423
RXJ1226+3332
CL1604+4304
CL1604+4321

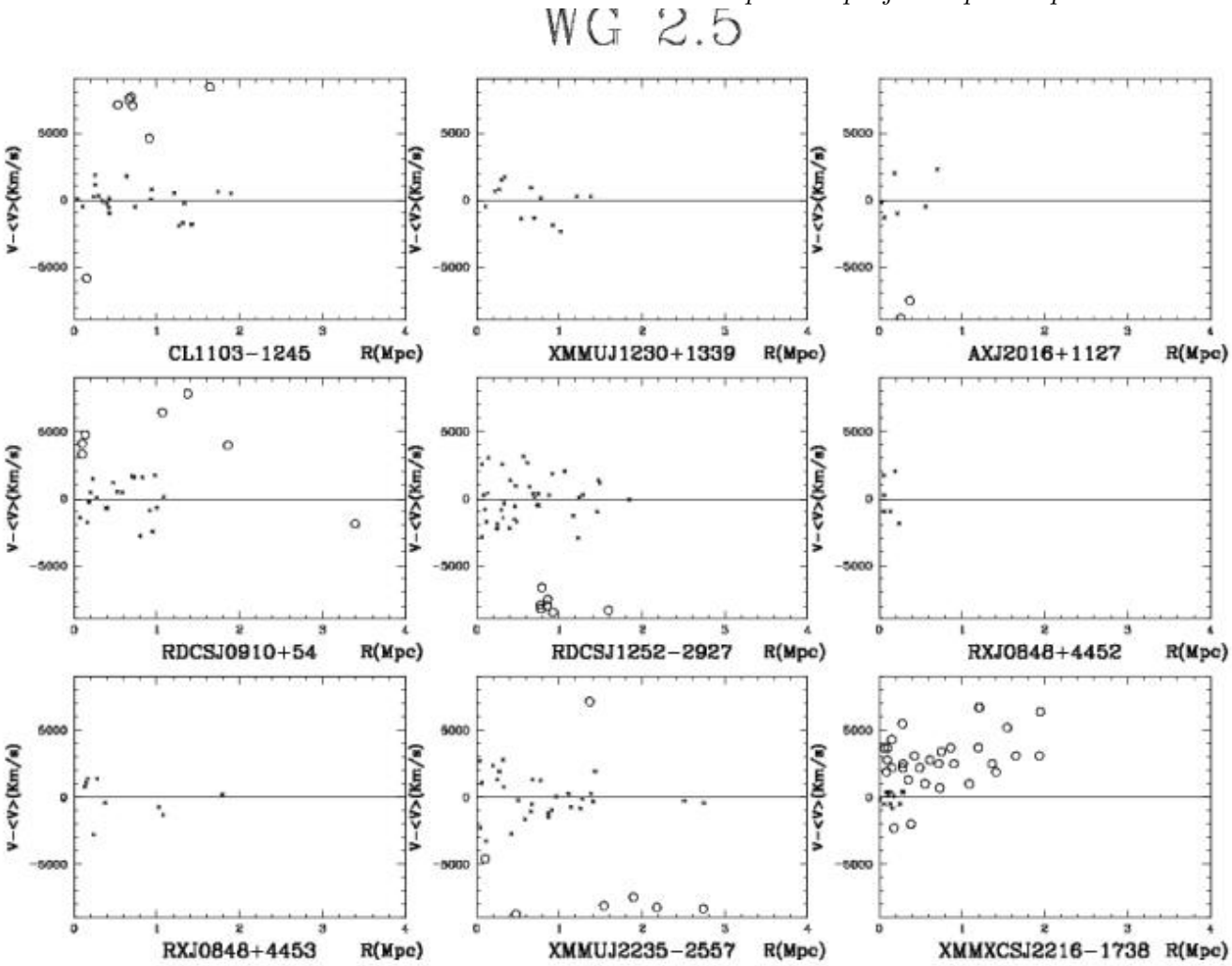

Figure A.5: Projected phase space derived by the WG 2.5 procedure.

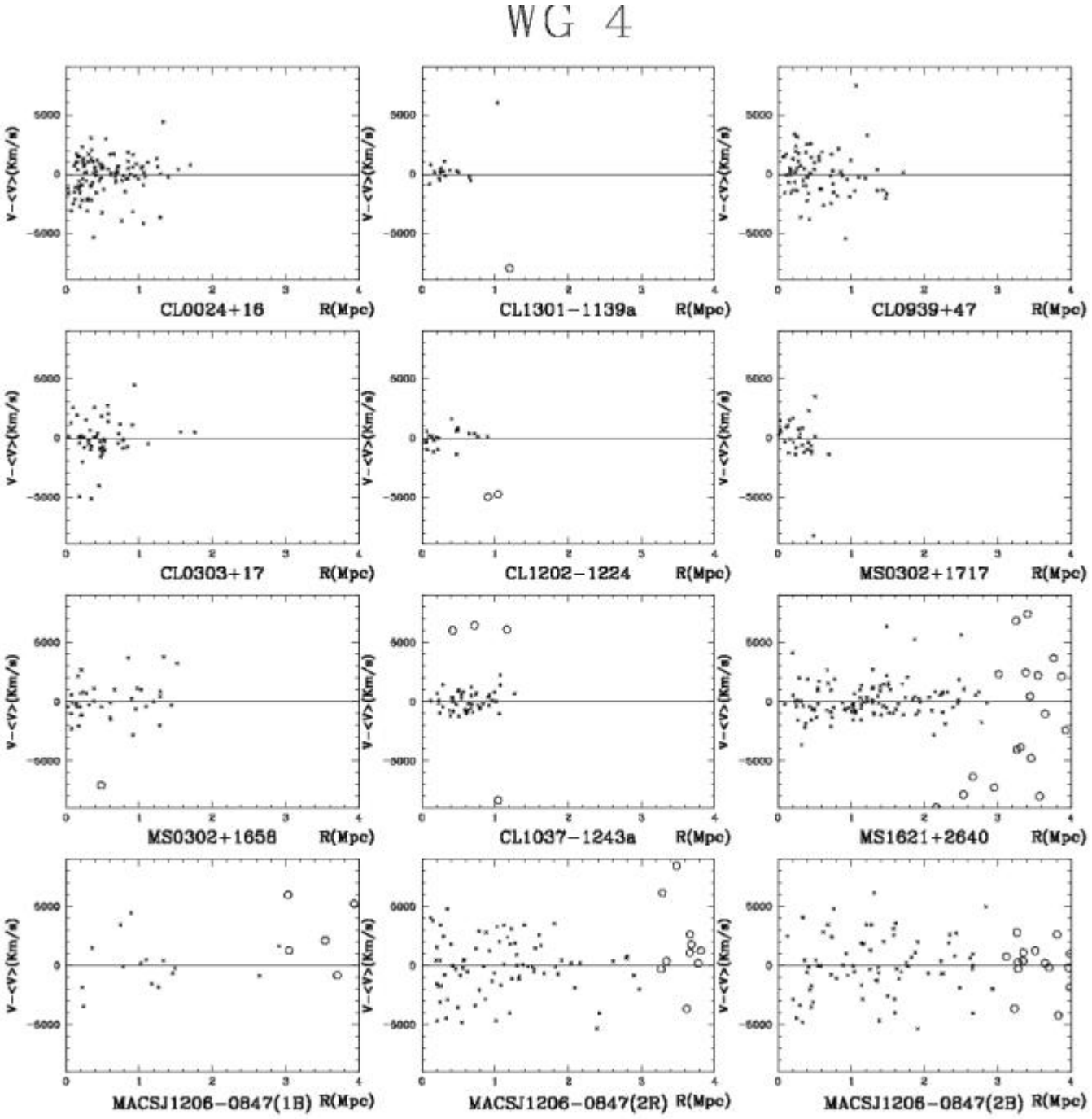
WG 4
V−<V>(Km/s)
R(Mpc)
CL0024+16
CL1301−1139a
CL0939+47
CL0303+17
CL1202−1224
MS0302+1717
MS0302+1658
CL1037−1243a
MS1621+2640
MACSJ1206−0847(1B)
MACSJ1206−0847(2R)
MACSJ1206−0847(2B)

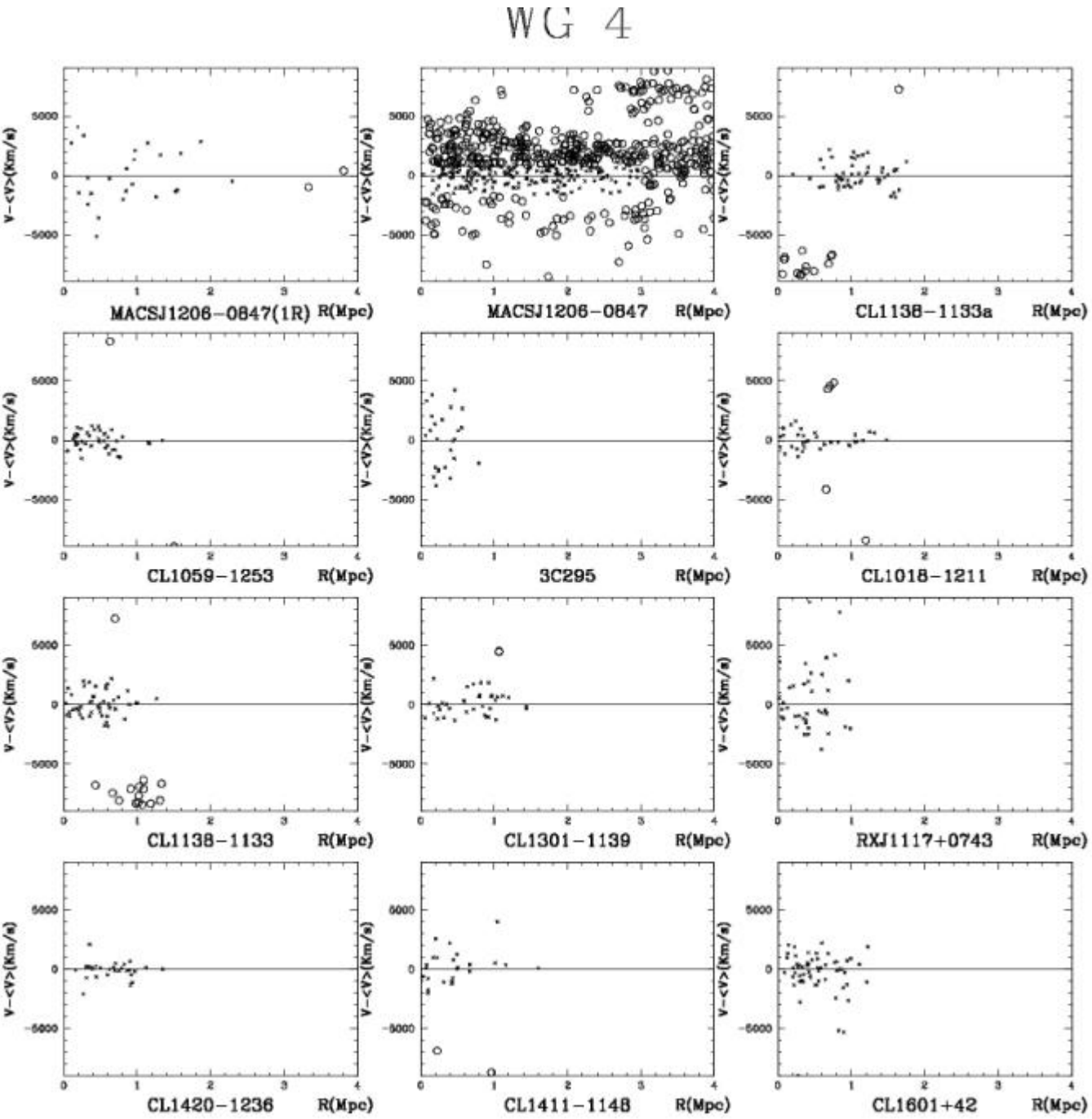
WG 4
V−<V>(Km/s)
R(Mpc)
MACSJ1206−0847(1R)
MACSJ1206−0847
CL1138−1133a
CL1059−1253
3C295
CL1018−1211
CL1138−1133
CL1301−1139
RXJ1117+0743
CL1420−1236
CL1411−1148
CL1601+42

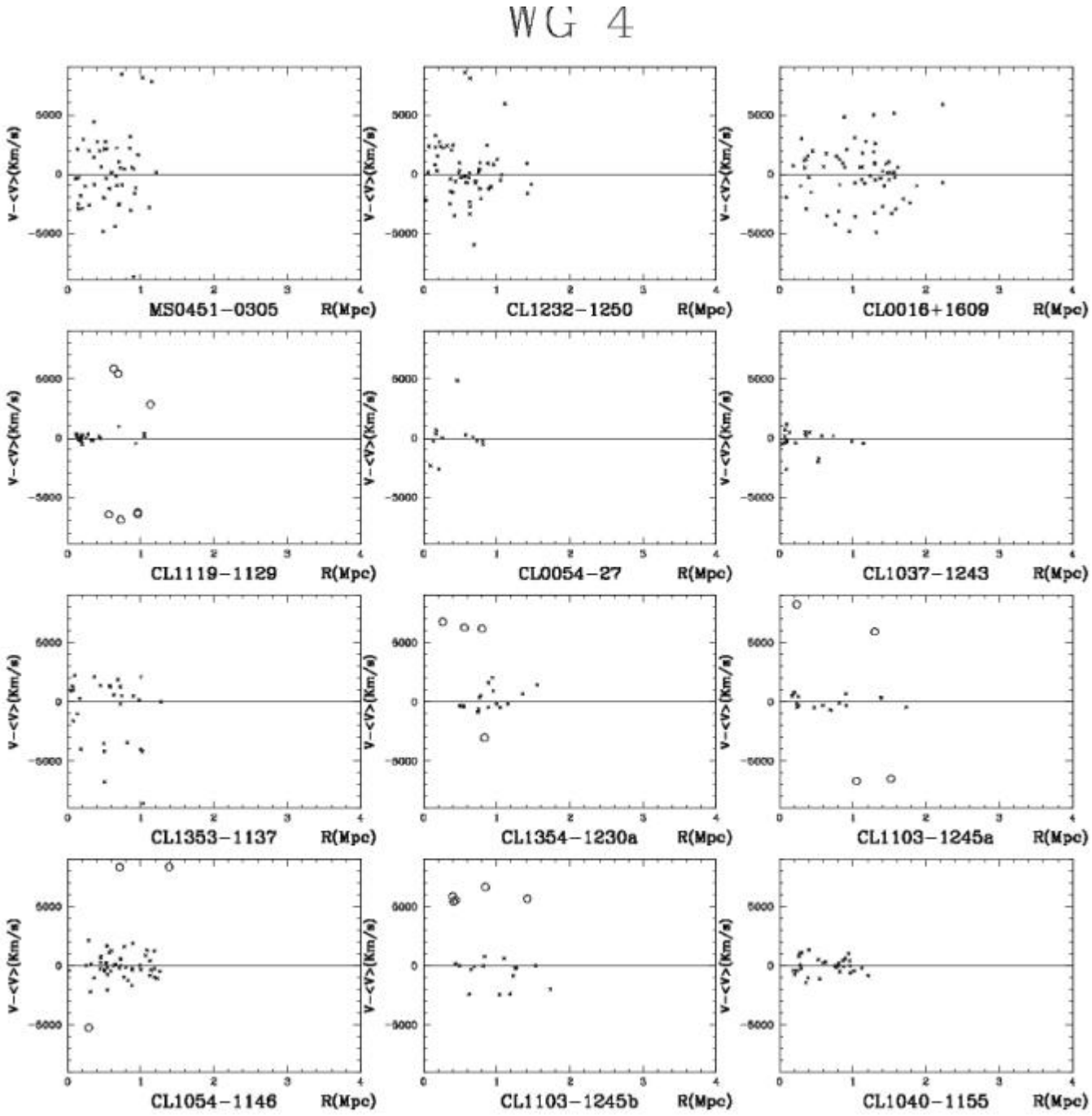
WG 4
MS0451−0305
CL1232−1250
CL0016+1609
CL1119−1129
CL0054−27
CL1037−1243
CL1353−1137
CL1354−1230a
CL1103−1245a
CL1054−1146
CL1103−1245b
CL1040−1155
V−<V>(Km/s)
R(Mpc)

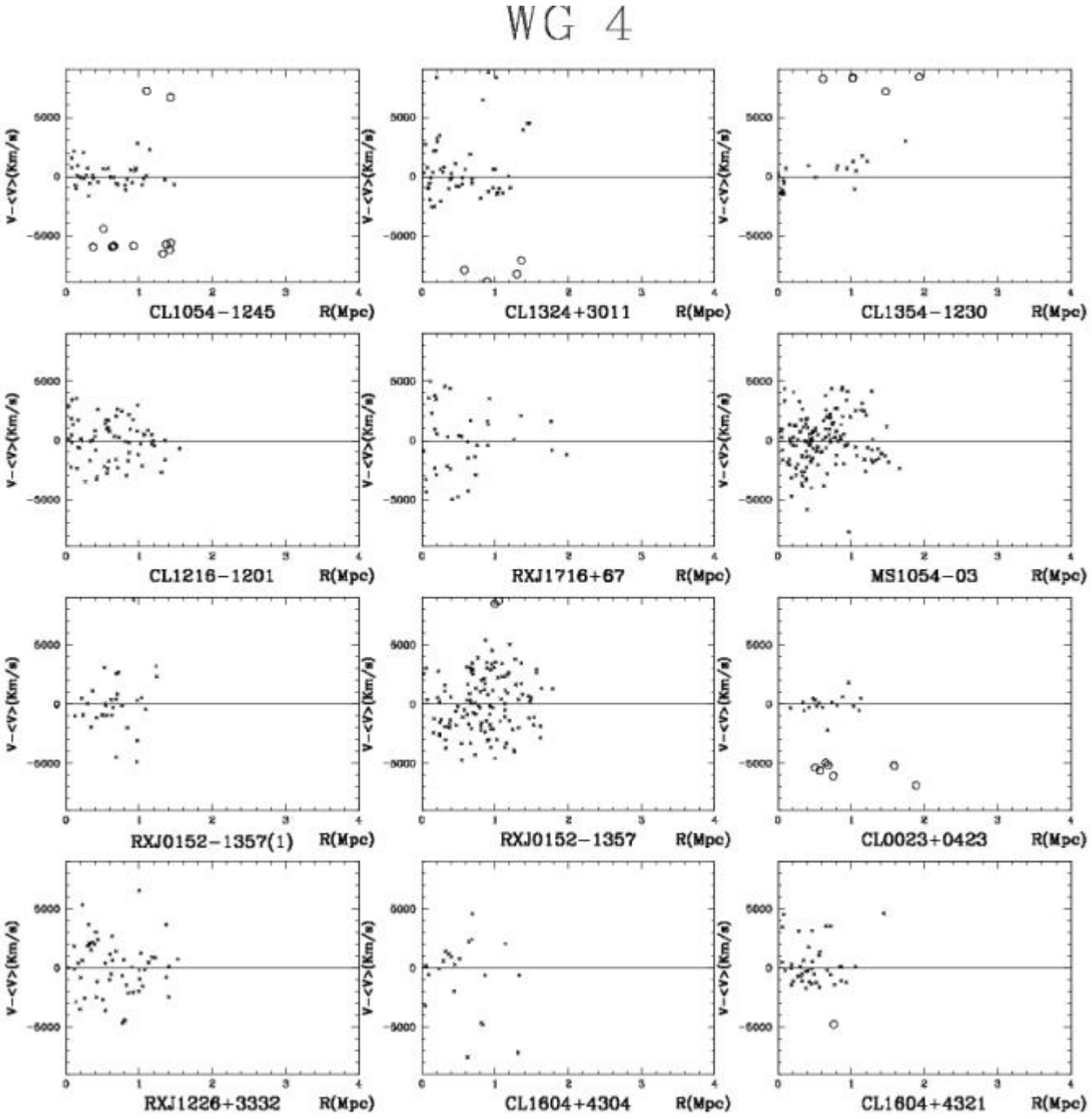
WG 4
V−<V>(Km/s)
R(Mpc)
CL1054−1245
CL1324+3011
CL1354−1230
CL1216−1201
RXJ1716+67
MS1054−03
RXJ0152−1357(1)
RXJ0152−1357
CL0023+0423
RXJ1226+3332
CL1604+4304
CL1604+4321

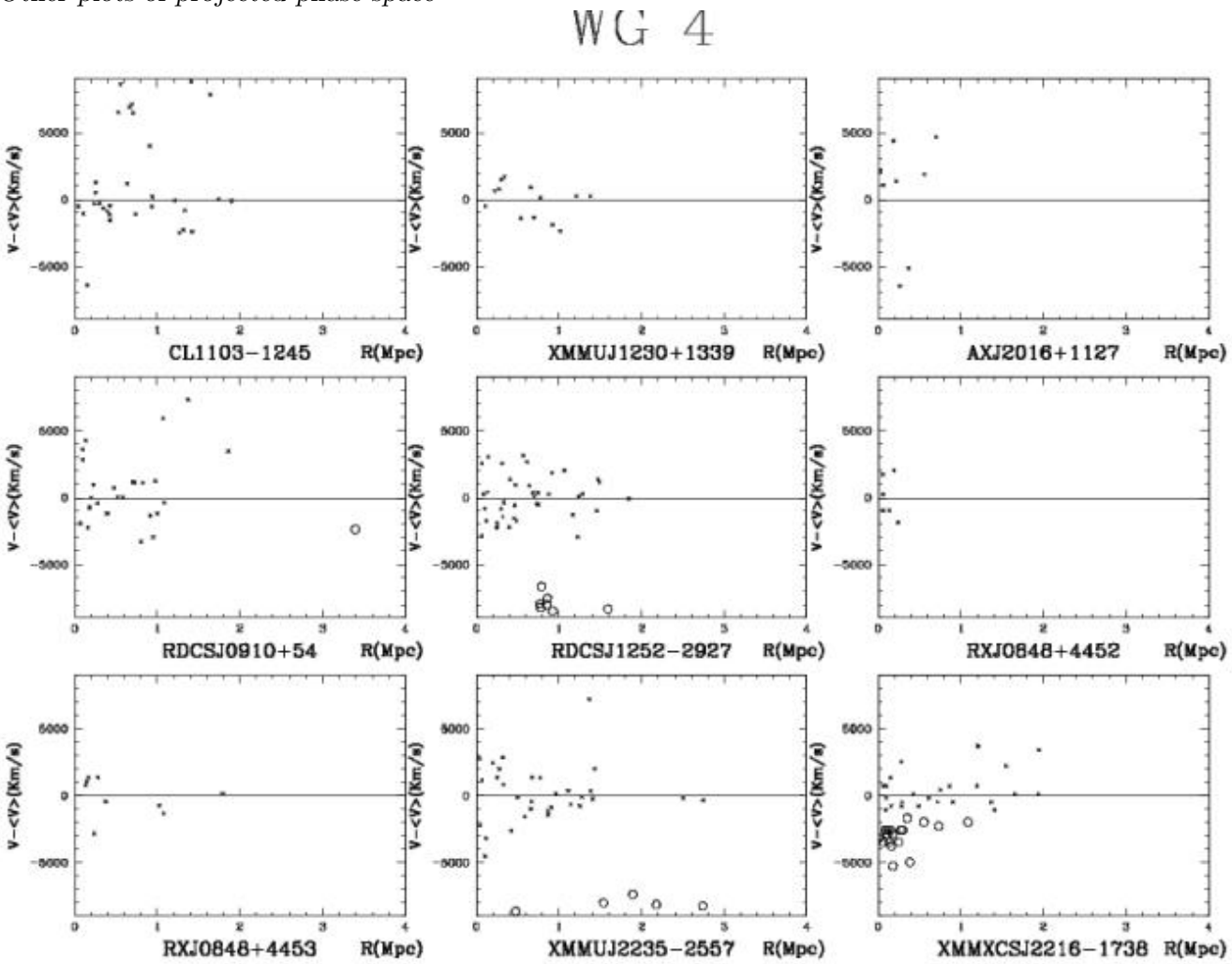

Figure A.6: Projected phase space derived by the WG 4 procedure.

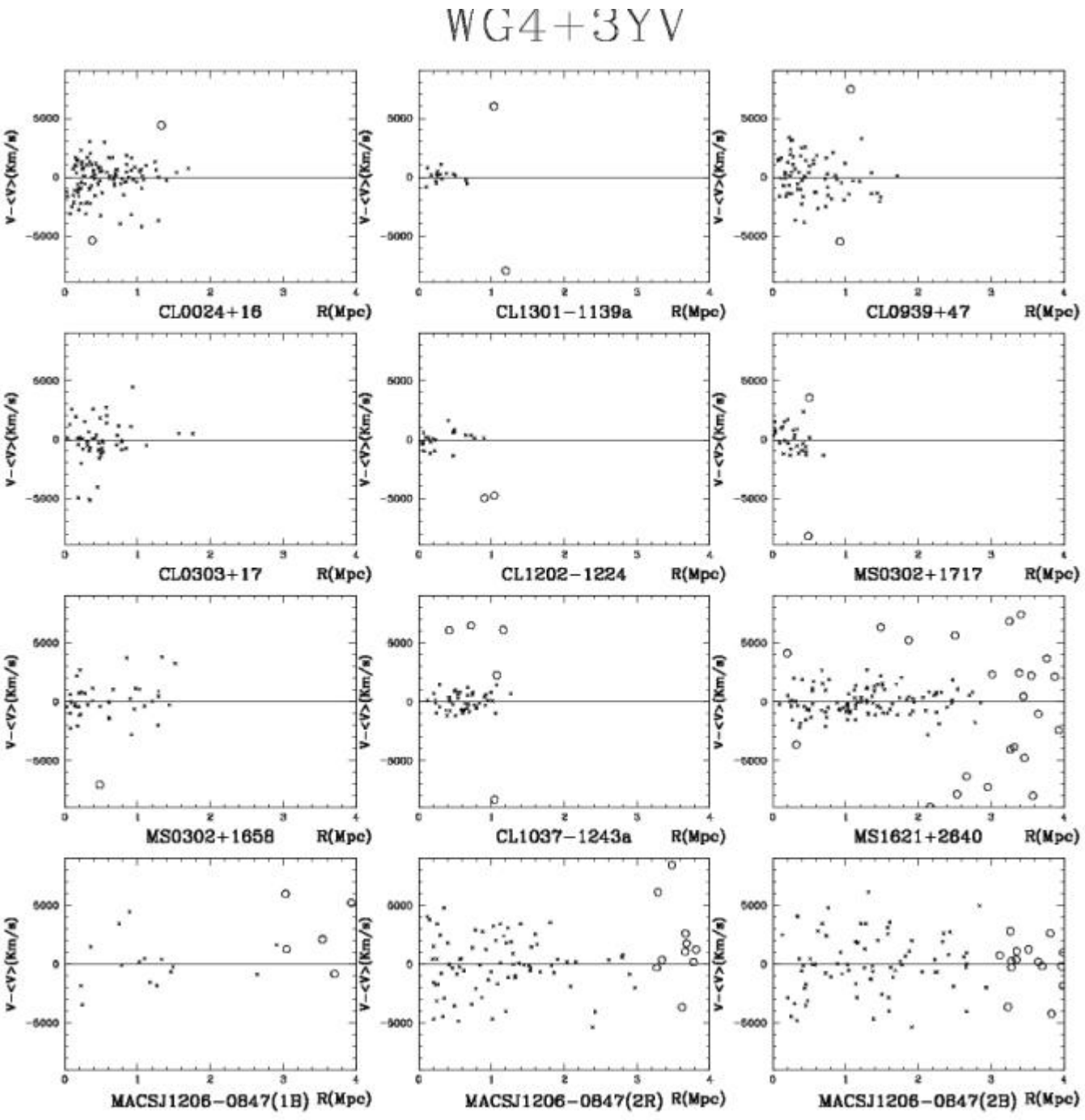
WG4+3YV
V−<V>(Km/s)
R(Mpc)
CL0024+16
CL1301−1139a
CL0939+47
CL0303+17
CL1202−1224
MS0302+1717
MS0302+1658
CL1037−1243a
MS1621+2640
MACSJ1206−0847(1B)
MACSJ1206−0847(2R)
MACSJ1206−0847(2B)

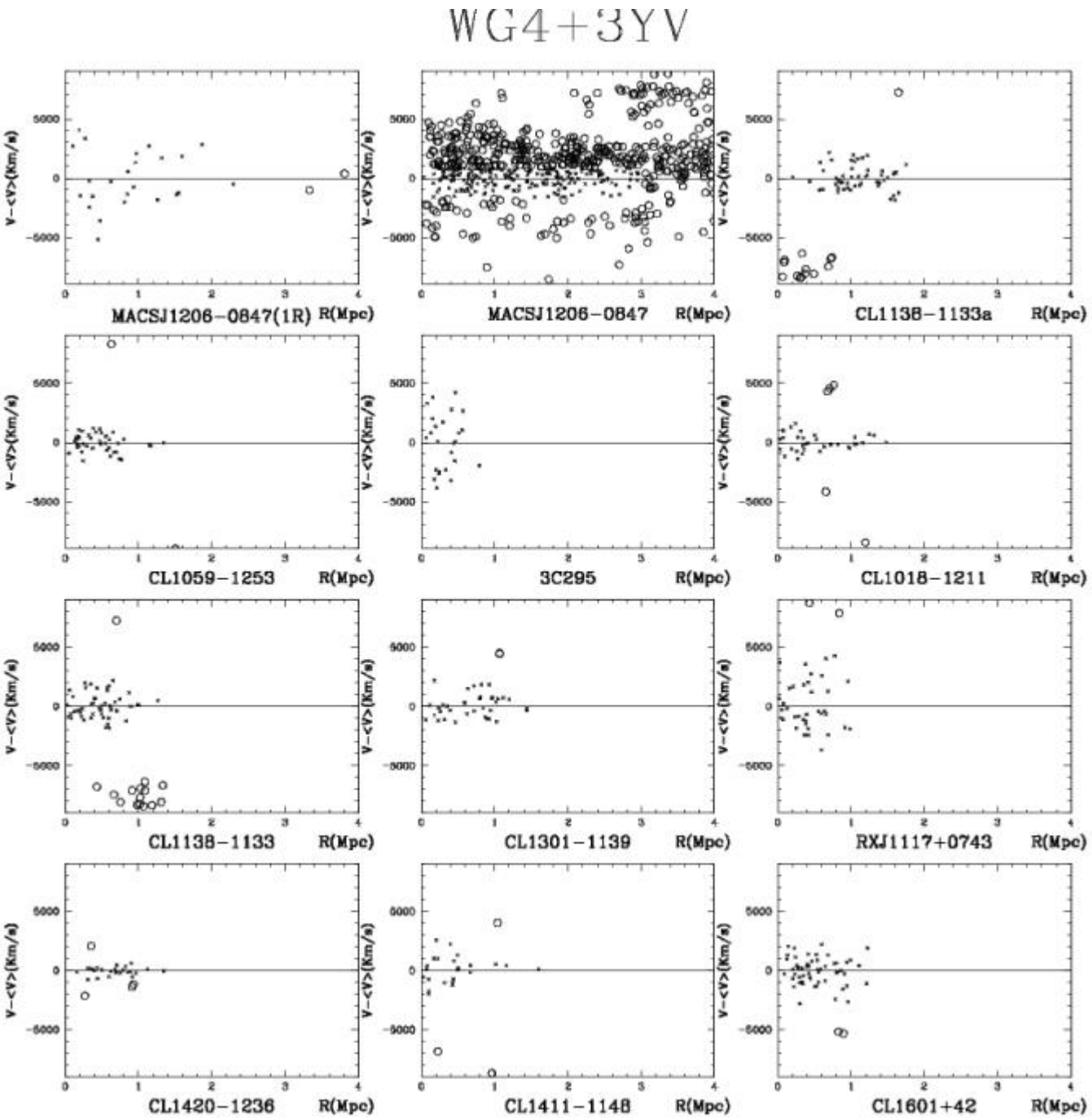
WG4+3YV
MACSJ1206−0847(1R)
MACSJ1206−0847
CL1138−1133a
CL1059−1253
3C295
CL1018−1211
CL1138−1133
CL1301−1139
RXJ1117+0743
CL1420−1236
CL1411−1148
CL1601+42
V−<V>(Km/s)
R(Mpc)

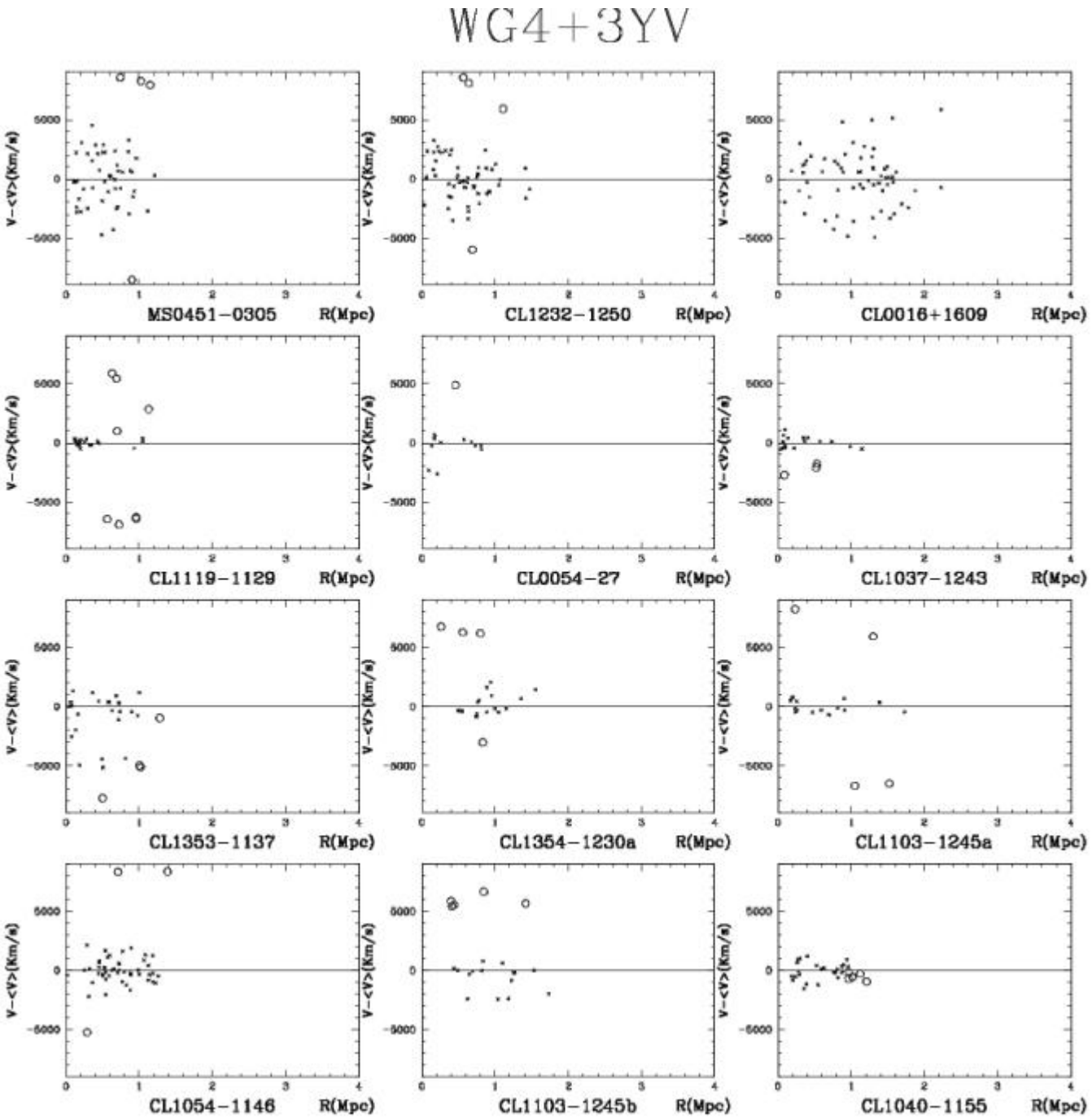
WG4+3YV
V−<V>(Km/s)
R(Mpc)
MS0451−0305
CL1232−1250
CL0016+1609
CL1119−1129
CL0054−27
CL1037−1243
CL1353−1137
CL1354−1230a
CL1103−1245a
CL1054−1146
CL1103−1245b
CL1040−1155

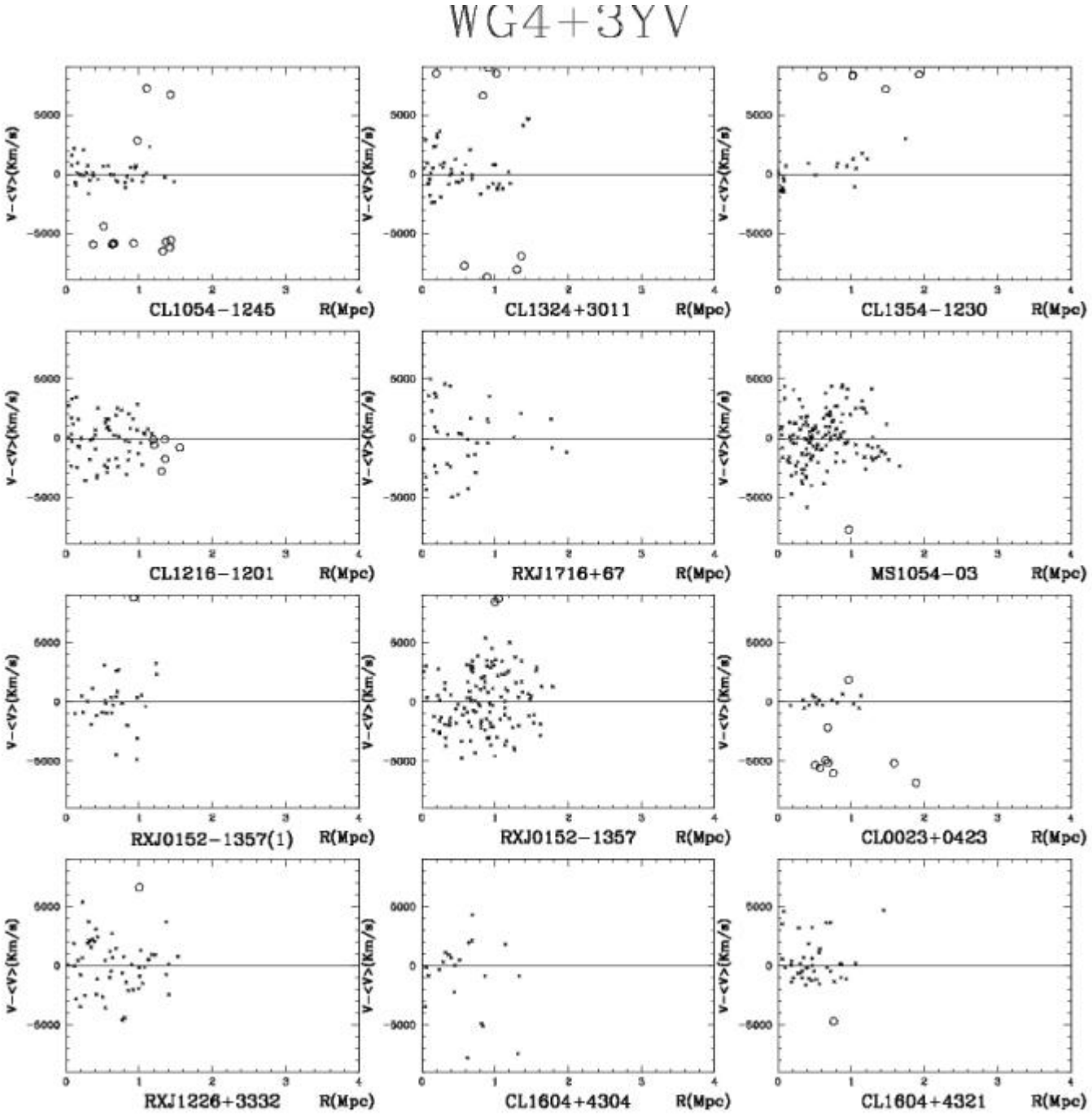
WG4+3YV
V−<V>(Km/s)
R(Mpc)
CL1054−1245
CL1324+3011
CL1354−1230
CL1216−1201
RXJ1716+67
MS1054−03
RXJ0152−1357(1)
RXJ0152−1357
CL0023+0423
RXJ1226+3332
CL1604+4304
CL1604+4321

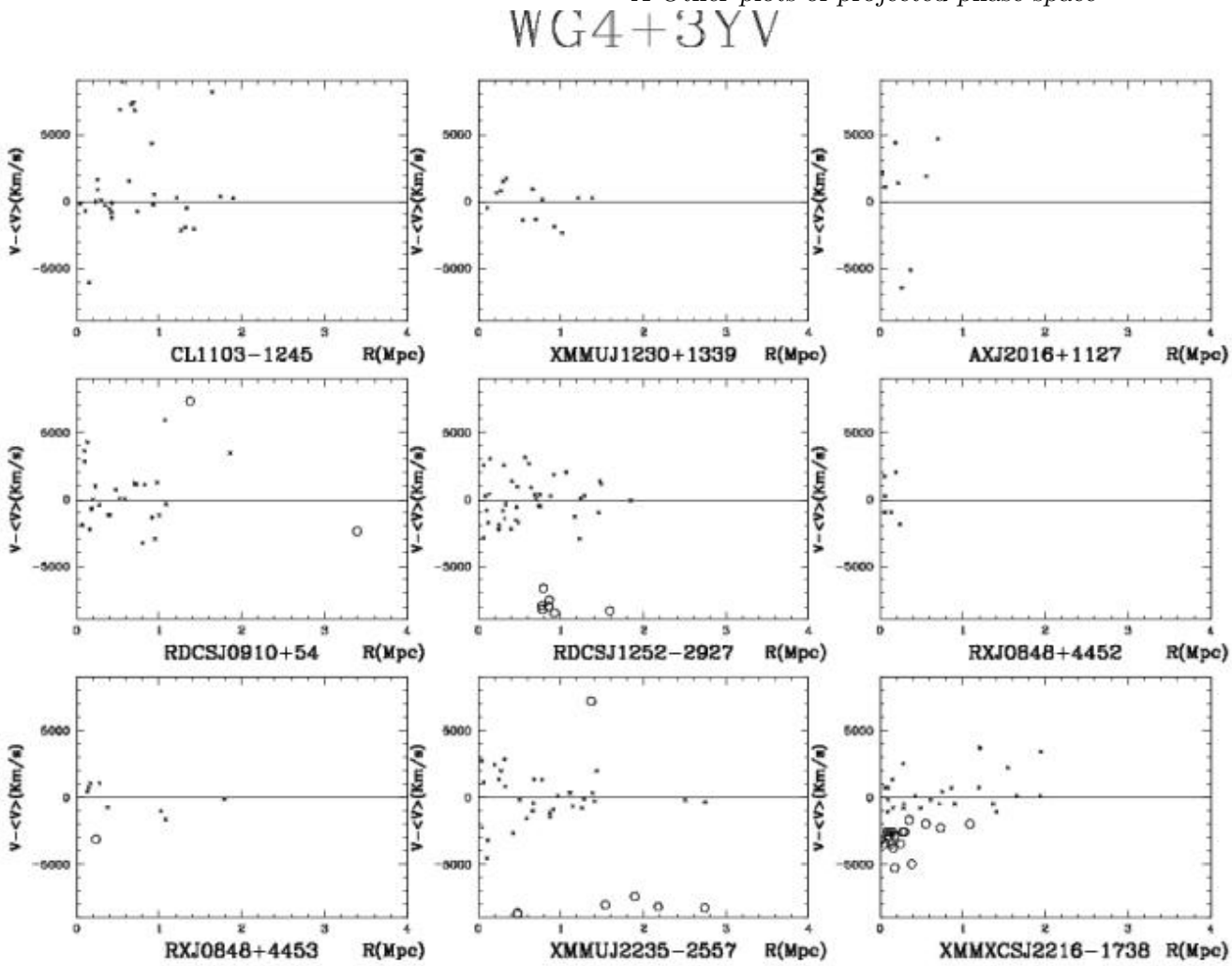

Figure A.7: Projected phase space derived by the WG4+YV procedure.

Appendix B

Robust velocity dispersion

A detailed examination of the kinematical properties of clusters requires the use of efficient statistical estimators which are insensitive to localized misbehavior in small datasets, resistant in the presence of outliers and robust for a broad range of non-Gaussian underlying populations. The standard deviation is the most commonly used estimator for the dispersion of a dataset, but it lacks both resistance and robustness. For this reason, we estimate the robust velocity dispersion using the biweight and the gapper estimators when the galaxy number is larger and smaller than 15, respectively (ROSTAT routines; see Beers et al., 1990).
In the estimators that follow, I make use of the so-called "order statistic" of a sample of n objects, defined from the data sorted in ascending order, i.e.,

$$x_i, x_{i+1}, ..., x_n, \tag{B.1}$$

where x_i is the ith smallest observation, and is referred to as the ith order statistic of the sample.

B.1 The biweight

The biweight velocity dispersion estimator S_{BI} is defined as

$$S_{BI} = n^{1/2} \frac{[\sum_{|u_i|<1} (x_i - M)^2 (1 - u_i^2)^4]^{1/2}}{|\sum_{|u_i|<1} (1 - u_i^2)(1 - 5u_i^2)|}, \tag{B.2}$$

where M is the sample median and u_i are given by

$$u_i = \frac{x_i - M}{c\text{MAD}}. \tag{B.3}$$

The constant c is known as the "tuning constant" and is chosen to give S_{BI} high efficiency for a broad range of distributions. The best balance of efficiency for the velocity dispersion estimator is found for $c = 9.0$. MAD is the median absolute deviation from the sample median and is defined as

$$\text{MAD=median}(|x_i - M|).$$

S_{BI} may be calculated with an iterative procedure or stopped after one step. The results are similar in both cases, since convergence is generally rapid, and usually requires no more than a few steps. For most samples the one-step estimator is sufficient. The biweight value

asymptotically approaches the standard deviation when the sample is taken from a Gaussian population. In the Gaussian situation (n=20) the biweight obtains 87% efficiency, instead, for deviation from the Gaussian distribution, it never dropped below 86% efficiency. However, this estimator does not perform well for samples as small as n=10.

B.2 The gapper

This estimator is based on the gaps between order statistics defined by

$$g_i = x_{i+1} - x_i, \qquad i = 1, ..., n-1 \tag{B.4}$$

and a set of approximately Gaussian weights:

$$w_i = i(n-i). \tag{B.5}$$

The gapper estimator is:

$$S_G = \frac{\sqrt{\pi}}{n(n-1)} \sum_{i=1}^{n-1} w_i g_i. \tag{B.6}$$

S_G possesses efficiency exceeding 90% for Gaussian samples as small as n=10, and moderately high efficiency for a variety of contaminated Gaussian samples.

Appendix C

Bootstrap and Jackknife errors

The bootstrap and jackknife methods belong to a class of "internal" error estimators based on dividing the data sample of galaxies into a set of similar subsamples. We name ξ the physical quantity for which we want to estimate the error.

C.1 Jackknife method

In the jackknife method, one forms a set of N copies of the original sample, each time leaving out one of the N galaxies. The covariance matrix, which represents the variation of each variable with respect to the others (included itself), is then estimated from:

$$C(\xi_i, \xi_j) = \frac{N-1}{N} \sum_{k=1}^{N} (\xi_i^k - < \xi_i >)(\xi_j^k - < \xi_j >), \tag{C.1}$$

where ξ_i^k is the measurement of ξ at separation r_i in the kth copy and $< \xi >$ is the mean of the N copies. However, for large samples the jackknife approach is impractical, since excluding a single galaxy has almost no effect. An alternative is to divide the full sample into N_{sub} disjoint subsamples, each containing N/N_{sub} galaxies. One can then proceed estimating a correlation function for N_{sub} jackknife copies of the original sample obtained by leaving out one subsample at a time.

C.2 Bootstrap technique

In the bootstrap method, one forms a set of N_{rs} resamplings of the original sample, each containing N galaxies (including duplicates) randomly picked from the original N galaxies with replacement (i.e. a galaxy is retained in the stack even if it has already been picked). Thus, although each resample consists of the same number of galaxies as the original sample, it will include some of the galaxies more than once, while others may not be included at all. In this case, the covariance matrix is estimated from:

$$C(\xi_i, \xi_j) = \frac{1}{N_{rs}} \sum_{k=1}^{N_{rs}} (\xi_i^k - < \xi_i >)(\xi_j^k - < \xi_j >), \tag{C.2}$$

where $< \xi >$ is the mean obtained from the N_{rs} resamplings. In practice for large samples, one chooses $N_{rs} << N$ but still large enough to provide a good measurement of the covariance matrix.

Appendix D

Statistical tests

I explain several statistical tests used in the kinematical analysis of clusters.

1. **t−test:** the t−test is a parametric test and assesses whether the means of two groups are statistically different from each other. I use this test to compare mean velocities obtained using different numbers of members estimated with different methods.

2. **F−test:** the F−test is a parametric test based on the analysis of variance and comparison between variances. It is used to test the null hypothesis, which affirms that the variances of two samples of data, representing the same physical quantity, are equal in statistical sense.

3. **Kolmogorov−Smirnov test:** the Kolmogorov−Smirnov test (KS test) is a nonparametric test of the equality of continuous, one-dimensional probability distributions that can be used to compare a sample with a reference probability distribution (one−sample KS test), or to compare two samples (two−sample KS test). The Kolmogorov−Smirnov statistic quantifies a distance between the empirical distribution function of the sample and the cumulative distribution function of the reference distribution, or between the empirical distribution functions of two samples in order to investigate if the two groups belong to the same population.
   In my case I use the two−sample KS test, which is one of the most useful and general nonparametric methods for comparing two samples, as it is sensitive to differences in both location and shape of the empirical cumulative distribution functions of the two groups.

4. **Wilcoxon test:** the Wilcoxon signed-rank test is a non-parametric statistical hypothesis test used when comparing two related samples, matched samples, or repeated measurements on a single sample to assess whether their population mean ranks differ.

5. **Sign test:** the sign test is a method to test for consistent differences between pairs of estimates of two samples. Given pairs of values, the sign test determines if one member of the pair tends to be greater than (or less than) the other member.
   The paired observations may be designated x and y. For comparisons of paired observations (x,y), the sign test is most useful if comparisons can only be expressed as x>y, x=y, or x<y. If, instead, the observations can be expressed as numeric quantities or as ranks, then the paired t-test or the Wilcoxon signed-rank test will usually have greater power than the sign test to detect consistent differences.
   If X and Y are quantitative variables, the sign test can be used to test the hypothesis that the difference between the median of X and the median of Y is zero, assuming continuous distributions of the two random variables X and Y, in the situation when we can draw

paired samples from X and Y. It can also test if the median of a collection of numbers is significantly greater than or less than a specified value.

The sign test is a non-parametric test which makes very few assumptions about the nature of the analyzed distributions - this means that it has very general applicability but may lack the statistical power of the alternative tests.

Appendix E

Results of the F−test

Table E.1 lists for all the 52 clusters the probabilities P that the values of velocity dispersion derived by the methods P+G, P+G(3Mpc) and P+G(1Mpc) are diverse, according to the F-test. When the value of probability is larger than 0.95, velocity dispersions are different.

Table E.1: Results of the F-test for the velocity dispersions obtained with the methods P+G, P+G(3Mpc) and P+G(1Mpc)

Cluster name	$P(\sigma_v$ vs $\sigma_{v,3\mathrm{Mpc}})$	$P(\sigma_v$ vs $\sigma_{v,1\mathrm{Mpc}})$	$P(\sigma_{v,3\mathrm{Mpc}}$ vs $\sigma_{v,1\mathrm{Mpc}})$
CL 0024+16	0.0000	0.4393	0.4393
CL 1301.7−1139a	0.0000	0.0000	0.0000
CL 0939+47	0.0000	0.2028	0.2028
CL 0303+17	0.0000	0.2031	0.2031
CL 1202.7−1224	0.0000	0.0000	0.0000
MS 0302.5+1717	0.0000	0.0000	0.0000
MS 0302.7+1658	0.0000	0.4832	0.4832
CL 1037.9−1243a	0.0000	0.4763	0.4763
MS 1621.5+2640*	0.1588	0.9451	0.9573
MACS J1206.2−0847*	0.8537	0.8120	0.9709
CL 1138.2−1133a	0.0000	0.6225	0.6225
CL 1059.2−1253	0.0000	0.1955	0.1955
3C 295	0.0000	0.0000	0.0000
CL 1018.8−1211	0.0000	0.3982	0.3982
CL 1138.2−1133	0.0000	0.1298	0.1298
CL 1301.7−1139	0.0000	0.3558	0.3558
RX J1117.4+0743	0.0000	0.0000	0.0000
CL 1420.3−1236	0.0000	0.6989	0.6989
CL 1411.1−1148	0.0000	0.2668	0.2668
CL 1601+42	0.0000	0.0788	0.0788
MS 0451.6−0305	0.0000	0.0188	0.0188
CL 1232.5−1250	0.0000	0.2425	0.2425
MS 0015.9+1609	0.0000	0.1349	0.1349
CL 1119.3−1129	0.0000	0.1580	0.1580
CL 0054−27*	0.0000	1.0000	1.0000
CL 1037.9−1243	0.0000	0.0489	0.0489
CL 1353.0−1137	0.0000	0.1524	0.1524

CL 1354.2−1230a	0.0000	0.6890	0.6890
CL 1103.7−1245a	0.0000	0.0228	0.0228
CL 1054.4−1146	0.0000	0.1750	0.1750
CL 1103.7−1245b*	0.0000	1.0000	1.0000
CL 1040.7−1155	0.0000	0.0649	0.0649
CL 1054.7−1245	0.0000	0.0270	0.0270
CL 1324+3011	0.0000	0.3382	0.3382
CL 1354.2−1230	0.0000	0.7149	0.7149
CL 1216.8−1201	0.0000	0.4288	0.4288
RX J1716+67	0.0000	0.2101	0.2101
MS 1054−03	0.0000	0.1012	0.1012
RX J0152.7−1357	0.0000	0.0046	0.0046
CL 0023+0423	0.0000	0.9458	0.9458
RX J1226.9+3332	0.0000	0.6017	0.6017
CL 1604+4304	0.0000	0.2890	0.2890
CL 1604+4321	0.0000	0.1158	0.1158
CL 1103.7−1245	0.0000	0.5951	0.5951
XMMU J1230.3+1339	0.0000	0.0167	0.0167
AX J2016+1127	0.0000	0.0000	0.0000
RDCS J0910+54	0.0681	0.4007	0.4535
RDCS J1252.9−2927	0.0000	0.1735	0.1735
RX J0848.9+4452	0.0000	0.0000	0.0000
RX J0848.6+4453	0.0000	0.7977	0.7977
XMMU J2235.3−2557	0.0000	0.6451	0.6451
XMMXCS J2215.9−1738	0.0797	0.1090	0.0334

NOTE.− * Clusters for which the F−test indicates a difference in at least one of the three comparisons.

I report in Table E.2 the probabilities P that the velocity dispersions derived by the methods P+G, ZHG, WG 2.5, WG 4 and WG4+YV aren't statistically the same. When the value of probability is larger than 0.95, velocity dispersions are different. The points "....." represent clusters which are excluded from the comparison because of their redshifts in disagreement with the P+G ones.

Table E.2: Results of the F-test for the velocity dispersions obtained with the methods P+G, ZHG, WG 2.5, WG 4 and WG4+YV

Cluster name	$P(\sigma_v$ vs $\sigma_{zhg})$	$P(\sigma_v$ vs $\sigma_{wg2.5})$	$P(\sigma_v$ vs $\sigma_{wg4})$	$P(\sigma_v$ vs $\sigma_{wg4+yv})$
CL 0024+16	0.6654	.....	0.9318	0.8025
CL 1301.7−1139a	0.0000	0.0000	0.0691	0.0000
CL 0939+47	0.0000	0.1516	0.7295	0.1516
CL 0303+17	0.0000	.....	0.8784	0.8462
CL 1202.7−1224	0.3651	0.0000	0.0000	0.0000
MS 0302.5+1717	0.3231	0.7192	0.7192	0.3231
MS 0302.7+1658	0.9057	0.9057	0.9364	0.9057
CL 1037.9−1243a	0.0000	0.3561	0.0000	0.3561
MS 1621.5+2640	0.6349	0.3276	0.9492	0.4787

MACS J1206.2−0847(1B)*	0.9582	0.9582	1.0000	1.0000
MACS J1206.2−0847(2R)*	0.9642	.....	0.9991	0.9642
MACS J1206.2−0847(2B)*	0.9996	.....	1.0000	0.9998
MACS J1206.2−0847(1R)*	0.9519	0.9788	0.9788	0.9519
MACS J1206.2−0847	.....	.....	.....	.....
CL 1138.2−1133a	.....	.....	.....	.....
CL 1059.2−1253	0.0000	0.0000	0.0000	0.0000
3C 295	0.0000	0.0000	0.0000	0.0000
CL 1018.8−1211	0.0000	0.0000	0.0000	0.0000
CL 1138.2−1133	0.0000	0.0000	0.0000	0.0000
CL 1301.7−1139	0.0000	0.9247	0.0000	0.0000
RX J1117.4+0743	0.0000	0.0000	0.9353	0.0000
CL 1420.3−1236	0.2202	0.3113	0.5099	0.6500
CL 1411.1−1148	0.0000	0.4199	0.4784	0.0000
CL 1601+42	0.0000	0.6765	0.5619	0.0000
MS 0451.6−0305*	0.6069	0.8839	0.9993	0.6069
CL 1232.5−1250	0.0000	0.2164	0.7016	0.0000
MS 0015.9+1609*	0.9913	0.9820	0.9996	0.9992
CL 1119.3−1129	0.0000	0.5094	0.0000	0.5094
CL 0054−27*	1.0000	1.0000	0.0000	0.8822
CL 1037.9−1243	0.9371	0.9371	0.0000	0.9371
CL 1353.0−1137*	0.0000	0.7408	.....	0.9894
CL 1354.2−1230a	0.0000	0.0000	0.0000	0.0000
CL 1103.7−1245a	0.0000	0.0000	0.0000	0.0000
CL 1054.4−1146	0.0000	0.0000	0.0000	0.0000
CL 1103.7−1245b	0.6465	0.0000	0.0000	0.0000
CL 1040.7−1155	0.0000	0.0000	0.0000	0.1621
CL 1054.7−1245*	0.3503	0.9757	0.3503	0.0000
CL 1324+3011*	0.0000	0.9872	0.9785	0.7272
CL 1354.2−1230	0.4302	0.4302	0.0000	0.0000
CL 1216.8−1201	0.0696	.....	0.1937	0.1980
RX J1716+67	.....	.....	.....	.....
MS 1054−03	0.1184	0.2726	0.2726	0.1184
RX J0152.7−1357(1)	0.6130	0.7189	0.7118	0.6130
RX J0152.7−1357	0.0000	.....	0.5595	0.0000
CL 0023+0423	0.1407	0.0000	0.5815	0.3651
RX J1226.9+3332*	0.8165	0.4974	0.9911	0.6760
CL 1604+4304*	0.3284	0.9998	0.9998	0.9991
CL 1604+4321*	0.7127	0.9798	0.9469	0.8933
CL 1103.7−1245*	0.0000	0.0000	1.0000	1.0000
XMMU J1230.3+1339	0.0000	0.0000	0.0000	0.0000
AX J2016+1127	0.0000	0.0000	.....	.....
RDCS J0910+54*	0.9623	0.3334	0.9707	0.9096
RDCS J1252.9−2927	0.0000	0.0000	0.0000	0.0000
RX J0848.9+4452	0.0000	0.0000	0.0000	0.0000
RX J0848.6+4453*	0.5534	0.9986	0.9999	0.5534
XMMU J2235.3−2557	.....	0.3187	0.3609	0.0000
XMMXCS J2215.9−1738	0.7063	.....	.....	.....

E Results of the F−test

NOTE.− * Clusters with one probability value larger than 0.95.

I compare the velocity dispersion values of the different cluster galaxy populations and I list the probability of difference in Table E.3.

Table E.3: Results of the F-test for the velocity dispersions related to the different galaxy populations

Cluster name	$P(\sigma_{blue}$ vs $\sigma_{red})$
CL 0024+16	0.6286
CL 1301.7−1139a	0.8802
CL 0939+47	0.5438
CL 0303+17*	0.9990
MS 0302.5+1717	0.7128
MS 0302.7+1658	0.7682
CL 1037.9−1243a	0.0460
MS 1621.5+2640	0.3495
MACS J1206.2−0847	0.9190
CL 1138.2−1133a	0.2763
CL 1059.2−1253	0.9356
3C 295	0.5243
CL 1018.8−1211	0.3017
CL 1138.2−1133*	0.9895
CL 1301.7−1139	0.8640
RX J1117.4+0743	0.9274
CL 1420.3−1236*	0.9505
CL 1411.1−1148	0.2986
CL 1601+42	0.2385
MS 0451.6−0305	0.3900
CL 1232.5−1250	0.1380
MS 0015.9+1609	0.5023
CL 1119.3−1129	0.3984
CL 1037.9−1243	0.7563
CL 1353.0−1137*	0.9913
CL 1354.2−1230a	0.4771
CL 1103.7−1245a	0.1580
CL 1054.4−1146*	0.9762
CL 1040.7−1155	0.4049
CL 1054.7−1245	0.3811
CL 1324+3011	0.8923
CL 1354.2−1230	0.5277
CL 1216.8−1201	0.0725
RX J1716+67	0.0375
MS 1054−03	0.8737
RX J0152.7−1357	0.9266
CL 0023+0423*	0.9910
RX J1226.9+3332	0.6987
CL 1604+4304*	0.9654
CL 1604+4321	0.4820

CL 1103.7−1245	0.9468
XMMU J1230.3+1339	0.3247
RDCS J0910+54	0.3607
RDCS J1252.9−2927	0.1359
XMMU J2235.3−2557	0.2608
XMMXCS J2215.9−1738	0.3185

NOTE.− * Clusters with one probability value larger than 0.95.

I write in Tables E.4 and E.5 the comparisons between $\sigma_{\mathrm{H}\alpha}$ (calculated for the Hα bright cluster members selected with the procedure based on the Hα limit flux: $F(\mathrm{H}\alpha)_{\mathrm{obs}} \geq 1 \times 10^{-16}$ erg cm^{-2} s^{-1}) and σ_{blue} (evaluated for the blue cluster members obtained with the technique which uses the color cuts and the EW[OII]s) for all the considered cluster member selection methods (P+G, ZHG, WG4+YV) applied to the sample A and the sample B (see Chapter 13 for the definition of these two samples), respectively. I consider only the velocity dispersions calculated for a number of Hα bright galaxies ≥ 5.

Table E.4: Sample A: results of the F-test for P+G, ZHG and WG4+YV

Cluster name	$P(\sigma_{\mathrm{H}\alpha,\mathrm{P+G}}$ vs $\sigma_{blue})$	$P(\sigma_{\mathrm{H}\alpha,\mathrm{ZHG}}$ vs $\sigma_{blue})$	$P(\sigma_{\mathrm{H}\alpha,\mathrm{WG4+YV}}$ vs $\sigma_{blue})$
CL 1216.8−1201	0.0475	0.0475	0.0475
RX J1716+67	0.3965	0.3965	0.3965
MS 1054−03	0.0589	0.5596	0.5596
RX J1226.9+3332*	0.2078	0.2078	0.2078

Table E.5: Sample B: results of the F-test for P+G, ZHG and WG4+YV

Cluster name	$P(\sigma_{\mathrm{H}\alpha,\mathrm{P+G}}$ vs $\sigma_{blue})$	$P(\sigma_{\mathrm{H}\alpha,\mathrm{ZHG}}$ vs $\sigma_{blue})$	$P(\sigma_{\mathrm{H}\alpha,\mathrm{WG4+YV}}$ vs $\sigma_{blue})$
CL 1216.8−1201	0.2354	0.2354	0.6978
RX J1716+67	0.1392	0.7120	0.7120
MS 1054−03	0.0589	0.5596	0.8068
RX J1226.9+3332	0.5791	0.4855	−

Appendix F

Results of the t−test

I use this test to compare the mean velocities obtained with different methods. Table F.1 lists the calculated probabilities p that the mean velocities derived by the methods ZHG, WG 2.5, WG 4 and WG4+YV are statistically diverse from those estimated by the P+G procedure. When the value of probability is larger than 0.95, mean velocities have a significant difference.

Table F.1: Results of the t-test for the mean velocities obtained with the methods P+G, ZHG, WG 2.5, WG 4 and WG4+YV

Cluster name	$\boldsymbol{p}\begin{pmatrix} < cz_g > \\ \text{vs} \\ < cz_{zhg} > \end{pmatrix}$	$\boldsymbol{p}\begin{pmatrix} < cz_g > \\ \text{vs} \\ < cz_{wg2.5} > \end{pmatrix}$	$\boldsymbol{p}\begin{pmatrix} < cz_g > \\ \text{vs} \\ < cz_{wg4} > \end{pmatrix}$	$\boldsymbol{p}\begin{pmatrix} < cz_g > \\ \text{vs} \\ < cz_{wg4+yv} > \end{pmatrix}$
CL 0024+16*	0.2800	0.9997	0.5139	0.4614
CL 1301.7−1139a	0.0000	0.0000	0.0000	0.0000
CL 0939+47	0.0000	0.1677	0.0614	0.1677
CL 0303+17*	0.0000	0.9918	0.0042	0.0309
CL 1202.7−1224	0.1647	0.0000	0.0000	0.0000
MS 0302.5+1717	0.2729	0.4093	0.4093	0.2729
MS 0302.7+1658	0.5608	0.5608	0.6133	0.5608
CL 1037.9−1243a	0.0000	0.1754	0.0000	0.1754
MS 1621.5+2640	0.0000	0.1557	0.0565	0.0592
MACS J1206.2−0847(1B)	0.1005	0.1005	0.0548	0.0548
MACS J1206.2−0847(2R)*	0.0651	0.9797	0.0940	0.0651
MACS J1206.2−0847(2B)*	0.6603	1.0000	0.5136	0.5274
MACS J1206.2−0847(1R)	0.6595	0.6413	0.6413	0.6595
MACS J1206.2−0847*	0.9663	1.0000	1.0000	1.0000
CL 1138.2−1133a*	1.0000	1.0000	1.0000	1.0000
CL 1059.2−1253	0.0000	0.0000	0.0000	0.0000
3C 295	0.0000	0.0000	0.0000	0.0000
CL 1018.8−1211	0.0000	0.0000	0.0000	0.0000
CL 1138.2−1133	0.0000	0.0000	0.0000	0.0000
CL 1301.7−1139	0.0000	0.8920	0.0000	0.0000
RX J1117.4+0743	0.0000	0.0000	0.1945	0.0000
CL 1420.3−1236	0.0914	0.2152	0.2921	0.1888
CL 1411.1−1148	0.0000	0.1188	0.1023	0.0000
CL 1601+42	0.0000	0.4544	0.0448	0.0000

			F Results of the t−test	
MS 0451.6−0305	0.2343	0.3561	0.1133	0.2343
CL 1232.5−1250	0.0000	0.0000	0.0035	0.0000
MS 0015.9+1609	0.9135	0.9341	0.8358	0.8294
CL 1119.3−1129	0.0000	0.0697	0.0000	0.0697
CL 0054−27	0.0244	0.0244	0.0000	0.0064
CL 1037.9−1243	0.3085	0.3085	0.0000	0.3085
CL 1353.0−1137*	0.0000	0.2780	0.9890	0.1401
CL 1354.2−1230a	0.0000	0.0000	0.0000	0.0000
CL 1103.7−1245a	0.0000	0.0000	0.0000	0.0000
CL 1054.4−1146	0.0000	0.0000	0.0000	0.0000
CL 1103.7−1245b	0.1434	0.0000	0.0000	0.0000
CL 1040.7−1155	0.0000	0.0000	0.0000	0.6584
CL 1054.7−1245	0.1094	0.6842	0.1094	0.0000
CL 1324+3011	0.0000	0.9002	0.7789	0.3680
CL 1354.2−1230	0.3167	0.3167	0.0000	0.0000
CL 1216.8−1201*	0.1801	1.0000	0.1743	0.5890
RX J1716+67*	0.9654	0.9654	0.9654	0.9654
MS 1054−03	0.1380	0.1372	0.1372	0.1380
RX J0152.7−1357(1)	0.2050	0.9353	0.1690	0.2050
RX J0152.7−1357*	0.0000	1.0000	0.0508	0.0000
CL 0023+0423	0.0256	0.0000	0.0637	0.1167
RX J1226.9+3332	0.3051	0.6042	0.2758	0.4378
CL 1604+4304	0.4362	0.8329	0.8329	0.5979
CL 1604+4321	0.5170	0.5835	0.8837	0.7560
CL 1103.7−1245	0.0000	0.0000	0.8081	0.4587
XMMU J1230.3+1339	0.0000	0.0000	0.0000	0.0000
AX J2016+1127*	0.0000	0.0000	0.9607	0.9607
RDCS J0910+54	0.9025	0.0334	0.9089	0.9158
RDCS J1252.9−2927	0.0000	0.0000	0.0000	0.0000
RX J0848.9+4452	0.0000	0.0000	0.0000	0.0000
RX J0848.6+4453	0.5308	0.0974	0.0676	0.5308
XMMU J2235.3−2557*	1.0000	0.2749	0.0597	0.0000
XMMXCS J2215.9−1738*	0.3632	1.0000	1.0000	1.0000

NOTE.− * Clusters with one probability value larger than 0.95.

Appendix G

Correlation coefficients

1. **Spearman's rank correlation coefficient:** this coefficient is a nonparametric measure of statistical dependence between two variables. It assesses how well the relationship between two variables can be described using a monotonic function. If there are no repeated data values, a perfect Spearman correlation of $+1$ or -1 occurs when each of the variables is a perfect monotone function of the other. A positive or negative Spearman correlation coefficient corresponds to an increasing or decreasing monotonic trend between X and Y, respectively. Spearman's coefficient, like any correlation calculation, is appropriate for both continuous and discrete variables, including ordinal variables.

2. **Kendall rank correlation coefficient:** it is a statistic coefficient used to measure the association between two measured quantities and is a measurement of rank correlation: the similarity of the orderings of the data when ranked by each of the quantities. If the agreement between the two rankings is perfect (i.e., the two rankings are the same) the coefficient has value 1. If the disagreement between the two rankings is perfect (i.e., one ranking is the reverse of the other) the coefficient has value -1. If X and Y are independent, then we would expect the coefficient to be approximately 0.

Appendix H

Literature tables used for the estimate of the Hα fluxes

The fit coefficients a_λ and b_λ for the $Color - (M_*/L)$ relation are calculated by Bell and de Jong (2001) for the Johnson filters and by Bell et al. (2003) for the Sloan system. They are presented in figure H.1:

STELLAR M/L RATIO AS A FUNCTION OF COLOR FOR THE FORMATION EPOCH MODEL WITH BURSTS, ADOPTING A SCALED SALPETER IMF

Color	a_B	b_B	a_V	b_V	a_R	b_R	a_I	b_I	a_J	b_J	a_H	b_H	a_K	b_K
$B-V$	−0.994	1.804	−0.734	1.404	−0.660	1.222	−0.627	1.075	−0.621	0.794	−0.663	0.704	−0.692	0.652
$B-R$	−1.224	1.251	−0.916	0.976	−0.820	0.851	−0.768	0.748	−0.724	0.552	−0.754	0.489	−0.776	0.452
$V-I$	−1.919	2.214	−1.476	1.747	−1.314	1.528	−1.204	1.347	−1.040	0.987	−1.030	0.870	−1.027	0.800
$V-J$	−1.903	1.138	−1.477	0.905	−1.319	0.794	−1.209	0.700	−1.029	0.505	−1.014	0.442	−1.005	0.402
$V-H$	−2.181	0.978	−1.700	0.779	−1.515	0.684	−1.383	0.603	−1.151	0.434	−1.120	0.379	−1.100	0.345
$V-K$	−2.156	0.895	−1.683	0.714	−1.501	0.627	−1.370	0.553	−1.139	0.396	−1.108	0.346	−1.087	0.314

Color	a_g	b_g	a_r	b_r	a_i	b_i	a_z	b_z	a_J	b_J	a_H	b_H	a_K	b_K
$u-g$	−0.221	0.485	−0.099	0.345	−0.053	0.268	−0.105	0.226	−0.128	0.169	−0.209	0.133	−0.260	0.123
$u-r$	−0.390	0.417	−0.223	0.299	−0.151	0.233	−0.178	0.192	−0.172	0.138	−0.237	0.104	−0.273	0.091
$u-i$	−0.375	0.359	−0.212	0.257	−0.144	0.201	−0.171	0.165	−0.169	0.119	−0.233	0.090	−0.267	0.077
$u-z$	−0.400	0.332	−0.232	0.239	−0.161	0.187	−0.179	0.151	−0.163	0.105	−0.205	0.071	−0.232	0.056
$g-r$	−0.499	1.519	−0.306	1.097	−0.222	0.864	−0.223	0.689	−0.172	0.444	−0.189	0.266	−0.209	0.197
$g-i$	−0.379	0.914	−0.220	0.661	−0.152	0.518	−0.175	0.421	−0.153	0.283	−0.186	0.179	−0.211	0.137
$g-z$	−0.367	0.698	−0.215	0.508	−0.153	0.402	−0.171	0.322	−0.097	0.175	−0.117	0.083	−0.138	0.047
$r-i$	−0.106	1.982	−0.022	1.431	0.006	1.114	−0.052	0.923	−0.079	0.650	−0.148	0.437	−0.186	0.349
$r-z$	−0.124	1.067	−0.041	0.780	−0.018	0.623	−0.041	0.463	−0.011	0.224	−0.059	0.076	−0.092	0.019

Figure H.1: Fit coefficients for the $Color - (M_*/L)$ relation taken from Bell and de Jong (2001) and Bell et al. (2003), and used in this thesis.

H Literature tables used for the estimate of the Hα fluxes

The solar values $M_{\odot}(\lambda)$ estimated by Binney and Merrifield (1998) for the Johnson filters and by Sparke and Gallagher (2007) for the Sloan system are reported in Table H.1:

Table H.1: Solar absolute magnitudes

Filter	$M_{\odot}(\lambda)$
U	5.61
B	5.48
V	4.83
R	4.42
I	4.08
J	3.64
H	3.32
K	3.28
u	6.55
g	5.12
r	4.68
i	4.57
z	4.60

The values of the fit coefficients a and b for the SFR$-M_*$ relation are computed by Whitaker et al. (2014) and are listed in figure H.2. In this study, I use the estimates of a and b for the redshift ranges $0.5 < z < 1.0$ and $1.0 < z < 1.5$.

Broken Power-law Fits

Redshift Range	a_{low}	a_{high}	b
$0.5 < z < 1.0$	0.94 ± 0.03	0.14 ± 0.08	1.11 ± 0.03
$1.0 < z < 1.5$	0.99 ± 0.04	0.51 ± 0.07	1.31 ± 0.02
$1.5 < z < 2.0$	1.04 ± 0.05	0.62 ± 0.06	1.49 ± 0.02
$2.0 < z < 2.5$	0.91 ± 0.06	0.67 ± 0.06	1.62 ± 0.02

Figure H.2: Fit coefficients for the SFR$-M_*$ relation: the characteristic mass is fixed at $\log(M_*/M_{\odot}) = 10.2$ (Whitaker et al., 2014).